European volcanological supersite in Iceland: a monitoring system and network for the future

Report

D5.5 - Earthquake location in a three-dimensional structure

Work Package:	*Long-term magma tracking*
Work Package number:	*5*
Deliverable:	*Earthquake location in a three-dimensional structure*
Type of Activity:	*RTD*
Responsible activity leader:	*Andy Hooper*
Responsible participant:	*Uppsala University*
Authors:	*Claudia Abril, Olafur Gudmundsson*

Type of Deliverable:	Report	[X]	Demonstrator	[ ]
	Prototype	[ ]	Other	[ ]
Dissemination level:	Public	[X]	Restricted Designated Group	[ ]
	Prog. Participants (FP7)	[ ]	Confidential (consortium)	[ ]

Seventh Framework Programme
EC project number: 308377

Abstract

This report is deliverable 5.5 of Workpackage 5 on "Long-term magma tracking", of the FutureVolc project (A European Volcanological Supersite in Iceland: A Monitoring System and Network for the Future). The main goal of the research reported on here is to improve the monitoring and, in general, the understanding of seismicity associated with volcanic and tectonic processes. For this purpose an earthquake relocation routine has been developed to improve the initial location estimation of earthquakes recorded by the South Iceland Lowlands (SIL) network of the Icelandic Meteorological Office (IMO), considering three-dimensional Earth structure.

The relocation routine applies a nested grid-search algorithm in a 30x30x30 km^3 volume surrounding the location estimate of the existing SIL system and uses three-dimensional empirical travel-time tables (ETTs) constructed for both P- and S-waves as input, together with estimates of errors in observations. ETTs and error estimates have been determined for 65 SIL stations using arrival-time data for about 300.000 located earthquakes from 1990 to 2012. The routine is insensitive to which 1D model has been used to estimate the previous location. It determines event depth relative to sea level.

The empirical travel times are estimated independently for P- and S-wave picks and are very strongly correlated for the two wave types. Nearby stations are also strongly correlated for both wave types. The spatial variation of the residuals is consistently comparable or somewhat less for S waves than P waves. This is a surprizing, but robust feature of the results which suggests relatively strong variations of the V_P/V_S ratio in the icelandic crust. Error estimates are also strongly correlated for the two wave types and between nearby stations.

Relocations result in modestly enhanced clustering of explosions and earthquakes, but we have not completed testing the relocations against well-located events in dense temporary networks. Uncertainty estimates of the relocated events are statistically better behaved than those of the current SIL system and should be more realistic than for the SIL locations. They are in general reduced, as is expected since three-dimensional heterogeneity is now taken into account. The empirical travel times can serve as a "cleaned" data set for local-earthquake tomography of the Icelandic crust, which in turn may be used to refine the ETTs.

Contents

1 Introduction

The current location software of the SIL system was written in the 1980's. It employs classical methods involving travel-time prediction in a one-dimensional velocity model, iterative linearization of the relationship between arrival-time observations and location and as uncertainties of the observations are not known the software uses pre-assigned weights determined based on the distance of each observation from its earthquake source and based on the phase type (P and S).

Earthquake location is a tiny inverse problem for modern computers. It involves what are generally redundant observations of arrival times that relate to only four parameters of location, namely origin time, latitude, longitude and depth, when the velocity structure is assumed to be known. The relationship between these observations and the 3 spatial location parameters is non linear, while their relation with origin time is linear. There is no need to linearize and iteratively solve this problem. It is effectively solved by an exhaustive grid search, which can trivially be nested in order to speed up the calculation. Extensive research was done in the 1990s exploring and developing non-linear search methods for earthquake location (e.g. Lomax et al. (2000)). The advantage of using such methods lies in the reduced risk of locking the location in a local minimum of misfit, i.e. not finding the global minimum, which is the optimal solution. Another advantage is that grid-search methods map the misfit surface completely and, thus, define the error of the location fully. This may not have a Gaussian distribution in space (and time), as is generally assumed for the classical, iterative, linearized solution. However, non-linear, grid-search methods are forced to assume a specific value distribution, which is done through the choice of norm used to define misfit. An L_2 norm is appropriate for a Gaussian value distribution, which is usually assumed, while an L_1 norm corresponds to a double-exponential distribution. We evaluate that assumption later. In the end, the quality of SIL earthquake locations can be significantly improved by modernizing its location software.

To treat the error of location properly we need to know the statistics of observational errors and treat the non-linearity of the problem fully. The grid search provides the latter. But, this is perhaps not worth so much if we do not know the error statistics. It is important to establish realistic estimates of error statistics to take full advantage of new methods of earthquake location (grid search). Error estimates of SIL earthquake locations can be significantly improved by more realistic error treatment.

The crust in volcanic areas is known to be very heterogeneous. For Iceland, specifically, we have a fairly robust idea about the level of heterogeneity in the upper crust, e.g. based on the comprehensive work of Palmason (1974), but also numerous subsequent studies of crustal structure (e.g. Bjarnarson et al. (1993); Gudmundsson et al. (1994); Staples et al. (1997); Tryggvason et al. (2002); Li and Detrick (2006); Gudmundsson et al. (2007), Schuler et al. (2015)). Such strong velocity heterogeneity will distort lo-

cations of earthquakes if not accounted for. By employing a one-dimensional velocity model the SIL network locations are affected. The SIL locations of the aftershocks of the May 28th, 2008 Olfus dual earthquake were demonstrably shifted by several hundreds of metres (Brandsdottir et al., 2008). Refined locations within dense networks of seismographs deployed in various parts of the neo-volcanic zones of Iceland have consistently demonstrated systematic bias in SIL depth determinations, which are too deep by several km (Jing, 2013; Jeddi et al., 2016). Therefore, it is important to account for the three-dimensional structure of the Icelandic crust to improve the precision of SIL earthquake locations.

Accounting for the effects of three-dimensional velocity structure on earthquake location requires a three-dimensional travel-time table for each seismograph contributing to the location. Such travel-time tables can be estimated in one of two ways. One is to build a three-dimensional model for the crust and predict the travel times based on that. The natural way of building that model is by local-earthquake tomography (LET). The other is to derive the travel-time tables directly from observations. We refer to such travel-time tables as empirical travel times (ETT).

In detail, the former strategy involves inversion of the same arrival-time data that are used for earthquake location for varying crustal velocity structure and earthquake locations simultaneously. Both parts (structure inversion and event relocation) of this inverse problem are non linear. This problem is much more complex than the earthquake-location problem alone. It involves many more parameters and through mutual dependence of the earthquake-location parameters on velocity structure all of the events become coupled. The method requires three-dimensional ray tracing or wave-front tracking to predict travel-time data and to construct ray paths and sensitivity kernels for velocity structure (Iyer and Hirahara, 1993; Aster et al., 2005). One complication with local-earthquake tomography is the uneven density of information. The seismographs of the SIL network are unevenly distributed throughout Iceland, but more significantly, the seismicity distribution is very uneven and clustered. Any parameterization that attempts to capture the small-scale velocity variations will risk parts of the velocity model being underdetermined by the information provided by data. Thus, the problem must be regularized. All available regularization strategies are global in nature. Therefore, it is difficult to tune the inversion to account for detailed structure where that might be resolved (e.g. Sambridge and Gudmundsson (1997)). Another complication lies in the coupling of earthquake-location parameters and velocity structure involving a common trade off between primarily origin time, event depth and velocity structure, which is very difficult to elucidate.

The latter strategy (ETT) requires a unique mapping of observed residuals for a given station to points in space. Previous work with this strategy has made use of preliminary earthquake locations for this mapping (Schultz et al., 1998; Nicholson et al.,

2004). First, measured arrival times are reduced to travel times using the preliminary origin times. Then these travel times are projected to the preliminary earthquake locations. This defines travel time as a three-dimensional function that is irregularly sampled at the earthquake locations. That can then be statistically analysed, e.g., by Kriging (Schultz et al., 1998) or generalized cross validation (Nicholson et al., 2004) in order to interpolate the function between its irregularly spaced samples and to estimate its spatially incoherent component, i.e. error. These are the choices we have for this strategy applied to the SIL catalog. The catalog consists of hundreds of thousands of events that are generally located with an uncertainty on the order of a kilometer. The origin time is uncertain by approximately 0.1 s. These uncertainties will unavoidably be transferred to the estimated travel times.

We have chosen the latter strategy for the following reasons:

- The ETT approach is limited in its spatial resolution by the mapping of travel times to uncertain preliminary event locations. But, so is the tomographic approach, e.g., through non-transparent trade off between structure and event locations and because its structural problem is inherently spatially aliased in parts.

- We estimate that the resolution limit of LET for the Icelandic crust as a whole based on SIL data is no better than about 10 km Tryggvason et al. (2002). Even with densified networks by temporary deployment the lateral resolution limitation is often quite severe. Jonsdottir et al. (2007) reported a lateral resolution no better than 7.5 km at Katla volcano in southern Iceland and Jeddi et al. (2016) report a lateral resolution of about 5 km despite a considerably denser network. Where deployments have been even denser a higher level of resolution has been achieved Schuler et al. (2015), but the sparser SIL network sees an aliased picture of that. Of course, we only have high-resolution tomographic information from limited areas, where high density deployments have been maintained over significant time periods. For most of Iceland the SIL network provides the highest quality information available. Therefore, the ETT approach will generally offer higher spatial resolution of travel-time estimation than predicted travel times based on tomographic results.

- The ETT estimation process is more direct and transparent than the local-earthquake tomography and allows for estimation of observational errors.

One limitation of the ETT approach is that it performs no consistency check between the travel-time tables for different stations. However, the stations of the SIL network are sufficiently sparse (typically at least 15 km apart) and the typical frequency of the picked phases sufficiently high (typically 10-15 Hz) that we can always find a physically feasible model to explain their differences.

Having completed the estimation of empirical travel-time tables and relocated events according to them, we have a refined earthquake catalog with cleaned arrival-time data where inconsistencies have been removed. This refined catalog lends itself well to application of the tomographic approach in which we can expect better refined locations than based on the raw arrival-time picks. The ETT estimation can then be further revised. This is beyond the scope of the present study, but remains an objective of our team.

One detail of the current SIL earthquake location system is somewhat irritating to users of the data who need to pay attention to focal depth. The depth estimate for each event is referenced to the average elevation of the nearest observing stations. In other words, the events have a floating depth reference. We have avoided this problem and reference our depth estimation explicitly to sea level and a specific reference velocity model.

In the following we describe first a detailed analysis of the SIL arrival-time observations that are used for earthquake location. We then describe how we reduce them, resulting in both estimates of empirical travel-time tables and arrival-time uncertainty. We continue to describe the modernized methodology of earthquake location and finally its effect, using both our estimates of empirical travel times and our estimates of uncertainty, on relocations of the entire SIL catalog. We conclude with a discussion about measures of the improvement of locations and about possible future directions of research and method improvement.

Many details of our estimation process are presented in appendices as well as details of the provided program to relocate SIL events, that is set up to work as an additional step to the system that is already in routine use. Therefore, two catalogs are naturally maintainable, i.e. a catalog which continues the practices of the SIL network as they have been, and a catalog of reanalyzed event locations from the past appended with reanalyzed future events with the methods outlined here. It is important to maintain both catalogs over time for comparison.

2 Data

The SIL network had 75 registered seismic stations at the end of 2012, distributed through the most seismically and volcanically active areas of Iceland. The SIL catalog had about 370.000 located earthquakes recorded from 1990 to 2012 and more than 2 million P-wave and 2.2 million S-wave arrival-time picks. We have limited our analysis to events with at least 6 arrival-time picks. This reduces the number of events to about 300.000. We have further limited our analysis to stations with at least 1200 picks of either P or S wave arrivals. This limits the number of stations to 65. All 75 stations of the SIL network are shown on a map in Figure 1 with those excluded from analysis

labelled with a red colour. The epicentres of all analyzed events in the catalog are shown in Figure 2. We have worked with all the arrival-time/travel-time information of the SIL database from this period. The data set we have used is a subset of the SIL catalog, obtained after a cleaning process. We have carefully checked the data for inconsistencies that we have corrected where we have been able to identify their cause. Otherwise, outliers have been removed from the data. In the subsequent relocation, only events with at least 6 arrival-time picks are relocated. Events with fewer piks are simply not relocated.

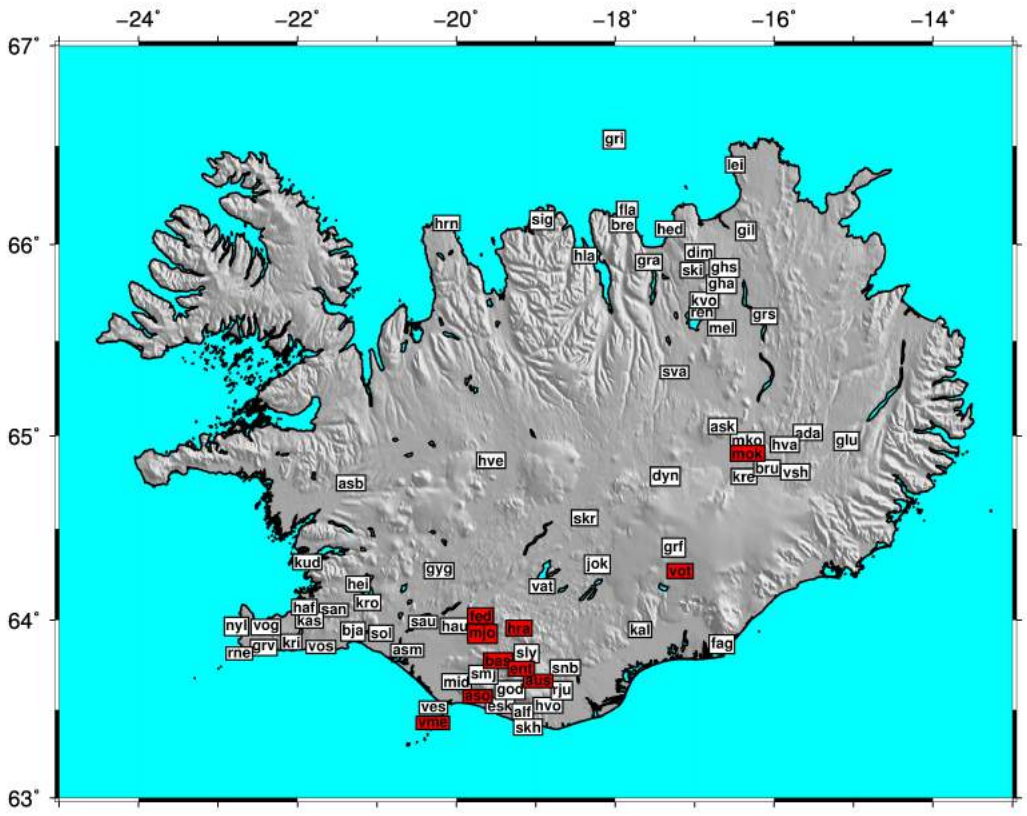

Figure 1: Distribution of stations in the SIL network. The stations for which we have estimated empirical travel times have a white background. Those that have been excluded from the analysis have a red background.

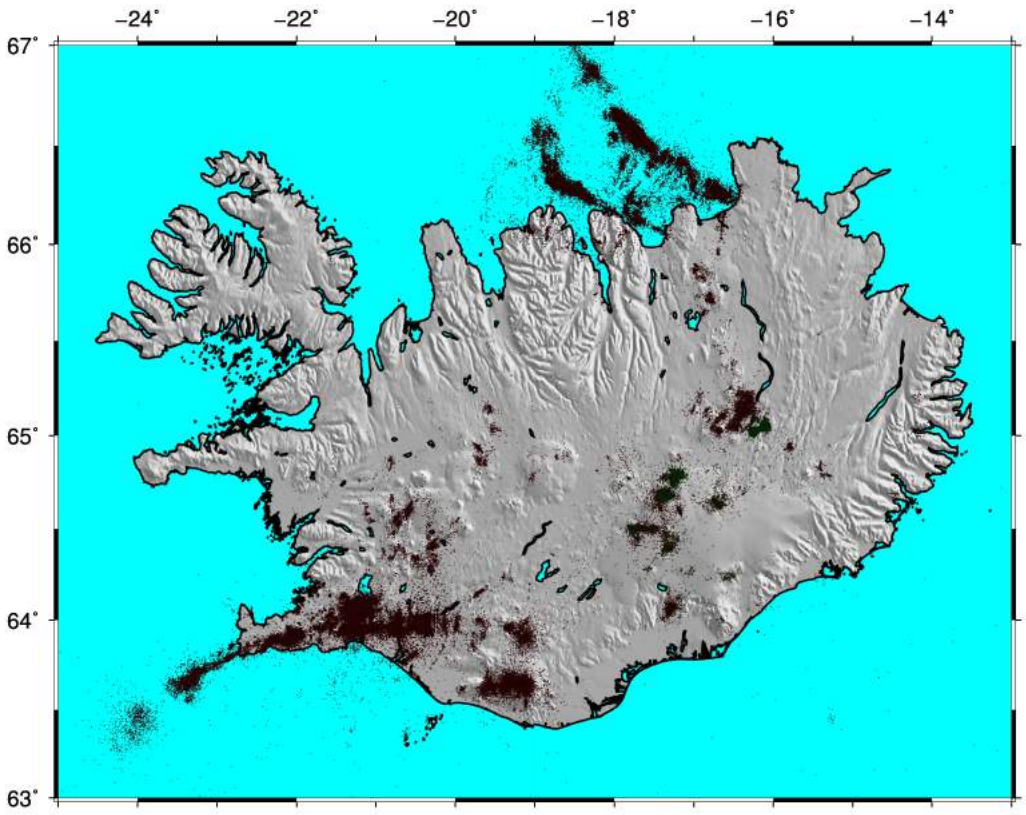

Figure 2: Map of seismicity recorded from 1990 to 2012 by the SIL network.

First we plotted all travel times for a given station against epicentral distance and source depth. This helped identify some inconsistencies in the data. Events in the SIL catalog have been located using the following five 1-D velocity models:

1. SIL
2. Northern
3. Iceland
4. Teleseismic
5. Vatnajökull

These are regional approximations of the crustal velocity structure for different regions of the country.

We identified two main classes of problems with the data. First, occasional discrepancies in archived travel-time reduction, sometimes identified as erroneous registration of the reference model, sometimes simply manifest as a discrepancy between registered arrival time and reduced travel time. These were corrected when possible, otherwise removed. Second, a small portion of the reduced travel times were found to lie more than two standard deviations away from the mean of their distribution. These were identified as outliers and removed. After editing discrepancies and removing outliers we have homogenized the dataset by referring all of it to a single model (the SIL model).

3 Construction of travel-time tables and error estimation

The basic observations that are used in earthquake location are arrival-time measurements from seismograms. In order to account for three-dimensional heterogeneity in refined event locations we need a description of travel times in the three-dimensional earth. Following previous approaches to estimate empirical travel times (ETTs) we use existing locations of the events in the catalog as a reference (Schultz et al., 1998; Nicholson et al., 2004). The existing reference location provides both an estimate of origin time and spatial location. We use this origin time to reduce all measured arrival times to travel times. We then project all estimated travel times on to the estimated event location in space (Nicholson et al., 2004). We can then regard the estimated travel times as a three-dimensional function $T(\mathbf{x})$ that is irregularly sampled. We describe this function as a combination of four terms

$$T(\mathbf{x}) = T_0(\mathbf{x}) + dT_d(\mathbf{x}) + dT_r(\mathbf{x}) + \delta T(\mathbf{x}) \tag{1}$$

The first is the predicted travel time for the given event and station locations in the one-dimensional reference velocity model, T_0. The second describess the average deviations of the observed residuals from the above reference. We refer to this component as deterministic, dT_d, simply because we evaluate it by smoothing or averaging over a prescribed scale. This estimation is equivalent to the empirical heterogeneity corrections of Piromallo and Morelli (2001). We ascribe the remainder of the travel-time residuals to small-scale random variations, dT_r , and error, δT.

We distinguish the last two terms (random terms) of this decomposition by their spatial coherence. The random structural component, dT_r, is assumed to possess spatial coherence, while the error component, δT, is assumed to be spatially incoherent.

The objective of defining a deterministic residual, dT_d, is simply to reduce the non-stationarity of the remaining residual. We define the first three terms in equation (1) as the empirical travel time T_{ETT}

$$T_{ETT}(\mathbf{x}) = T_0(\mathbf{x}) + dT_d(\mathbf{x}) + dT_r(\mathbf{x}) \tag{2}$$

As discussed in the introduction, the mapping of travel times on to a preliminary event location is inaccurate because the preliminary location is uncertain. Therefore, the error in the above description is not simply a picking error. It also includes an error of reference, i.e. an error of the origin time used to reduce measured arrival time to a travel time. Furthermore, the mapping is imprecise because of errors in the spatial coordinates of the earthquake location. To the extent that these reference errors are random in a given region they will be incoherent and will be absorbed in the error term in equation (1). Any spatial bias of the starting-event location will map into an error in the ETT.

3.1 Prediction of the reference velocity model

The first travel-time component in equation (1) is calculated with a ray tracer for a one-dimensional reference velocity model. We choose to use the SIL model for reference. The ray tracer assumes a nodal representation of a continuous velocity model and interpolates linearly between the nodes. It makes use of analytical solutions for both incremental epicentral distance and travel time in each layer of linear velocity variation. It is used to construct irregularly sampled travel time as a function of distance and source depth, which is then interpolated to construct a regularly sampled travel-time table. Rays are traced up to sea level without considering the specific elevation of each station. However, the station elevation will simply manifest itself as a distance dependent correction, which will be absorbed in the remaining components of equations (1) and (2). In this way, the refereece model is anchored at sea level and event locations based on this estimate of travel time will explicitly be referenced to sea level. The ray tracer is tested to be accurate to within approximately one millisecond at distances less than 150 km. Figure 3 shows the P and S velocities of the SIL model. Figure 4 shows travel times in these models for a station at sea level. The travel time differences between the models are less than 2 seconds at distances up to 150 km, excluding the model labeled “teleseismic”. This model has a strange V_P/V_S ratio near the surface and its “teleseismic” label is a misnomer. It is not used to locate events as far a field as 3000 km.

As a result of this calculation we have redefined the predicted travel time for a one-dimensional velocity model, which we choose as the SIL velocity model. This defines the term $T_0(\mathbf{x})$ in equations (1) and (2). It is important to note that we have taken care with the reference in depth. The computed travel time is referenced to sea level.

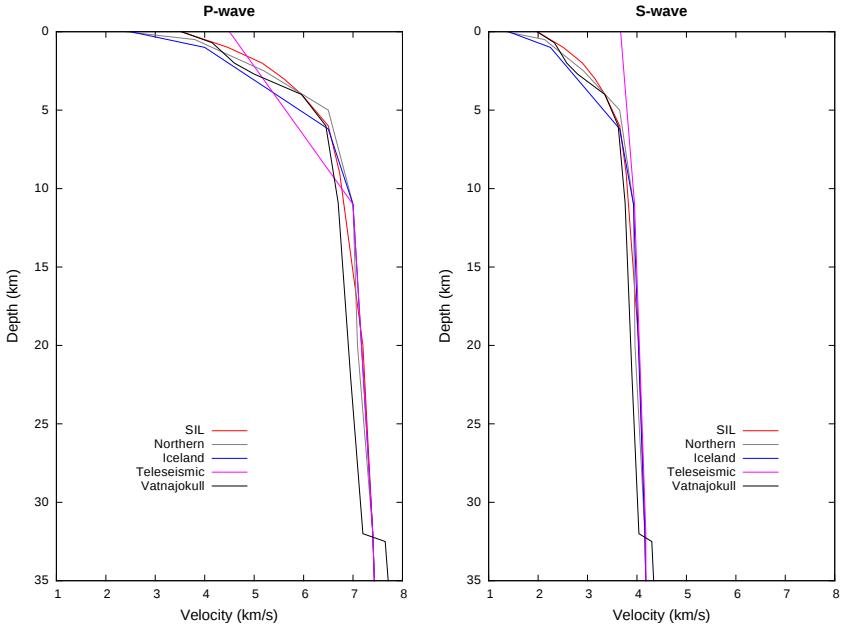

Figure 3: 1-D velocity models used to locate events in the SIL catalog. These are regional approximations of the crustal velocity structure for different regions in Iceland.

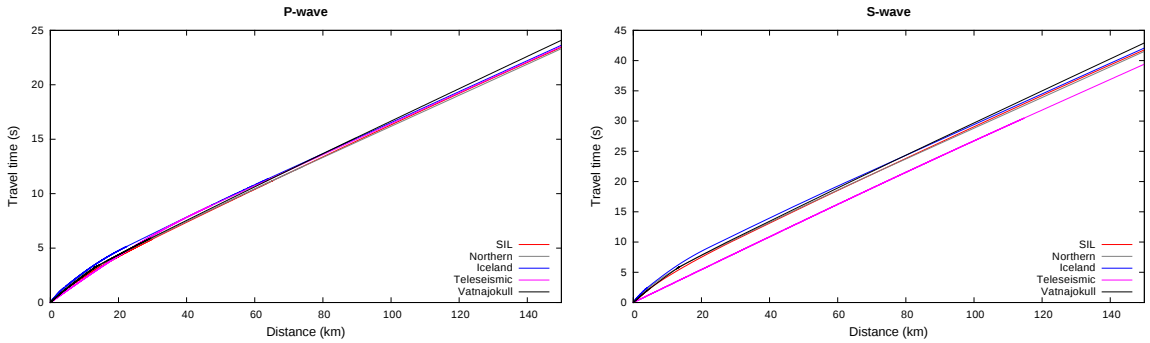

Figure 4: Travel times in the models in Figure 3 for a source at the surface.

3.2 The deterministic component

The second and third components of equations (1) and (2) are estimated from the travel-time residuals of the SIL database redefined with reference to the reworked predictions described above. The second component can be regarded as variations of travel time caused by broad heterogeneities in crustal structure or empirical heterogeneity corrections (Piromallo and Morelli, 2001). This term is introduced in order to reduce spatial non-stationarity in the residuals. This component is estimated for each station of the SIL network by two-dimensional interpolation using a moving average over a Gaussian function with a half width of 10 km. The third component can be

regarded as due to small-scale random variations of velocity structure.

The maps in Figure 5 show examples of the deterministic component of P-wave residuals for stations ada and sol. The continuous-colour scale shows a smoothed interpolant of the residuals at the irregular distribution of earthquake epicentres for the specific stations. The contours indicate the combined weights of the data contributing to the estimate at each point. A summary of maps, identical to those presented in Figure 5, is compiled in Appendix A for all the stations (65) in the SIL network for which we have substantial data. The smoothed residuals are shown together for the P and S waves at each station for comparison. The P and S residuals behave similarly where the data density is substantial. We have also gathered plots of the P-wave residuals at adjacent stations in Appendix B and of S-wave residuals at adjacent stations in Appendix C for comparison. Again, there is considerable coherence from one station to the next.

The maps in Figure 6 show the remaining travel-time residuals after removing the smoothed interpolated deterministic term for stations ada and sol. An overview for all stations is presented in Appendix D in the same format. Figure 7 shows examples of distribution histograms of these reduced residuals and their distribution vs. epicentral distance for the same pair of stations. A summary of these residuals is presented in Appendix E for comparison. The mean residual varies little with epicentral distance where the statistics are substantial. The width of the residual distribution generally increases with distance.

After the deterministic component has been estimated and subtracted, the remaining travel-time residuals are treated as stochastic. The stochastic component is assumed to consist of a structural signal with spatial coherence and noise, which is spatially incoherent.

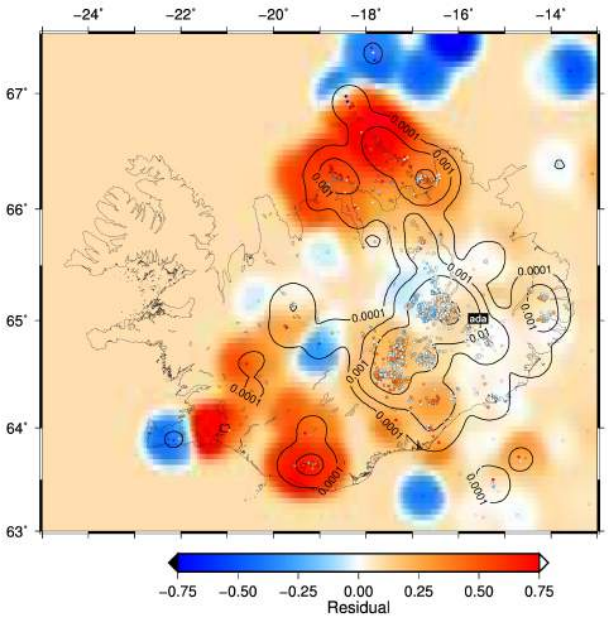

(a) The deterministic component of P-wave residuals at station ada

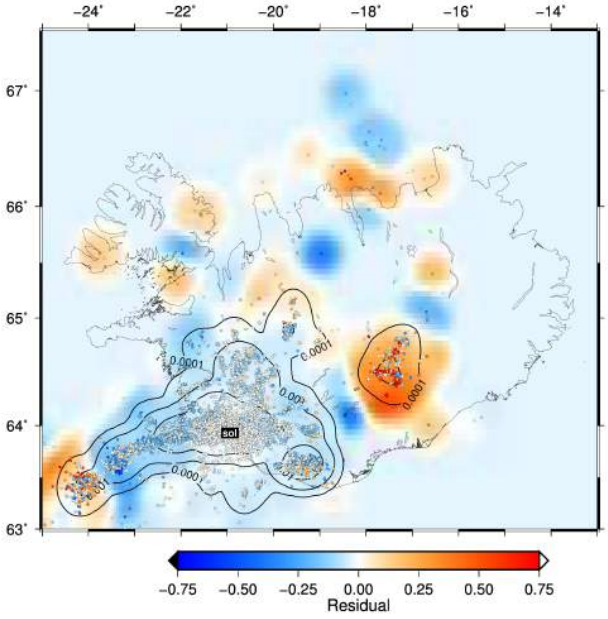

(b) The deterministic component of P-wave residuals at station sol

Figure 5: P-wave travel time residuals (circles) and the deterministic component of travel-time residuals (continuos color) calculated by two-dimensional interpolation using a moving average over a Gaussian function with a half width of 10 km. The contours indicate the combined weights of the data contributing to the estimate at each point. This weight is high where data exist, low where data are missing.

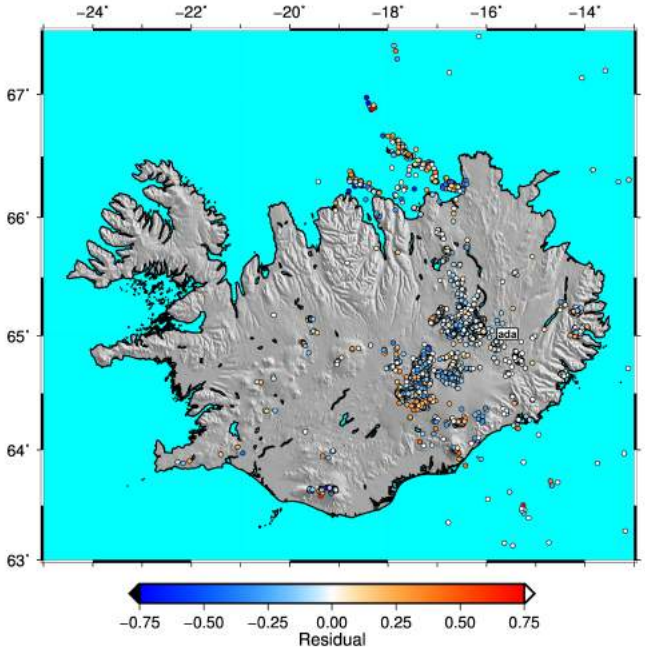

(a) Station ada

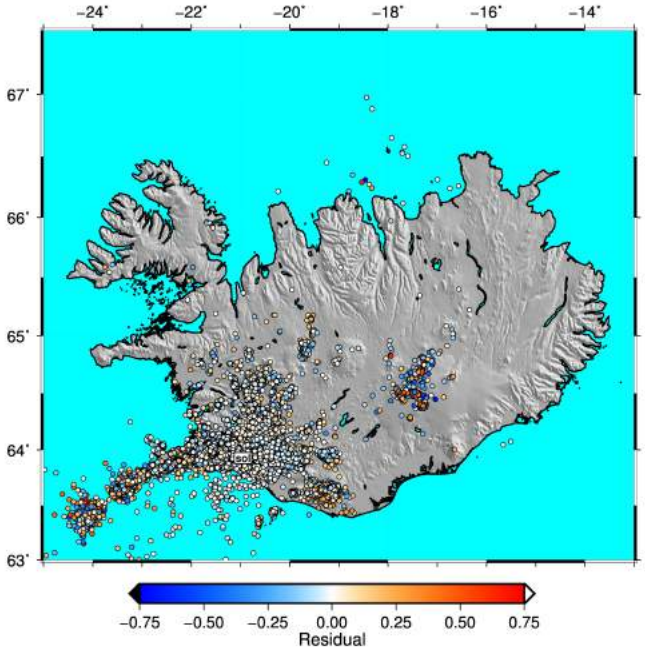

(b) Station sol

Figure 6: Remaining travel-time residuals of P-waves after removing the deterministic term.

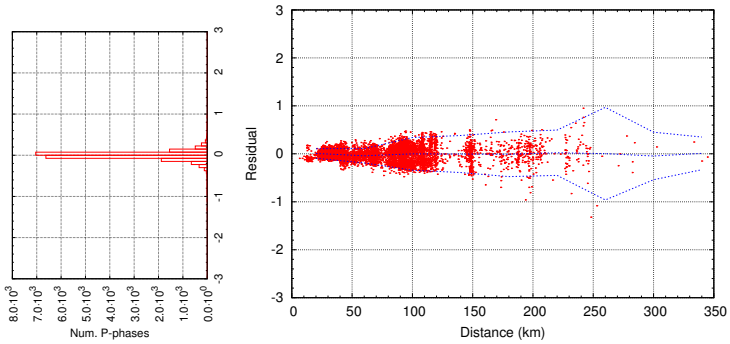

(a) Station ada

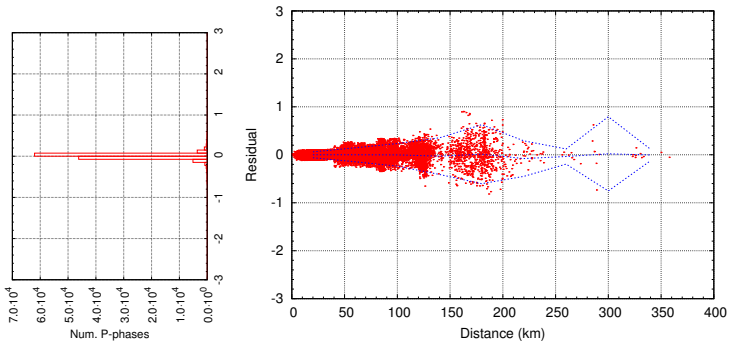

(b) Station sol

Figure 7: Distribution of remaining travel time residuals after removing the deterministic term. Histograms of P residuals are approximately double-exponential distributions centered near zero. Distributions of residuals with epicentral distance are also presented, where the blue lines represent the mean (μ) and the width of the distribution ($\mu \pm 2\sigma$, σ is one standard deviation). Residuals are centered near $\mu = 0$ and σ increases with distance.

3.3 Stochastic component and Noise

Having removed what we term the deterministic component of the travel-time function (for each station) we expect the remaining residuals to be more stationary in space. We tested the Kriging method to separate the spatially coherent component of the remaining residuals from their spatially incoherent part. This requires estimation of variograms, i.e. mapping of covariance as a function of scale, from which the two components can be separated. However, we find both the spatially coherent signal and the error variance to still be strongly non-stationary, which is not unexpected, and unstable. We have, therefore, abondoned the original plan to use the Kriging method of Schultz et al. (1998). In order to study the non stationarity further we have borrowed a method from global seismology to map the non-stationary statistics of travl-time residuals. This is based on the concept of summary rays (Morelli and

Dziewonski, 1987; Gudmundsson et al., 1990), i.e., bundles of ray paths with similar geometry. The summary rays are parameterized with two parameters, scale and distance. The scale (radius), a, defines the size of a ball enclosing earthquake sources in a summary ray. The distance is hypocentral distance. Both parameters are discretized and variances are estimated as a function of both in a discrete way. The variance is estimated as

$$\sigma^2(x_k) = \sum_{i=1}^{n_k} \frac{(\delta t_i - \overline{\delta t_k})^2}{n_k - 1} \tag{3}$$

where n_k is number of ray paths in the $k-$th summary ray, $\overline{\delta t_k}$ is the mean and t_i are the individual residuals. Summary rays with a minimum of 100 ray paths are considered for estimation. The average of variances of summary rays of size a and at a distance R from the station are calculated. Only averages calculated with at least 15 summary rays are considered. Figure 8 shows the results for stations gra and gha.

This analysis is a way of estimating non-stationary statistics of travel-time residuals in an earth where lateral heterogeneity is assumed to be laterally stationary, but non-stationary in depth. Thus, the non-stationarity can be parameterized only in terms of distance. The scale variable is introduced to track how the statistics vary with scale, i.e., in order to separate a coherent component from an incoherent component, as in a variogram for Kriging analysis. We do not expect this geometrical idealization to hold for the icelandic crust. Indeed, we find that it does not. We expect the rift zones to differ in their velocity structure from the Tertiary districts in Iceland. We also expect individual volcanoes to distinguish themselves from the rift zone they are found in. However, we do not have sufficient statistics to resolve lateral non-stationarity. The reason for the lack of statistical coverage is that earthquakes are not evenly distributed throughout the country. On the other hand, from the view of an individual stations, distance specifies 2D location reasonably well, i.e., given distance we know the seismogenic location reasonably well. So, distance parameterizes 2D non-stationarity reasonably well.

3.3.1 Error Variance

At small scales, variance of the structural signal vanishes and the variance represents an incoherent component, noise. Variance of noise can be stationary (i.e. independent of distance), or noise statistics can be non-stationary, where variance varies with position or distance. Figure 8 shows a non-stationary behavior of noise in the SIL travel times. We find, that in general the variance varies both with scale and distance, but does not decrease as scale is decreased beyond about 0.5 km at any given distance. This is comparable to the lateral uncertainty of the reference earthquake locations in the catalog in general. Therefore, we choose 0.5 km as a scale to estimate the variance of the incoherent component, i.e., noise. This estimate is generally stable. However,

because of the irregular spatial distribution of seismicity, some stations have sparse data or no data to estimate the noise variance at some epicentral distances. Assuming that the incoherent errors of travel times of nearby stations are caused by similar processes, we have estimated missing noise variances estimates using a 2D spatial inter/extrapolation of those variances that are constrained by substantial statistics.

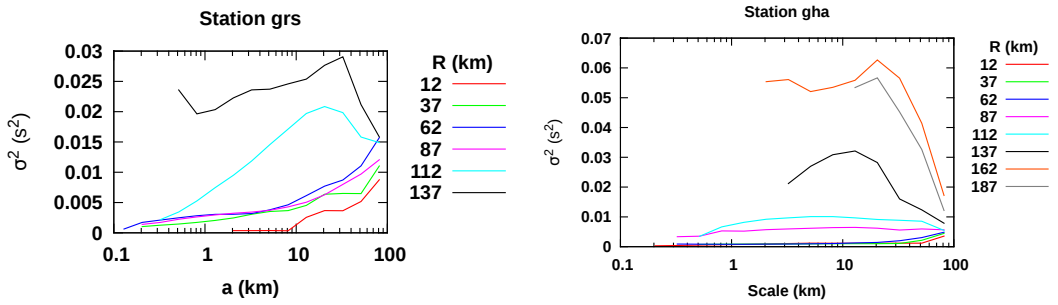

Figure 8: Variances of summary rays estimated as a function of scale a and hypocentral distance R.

The SIL stations are grouped using 7 geographical regions

- North Iceland
- Krafla
- Askja
- Vatnajökull
- Katla
- South Iceland Lowlands
- Reykjanes Peninsula

The variances of noise of the SIL stations distributed within the previously defined regions are presented in Figures 9 and 10, for P- and S-waves. Variance, reported from 0 to 150 km hypocentral distance, is estimated based on both direct observations and interpolation between stations having a robust estimation. These are combined in a specific function for each station. Noise variance generally increases with hypocentral distance. This is, however, not a universal feature. The variance has a similar behavior at all stations within each region. The noise variance generally increases slowly at short distances and universally at a faster rate at distances approaching 150 km, where waves have passed through the lower crust and may start to interact with Moho. Attenuation and a weak velocity gradient in the lower crust are expected to

cause low amplitude and more emergent arrivals at distance, in accordance with this general behaviour.

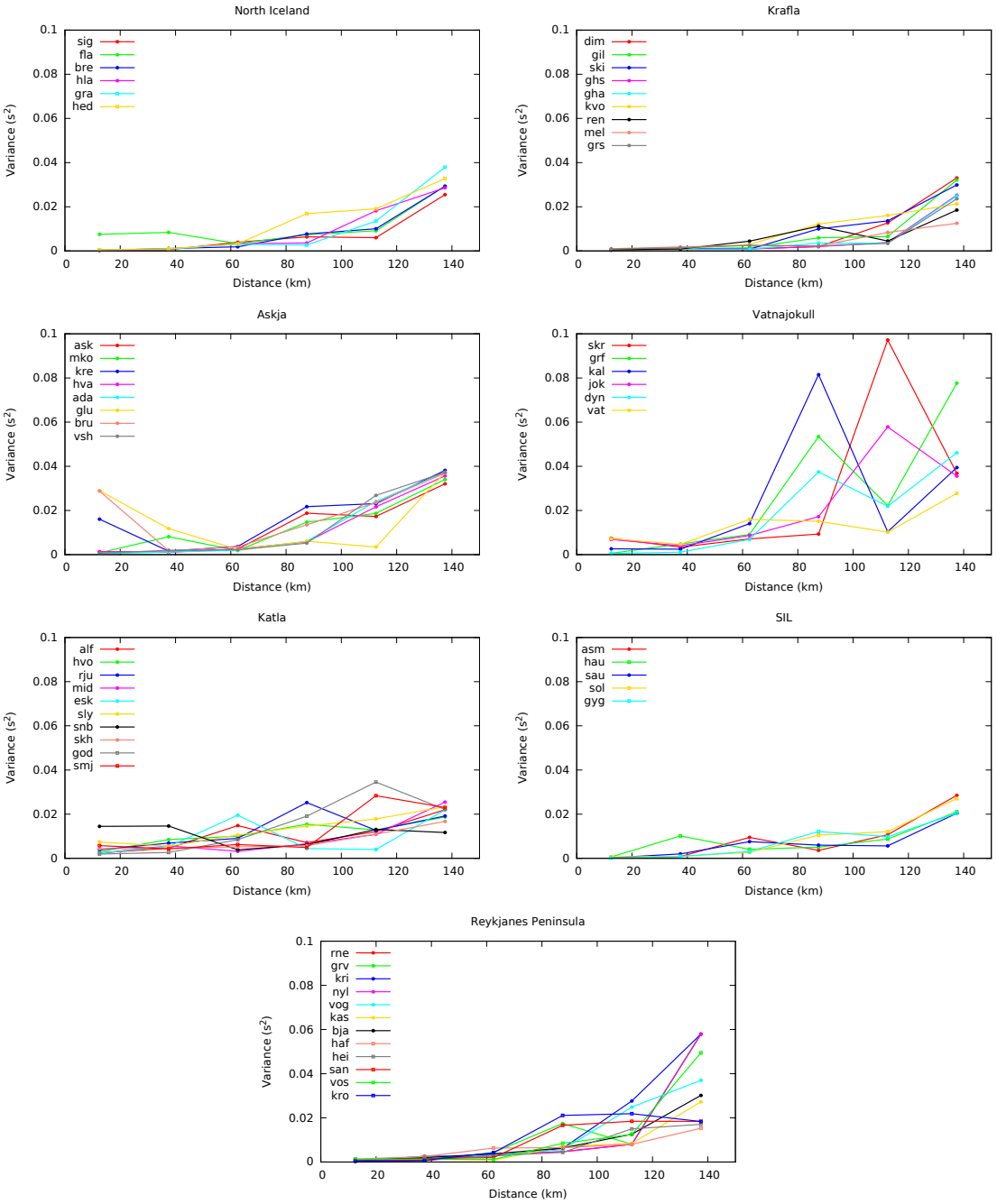

Figure 9: Noise variance for P-wave residuals at 56 SIL stations. The 9 remaining stations are located far from the established regions and are not included in the figure.

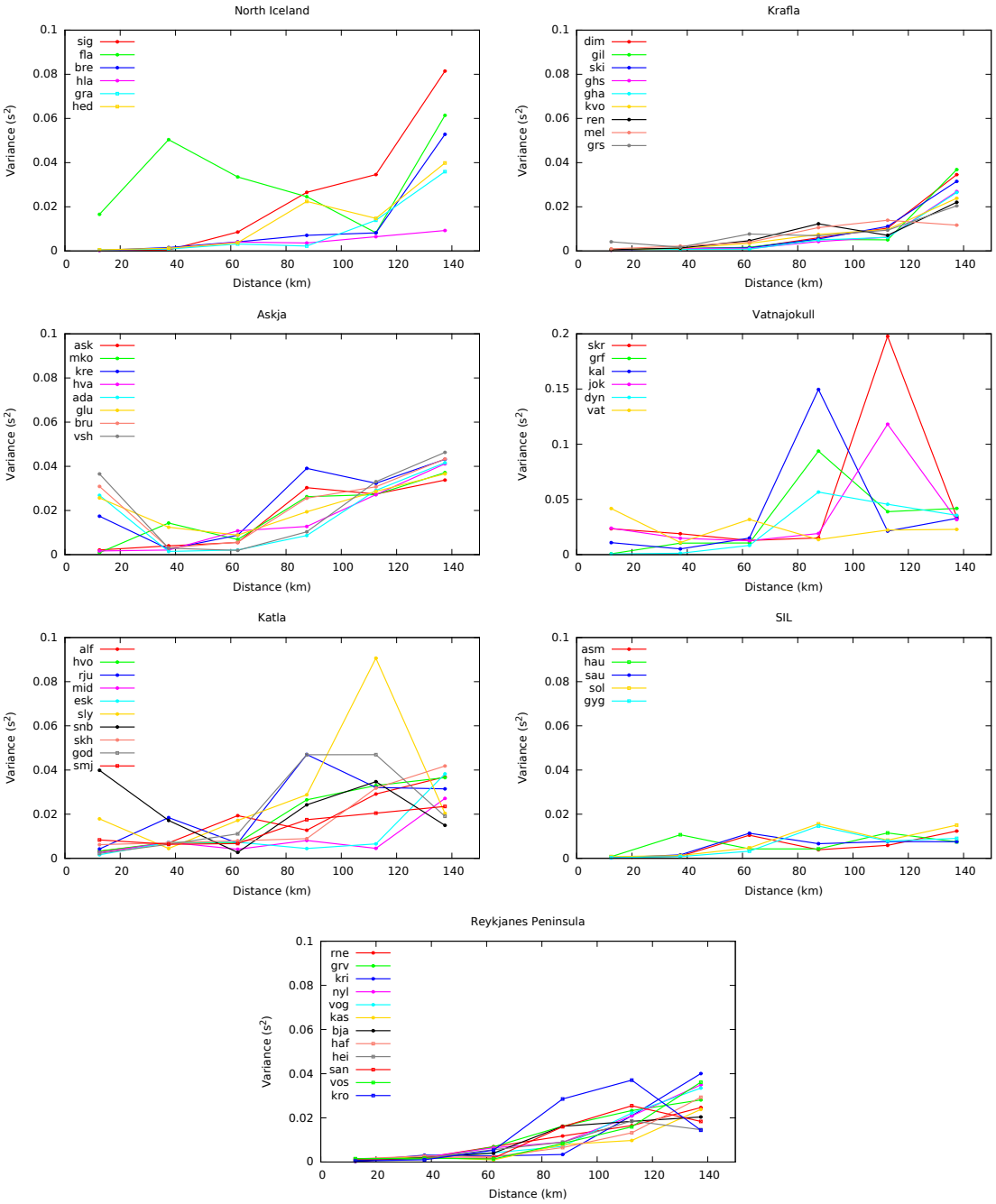

Figure 10: Noise variance for S-wave residuals at 56 SIL stations. The 9 remaining stations are located far from the regions established and are not included in the figure.

3.3.2 Stochastic structural component

We have already explained why we have abandoned the non-stationary Bayesian Kriging approach of Schultz et al. (1998). We are not able to simply characterize the variograms at different distance because of strong non stationarity and sparse statistics. In order to estimate the stochastic structural component and separate it from the noise component, we could use the generalized cross validation approach of Nicholson et al. (2004). However, we find with synthetic tests that the damped bootstrap trade off used in generalized cross validation does not always honour the noise variance in the interpolated data (depending on their spatial behaviour). Therefore, we used a damped, local 3D spline interpolant to fit the observations at each point so that the residual interpolant misfit explicitly honours the already estimated noise variance. The second-order polynomial function used for fitting was

$$f(x, y, z) = a_0 + a_1 x + a_2 y + a_3 z + a_4 x^2 + a_5 y^2 + a_6 z^2 + a_7 xy + a_8 xz + a_9 yz \quad (4)$$

where $f(x, y, z)$ is the interpolant and the constants a_i are chosen to fit neighbouring data to the sampling point $P(x_0, y_o, z_0)$ at which the structural component is to be evaluated. The neighbours are chosen as the 100 nearest neighbours within a radius of 10 km. If there are fewer than 100 data within 10 km, then the fit is applied to those, though not fewer than 10, in which case no interpolation is performed and the sample value is adopted. The fit is done by damped-least squares and the damping chosen such that the residual variance equals the estimated noise variance accounting for the appropriate number of degrees of freedom. This estimation process effectively smoothes the residuals spatially so that the estimated error variance is not absorbed by the estimate where sampling is dense, but will be inaccurate where it is sparse. Note, that this stochastic structural component is considerably smaller than the deterministic component estimated earlier. The resulting, smoothed, irregularly sampled travel-time residual is then interpolated on to a regularly sampled grid in space to construct an ordered travel-time table.

Results of the interpolant have been tested by measuring the degree of spatial correlation of the predicted stochastic and noise components. The autocorrelation a of a stationary function, $f(\mathbf{x})$ with isotropic statistics, evaluated at $\mathbf{x}_j$ and $\mathbf{x}_k$, is:

$$a_{j,k} = E\{f(\mathbf{x}_j) f(\mathbf{x}_k)\} = a(||\mathbf{x}_j - \mathbf{x}_k||) \quad (5)$$

where $E\{\}$ is the expectation operator, i.e. only a function of offset. We estimated the autocorrelation by binning $a_{j,k}$ in distance and calculating the average (expectation) of all samples within each distance bin (Nicholson et al., 2004).

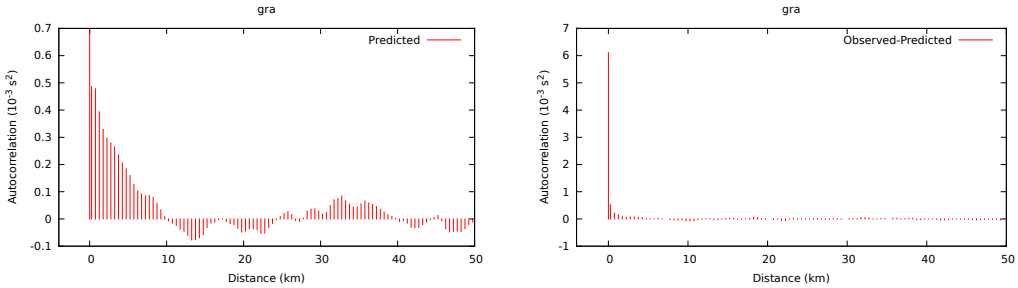

(a) Stochastic component of P-wave residuals.

(b) Noise component of P-wave residuals.

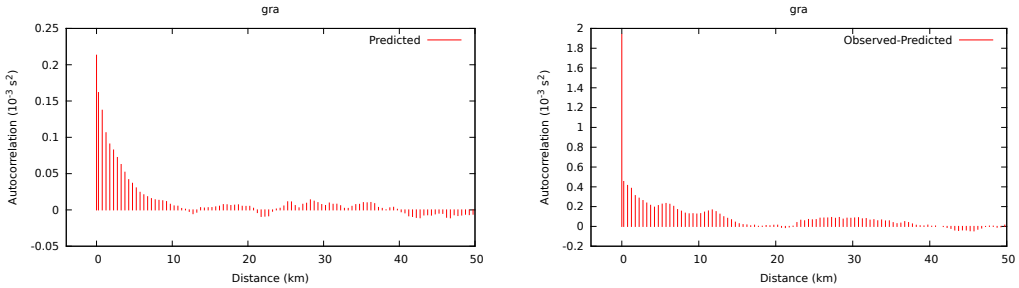

(c) Stochastic component of S-wave residuals

(d) Noise component of S-wave residuals.

Figure 11: Autocorrelation of stochastic structural component and noise for P- and S-wave residuals at station gra.

Figure 11 shows autocorrelation functions calculated for stations gra for P- and S-waves. The autocorrelation of the stochastic structural component is coherent over a scale on the order of 10 km while the autocorrelation of noise (observed minus predicted data) has only a significant amplitude at zero offset, i.e. the noise component is incoherent. This result indicates that the stochastic and noise components at gra are well separated. We obtained similar results for P-wave residuals at many stations.

However, for some stations, like ask (see page F9 in Appendix F), the structural and noise components were not so well separated. In general, the separation was less effective for S-waves than for P-waves. Moreover, noise separation results vary depending on the region. For example, results were poor for some of the stations in the Askja region, where the estimated noise functions had the most complex behaviour (see Appendix F). A summary of autocorrelations for both the stochastic structual component and the noise components for P-wave and S-wave residuals is compiled in Appendices E and F.

Finally, the ETTs for P- and S-waves at each SIL station were estimated by summing the three estimated travel-time components: 1) the one-dimensional SIL model com-

ponent; 2) the deterministic component corresponding to the spatial average of residuals; and 3) the stochastic structural component. These are more or less cleaned of noise. Additionally, non-stationary noise variance has been estimated up to hypocentral distances of 150 km. The ETTs and noise variance are the input information of the relocation algorithm described in the following section, allowing us to account for three-dimensional heterogeneity to a degree and to estimate location uncertainty rigorously.

4 Earthquake relocation

The relocation routine was implemented using a nested grid-search algorithm (Lomax et al., 2009) in three-dimensional space and a linear calculation in time. The initial estimate of location parameters (x_0, y_0, z_0, t_0) is taken from the SIL catalog. The routine calculates the final location in three steps, where the main parameters are the grid size and spacing. We pay special attention to the estimation of uncertainty of the final location.

1. A cubic grid of 30 km size in each dimension and 0.5 km spacing is defined around the initial location. For each node of the grid, travel times are predicted by interpolating the ETTs. A least-squares misfit between observed arrival times and the predicted arrival times is defined and the earthquake origin time t_0 is calculated by

$$t_O = \frac{\sum_{i=1}^{N}(t_i^{obs} - t_i^{ETT})/\sigma_i^2}{\sum_{i=1}^{N} 1/\sigma_i^2} \tag{6}$$

   so that its misfit is minimized. Here i indexes the observation (SIL station and phase) so that t_i^{obs} is the reported P- or S-arrival time in the database and t_i^{ETT} is the corresponding travel time prediction calculated from the ETTs. Thus, a minimum misfit is defined at each nodal point int the grid.

   The new estimated location will correspond to the node coordinates and origin time which represent the minimum misfit Q, given by

$$\begin{aligned} Q =& (\mathbf{d} - G(\mathbf{m}))^T \mathbb{C}^{-1} (\mathbf{d} - G(\mathbf{m})) \\ =& (\mathbf{t}_i^{obs} - \mathbf{t}_i^{ETT})^T \mathbb{C}_d^{-1} (\mathbf{t}_i^{obs} - \mathbf{t}_i^{ETT}) \end{aligned}$$

   where $\mathbf{m}$ is a vector of 4 model parameters (4 earthquake location parameters), $G(\mathbf{m})$ are the travel times predicted by the ETTs, and the covariance matrix $\mathbb{C} = \mathbb{C}_d$ is given by the estimated noise covariance, assuming that observation errors are independent (so it is diagonal). Note that $G(\mathbf{m})$ is a non-linear function.

2. The covariance matrix $\mathbb{C}$ is modified according to

$$\mathbb{C} = \mathbb{C}_d + \Omega^2 \mathbb{I} \tag{7}$$

introducing a constant Ω, which represents the calculation uncertainty of the travel-time tables. Ω is chosen such that misfit Q fulfills the condition

$$Q_{min} = N - M \tag{8}$$

i.e. the minimum misfit is the number of degrees of freedom or the expectation of the corresponding χ^2 distribution, assuming Gaussian statistics of residuals, given by the number of data N and the number of parameters M to be determined (i.e. 4). In general, $\Omega << C$, i.e. the modification of the error estimate is small. In other words, the uncertainty of the ETTs appears to be small and the estimates of error variance appear to be complete. The errors as described suffice to explain the residual misfit. Renormalized error misfit is then used to estimate location error assuming Gaussian error statistics, i.e., the probability distribution of the location is described by:

$$\wp(Q) \propto \exp\left(-Q/2\right) \tag{9}$$

3. The grid search is repeated in a similar way to step 1. A new cubic grid is defined, now 1 km in size and with a 0.1 km spacing, around the location result of step 1. The initial covariance matrix is also taken as the result from step 2. When the minimum misfit is found, Ω is again tuned in order to fulfill the condition in equation (8).

The covariance matrix of model parameters is calculated solving

$$\begin{aligned} \mathbb{A} &= [\mathbb{G}^T \mathbb{C}^{-1} \mathbb{G}]^{-1} \mathbb{G}^T \mathbb{C}^{-1} \\ \mathbb{C}_m &= \mathbb{A} \mathbb{C} \mathbb{A}^T \end{aligned} \tag{10}$$

which is the covariance matrix of a least-squares problem.

Our approach to error estimation differs from standard practice in earthquake location. In short, this is done without any prior estimates of observational error and, therefore, more or less arbitrary weights are assigned to arrival-time picks, which effectively define a data covariance matrix with assigned relative errors. The residual misfit is then used to estimate data variance in absolute terms and the effective data covariance matrix is scaled accordingly by multiplication. We have prior estimates of data covariance as a result of our ETT estimation. We also use the residual variance as an estimate of "data" uncertainty, but we treat excess variance as an additional error process, independent of observational errors, which we justify by recognizing that

our data prediction, i.e., our ETT estimates, are uncertain. The standard practive of scaling a-priory weights as a description of errors uses essentially the same argument, but implicitly assumes that the prediction error is proportional to the observational error, which is a poorly justified assumption.

Using residual misfit to define uncertainty will occationally result in unrealistically small error estimates because the residual misfit can be small by chance. Because of this, we apply a minimun data uncertainty by disallowing Ω^2 in the equation (7) above to be negative. Thus, this situation of unrealistic error estimation is avoided.

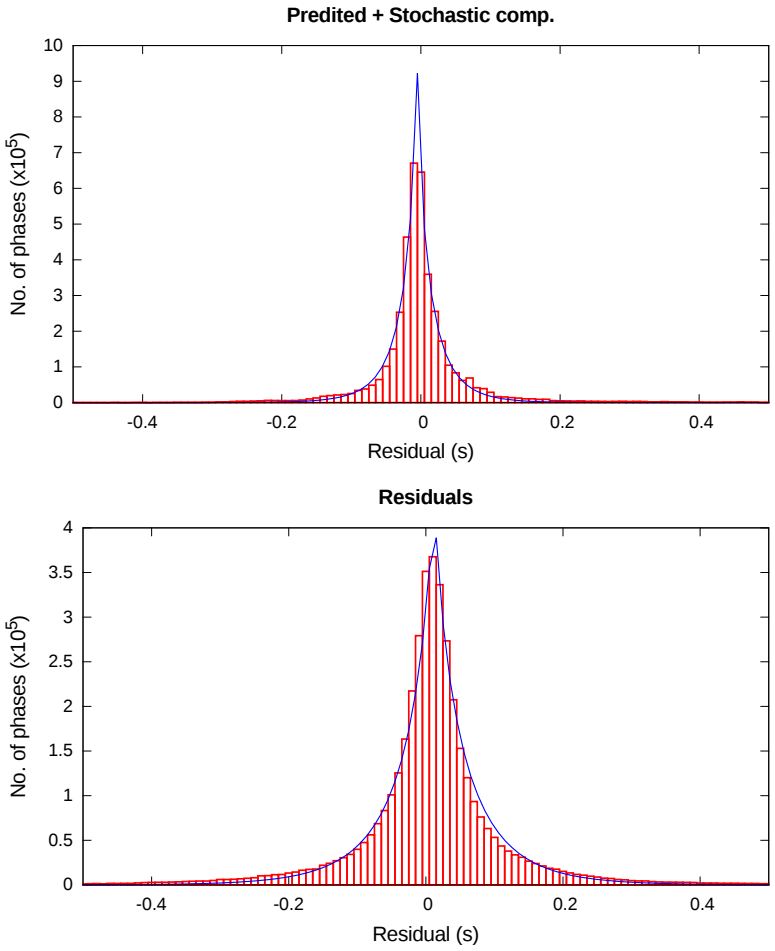

Figure 12: The distributions of the stochastic component of ETTs (above) and residual-data erros (below). The distributions have been fitted with an exponential distribution of the form $p(t) = Ae^{-(|t|/a)^q}$, where the constant $q = 0.75$ for the stochastic ETTs and $q = 0.8$ for the error residuals.

We have chosen a least-squares approach to the earthquake relocation. However, the histogram of estimated noise residuals in Figure 12 is better characterized as a double-exponential distribution. This suggests that an L_1 norm would be a more appropriate choice for the residual misfit than an L_2 norm. We have not chosen to work with the L_1 norm because this is more cumbersome. In particular, this makes all four dimensions of the earthquake relocation problem non linear, including the origin time. Therefore, this would require a 4D grid search, whereas the least-squares problem can be solved with a 3D grid search as the origin-time component of the problem is linear. Modification of the approach to work with an appropriate data error distribution remains a future objective of our team.

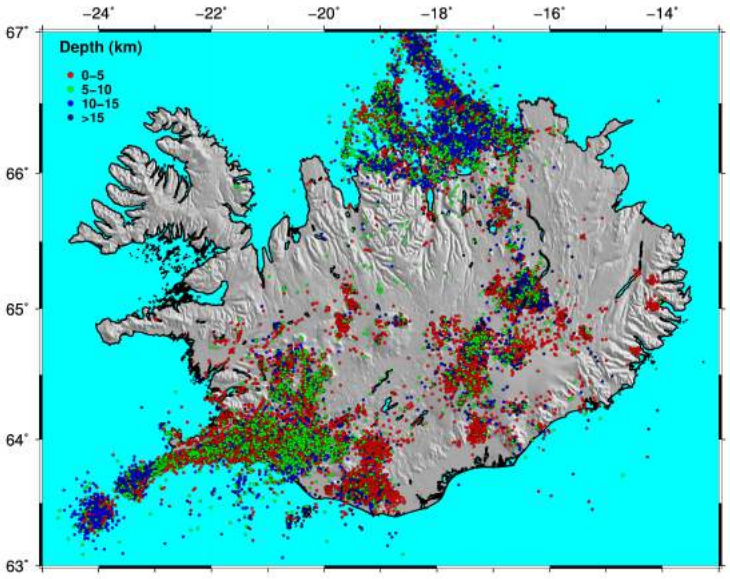

(a) SIL

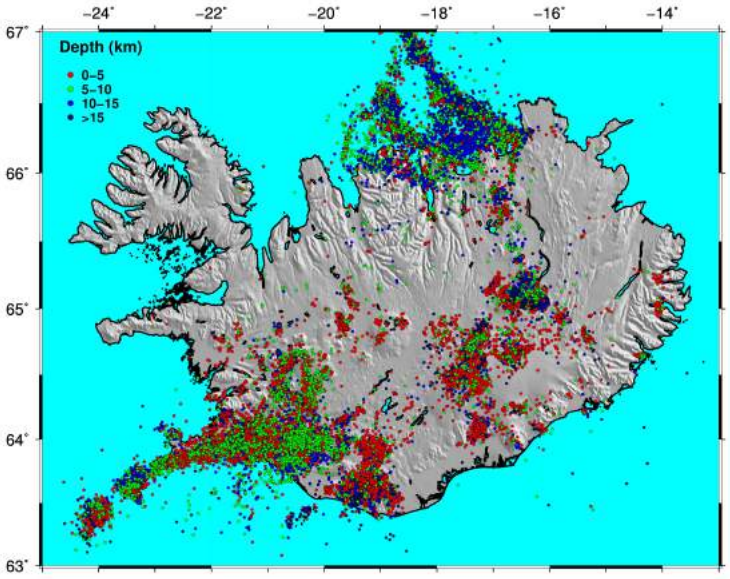

(b) RELOCATION

Figure 13: Seismicity in Iceland between 1990 and 2012. Colour indicates depth as defined in legend. Only those events that have been reanalysed are included (∼300.000 events).

5 Results

Some examples of results for empirical travel times and noise estimates have been shown in previous sections. Here we discuss them more thoroughly and present relocations of the SIL catalog (1990-2012).

The results for estimated empirical travel times are presented comprehensively in Appendices A, B, C, D and E as well as Figure 12. Results of noise estimation are shown in Figures 9 and 10 and in Appendix F. Relocation results are presented in Figures 13 to 19 and in Appendix G.

5.1 Empirical Travel times

The empirical travel time is defined as composed of three terms: 1) the prediction of a one-dimensional reference velocity model, chosen as the SIL model; 2) large-scale variations from that prediction, which we estimate by a running average over a specified scale, chosen to have a half width of 10 km; 3) random small-scale variations that are treated as random. The deterministic large-scale variations have an average variance of about 0.25 s2, while the random small-scale variations have a variance ranging between 10-3 and 10-2 s2. Therefore, the random component of the ETTs stands for about 7 to 20% of their amplitude. The deterministic component dominates over the random component. We present only a map overview of the deterministic component of the ETTs because this is dominant and defined in 2D (and therefore easily represented graphically) while the full ETTs are three-dimensional and more difficult to display. The deterministic ETT components are summarized for all 65 SIL stations in Appendices A to C. The maps show results from both P- and S-wave residuals.

The figures in Appendix A are organized with four maps per page. Those show both P- and S-wave residuals and their interpolations for a pair of stations as indicated on each page. The stations are chosen as neighbours. This allows for a comparison of results for P-wave residuals versus S-wave residuals and to some degree a study of geographical coherence of results comparing different stations. Note that this is better done by comparing the figures in Appendices B and C.

It is evident from the comparison of P-wave and S-wave results at individual stations that their spatial variation correlates strongly in general. It is also evident that the amplitudes of the residual patterns are similar, but in general somewhat smaller for S-wave residuals than for P-wave residuals. This suggests that the Vp/Vs velocity ratio deviates significantly from that assumed for the SIL model in the Icelandic crust.

The figures in Appendix B are again organized with four maps per page. Those show P-wave residuals and their interpolations for a number of nearby stations as indicated,

allowing for a geographical comparison of P-wave results.

The figures in Appendix C are also organized with four maps per page. Those show S-wave residuals and their interpolations for a number of nearby stations as indicated, allowing for a geographical comparison of S-wave results.

This comparison shows that the travel-time residuals are quite coherent from one station to the next when they are closely spaced. Note that the residual mean has not been removed. This is indicated by the background colour and reflects a combined effect of station elevation and possibly anomalous shallow structure immediately beneath each station. Such an effect is particularly clear for station fla (page B15), which has a significantly positive average. Nearby station bre has a very different average despite the fact that it is only a few km away. The residual patterns of the two stations are very similar. Station ves (page B7) also has a significantly positive average, as do stations in the highlands (page B11). Station kud in western Iceland (page B20) is at the other end of the spectrum with a significantly negative (fast) average.

The figures in Appendix D present information about residuals after removal of the deterministic component for P- and S-waves, i.e. the combined stochastic component containing both a small spatially coherent travel-time signal and a spatially incoherent error variation. This information is summarized for each analyzed station on each page. The station code is indicated at the top of each page. The residuals are generally small compared to the deterministic part presented in appendices A to C. However, some structure is present, some of it visibly spatially coherent, but much of it not apparently spatially coherent. Note for example how similar the distant seismicity in the Askja region appears at stations in SW Iceland in the scatter of the residuals.

We also show distribution histograms of the residuals and their variation with epicentral distance. Solid blue curves on the epicentral plots represent the mean as a function of epicentral distance and the mean plus/minus one standard deviation, also as a function of epicentral distance. The mean of the residuals is generally quite small as a function of epicentral distance. The variance of the residuals generally increases with distance. Note that the variance of S-wave residuals is generally comparable to that of the P-wave residuals, if not smaller.

The figures in Appendix E show auto-covariance functions of the estimated stochastic structural component of empirical travel times for both P-wave and S-wave residuals. Results from three adjacent stations are presented on each page with the station code indicated above each frame. The structure of the auto-covariance is often complex, which is not surprising since this is a simple representation of the functions variation that assumes spatial stationarity and the sampling geometry is complex.

Nevertheless, the figures indicate the degree of variation (as variance) and have maximum amplitude around zero offset, often contained in a peak with a width of 3 - 15 km, roughly confined to the averaging scale used to estimate the deterministic component of the ETTs. In some cases there is a suggestion that some of the error may have been partially absorbed in the ETTs where a peak is present at zero offset, i.e. an incoherent peak. The structure of the P-wave and S-wave auto-covariance is often similar, suggesting a correlation of P- and S-wave residuals on small scales.

5.2 Noise estimates

The noise variance estimates are summarized in Figures 9 and 10. The noise variance is generally small at short distance, on the order of $0.001-0.01$ s^2 for P-wave residuals, somewhat bigger for S. The variance increases markedly with distance. At a distance of 140 km it is generally on the order of $0.02 - 0.06$ s^2. These numbers translate into standard deviations in the range of $0.03 - 0.1$ s at short distance and about 0.2 s at 140 km. There are exceptions from this general description. Station fla in the north is known as a difficult station and its error estimates are large. Stations bru, glu and kre north of Vatnajökull and snb east of Myrdalsjökull appear with a large error variance at short distance. A number of stations in central Iceland have variance peaks at intermediary distance, consistent for P- and S-wave residuals (which are independently estimated). These can be associated with seismicity in the Katla region.

The auto-covariance functions of the residuals after removal of complete ETTs are shown in appendix F combining results for P-wave and S-wave residuals in each figure. Three nearby stations are presented on each page with the station code indicated above each frame. The structure of the auto-covariance is with some exceptions very simple, i.e. a large value at zero offset followed by significantly smaller variation around zero covariance at finite offset. This indicates that the identification of the noise component as a spatially incoherent signal has been successful. In the relatively few cases where significant signal remains at finite offset, in particular where that is correlated for P- and S-wave residuals, that suggests that some of the spatially coherent signal has leaked into the error estimate. In exceptional cases the noise covariance behaves erratically. This occurs exclusively at stations with quite few data. The behavior of station fag is strange and not understood.

Figure 12 shows a distribution histogram for the ETTs (their stochastic component) and noise. The two distributions have similar shape, but different widths. Both are best characterized by an exponential distribution of a norm with an exponent that is somewhat less than 1. The error distribution is approximately twice as wide as the stochastic ETT distribution. This global distribution of nise is in general agreement with the noise distributions for individual stations. As mentioned earlier, this means that the choice of an L_2 norm in the definition of misfit for the reloctation

algorithm outlined above may not be optimal. An L_1 norm would be more appropriate. Modifying the algorithm using an L_1 norm complicates it (Rodi, 2006), but is certainly doable. Note that the curve fitting to the distributions (resulting in an exponent near $q = 0.8$) is done in the log-lin domain, i.e. the logarithm of the distribution value is fitted. This emphasizes the tail of the distribution compared to the peak of the distribution. But, in terms of norm choice for the misfit definition chosen for relocation it is the tail that is important as this describes the appropriate down weighting of outliers.

5.3 Relocations of the SIL catalog

The relocation algorithm outlined in section 3 above was applied to the entire SIL catalog from the period 1990 to 2012. This catalog contains about 370.000 events. However, 70.000 of them did not fulfill the criterion that they be recorded with at least 6 picks. Those are excluded to ensure that a minimal level of redundancy exists in the data for error estimation. Figure 13 shows an overview of the relocated epicentres (about 300.000 events) and the original SIL locations for reference. Limited detail is visible in this overview. Therefore, results for a number of sub regions of Iceland are presented in Appendix G. We chose as sub regions those that the Icelandic Meteorological Office uses to present seismicity on their web, with a few exceptions. The regions are listed in the table below with a pointer to page number in the Appendix.

REGION	**Page**
Eastern Fjords	G3
Hengill	G4
Hofsjökull	G5
Langjökull	G6
Myrdalsjökull	G7
Northern Volcanic Zone	G8
Reykjanes Peninsula	G9
Reykjanes Ridge	G10
Southern Iceland	G11
Western Iceland	G12
Tjörnes Fracture Zone	G13
Vatnajökull	G14
Vestmanna Islands	G15

The maps show epicentres coloured according to depth as indicated in the legends. The events are plotted in time order. SIL epicentres are plotted in the top frame, relocated events in the lower frame.

The effects of relocations on the epicentral distribution are not dramatic, but noticeable. We point out that, in particular on the outskirts of the SIL network the

clustering of epicenters is clearly enhanced. This is perhaps most noticeable in the Tjörnes Fracture Zone, where the Husavik-Flatey lineament is clearly focused. Also, the curious transverse bands of seismicity in between the Grimsey lineament and the Húsavík-Flatey are focused.

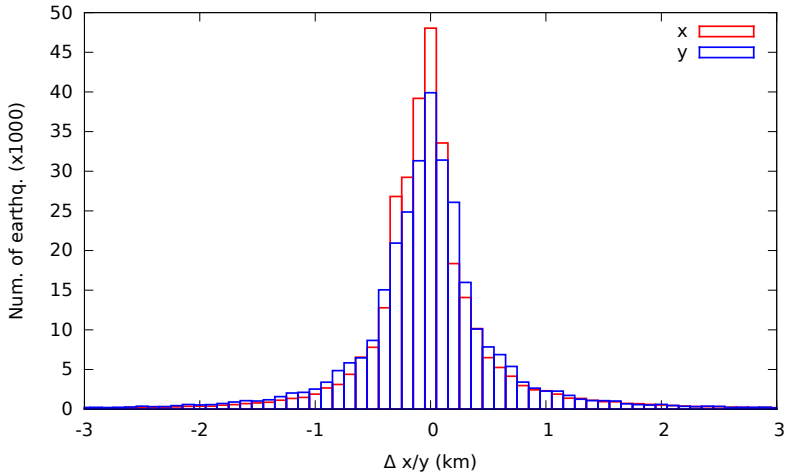

Figure 14: Histogram shows movements in x (east-west) and y (north-south) of events when relocated.

Seismicity on the Reykjanes Ridge is somewhat focused, although almost certainly still artificially diffuse in the relocated distribution. Some of the artificial events (associated with construction) in the east of Iceland are slightly more clustered in the relocated distribution. Another significant effect of the relocations is that the depth distribution of events is clearly more coherent in space, which is most evident in the regions of dense seismicity, e.g., in the Tjörnes Fracture Zone.

Histograms of the events movements by relocation are shown in Figures 14 and 15. The horizontal movements are presented in Figure 14 where x stands for east and y for north. The movement distibutions are similar for both horizontal coordinates, which both approximately following a Gaussian distribution. The width of the Gaussian distributions is approximately 350 m. The vertical movements are shown in Figure 15. Their distribution width is about double that for the horizontal movements, about 700 m. These location shifts correspond to time shifts on the order of $0.05 - 0.10$ s (using a velocity of 5 km/s). They are comparable to the observational errors and much less than the structural signal in the ETTs.

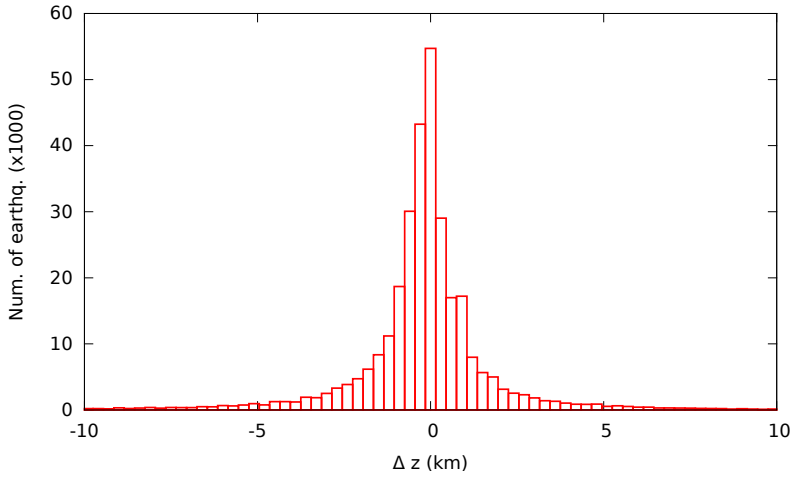

Figure 15: Histogram shows movements in z (vertical) of events when relocated.

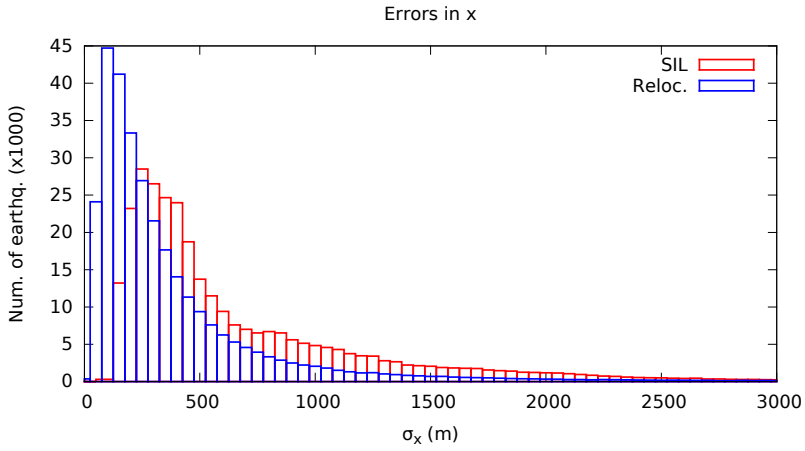

Figure 16: Distribution of error estimates in the east-west direction. Red: for the SIL catalog; Blue: for the relocated catalog.

6 Conclusions

About four million arrival-time picks from SIL recordings at 65 stations of about 300.000 earthquakes have been analyzed to estimate empirical travel times, which represent effects of wave propagation in the heterogeneous Icelandic crust. These deviate from the travel-time predictions of a 1D reference model with a standard deviation of about 0.5 s and vary down to scales of about 1 km. This is where the uncertainty of the travel-time mapping limits the resolution.

The ETT estimation process has also resulted in estimates of arrival time errors at the 65 stations as functions of epicentral distance. The behavior of the error is in most

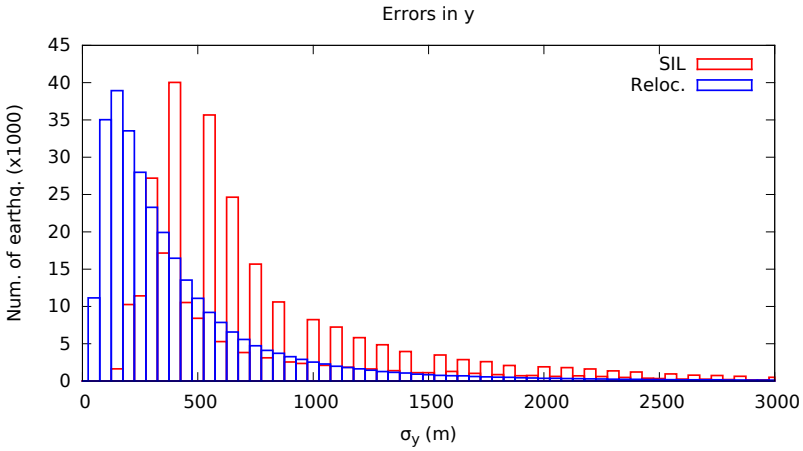

Figure 17: Distribution of error estimates in the north-south direction. Red: for the SIL catalog; Blue: for the relocated catalog.

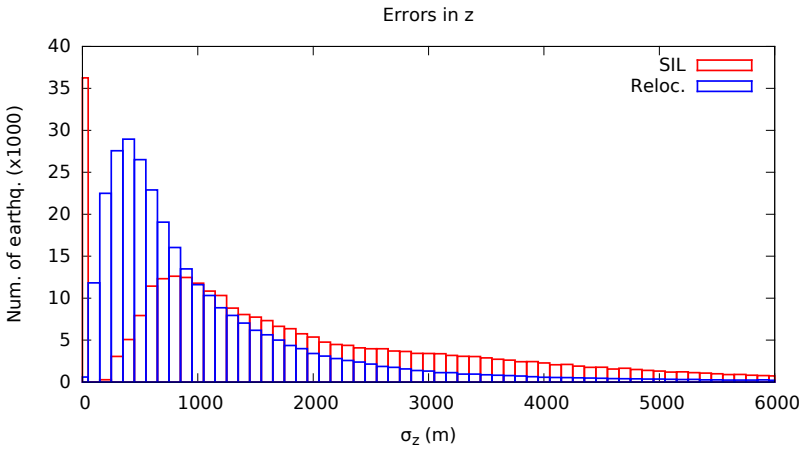

Figure 18: Distribution of vertical error estimates. Red: for the SIL catalog; Blue: for the relocated catalog.

cases simple with distance. Notable exceptions include SIL stations that are known by SIL staff to have large uncertainty. Events in the Katla region also result in large uncertainties at stations to the north in the central highlands.

A relocation algorithm has been developed based on probabilistic non-linear inversion where care has been taken with the estimation of uncertainty. The normalized misfit for the relocations using the ETTs as solutions to the forward problem and uncertainty estimates for normalization are generally near their expected value. This suggests that both the ETTs and the error variances are realistically estimated.

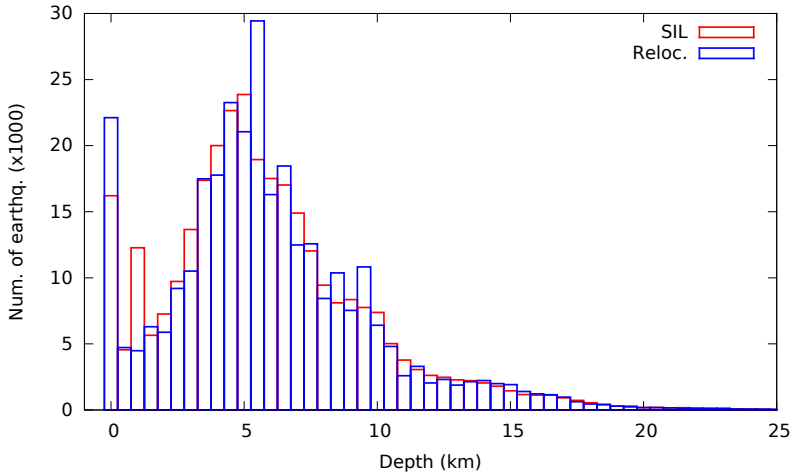

Figure 19: Depth distribution of events. Red: in the SIL catalog; Blue: in the relocated catalog.

The entire SIL catalog up to the end of 2012 has been relocated. The relocations modestly enhance the degree of clustering of epicenters, particularly in the seismogenic regions that re peripheral to the SIL network. The spatial distribution of event foci is considerably simplified, while the depth distribution itself is not significantly affected. Event depth is now referenced to sea level.

Uncertainty estimates of the relocations are smaller than those for the SIL catalog. This is inevitable, because the ETTs do take three-dimensional heterogeneity in to account, albeit imperfectly. The uncertainty estimates for the relocations should, however, be more realistic for a number of reasons. First, they are based on actual and robust estimates of observational uncertainty. Second, they are based on a probabilistic inversion, which maps the location misfit fully. Third, some unrealistic assumptions are avoided in the error estimation.

We have identified an inconsistency in our relocation approach. The error distribution of travel times is not Gaussian as we have assumed. Instead, the distribution is more like a double-exponential distribution suggesting that an L1 norm should be used to describe their misfit. This will be our next step in this analysis.

The ETTs are estimates of observed travel time that has had a noice component removed. The estimated ETTs therefore lend themselves well to use in a LET tomographic study of the Icelandic crust. This will be another future step in our analysis, which may improve the event locations that are used for the mapping of travel times for each station.

Li et al. (2016) have recently developed methods of relocation and collapsing of event

locations in a catalog, which is heavily based on robust uncertainty information. It is natural to apply these to the relocated SIL catalog because with it we have more robust location error estimates than ever before in Iceland.

References

A. Lomax, J. Virieux, P. Volant, and C. Berge-Thierry. *Probabilistic earthquake location in 3D and layered models - Introduction of a Metropolis-Gibbs method and comparison with linear locations, In Advances in Seismic Event Location (ed. Thurber, CH, and N Rabinowitz).* 2000.

G. Palmason. Crustal structure of Iceland from explosion seismology, Ph.D. Thesis, Societas Scientiarum Islandica, 1974.

I.T. Bjarnarson, W. Menke, O.G. Flovenz, and D. Caress. Tomographic image of the Mid-Atlantic plate boundary in sourthwestern Iceland. *J. Geophys. Res.*, 98: 6607–6622, 1993.

O. Gudmundsson, B. Brandsdottir, W. Menke, and G.E. Sigvaldason. The crustal magma chamber of the Katla volcano in south Iceland revealed by 2-D seismic undershooting. *Geophys. J. Int.*, 119:277–296, 1994.

R.K. Staples, R.S. White, B. Brandsdottir, W. Menke, P.K.H. Maguire, and J.H. McBride. Faroe-Iceland Ridge Experiment .1. Crustal structure of northeastern Iceland. *J. Geophys. Res.*, 102(B4):7849–7866, 1997.

A. Tryggvason, S.Th. Rognvaldsson, and O.G. Flovenz. Three-dimensional imaging of the P- and S-wave velocity structure and earthquake locations beneath Southwest Iceland. *Geophys. J. Int.*, 151:848–866, 2002.

A. Li and R.S. Detrick. Seismic structure of Iceland from Rayleigh wave inversions and geodynamic implications. *Earth. Planet. Sci. Lett.*, 241:901–912, 2006.

O. Gudmundsson, A. Khan, and P. Voss. Rayleigh-wave group velocity of the Icelandic crust from correlation of ambient seismic noise. *Geophys. Res. Lett.*, 34:L14314, 2007.

J. Schuler, T. Greenfield, R.S. White, S.W. Roecker, B. Brandsdottir, J.M. Stock, J. Tarasewicz, H.R. Martens, and D. Pugh. Seismic imaging of the shallow crust beneath the Krafla central volcano, NE Iceland. *J. Geophys. Res.*, 120:7156–7173, 2015.

B. Brandsdottir, M. Parsons, R.S. White, O. Gudmundsson, J. Drew, and B.S. Thorbjarnardottir. The May 29th 2008 earthquake aftershock sequence within the South Iceland Seismic Zone: Fault locations and source parameters of aftershocks. *Jokull*, 60:23–46, 2008.

L. Jing. Seismic tomography and surface deformation in Krysuvik, SW Iceland, M.Sc. Thesis Massachusetts Institute of Technology, 2013. URL `http://hdl.handle.net/1721.1/87506`.

Z. Jeddi, A. Tryggvason, O. Gudmundsson, and R. Bodvarsson. The Katla volcanic system imaged using local earthquakes recorded with a temporary seismic network, manuscript in preparation, 2016.

H. Iyer and K. Hirahara. *Seismic tomography.* Chapman & Hall, New York, 1993.

C.A. Aster, B. Borchers, and C.H. Thurber. *Parameter estimation and inverse problems. International Geophysics Series 90 (ed. R. Domowska, J.R. Holton and H.T. Rossby).* Elsevier Academic Press, Burlington, 2005.

M. Sambridge and O. Gudmundsson. Tomographic systems of equations with irregular cells. *J. Geophys. Res.*, 103(B1):773–781, 1997.

C.A. Schultz, S.C. Myers, J. Hipp, and C.J. Young. Nonstationary Bayesian kriging: A predictive technique to generate spatial corrections for seismic detection, location, and identification. *Bull. Seism. Soc. Am.*, 88:1275–1288, 1998.

T. Nicholson, M. Sambridge, and O. Gudmundsson. Three-dimensional empirical travel times: construction and applications. *Geophys. J. Int.*, 156:307–328, 2004.

K. Jonsdottir, A. Tryggvason, R. Roberts, B. Lund, H. Soosalu, and R. Bodvarsson. Habits of a glacier-covered volcano: seismicity patterns and velocity structure of Katla volcano, Iceland. *Annals of Glaciology*, 45:169–177, 2007.

C. Piromallo and A. Morelli. Improving seismic event location: an alternative to three-dimensional structural models. *Pure appl. Geophys.*, 158:319–348, 2001.

A. Morelli and A.M. Dziewonski. Tomography of the core-mantle boundary and lateral homogeneity of the liquid core. *Nature*, 325:678–683, 1987.

O. Gudmundsson, J.H. Davies, and R.W. Clayton. Stochastic analysis of global traveltime data: mantle heterogeneity and random errors in the ISC data. *Geophys. J. Int.*, 102:25–43, 1990.

A. Lomax, A. Michelini, and A. Curtis. *Earthquake Location, Direct, Global-Search Methods, in Complexity In Encyclopedia of Complexity and System Science, Part 5.* Springer, New York, 2009.

W. Rodi. Grid-search event location with non-Gaussian error models. *Phys. of the Earth and Planetary Interiors*, 158(1):55–66, 2006.

K.L. Li, O. Gudmundsson, A. Tryggvason, R. Bodvarsson, and B. Brandsdottir. Focussing patterns of seismicity with relocation and collapsing. *J. Seismol.*, 20:1–16, 2016.

Appendix A

The deterministic component of empirical travel time: Comparison of P- and S-wave results

The following maps show the travel-time residuals relative to predictions of the SIL model (circles) and the deterministic component (continuos colour) of empirical travel times for all 65 stations in the SIL network that we have analysed. The maps show data and results from both P- and S-wave residuals. The two-dimensional interpolation that defines the deterministic component of the empirical travel time is calculated using a moving average over a Gaussian function that is 10 km in width. The contours indicate the combined weights of the data that contribute to the estimate at each point and are a useful guide about robustness. The running average is based on many nearby data where this combined weight is high.

The figures are organized with four maps per page. Those show both P- and S-wave residuals and their interpolations for a pair of stations as indicated. The stations are chosen as neighbours. This allows for a comparison of results for P-wave residuals versus S-wave residuals and to some degree a a study of geographical coherence of results comparing different stations. Note that this is better done by comparing the figures in Appendices B and C.

It is evident from the comparison of P-wave and S-wave results at individual stations that their spatial variation correlates strongly in general. It is also evident that the amplitudes of the residual patterns are similar, but in general somewhat smaller for S-wave residuals than for P-wave residuals. This suggests that the V_P/V_S velocity ratio deviates significantly from the assumed $\sqrt{3}$ for the SIL model in the icelandic crust.

P-wave S-wave

nyl

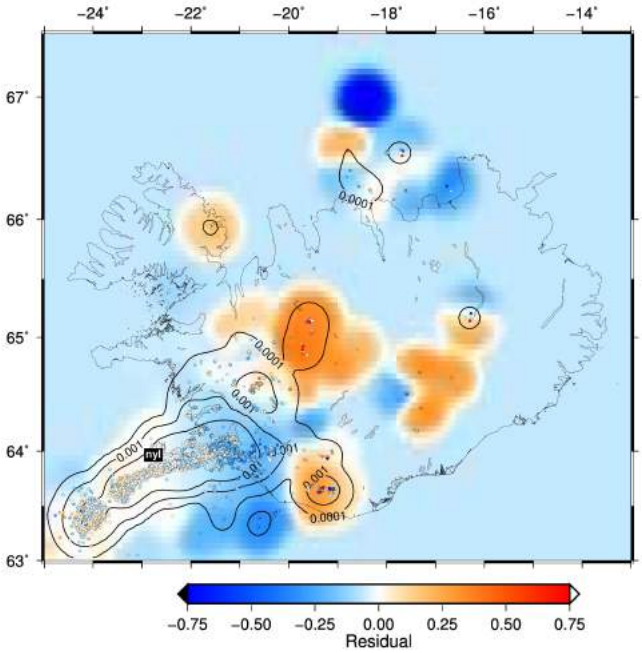

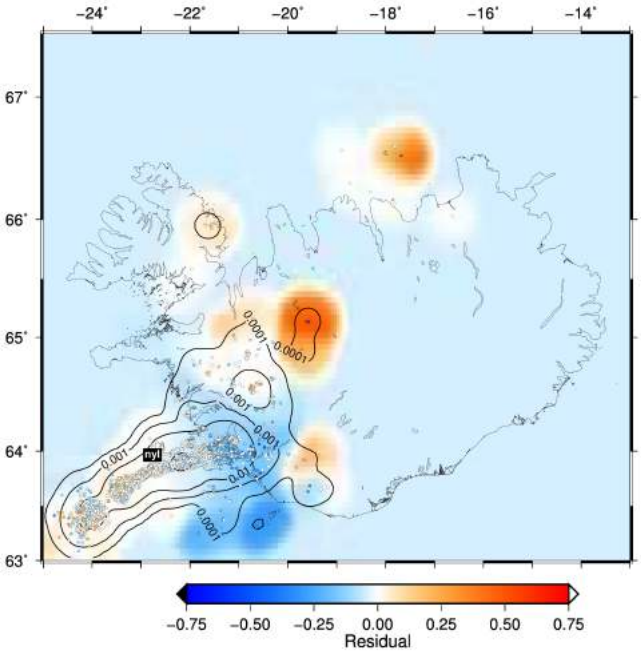

rne

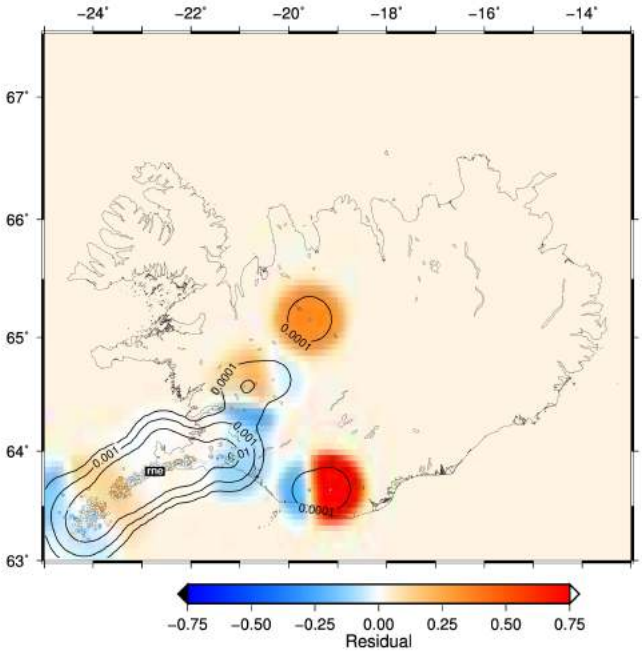

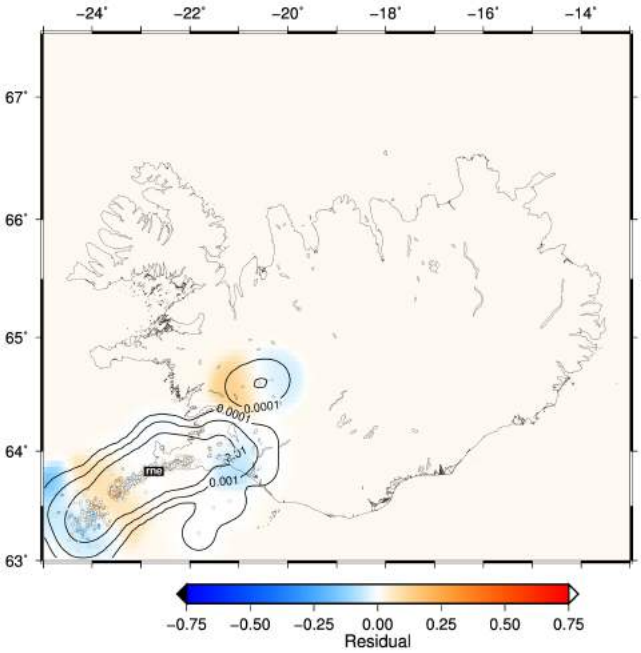

P-wave S-wave

vog

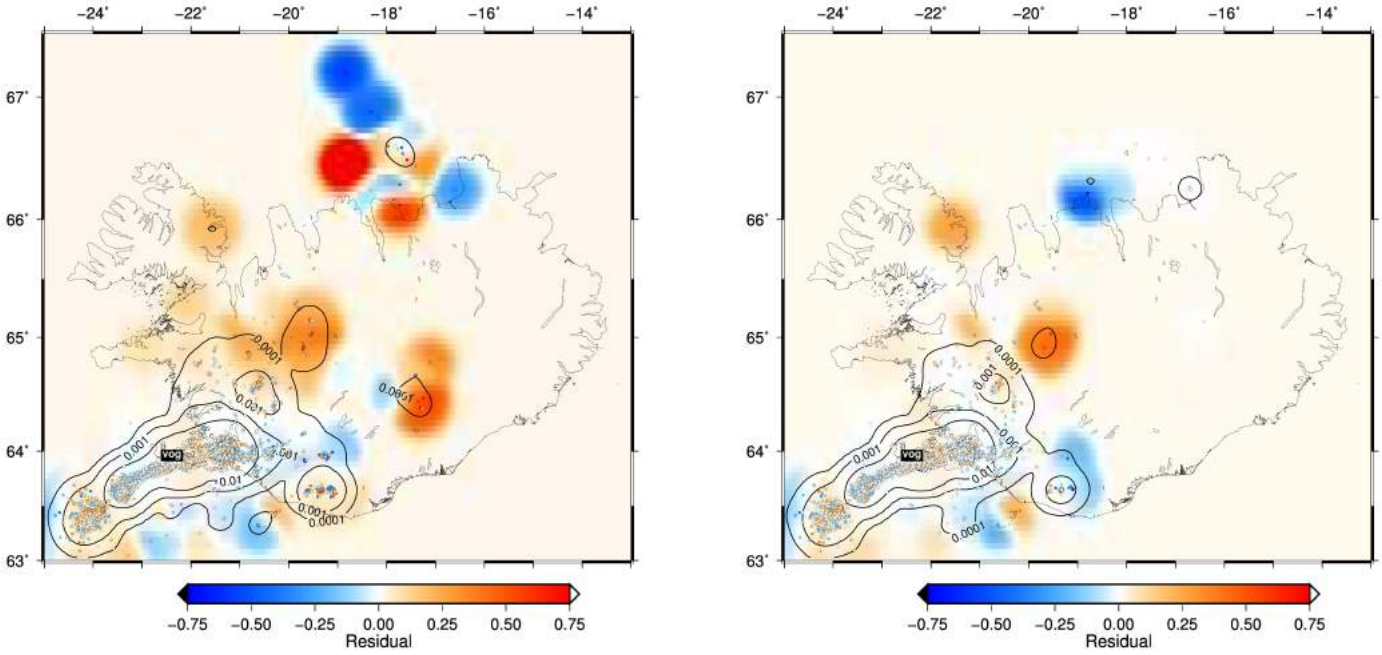

grv

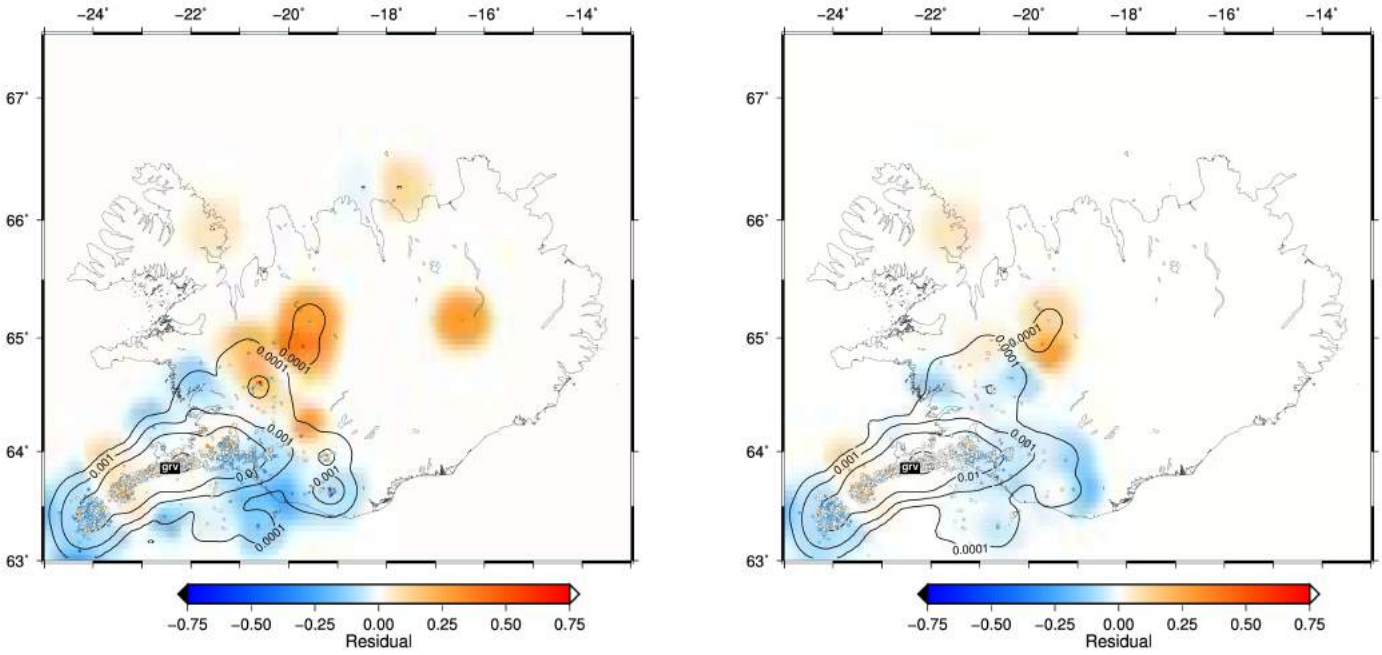

P-wave S-wave

kri

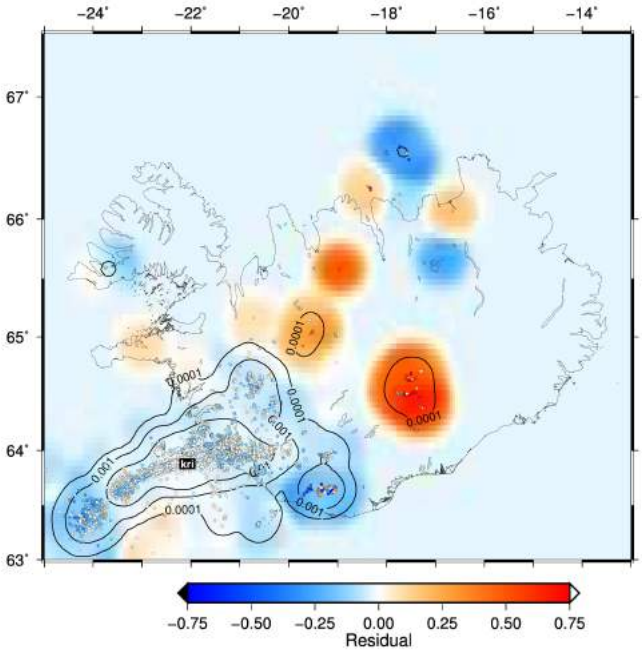

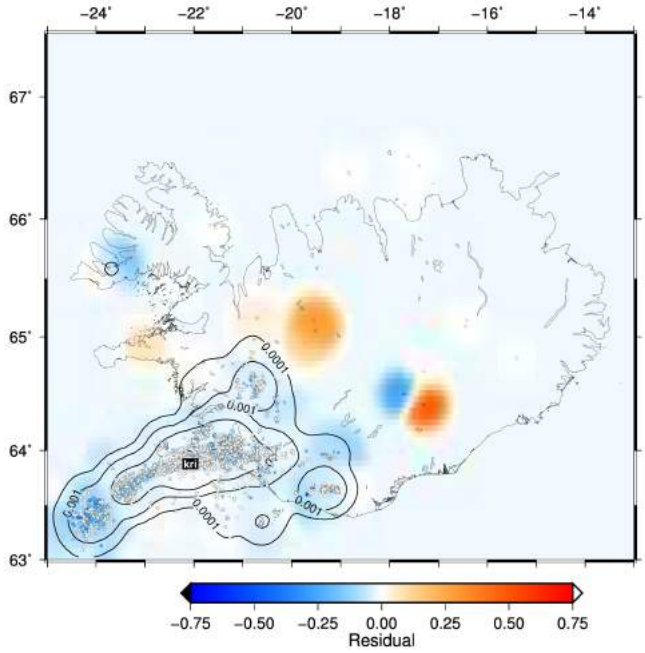

vos

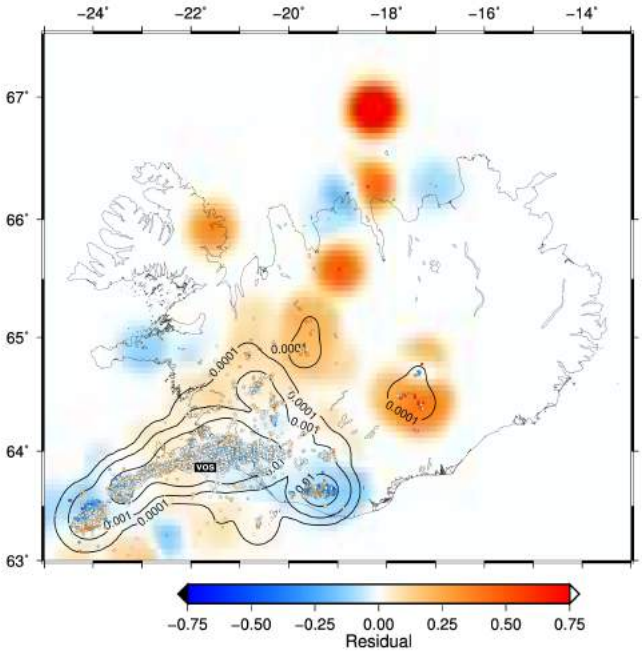

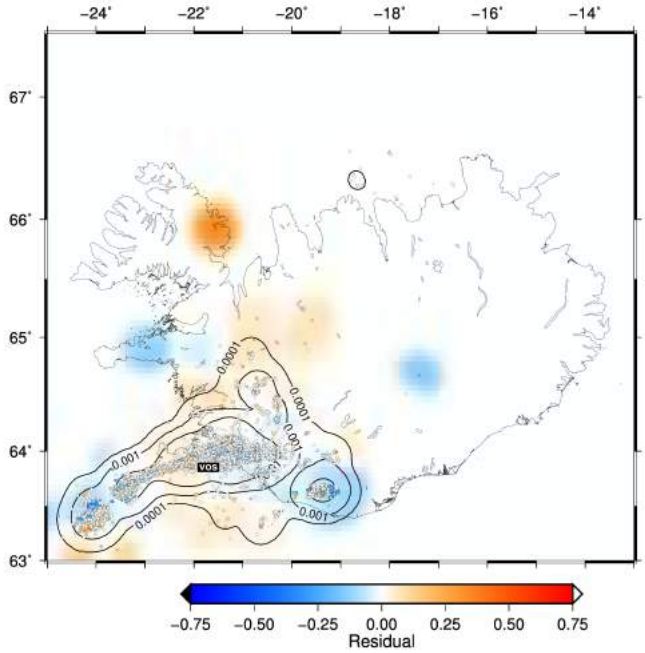

P-wave S-wave

kas

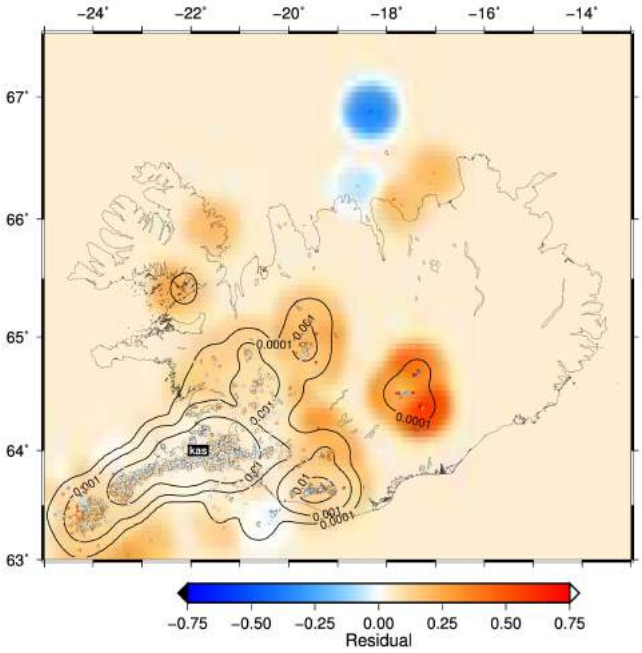

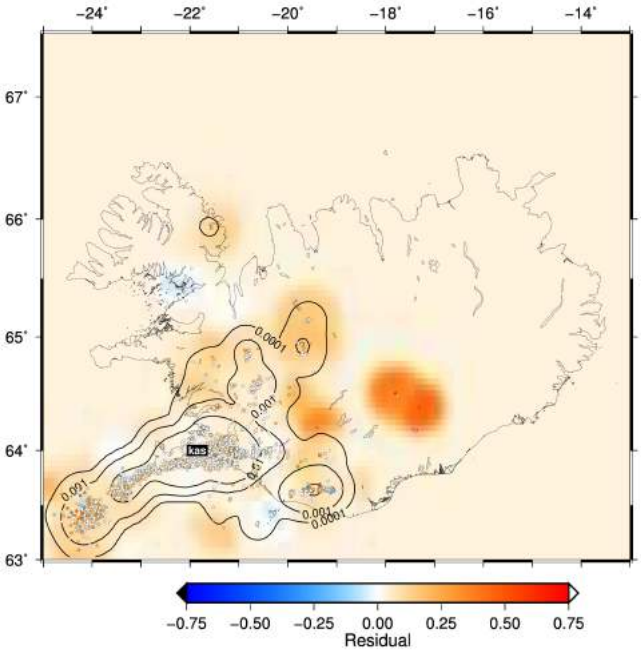

haf

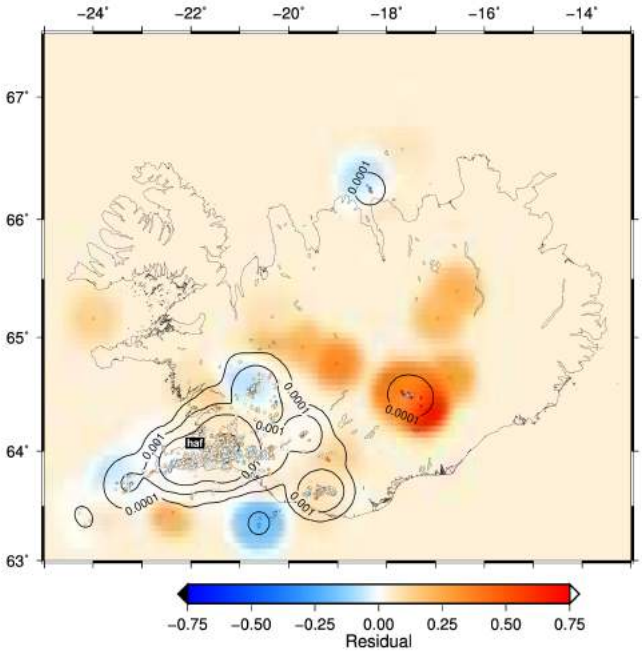

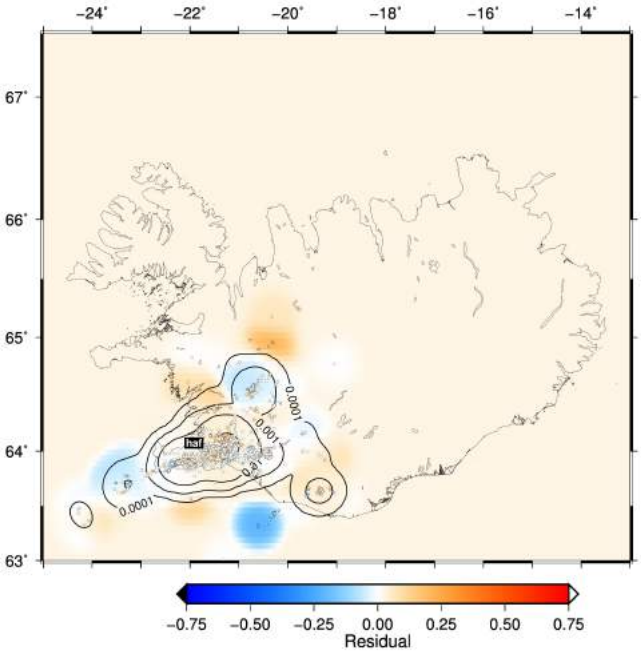

P-wave S-wave

bja

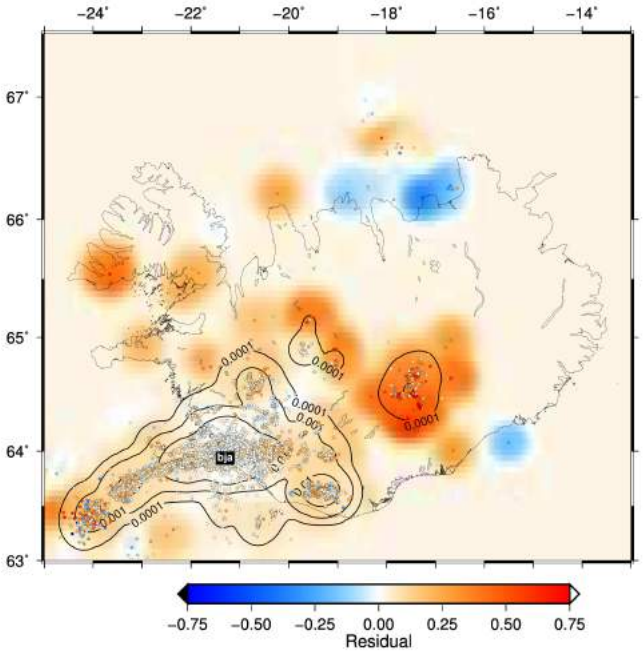

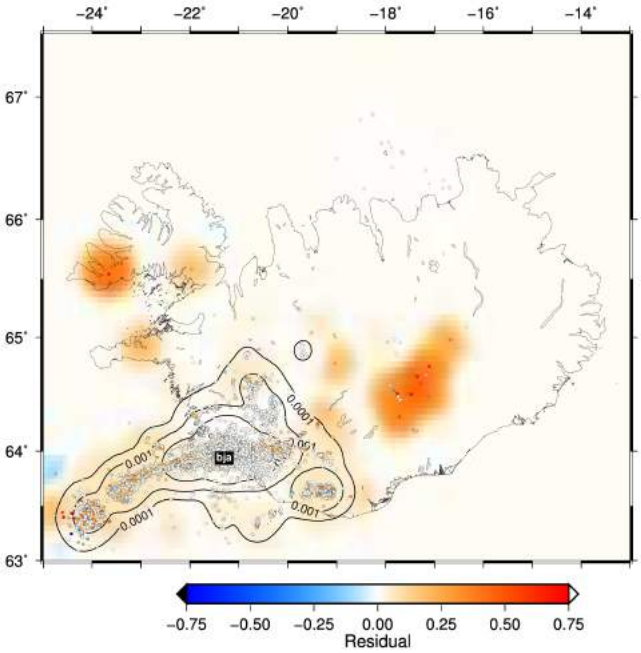

san

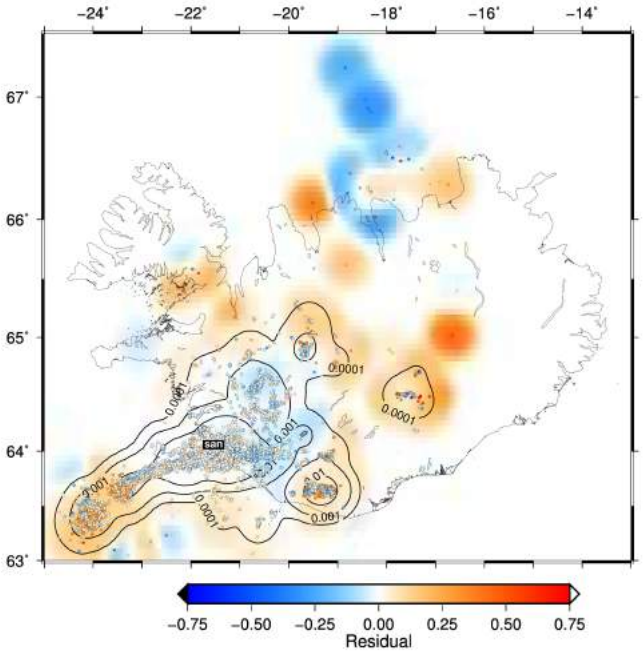

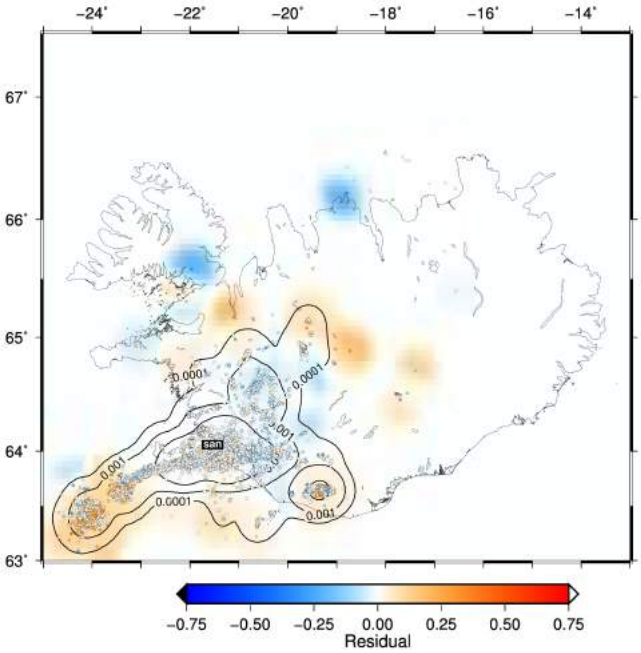

P-wave S-wave

kro

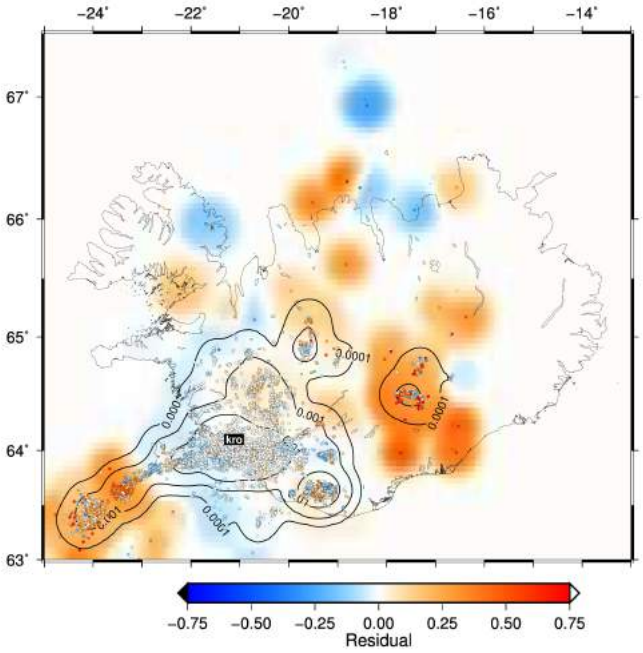

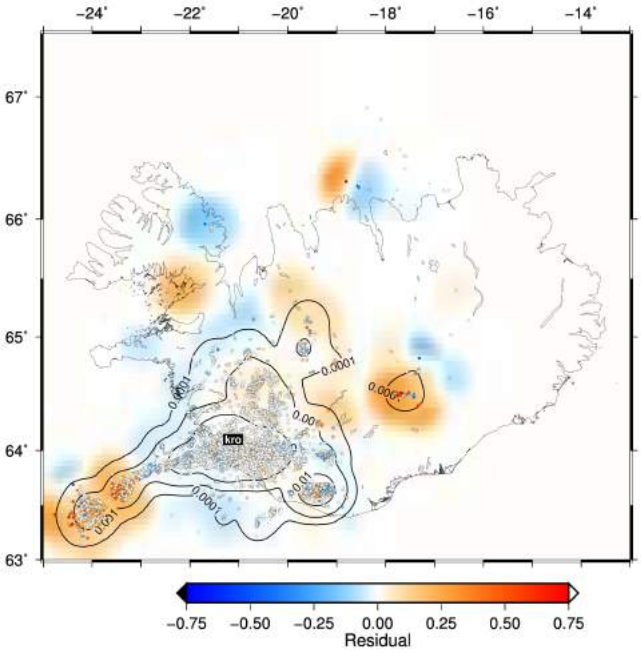

hei

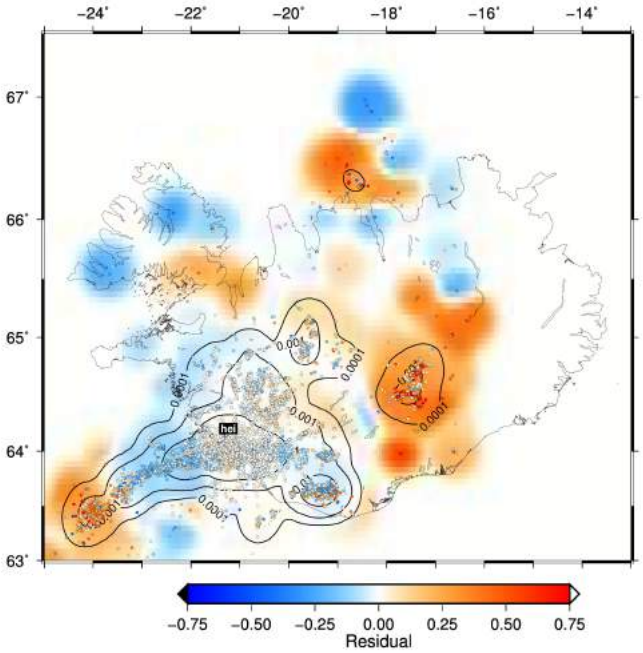

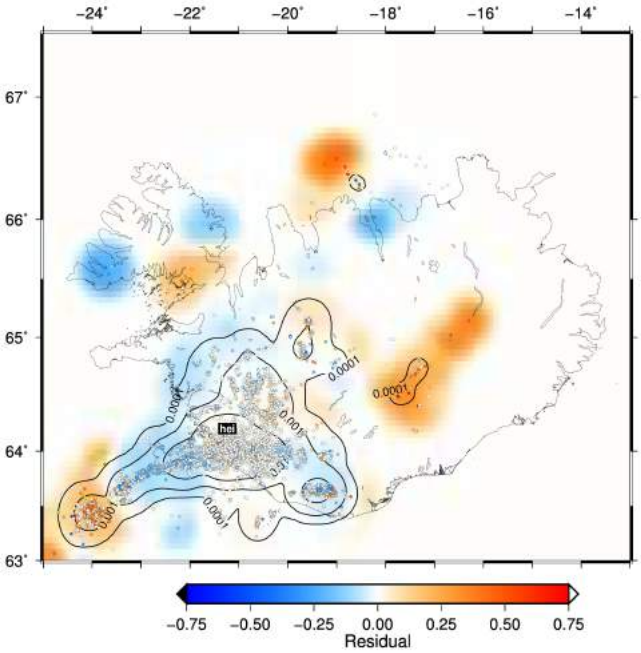

P-wave S-wave

sol

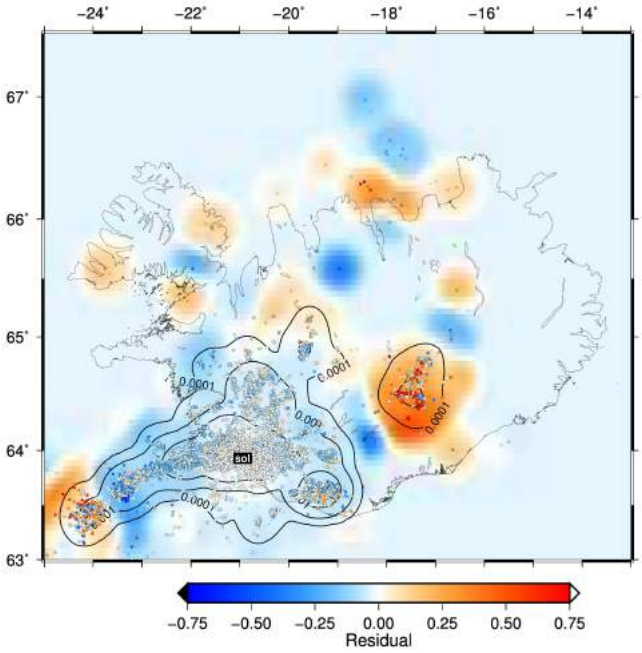

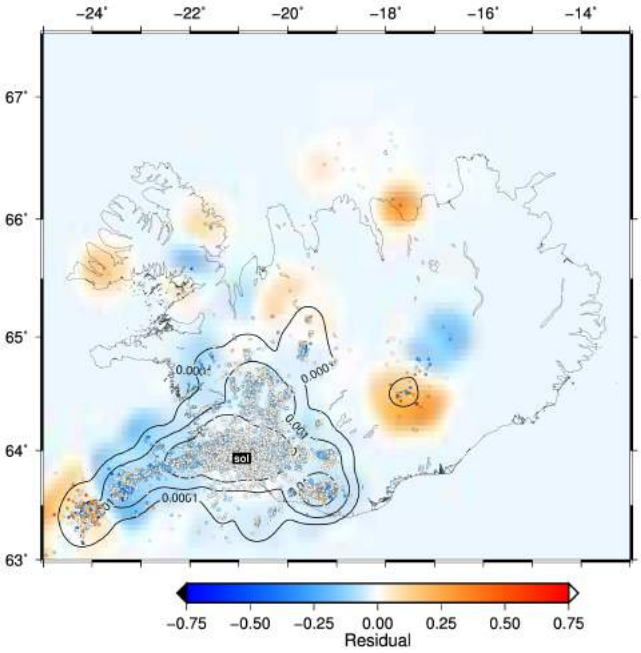

asm

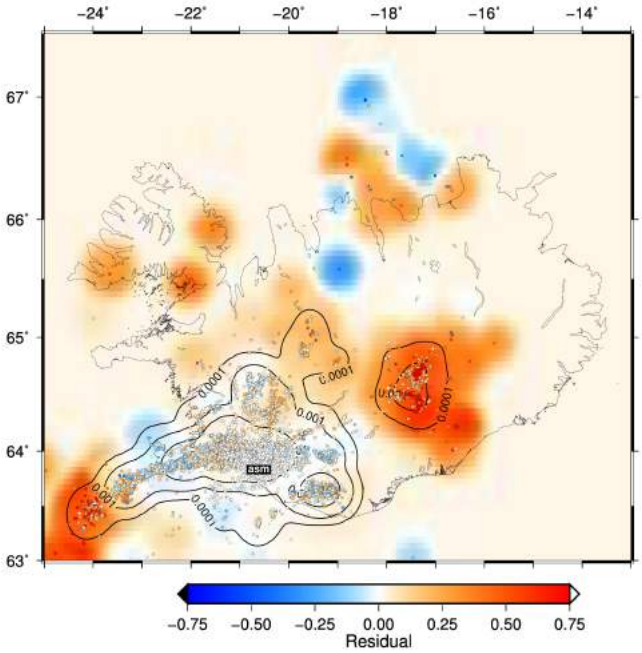

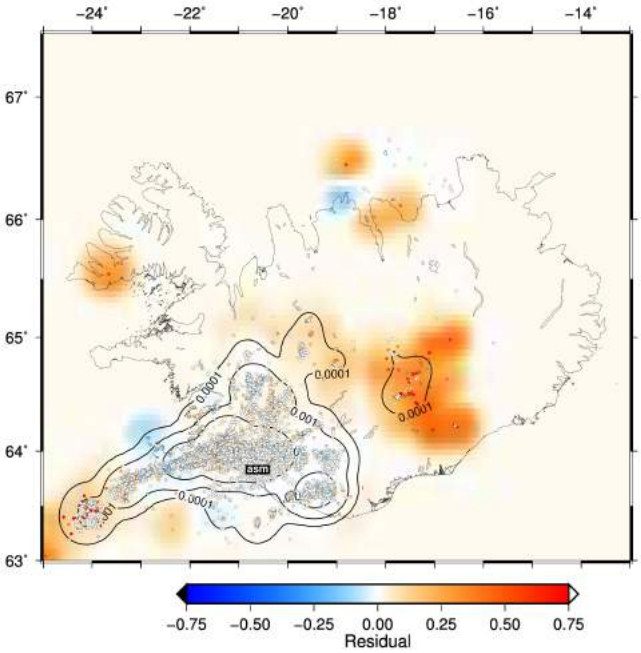

P-wave S-wave

sau

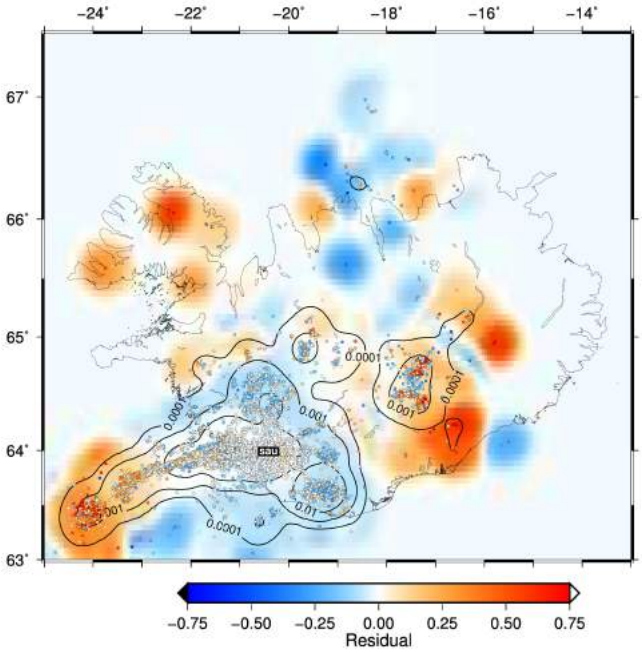

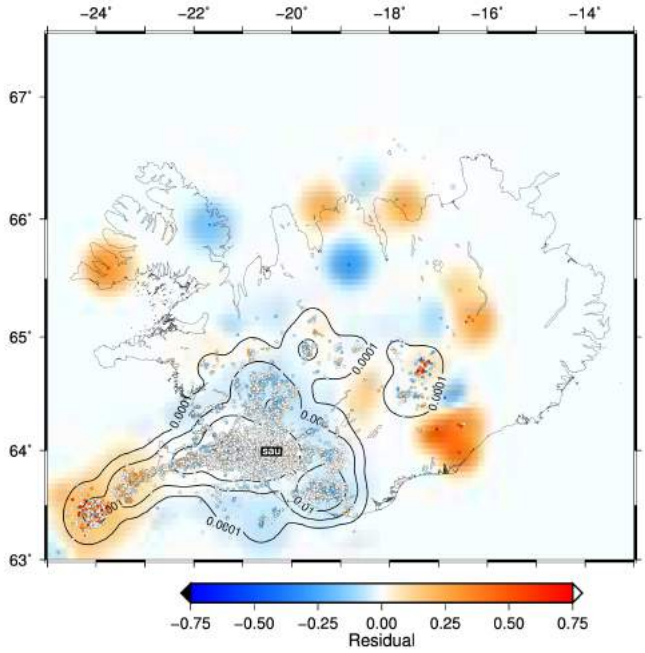

hau

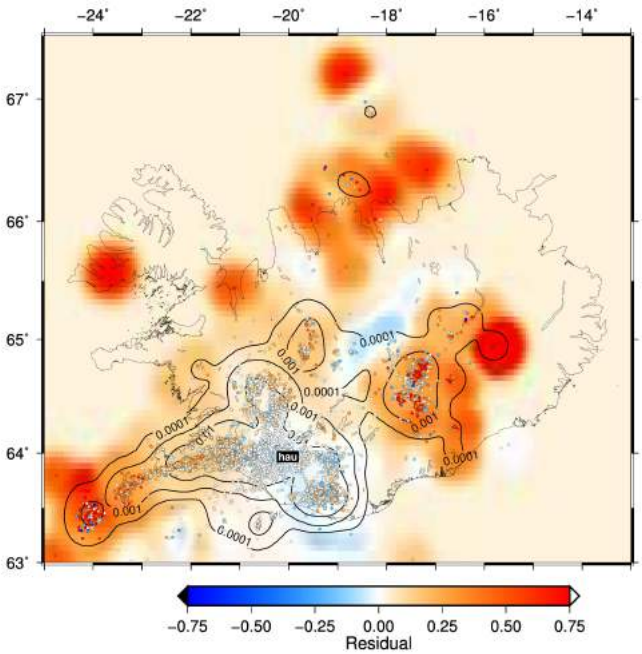

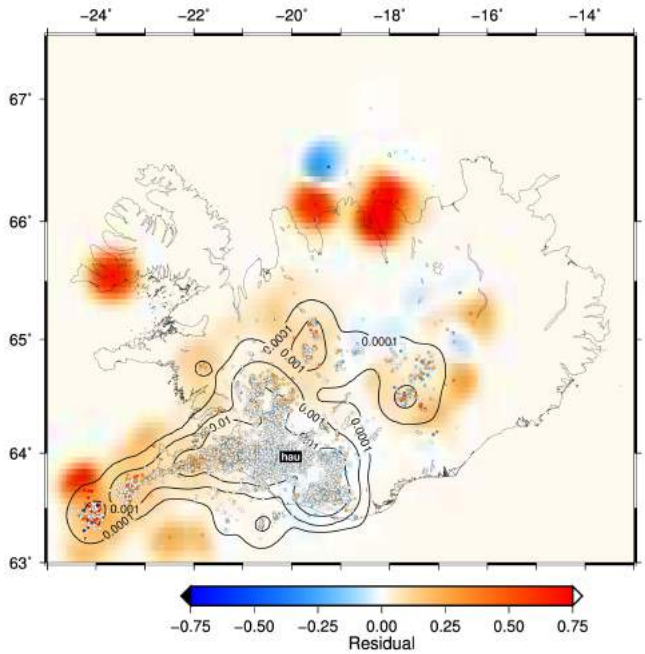

P-wave S-wave

ves

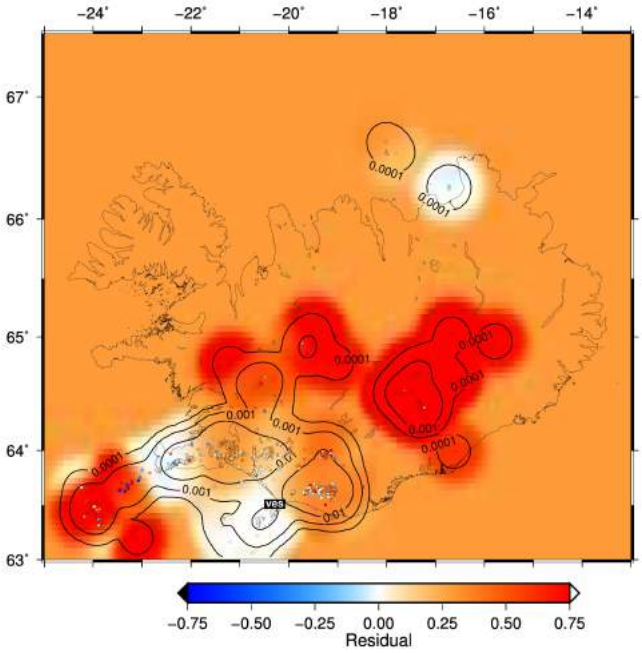

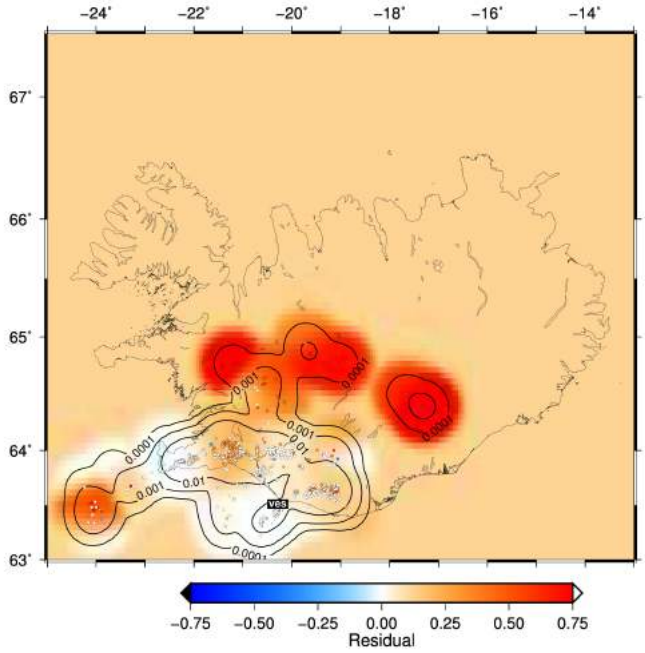

mid

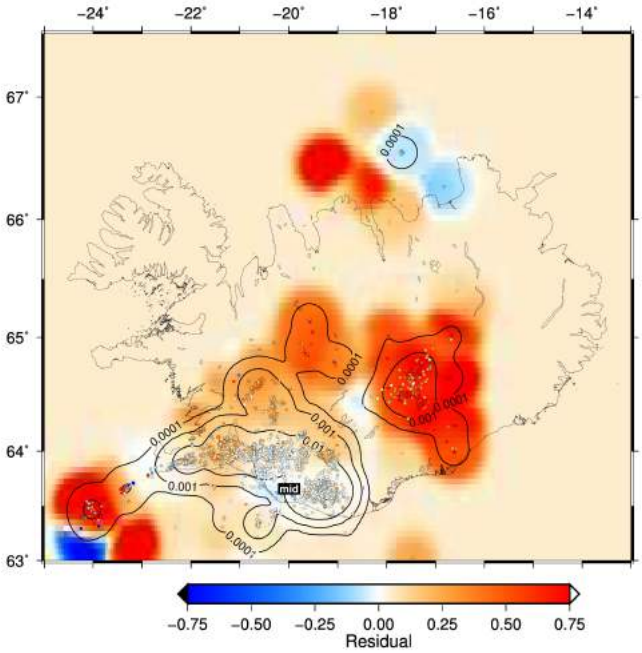

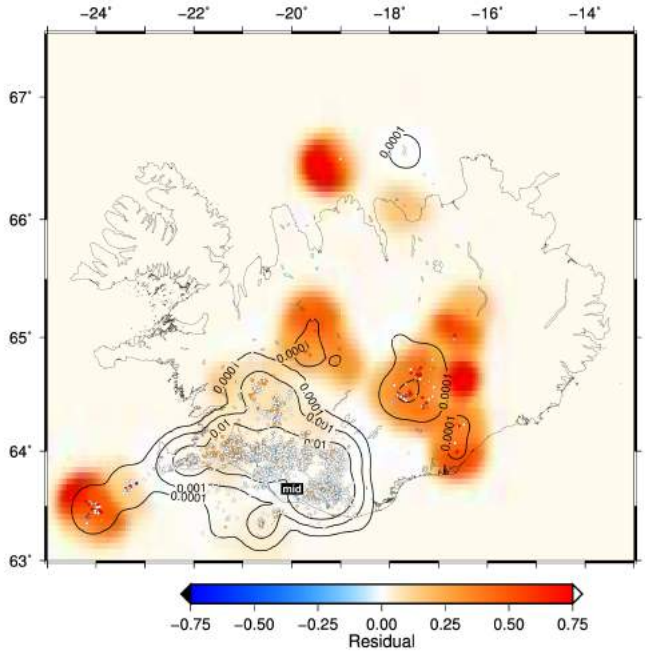

P-wave S-wave

smj

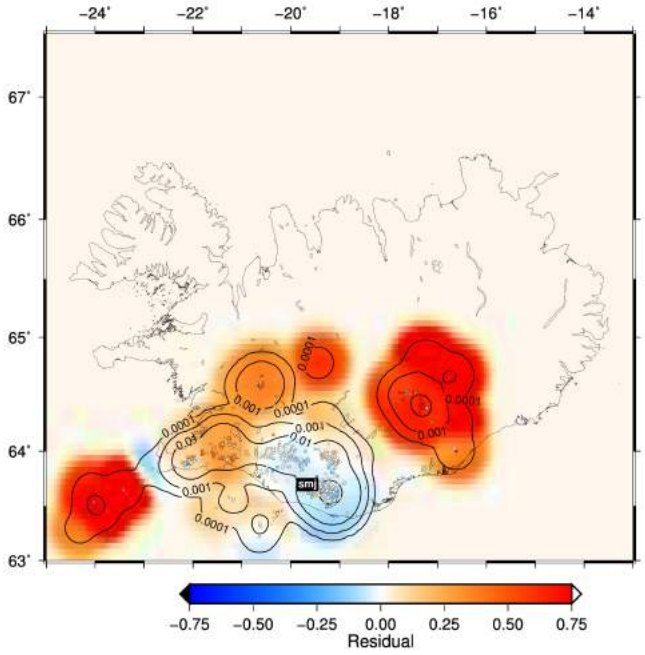

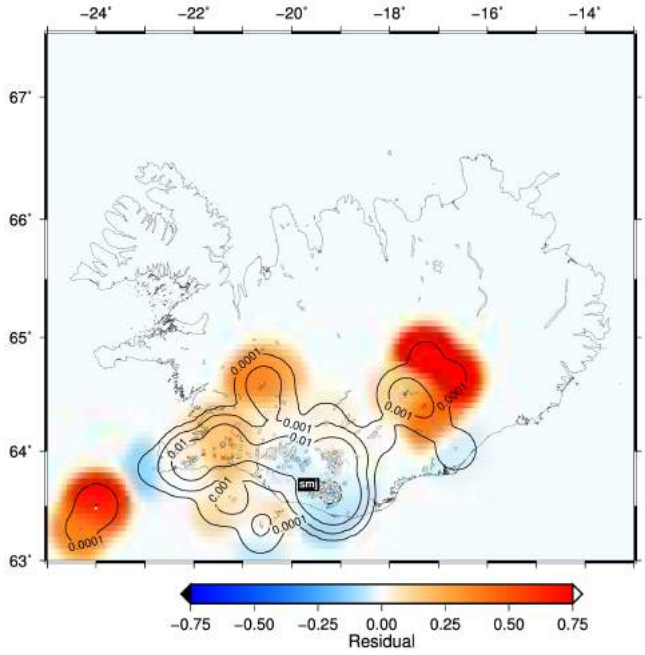

god

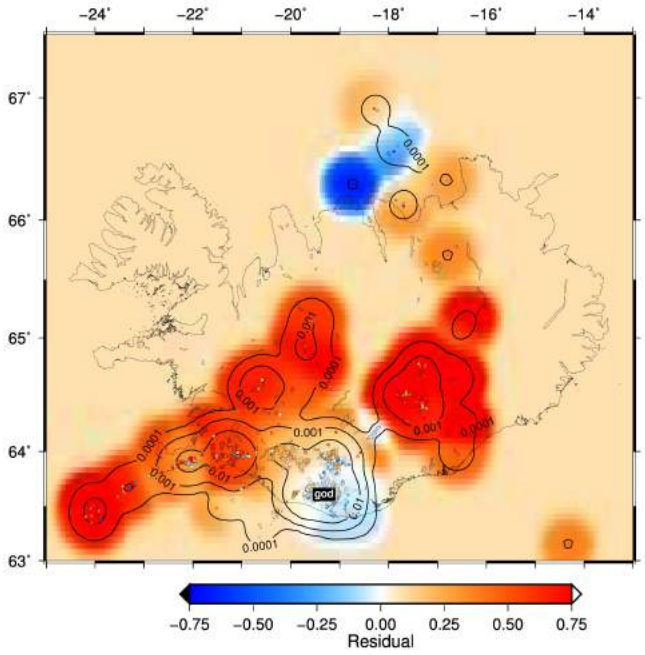

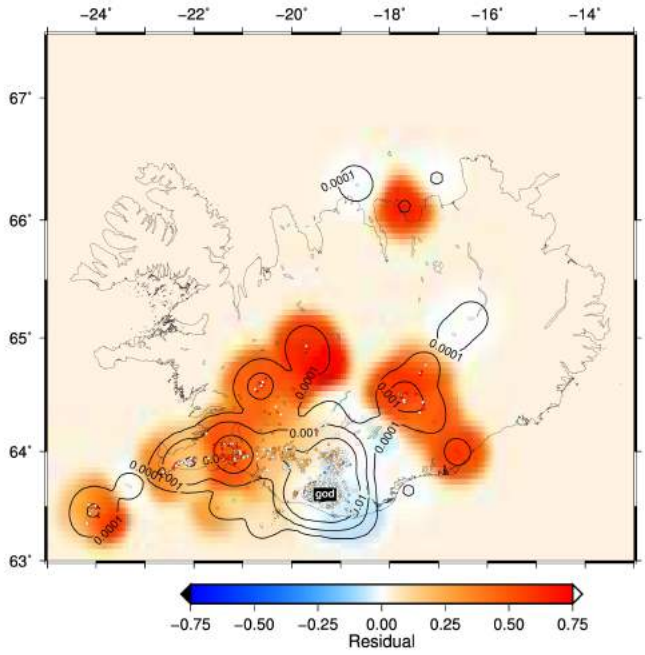

P-wave S-wave

esk

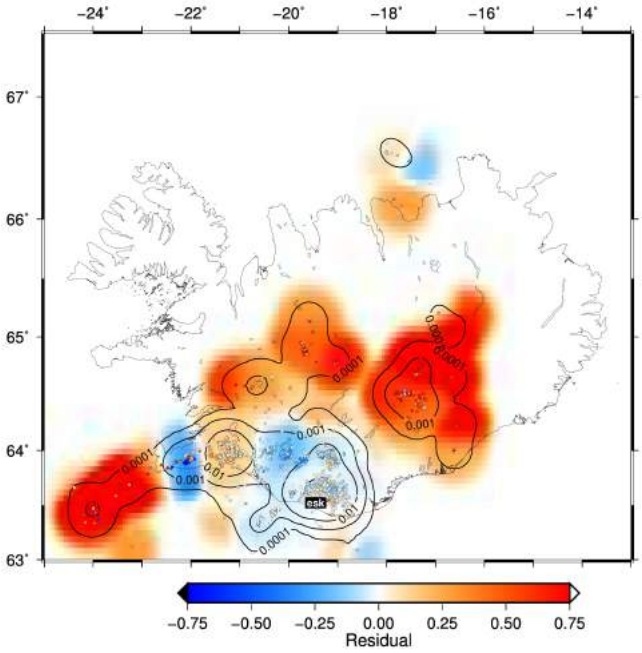

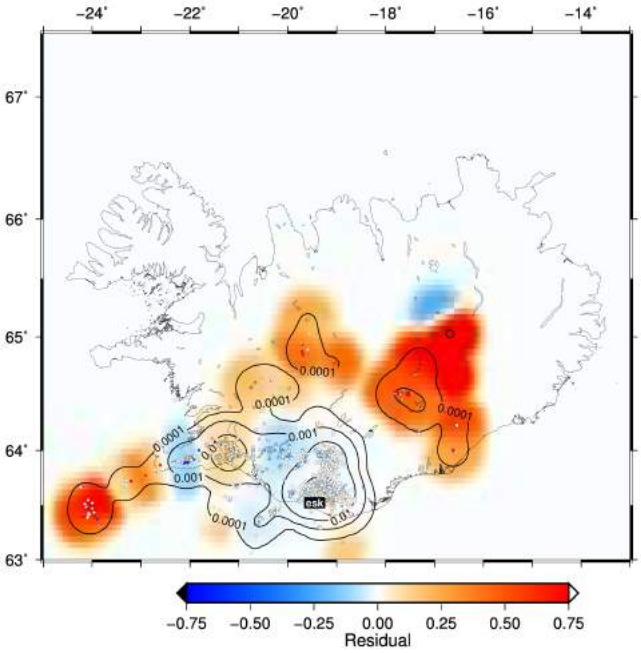

alf

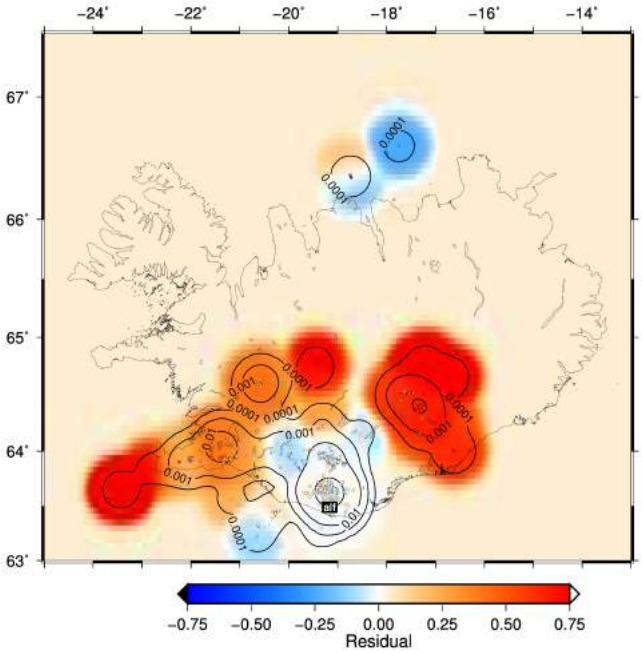

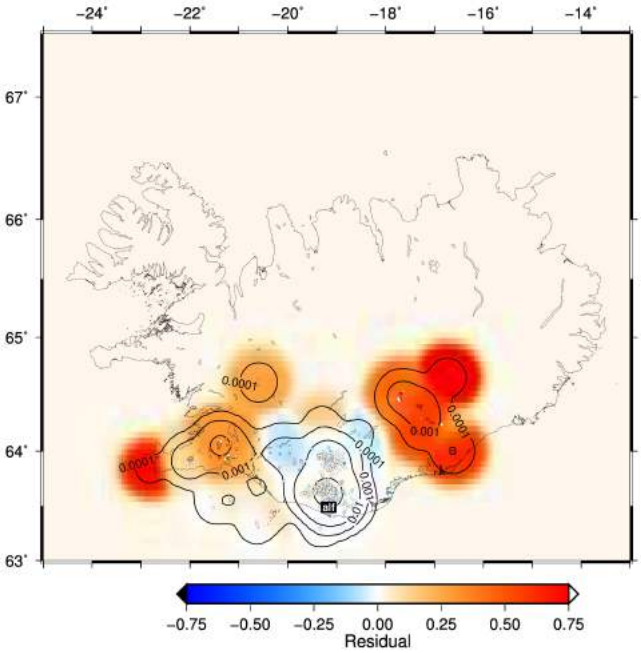

P-wave S-wave

skh

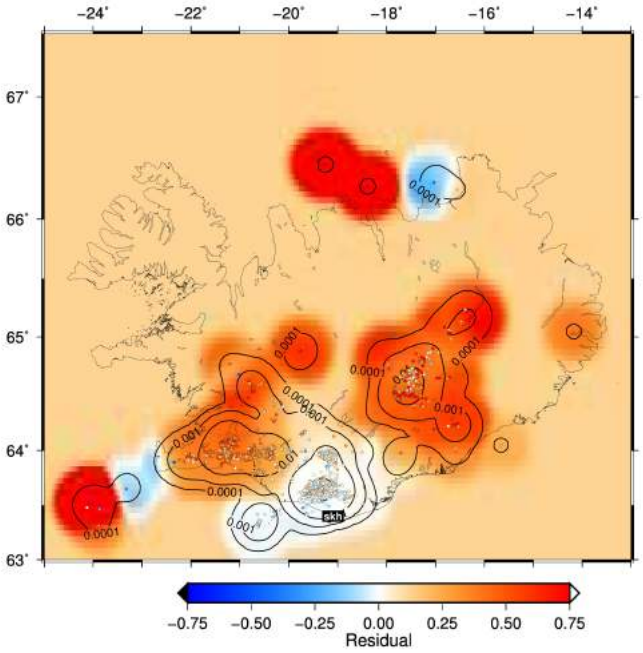

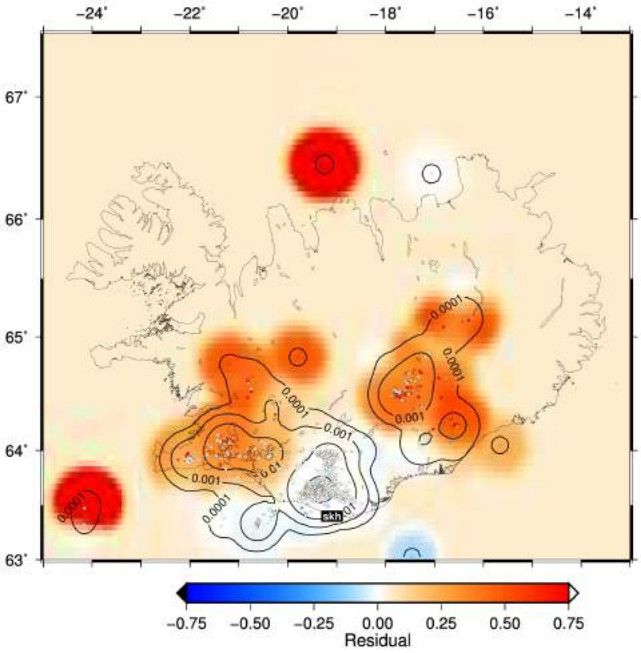

hvo

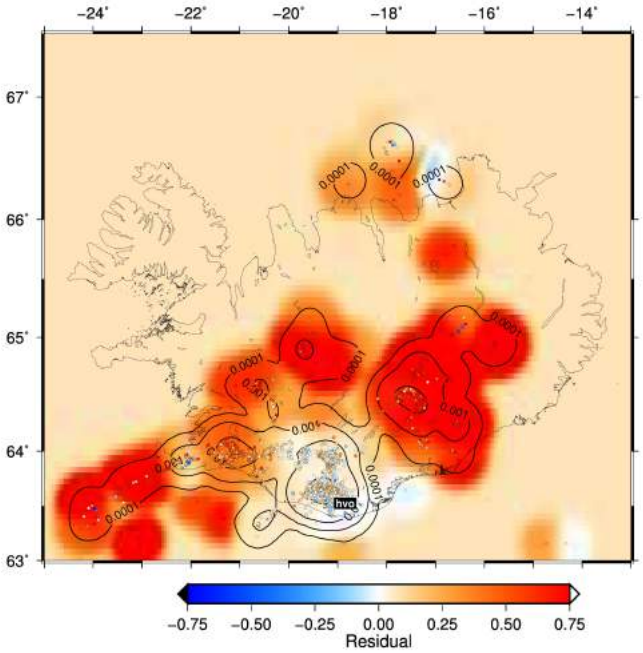

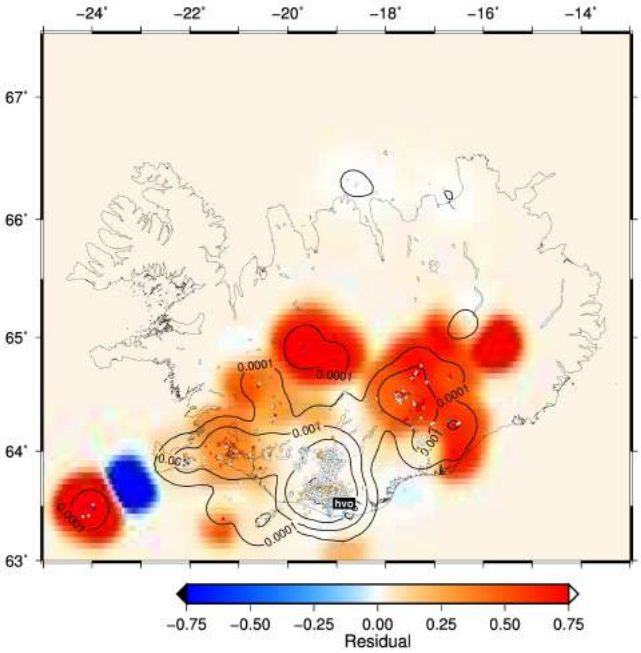

P-wave S-wave

rju

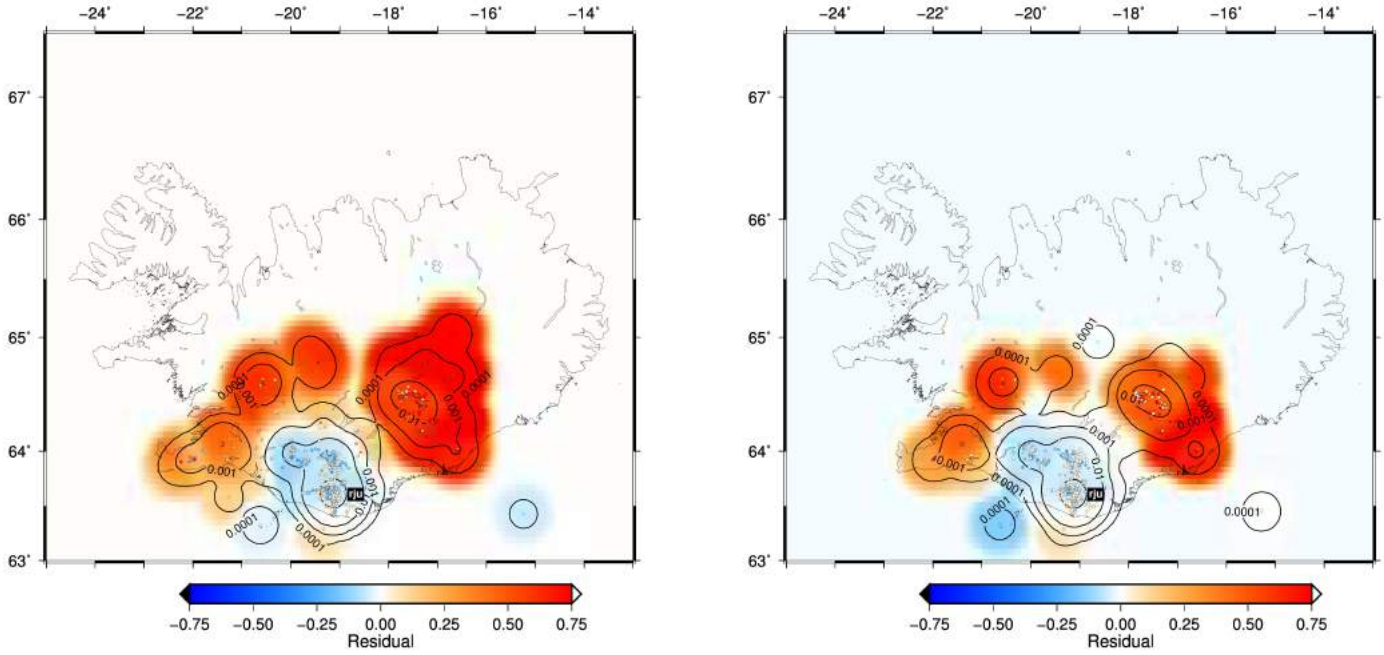

snb

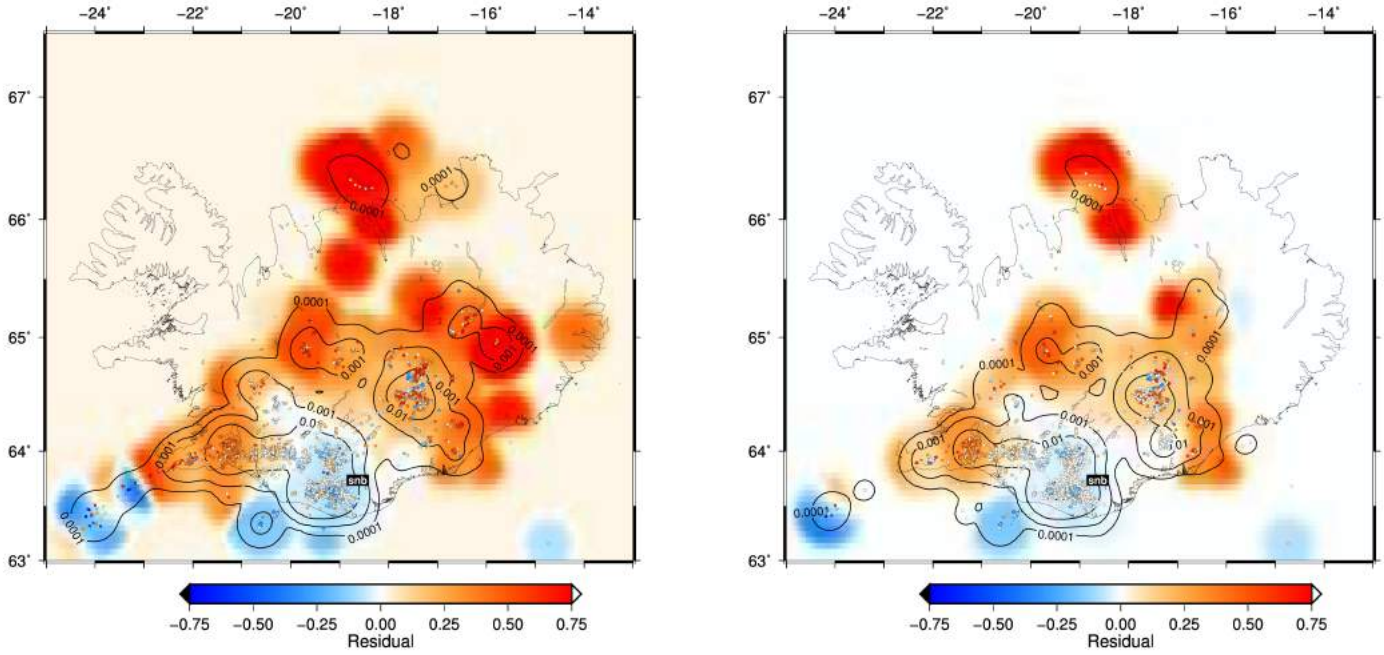

P-wave S-wave

sly

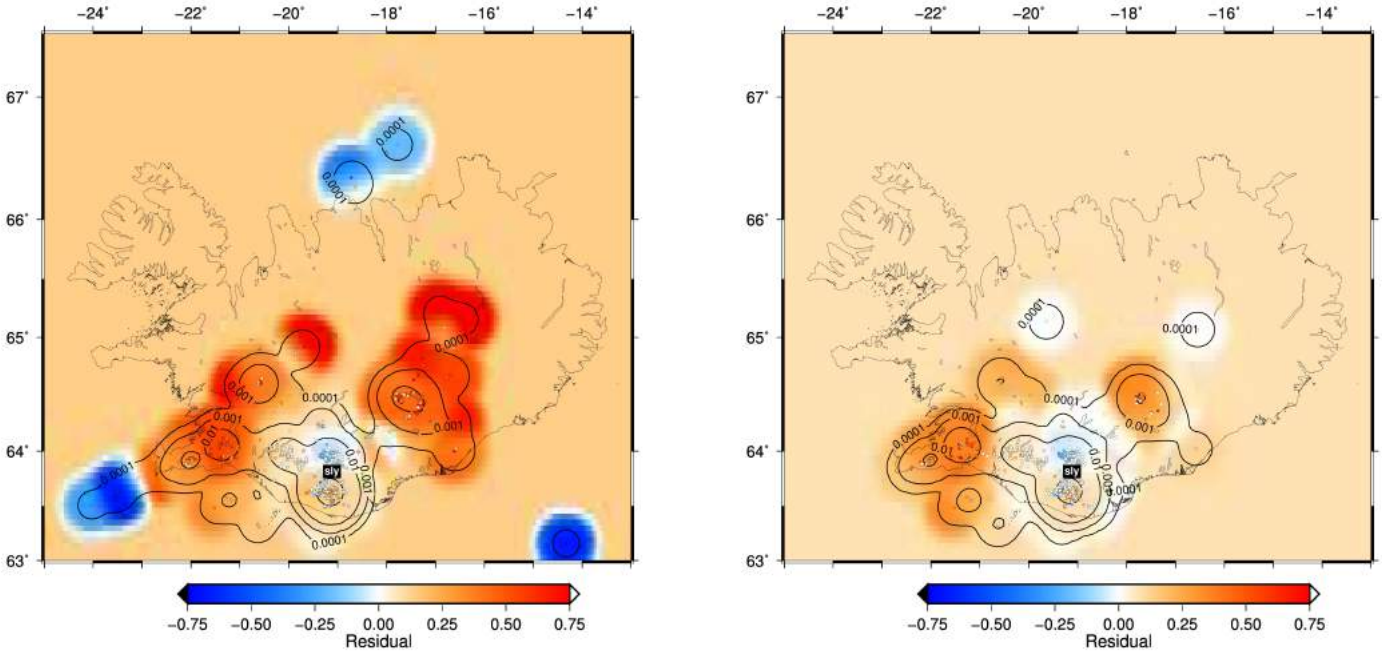

P-wave S-wave

fag

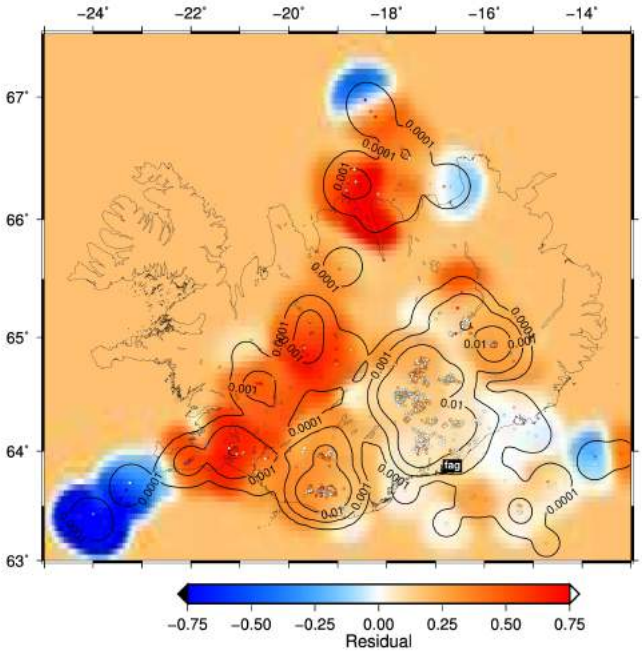

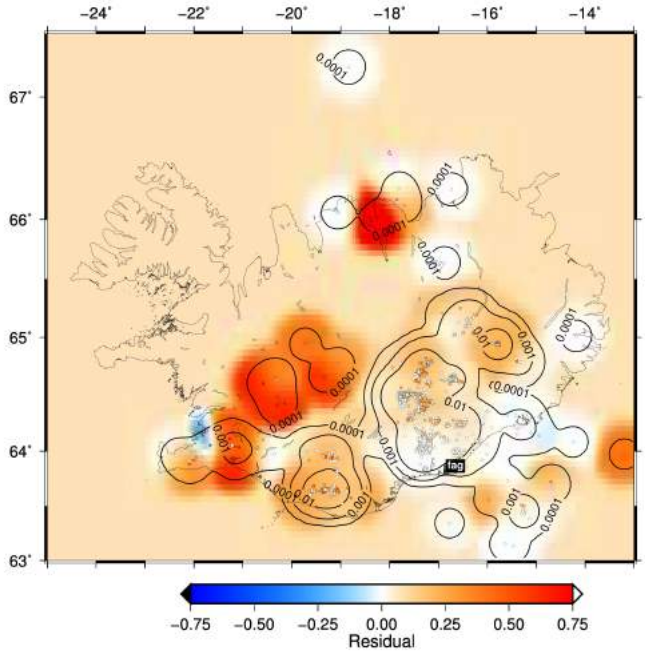

kal

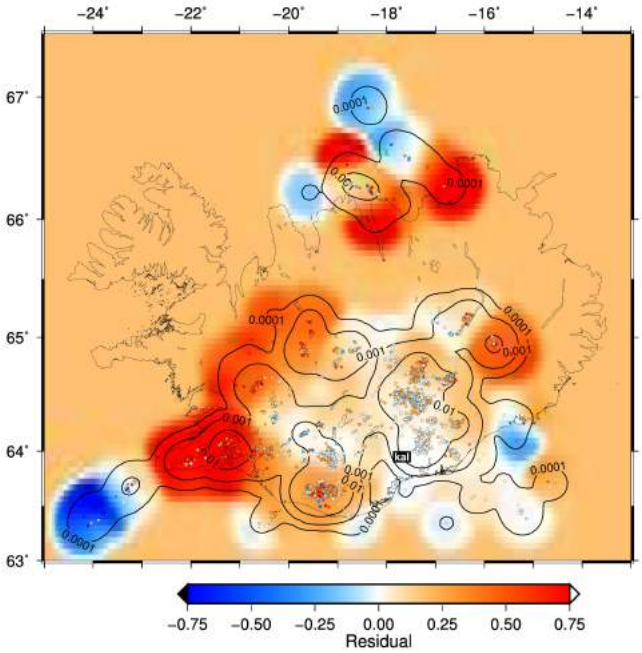

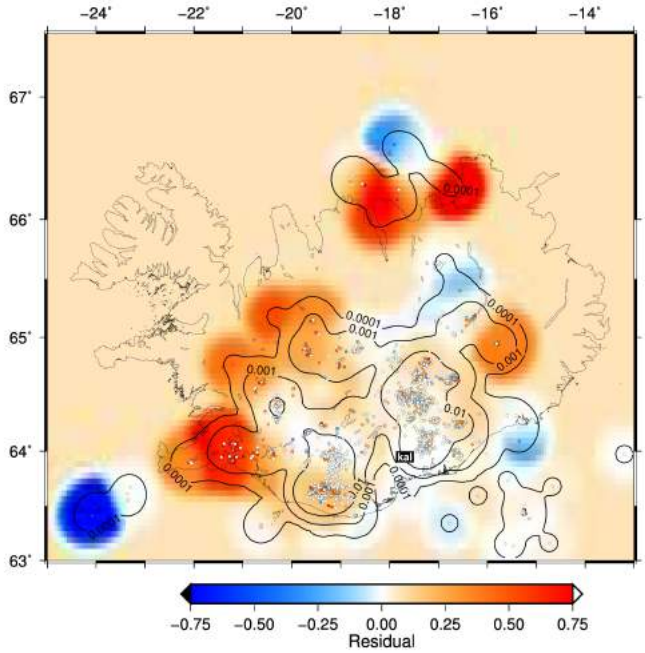

P-wave S-wave

grf

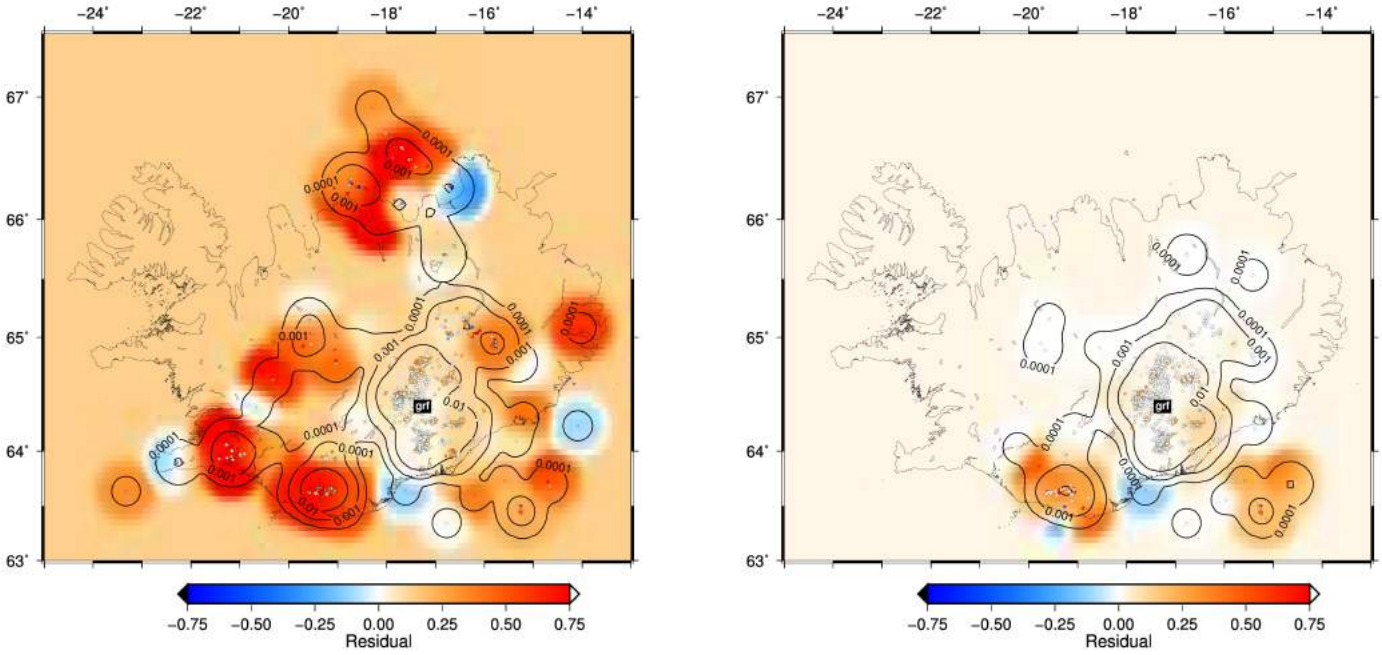

P-wave S-wave

vat

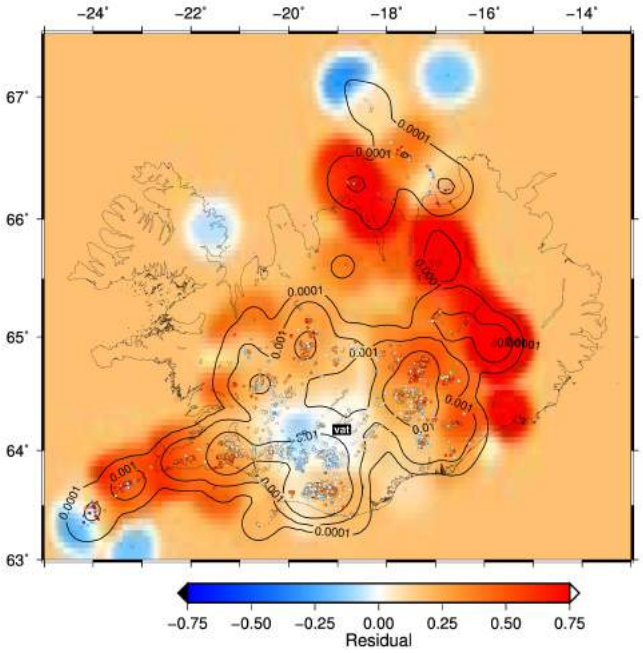

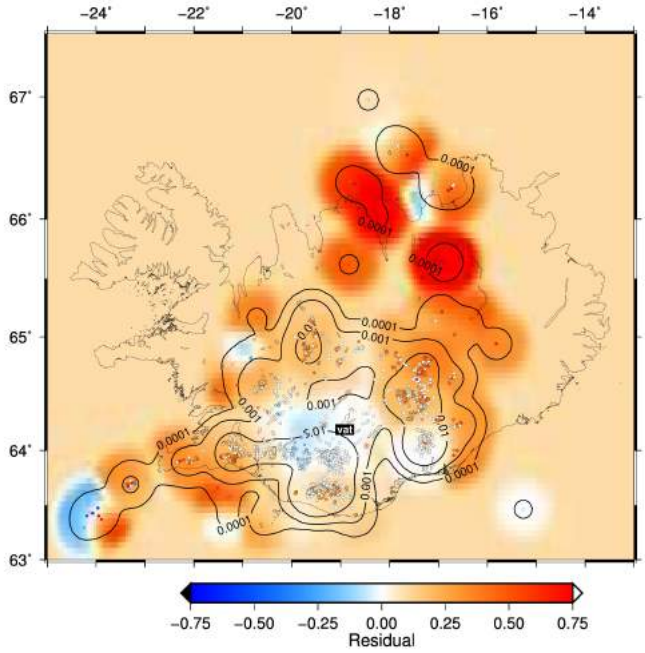

jok

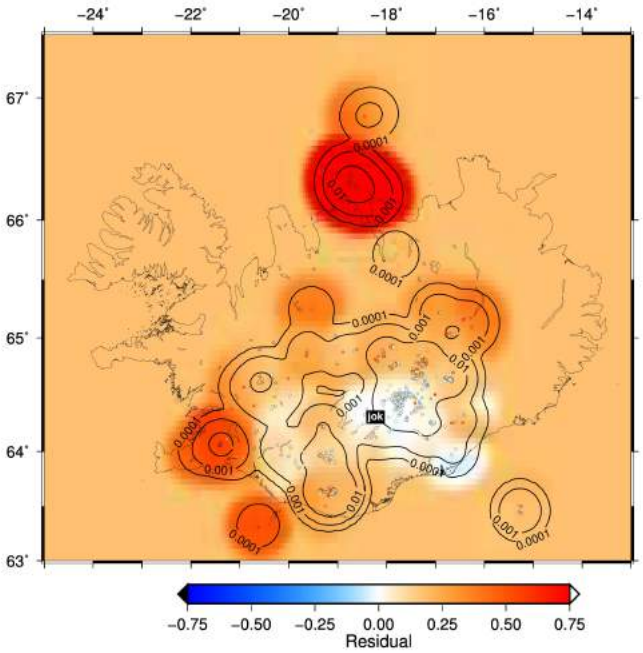

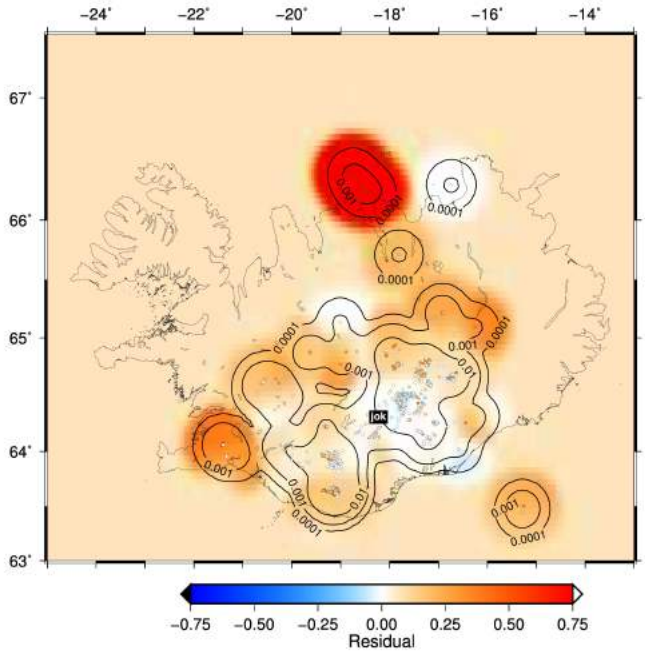

P-wave S-wave

skr

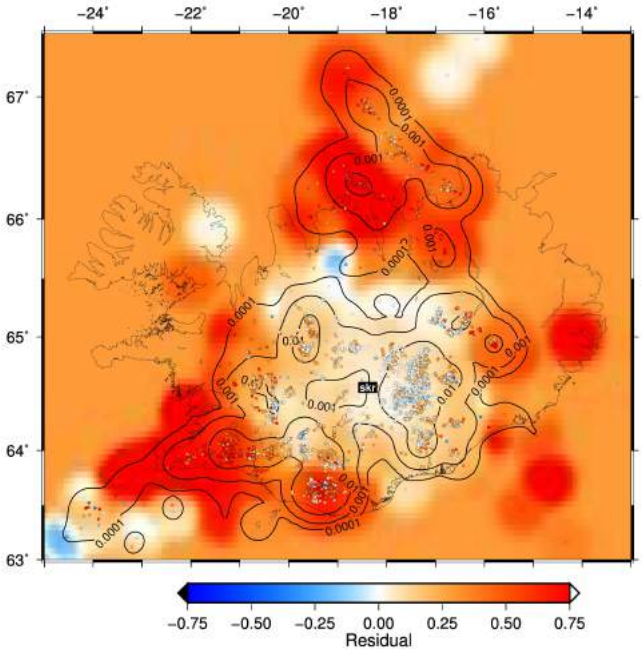

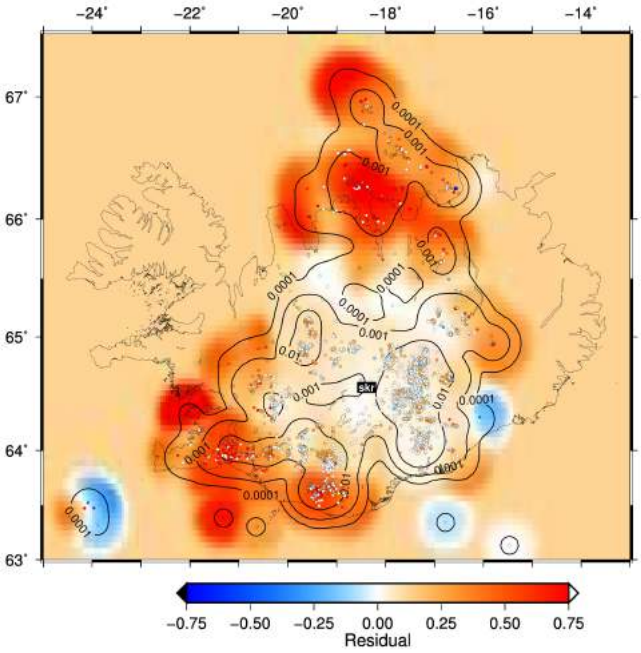

dyn

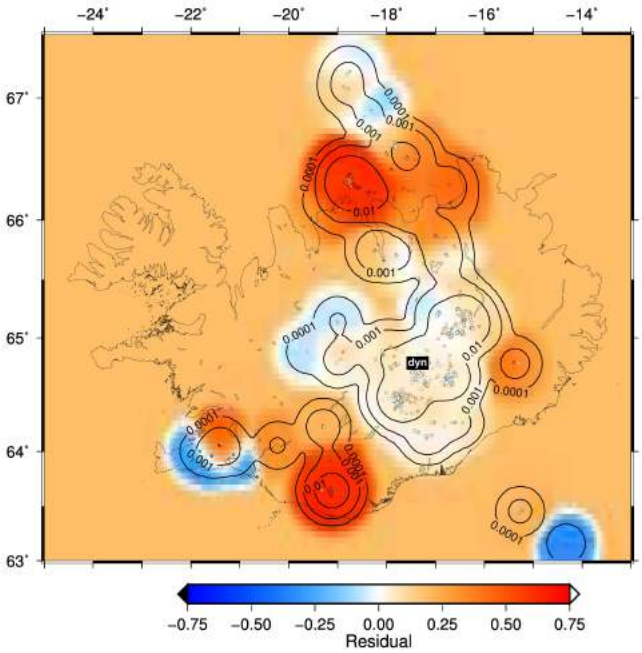

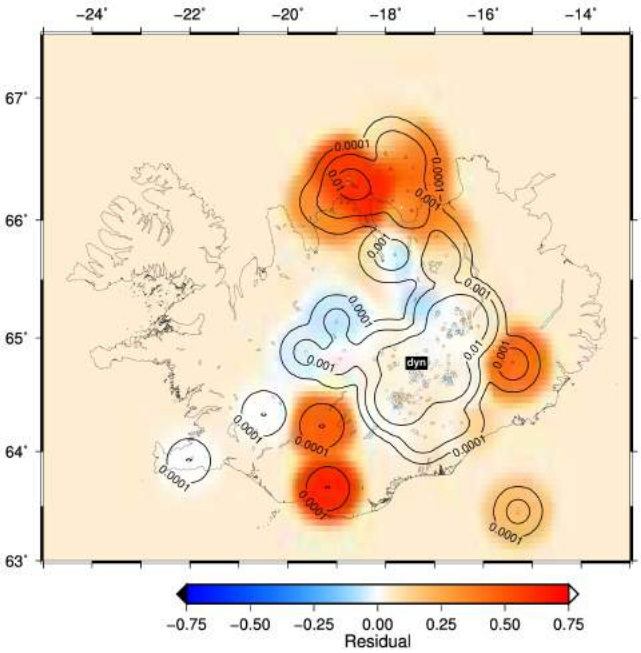

P-wave S-wave

mko

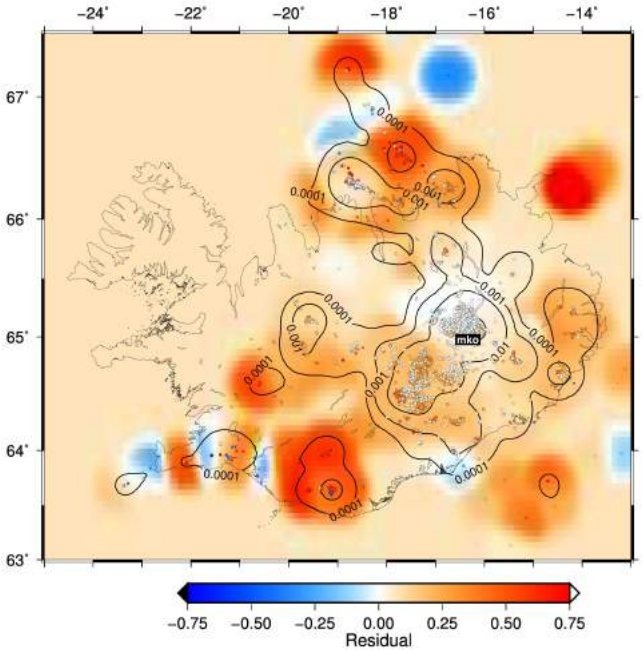

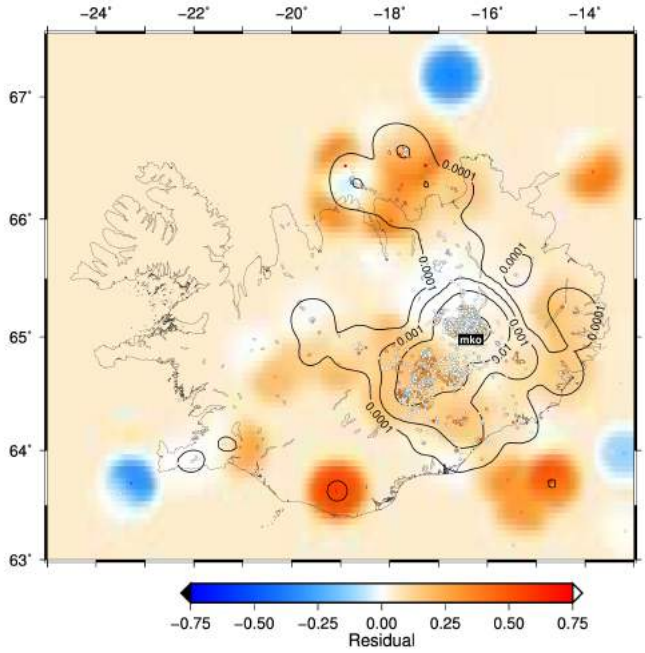

vsh

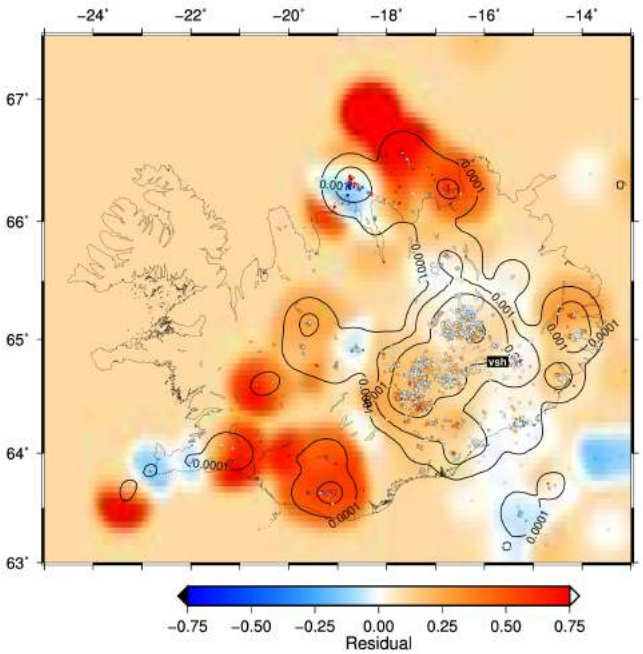

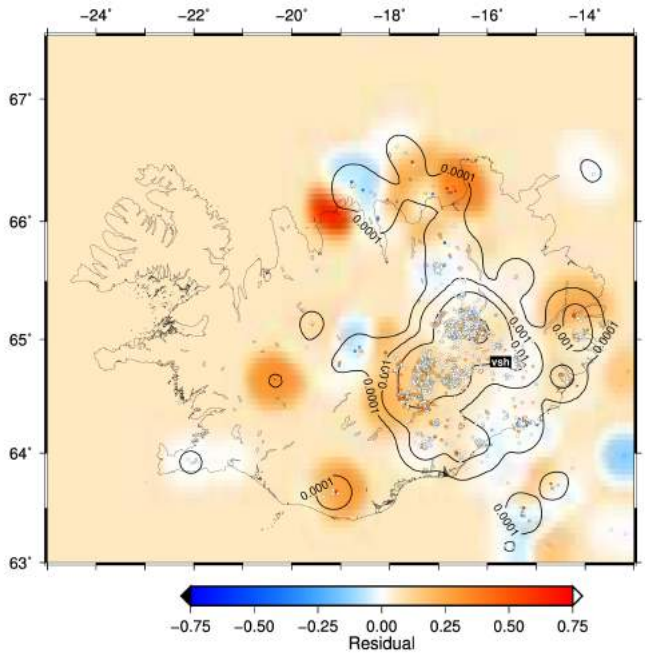

P-wave S-wave

bru

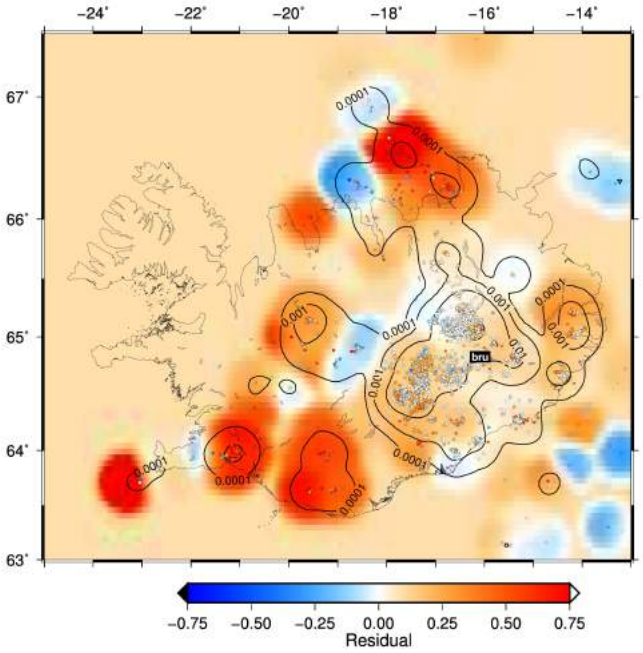

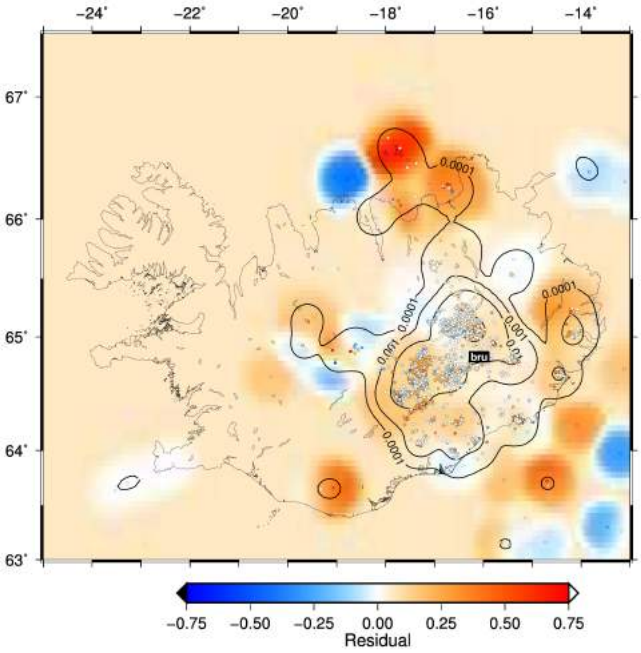

kre

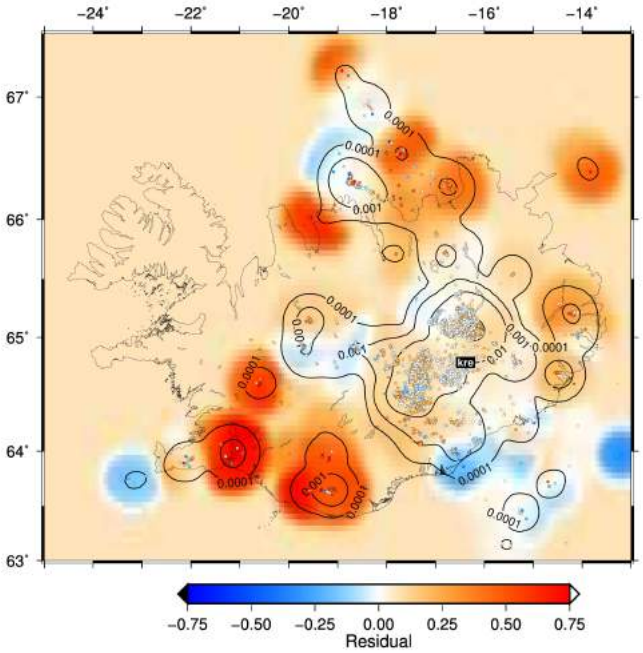

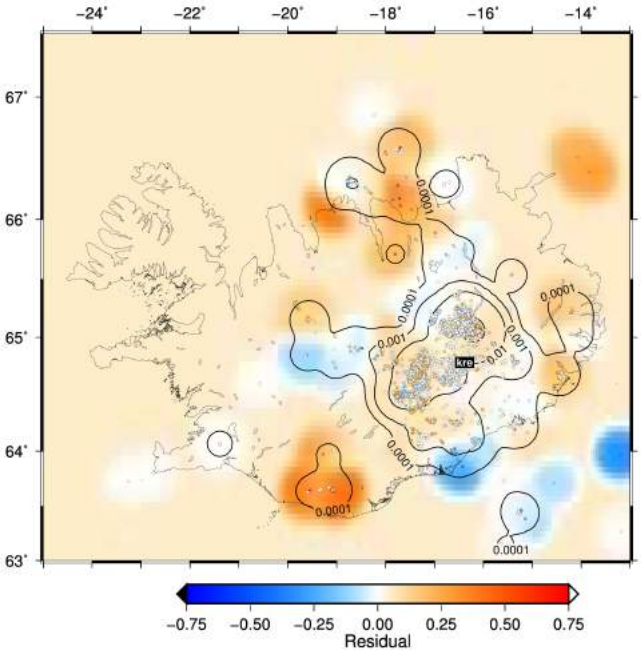

P-wave S-wave

hva

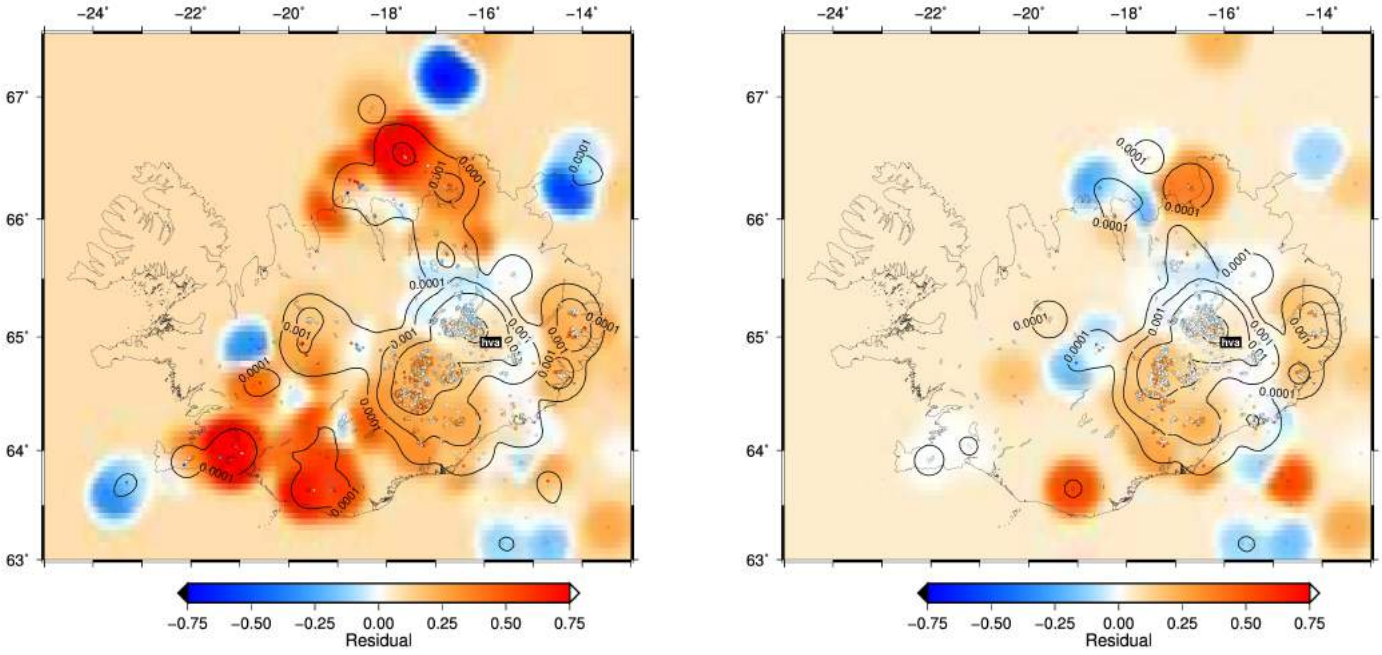

ada

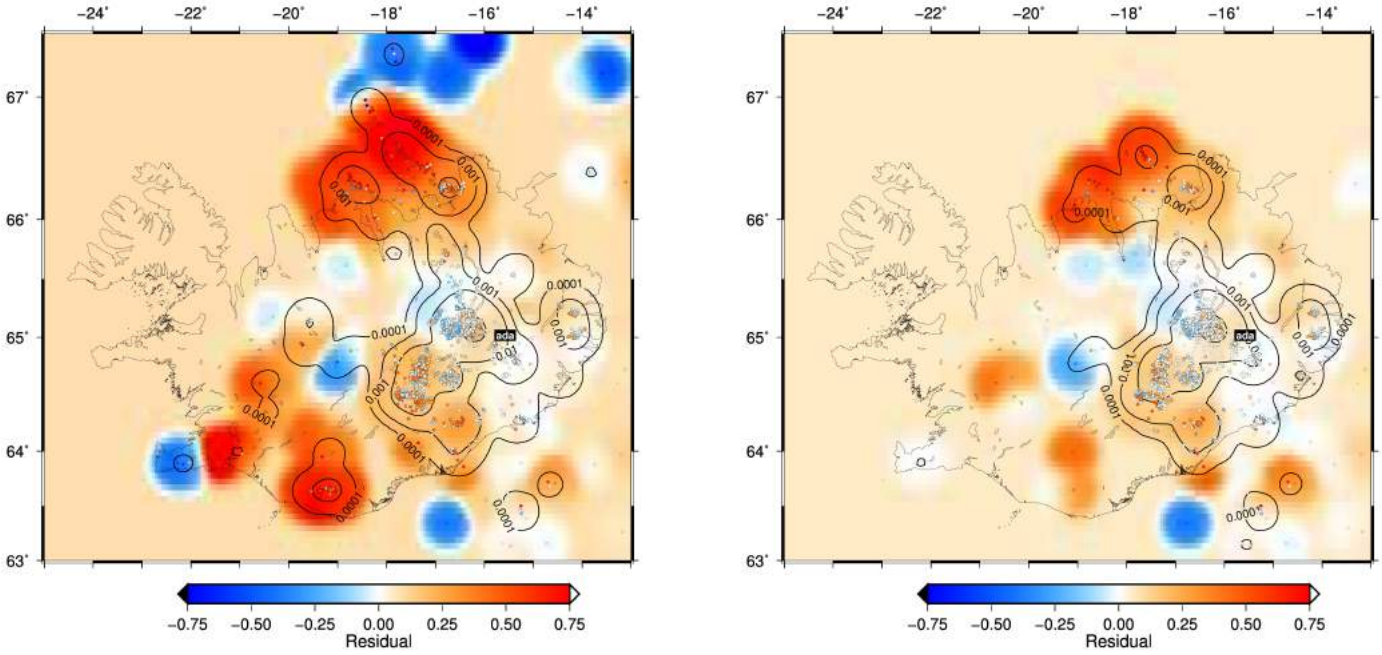

P-wave S-wave

glu

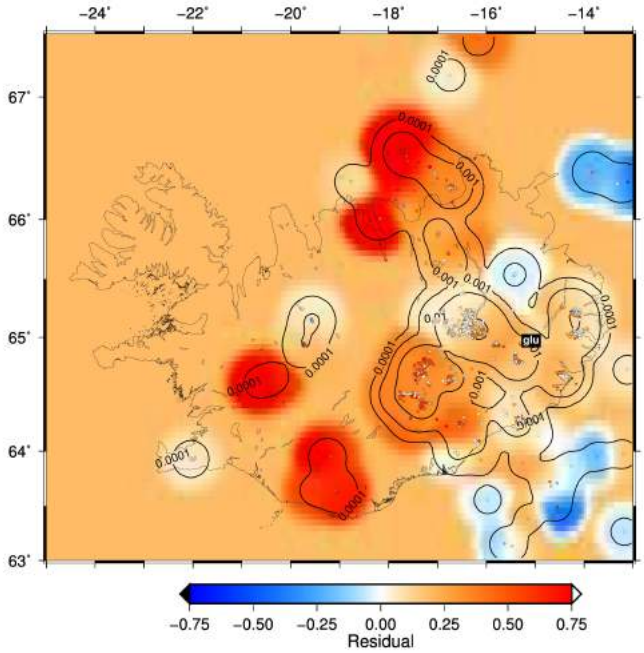

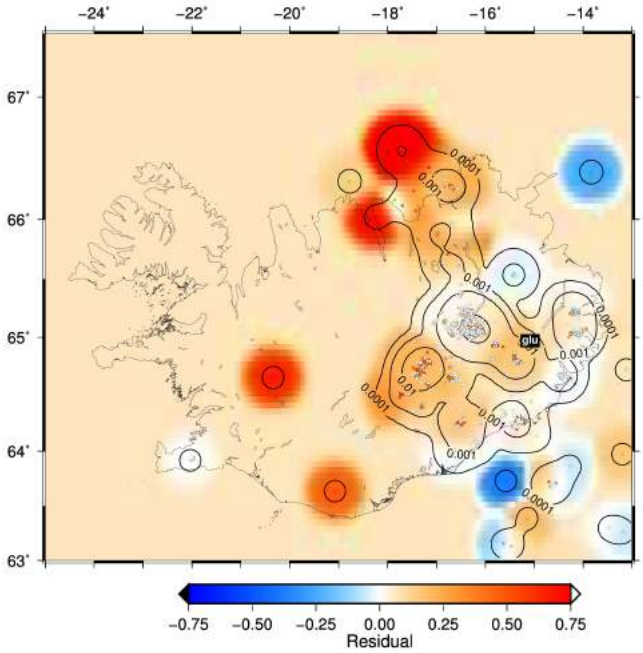

P-wave S-wave

sig

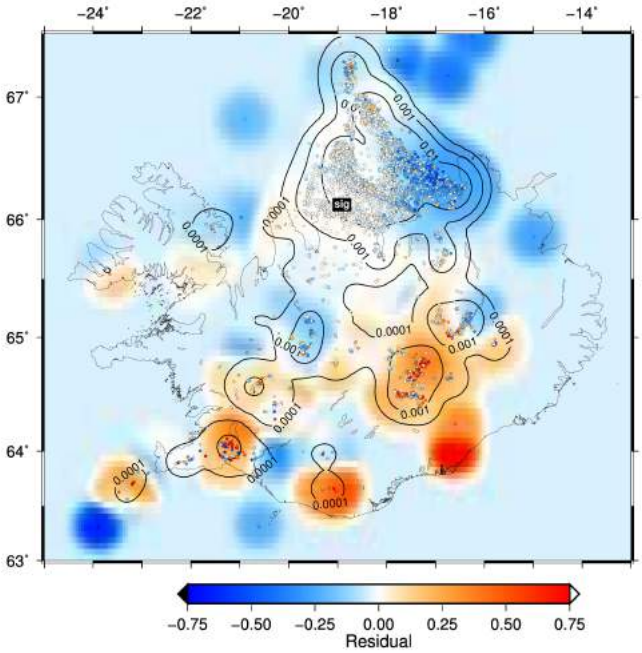

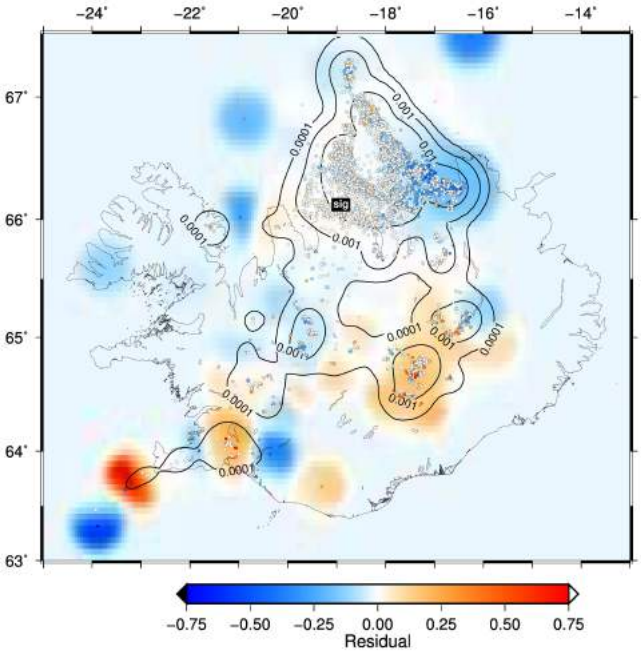

hla

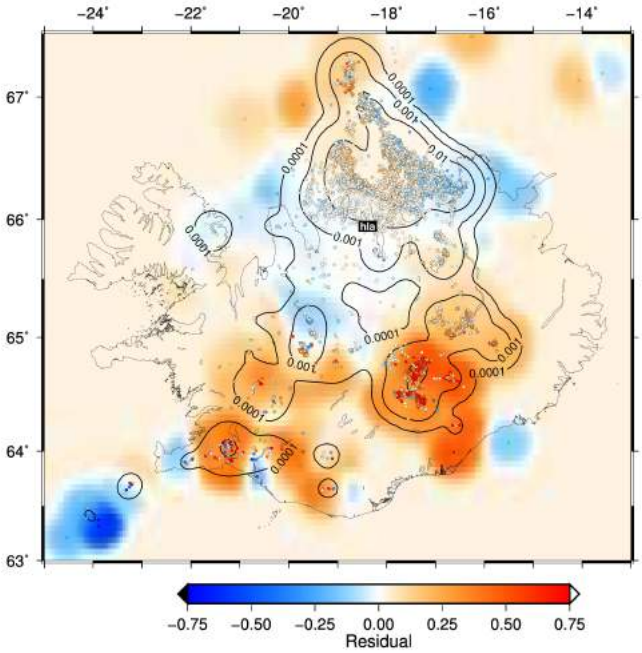

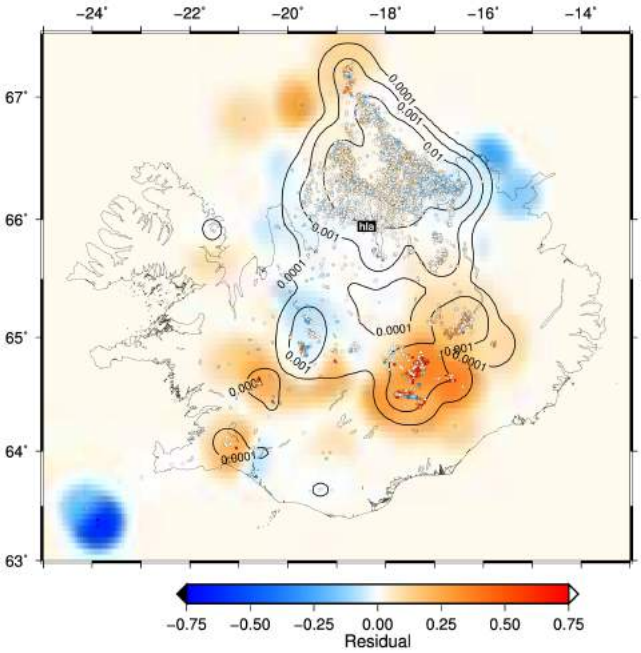

P-wave S-wave

fla

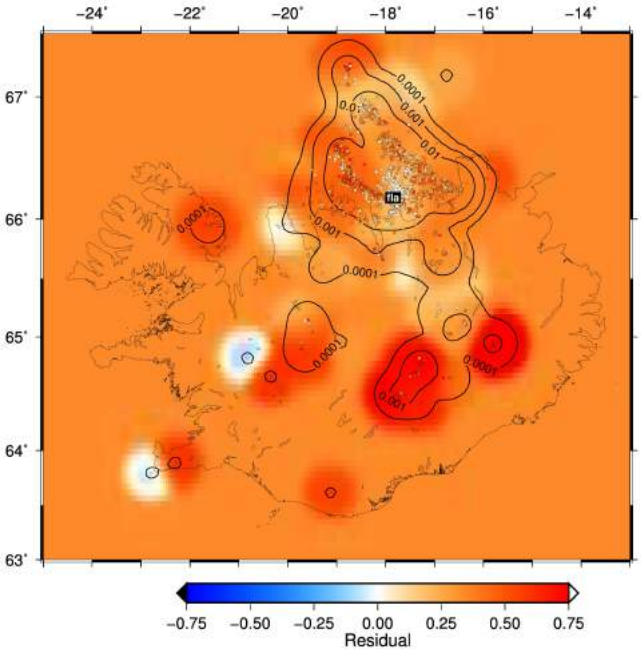

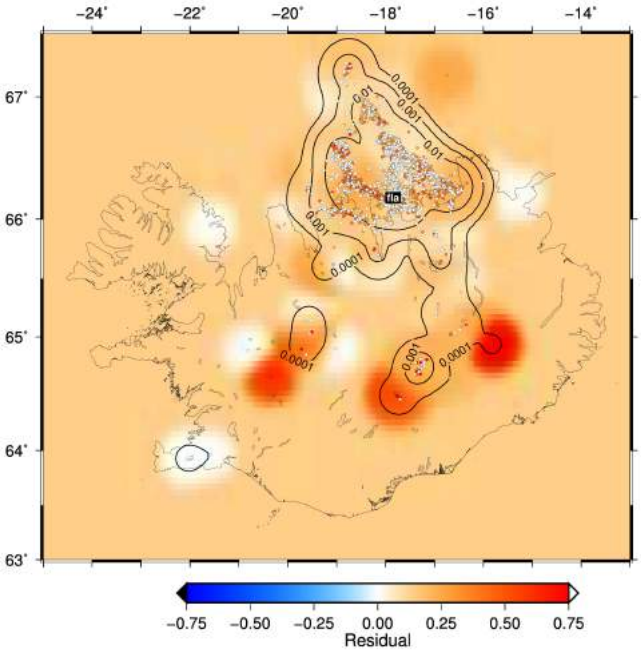

bre

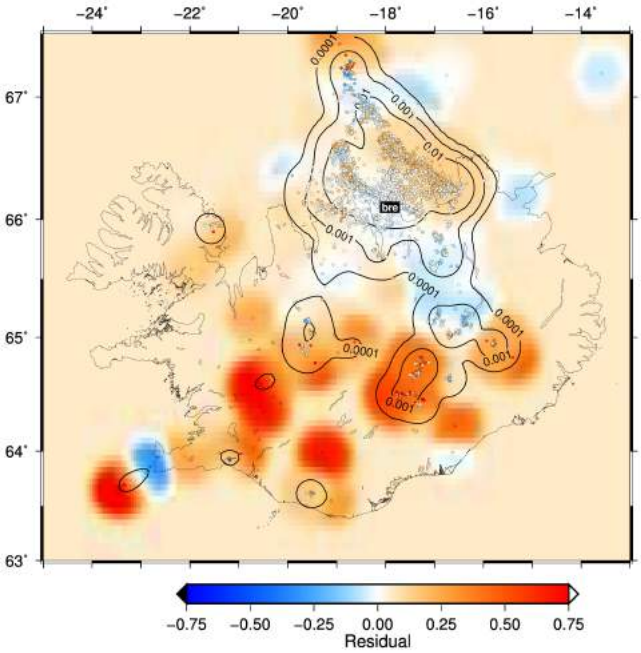

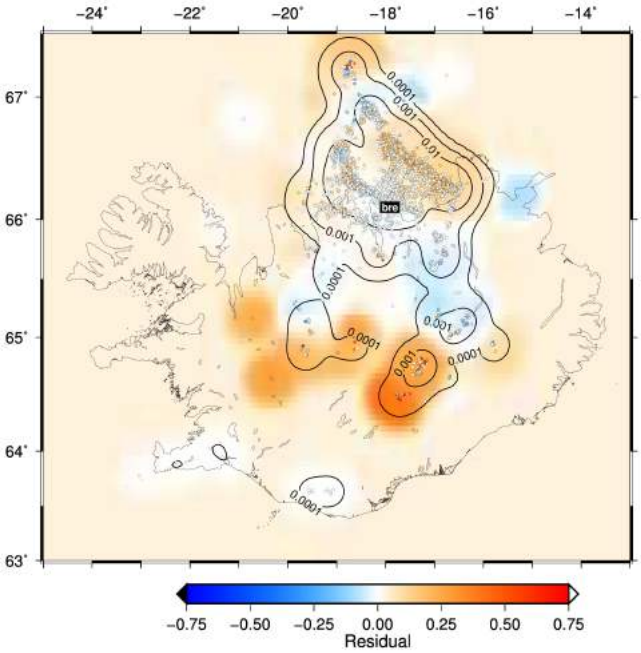

P-wave S-wave

ren

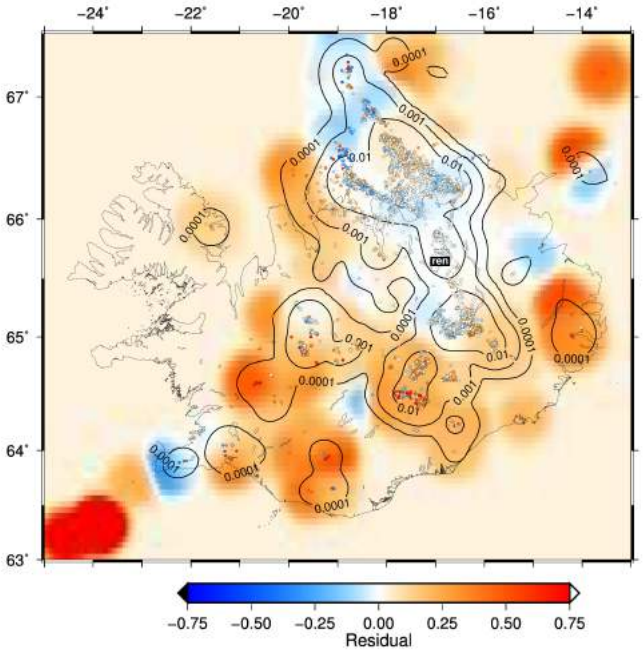

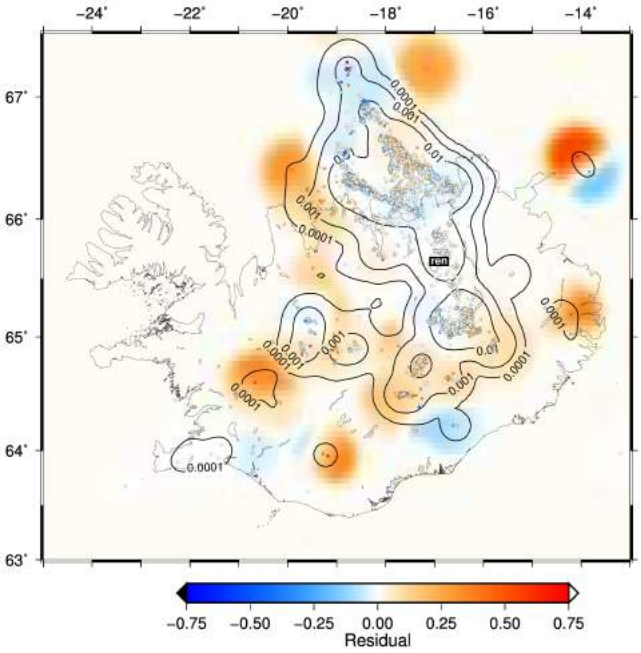

kvo

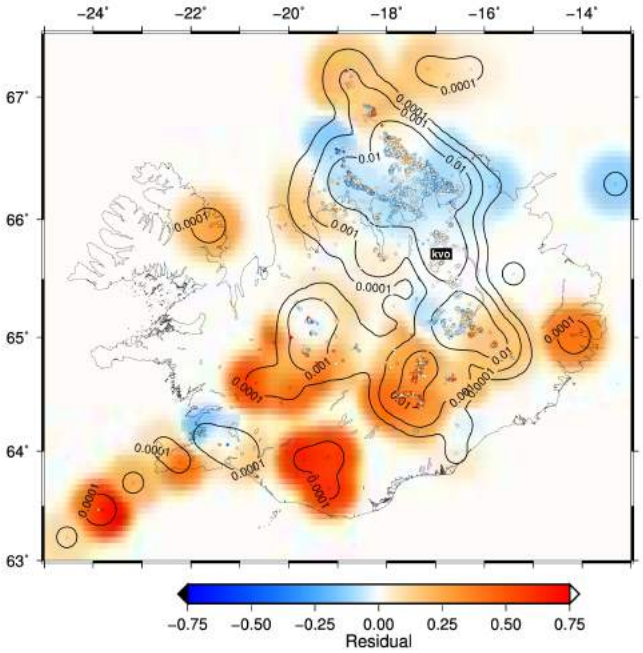

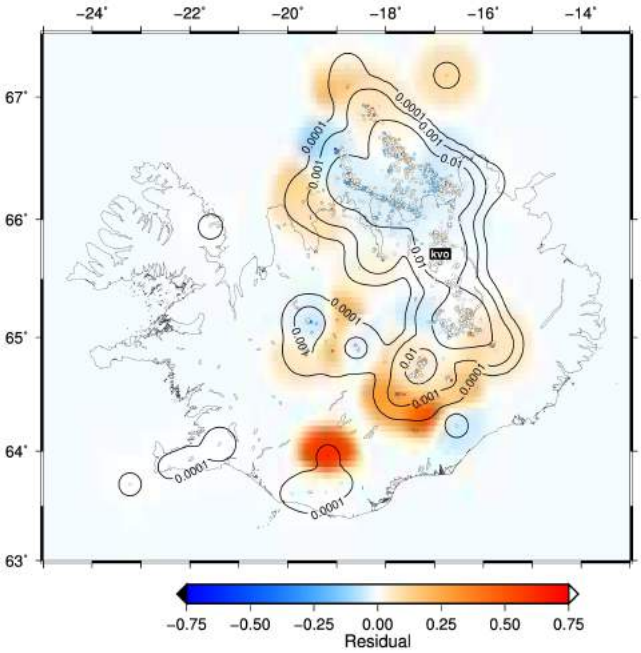

P-wave S-wave

gha

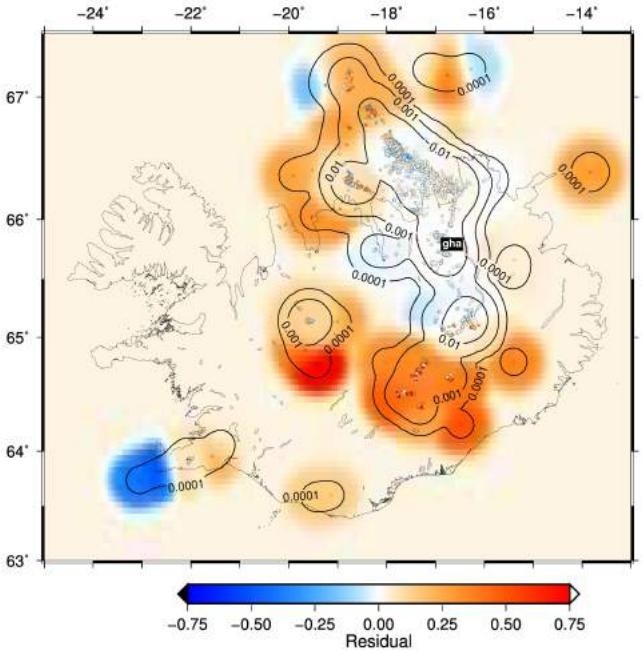

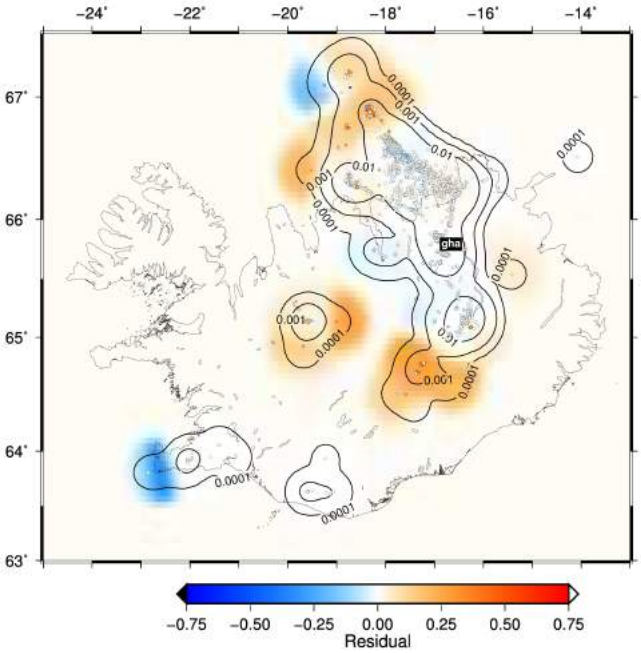

ghs

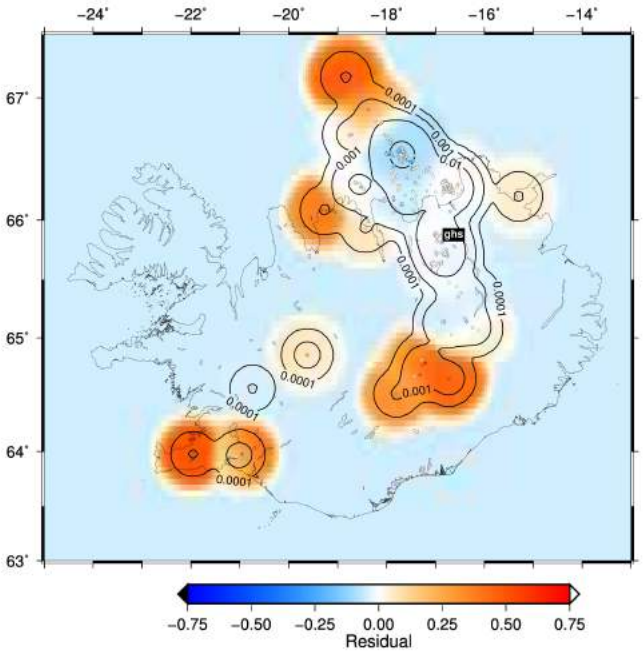

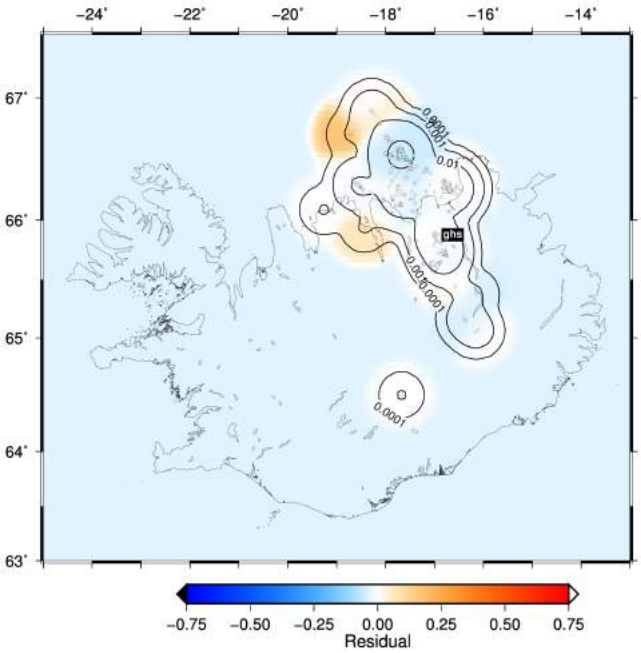

P-wave S-wave

ski

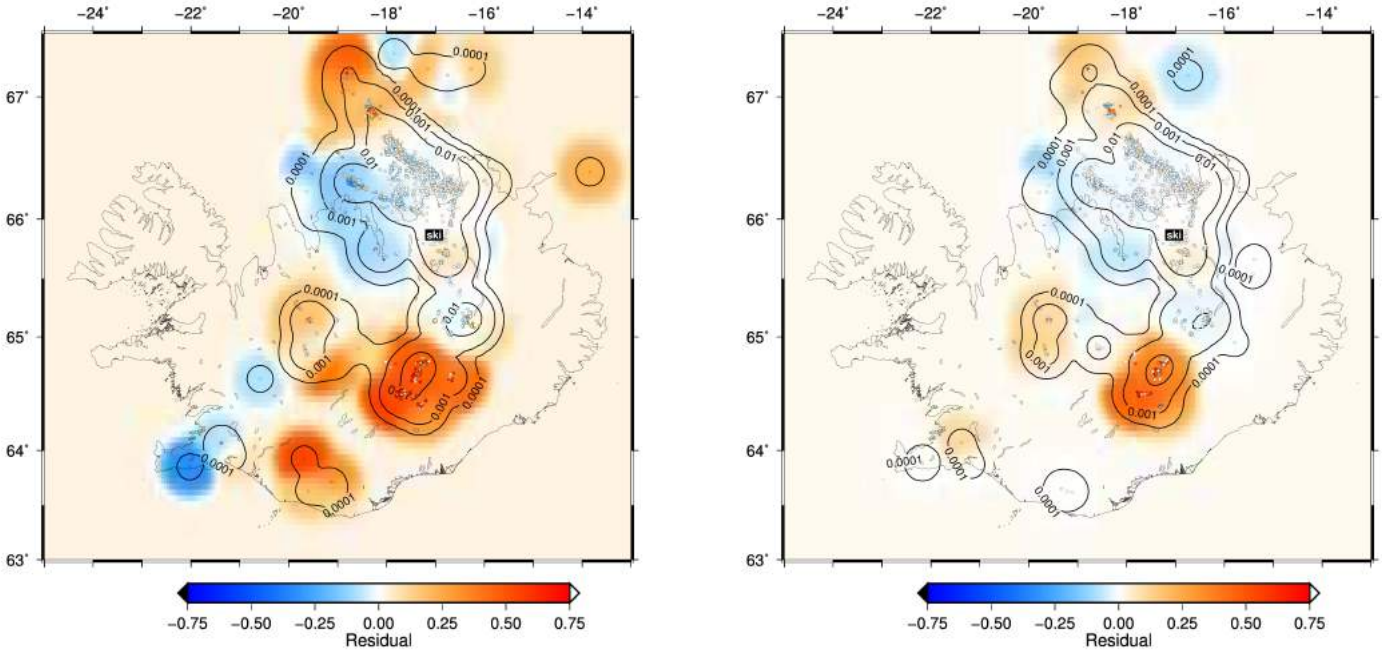

dim

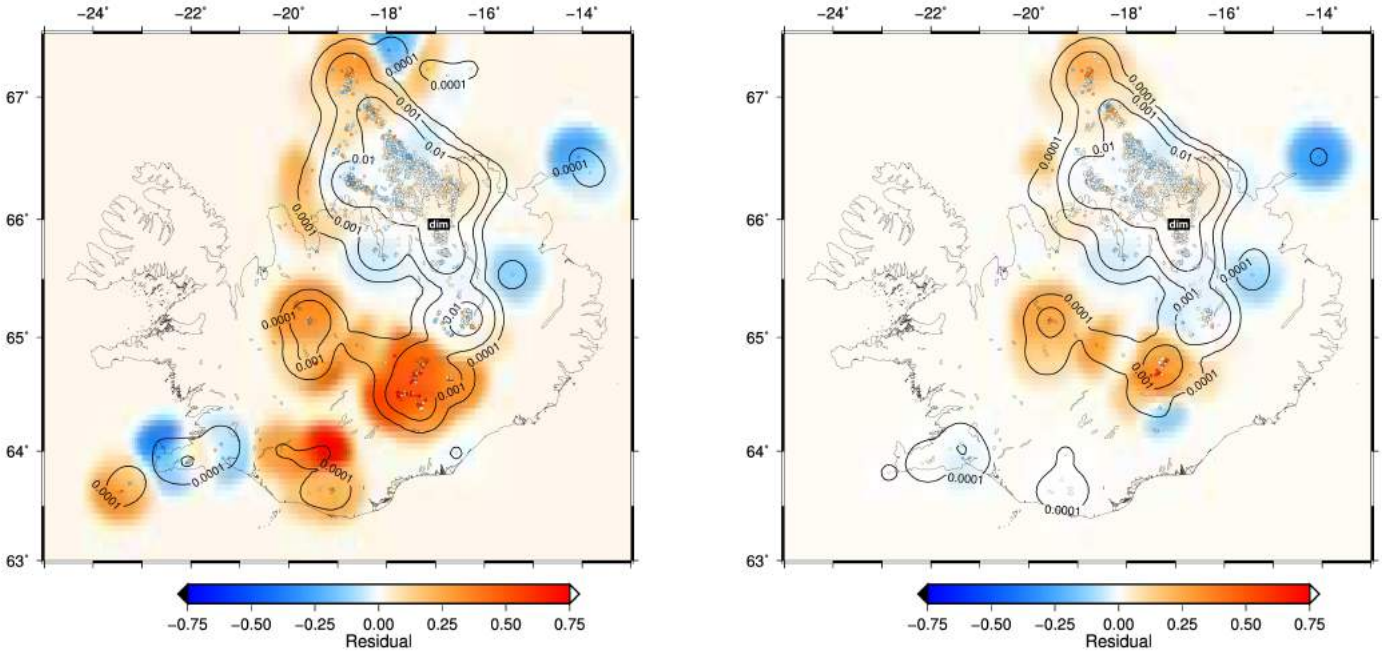

P-wave S-wave

gra

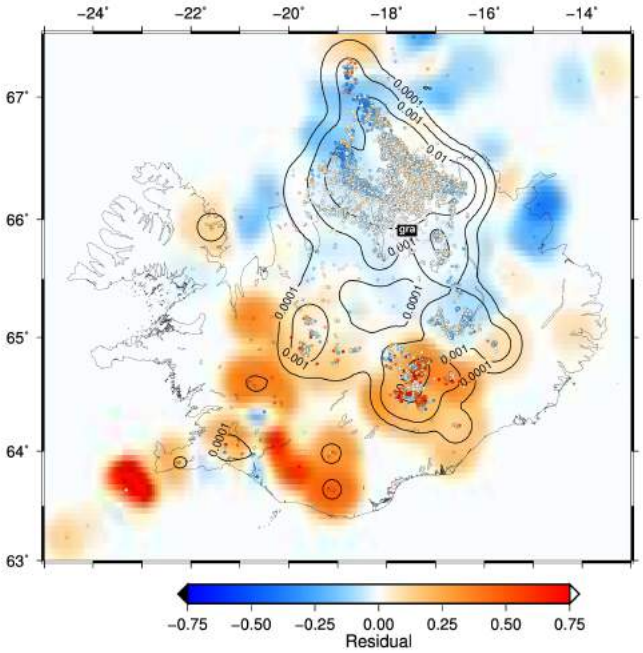

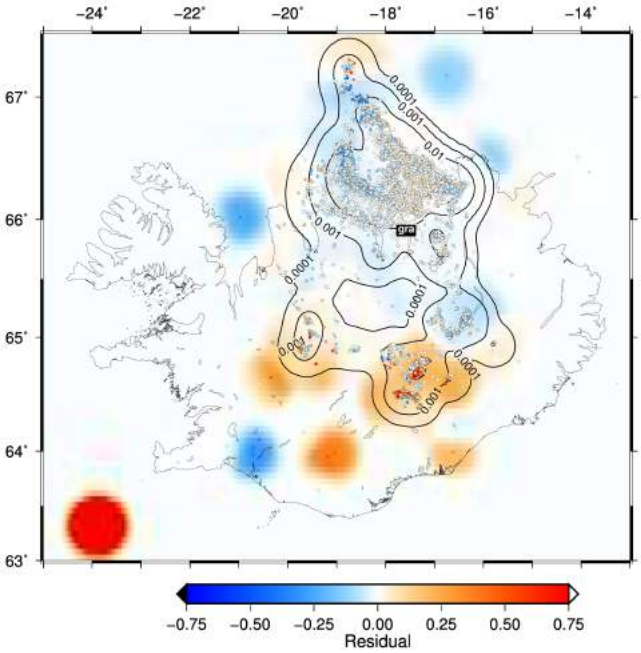

hed

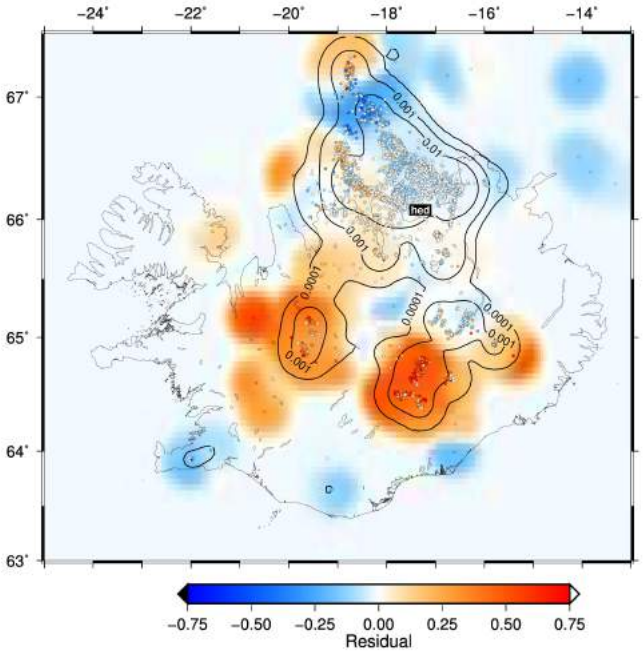

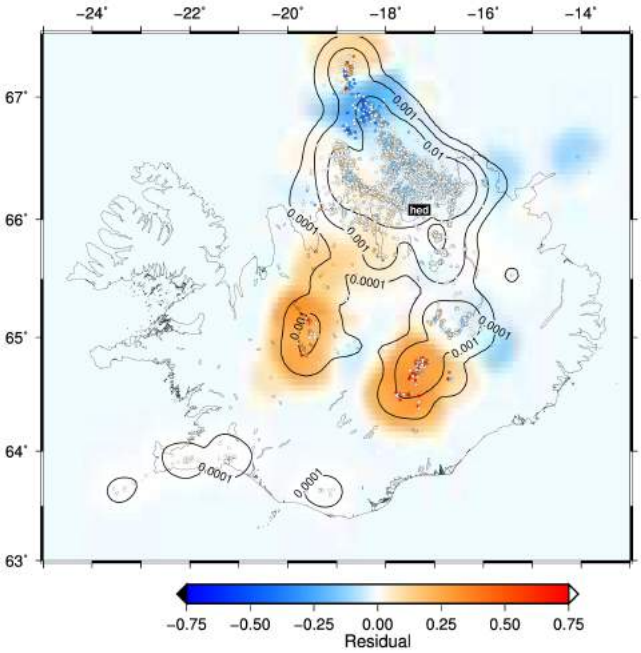

P-wave S-wave

ask

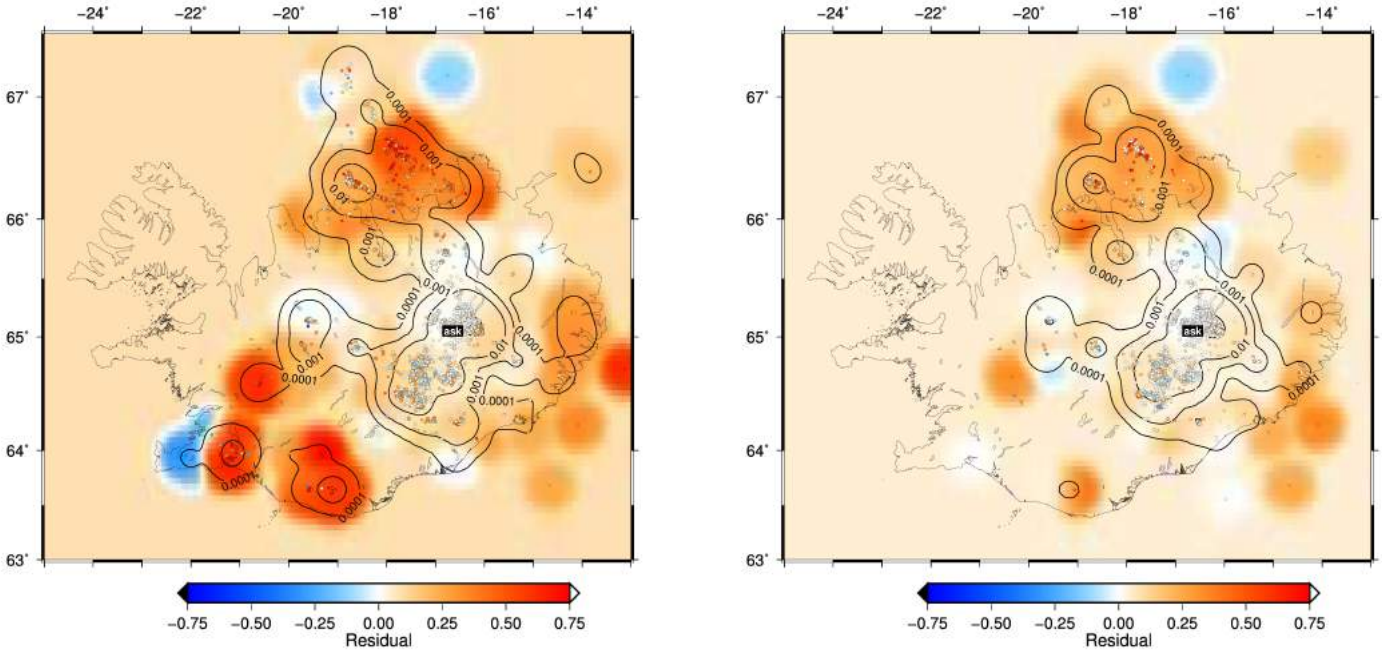

sva

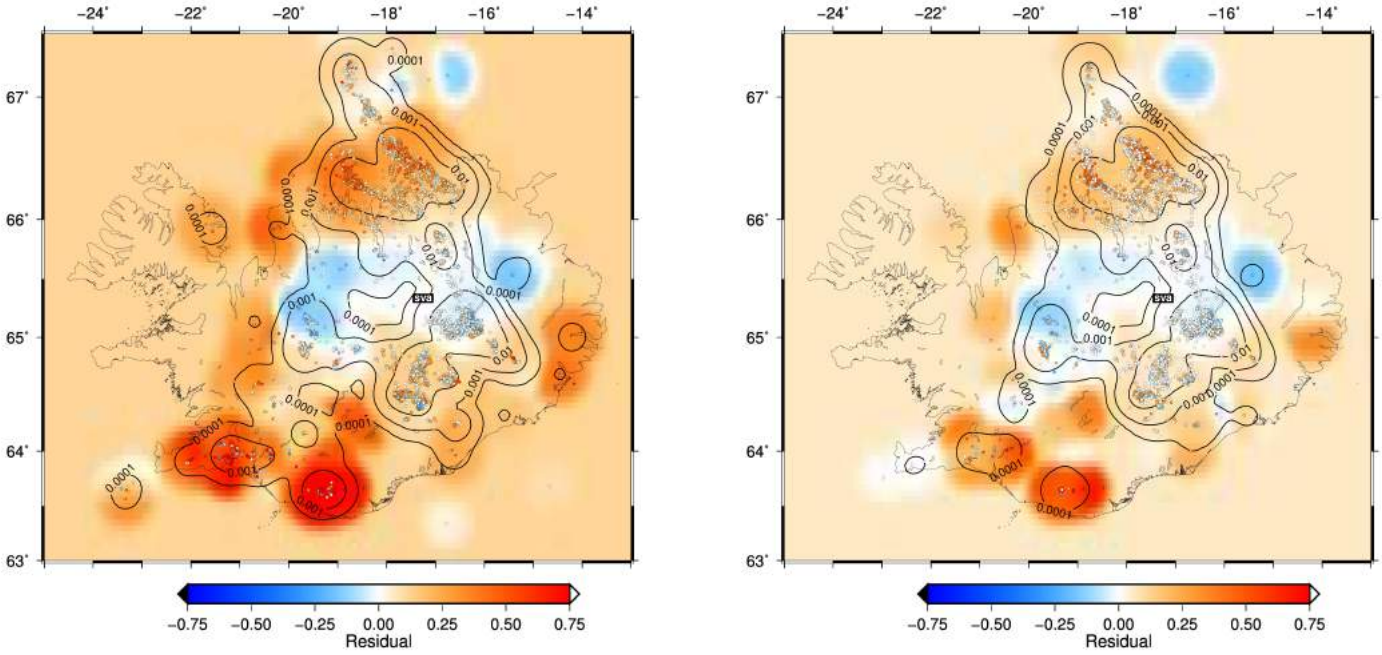

P-wave S-wave

mel

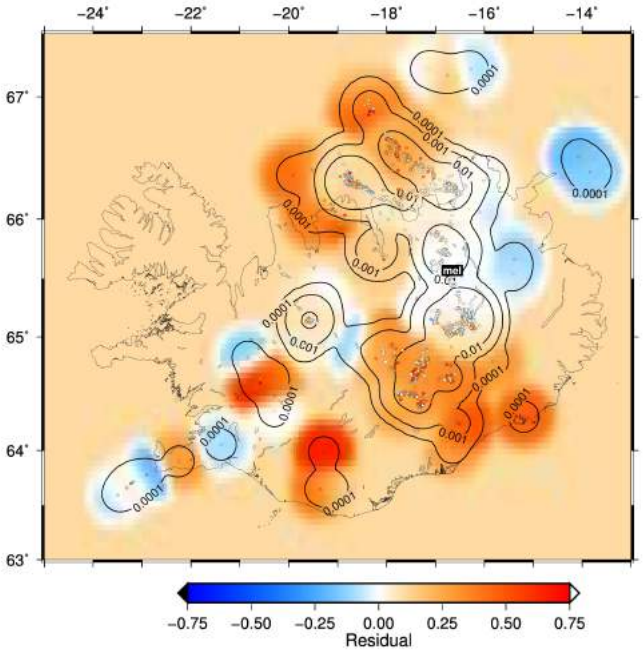

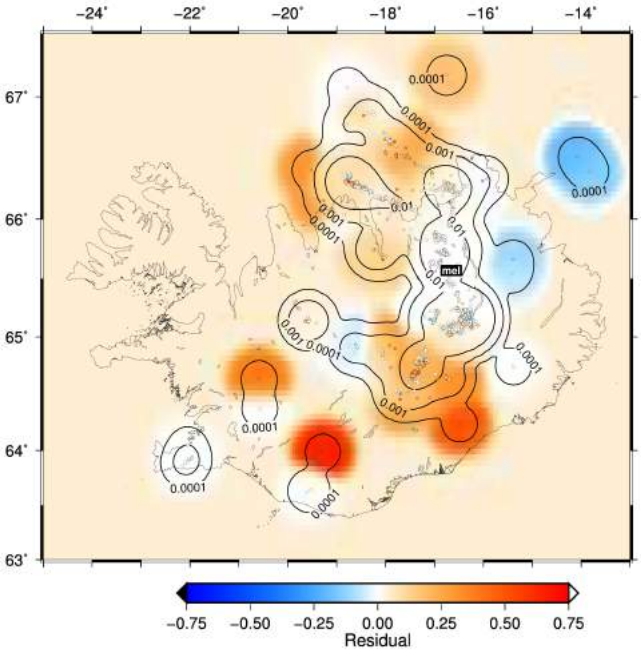

grs

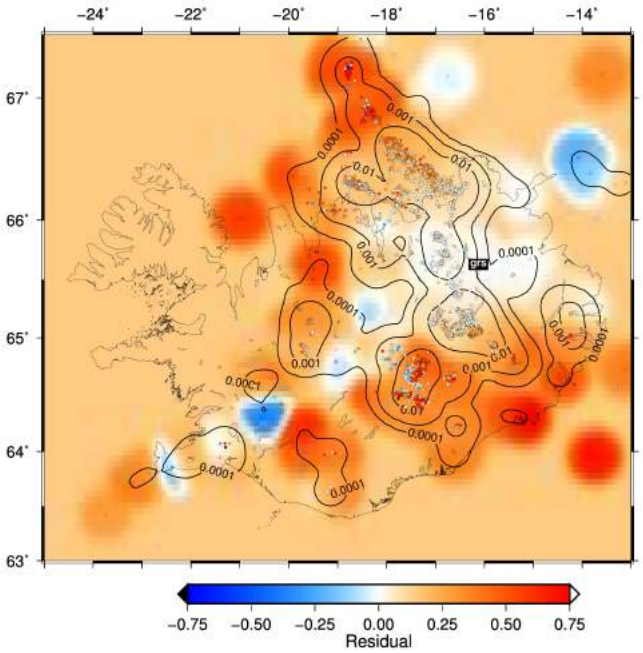

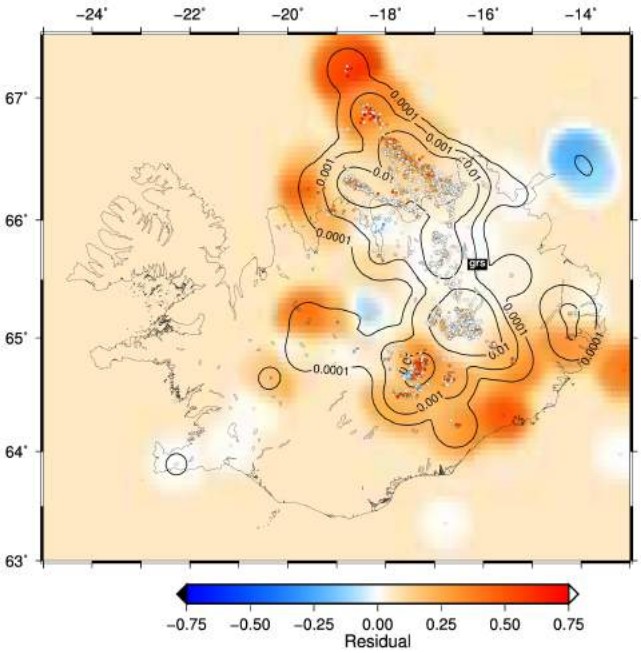

P-wave S-wave

hrn

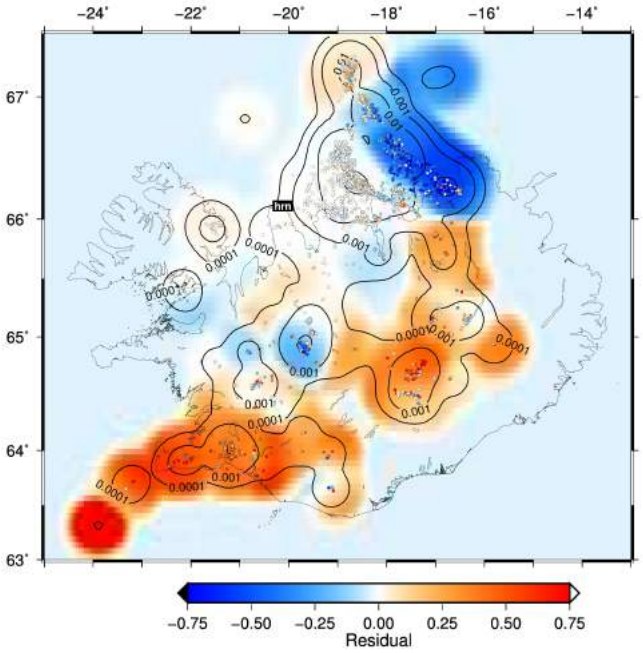

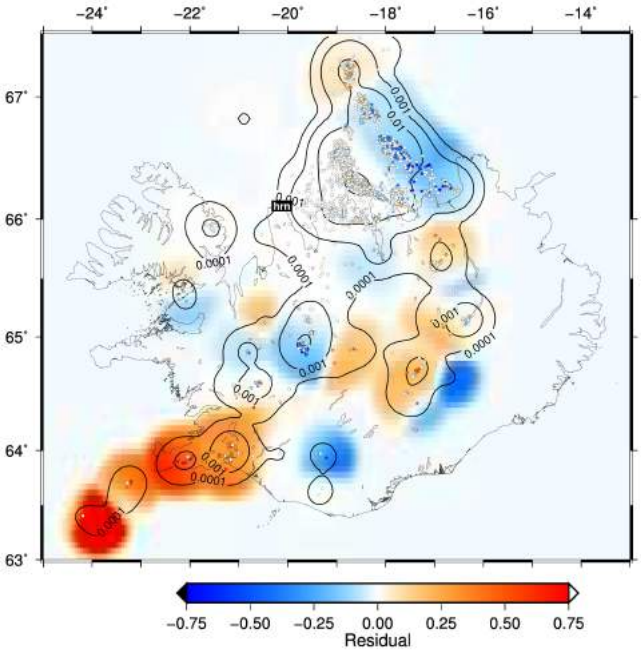

gri

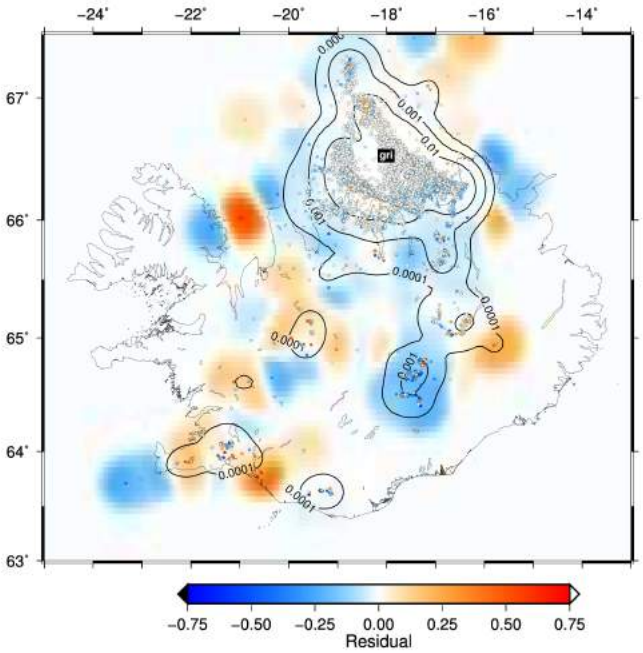

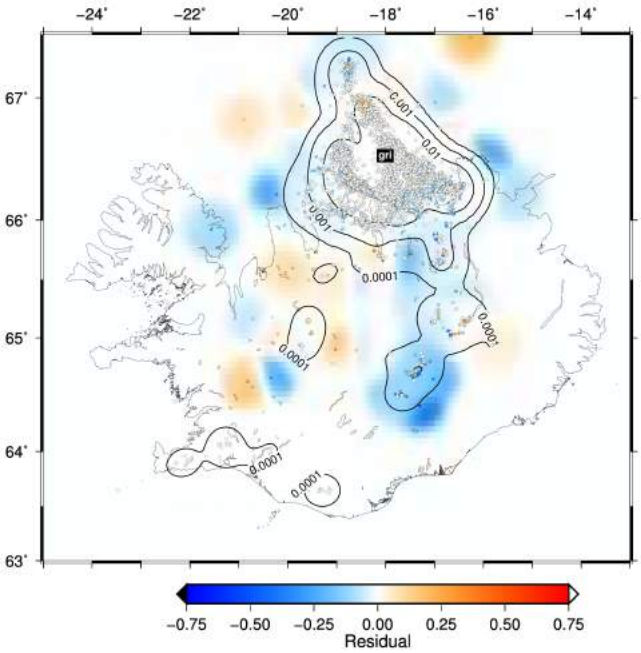

P-wave S-wave

lei

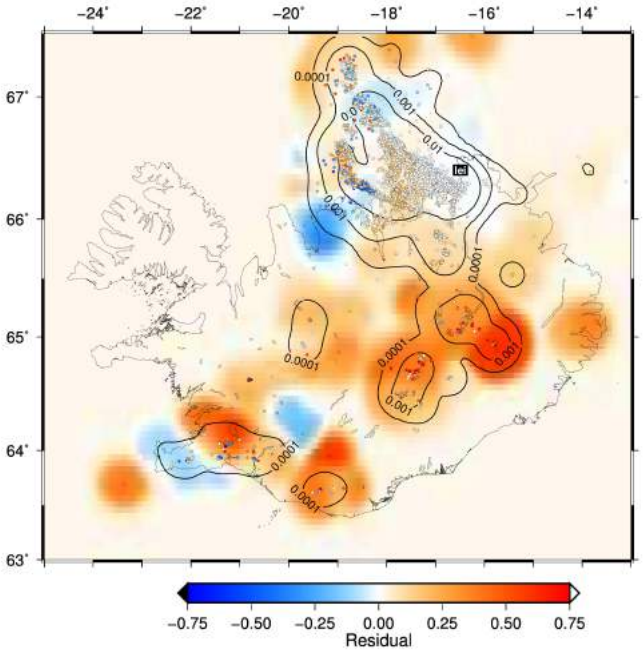

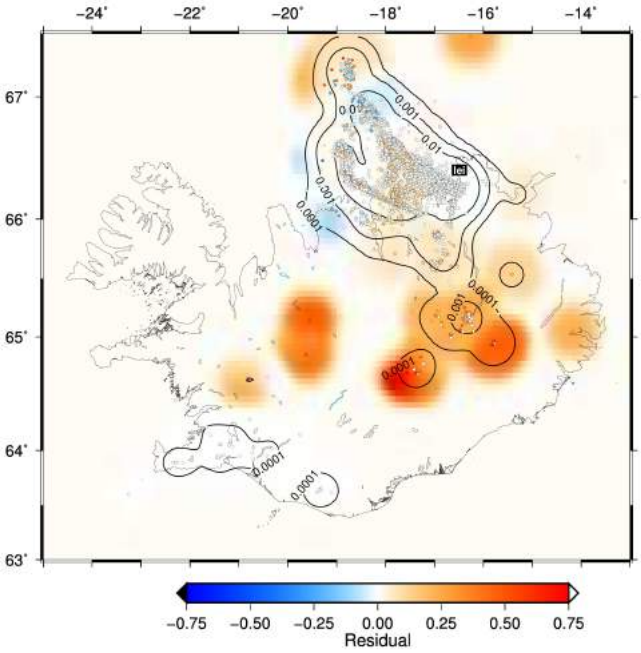

gil

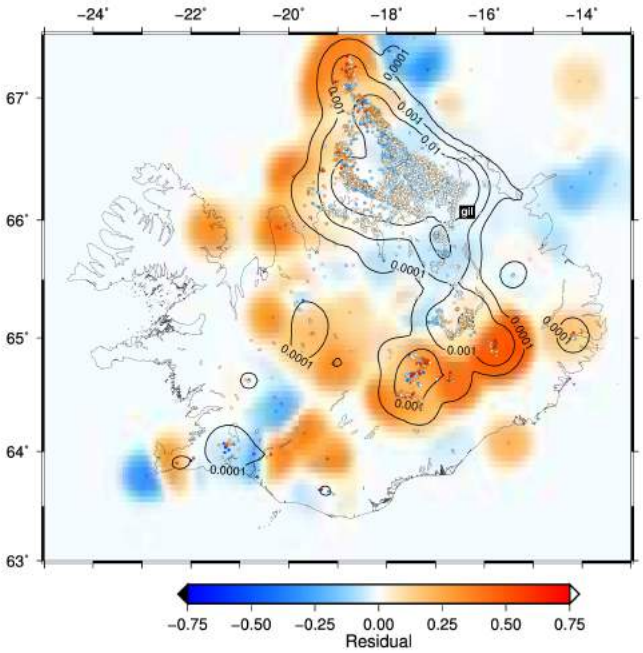

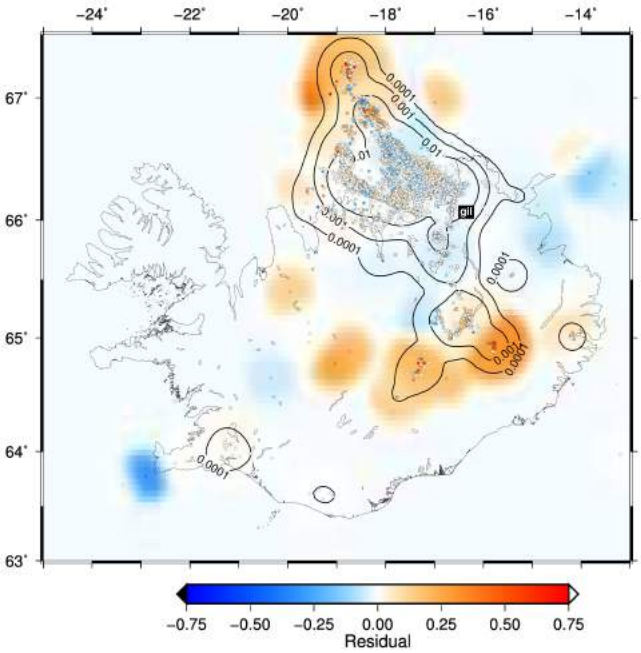

P-wave S-wave

asb

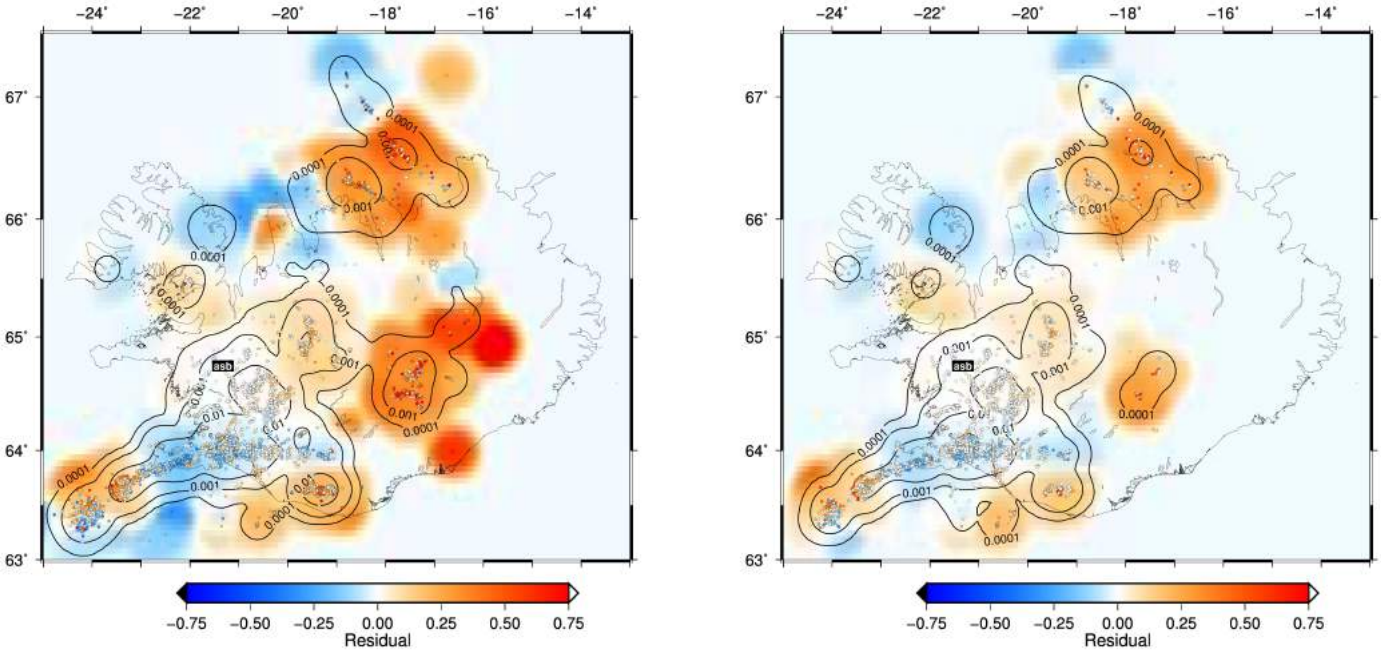

hve

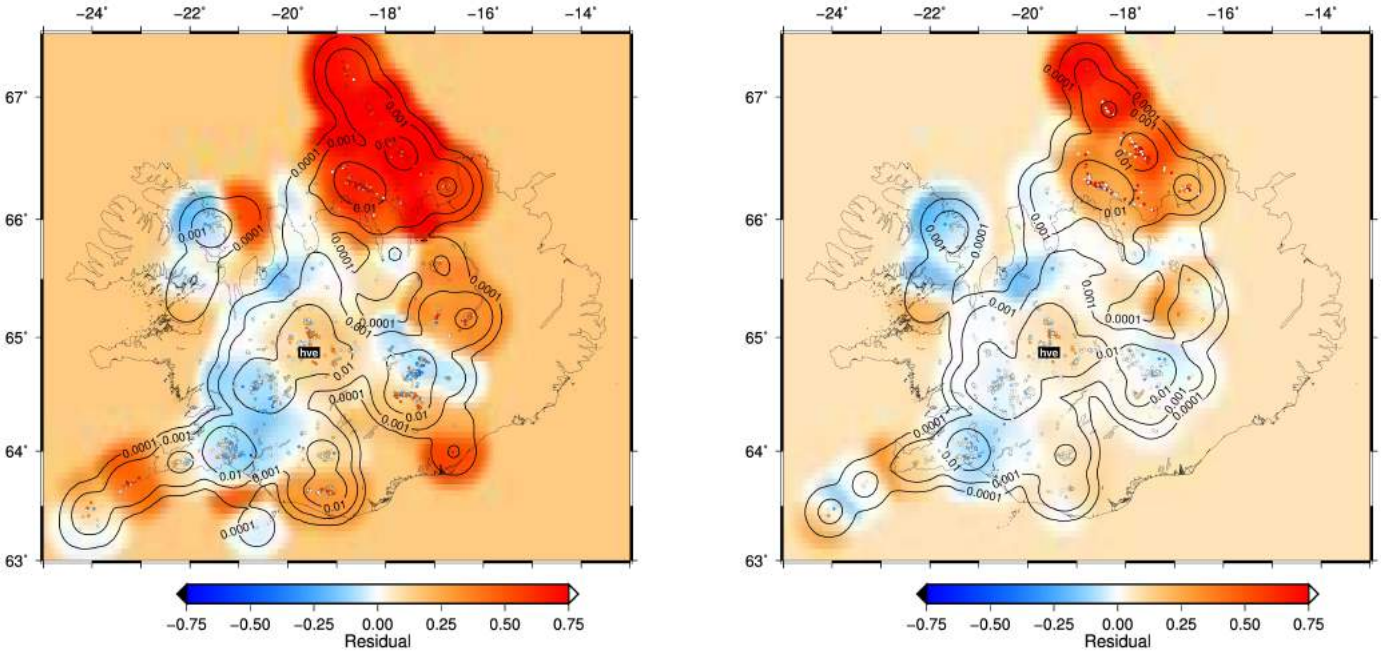

P-wave S-wave

kud

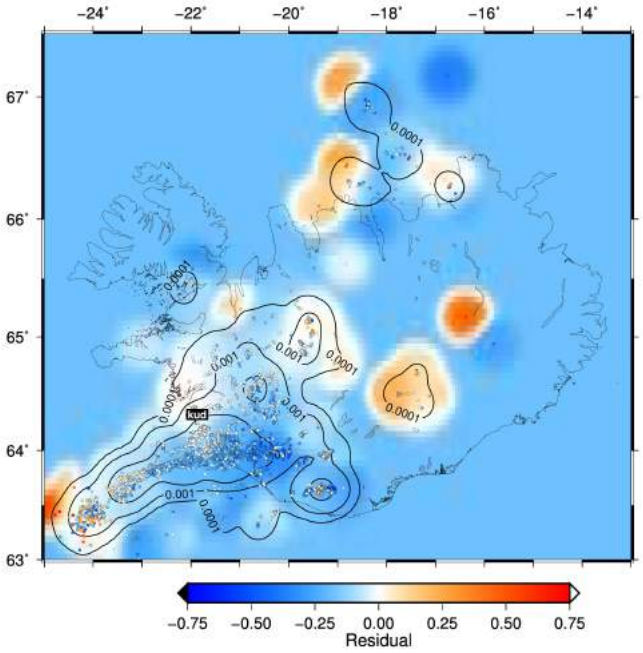

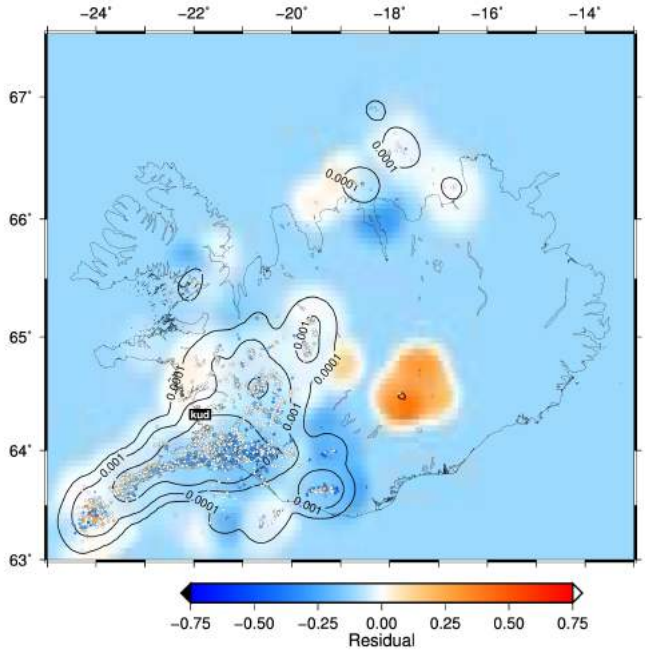

gyg

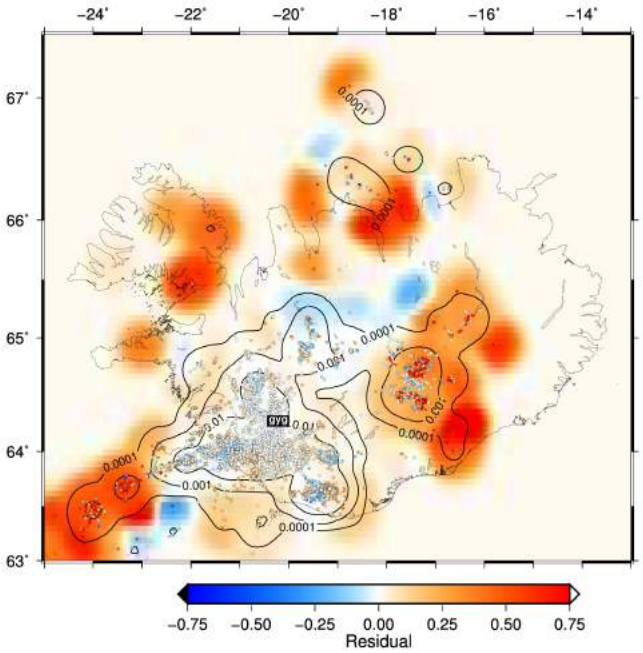

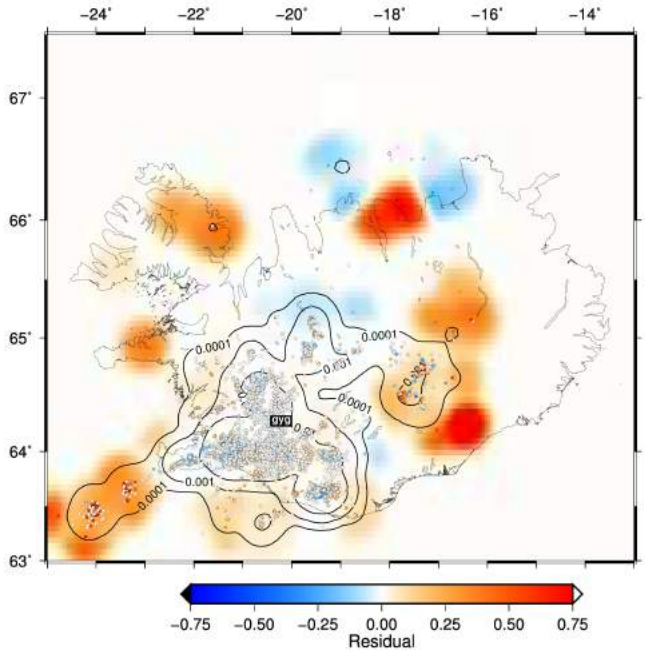

Appendix B

The deterministic component of empirical travel time: Station by station comparison of P-wave residuals.

The following maps show the travel-time residuals relative to predictions of the SIL model (circles) and the deterministic component (continuos colour) of empirical travel times for all 65 stations in the SIL network that we have analysed. The maps show data and results from P-wave residuals only. The two-dimensional interpolation that defines the deterministic component of the empirical travel time is calculated using a moving average over a Gaussian function that is 10 km in width. The contours indicate the combined weights of the data that contribute to the estimate at each point and are a useful guide about robustness. The running average is based on many nearby data where this combined weight is high.

The figures are organized with four maps per page. Those show both P-wave residuals and their interpolations for a number of nearby stations as indicated. This allows for a geographical comparison of results.

It is evident from this comparison that the travel-time residuals are quite coherent from one station to the next when they are closely spaced. Note that the residual mean has not been removed. This is indicated by the background colour and will reflect a combined effect of station elevation and possibly anomalous shallow structure immediately beneath each station. Such an effect is particularly clear for station fla (page B15), which has a significantly positive average. Nearby station bre has a very different average dispite the fact that it is only a few km away. The residual patterns of the two stations are very similar. Station ves (page B7) also has a significantly positive average, as do stations in the highlands (page B11). Station kud in western Iceland (page B20) is at the other end of the spectrum with a significantly negative (fast) average.

nyl

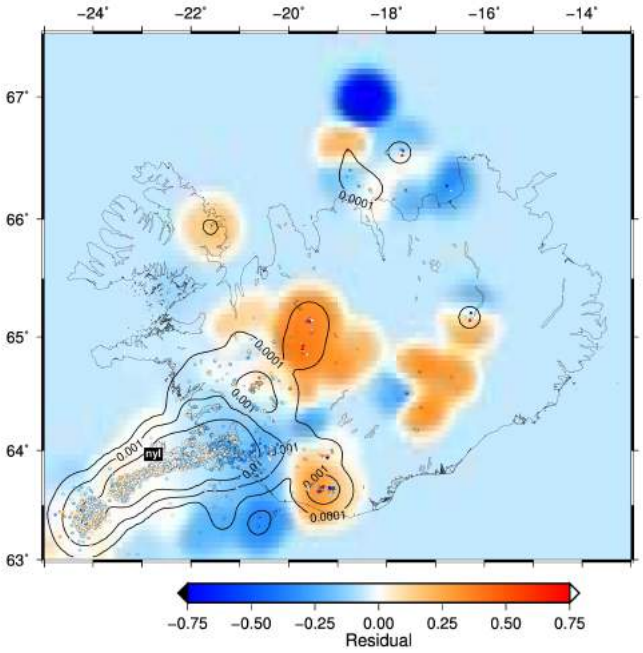

rne

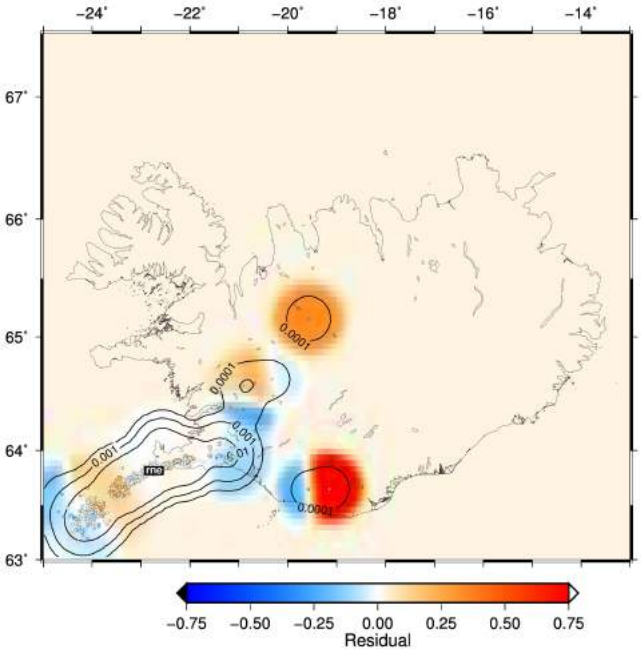

vog

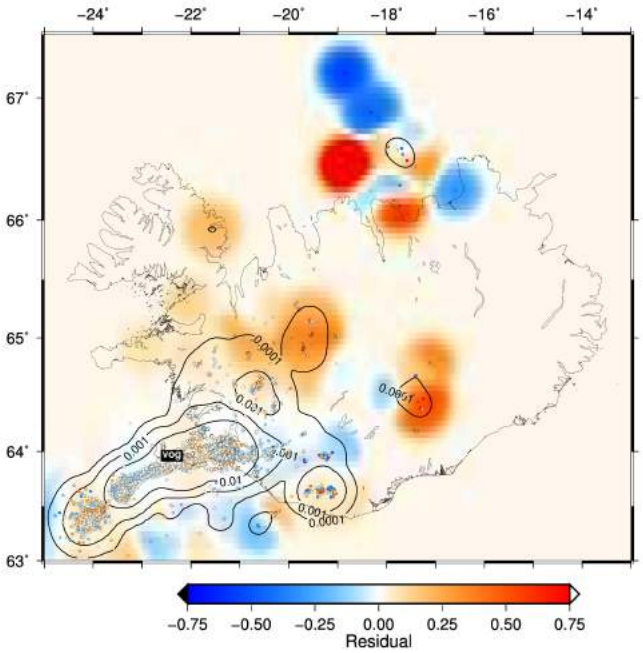

grv

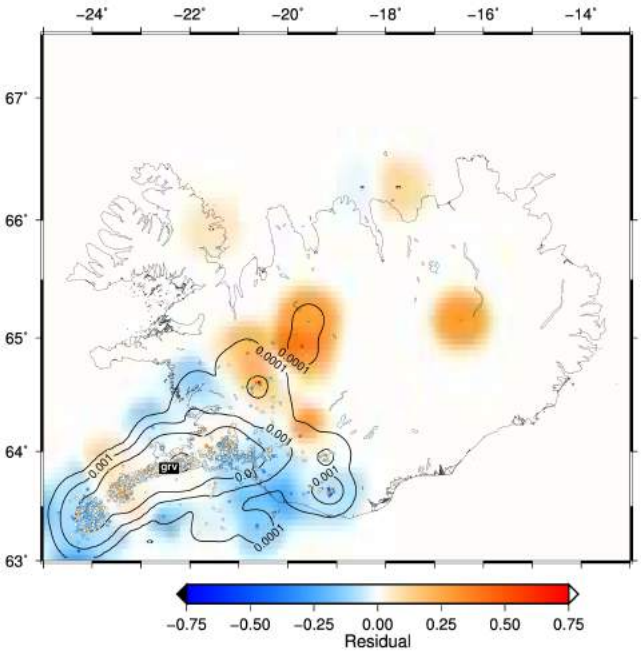

kri

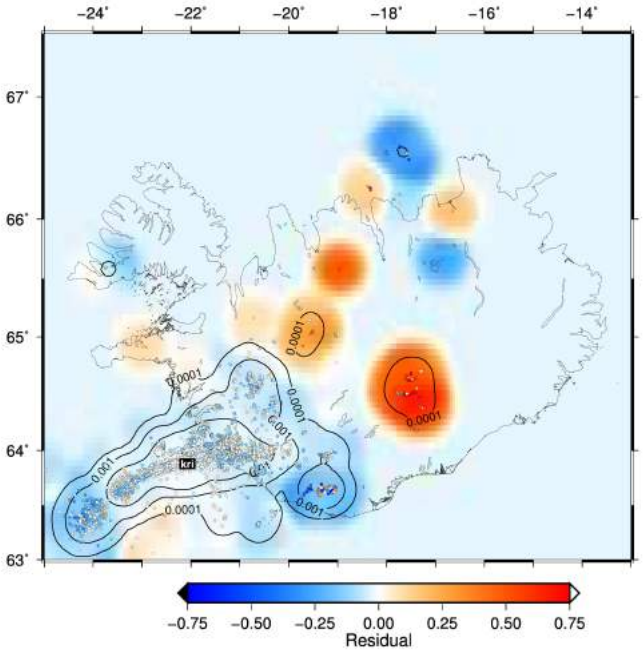

vos

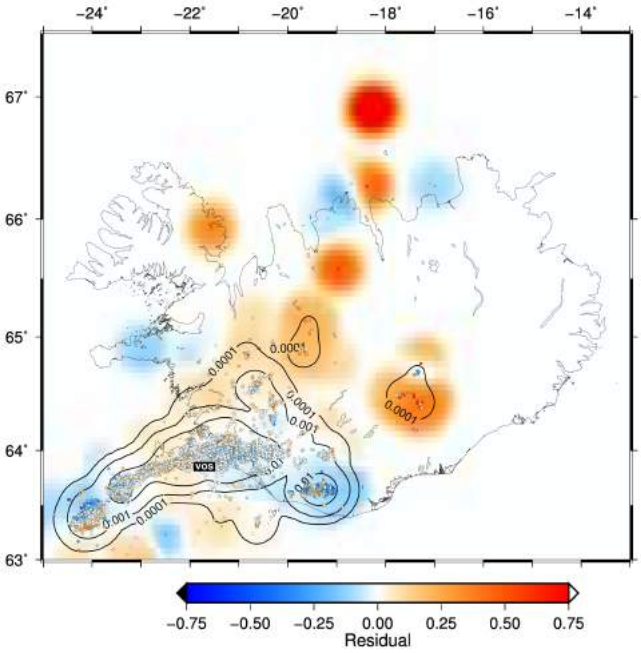

kas

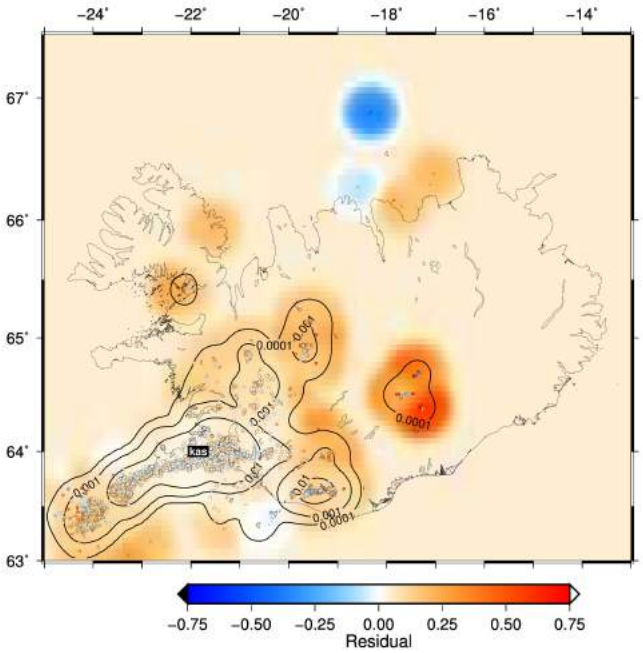

haf

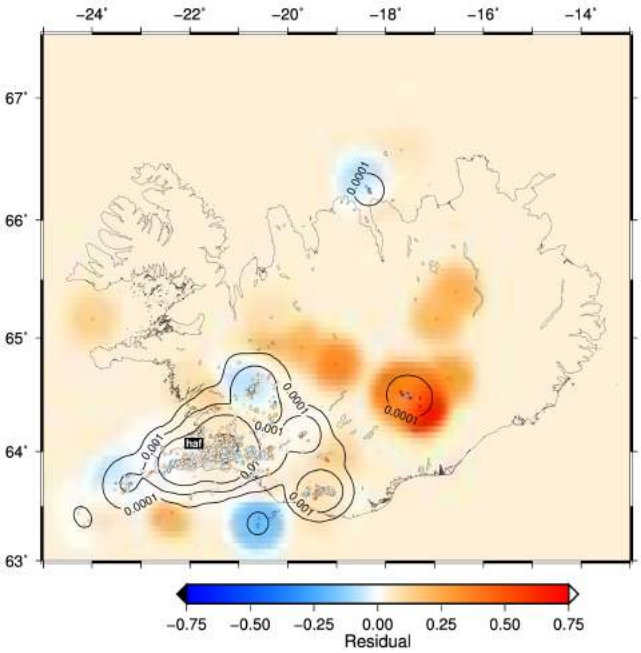

bja

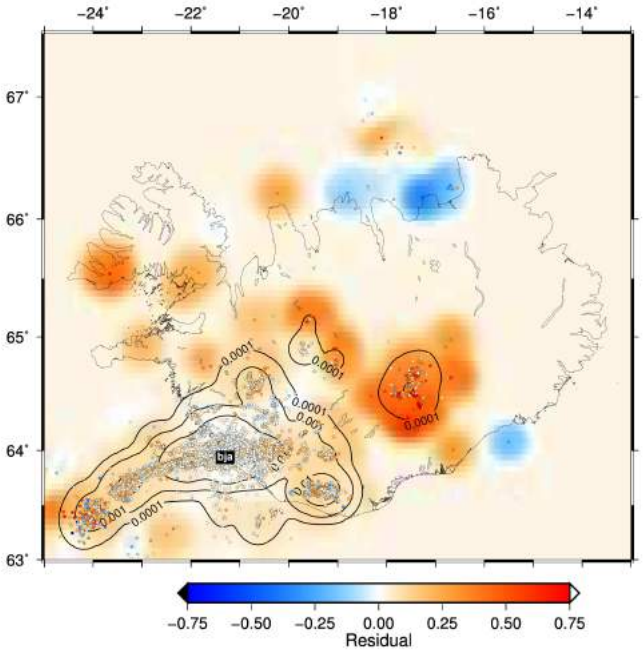

san

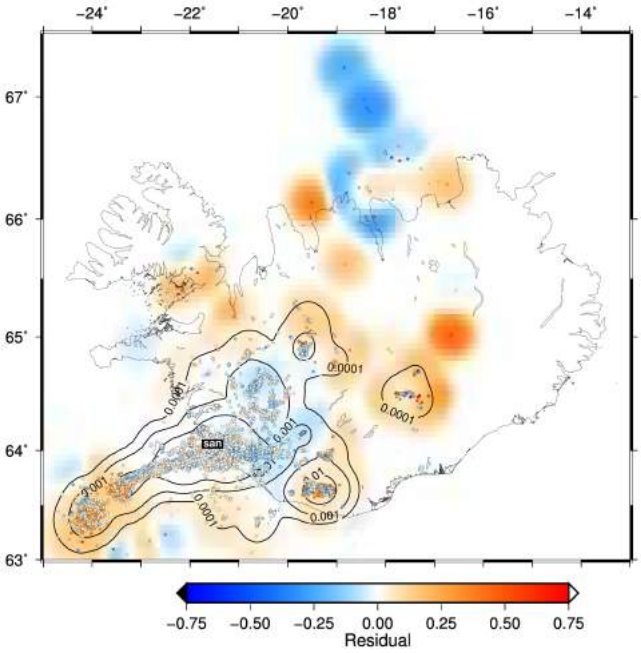

kro

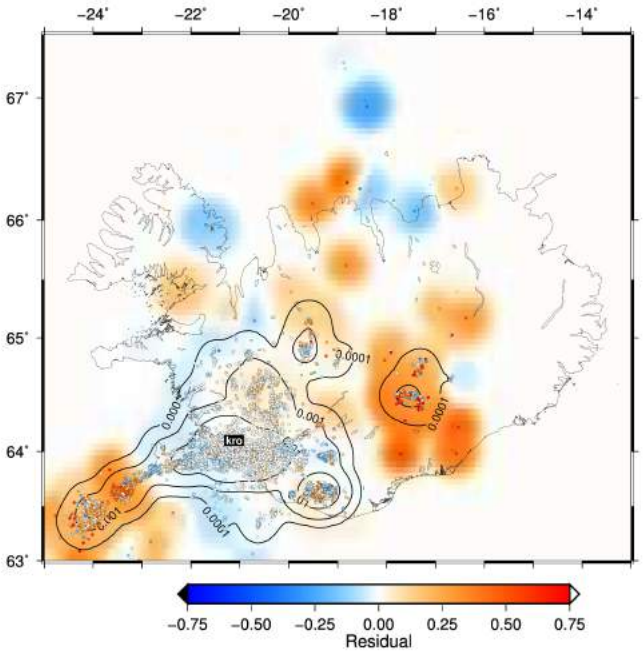

hei

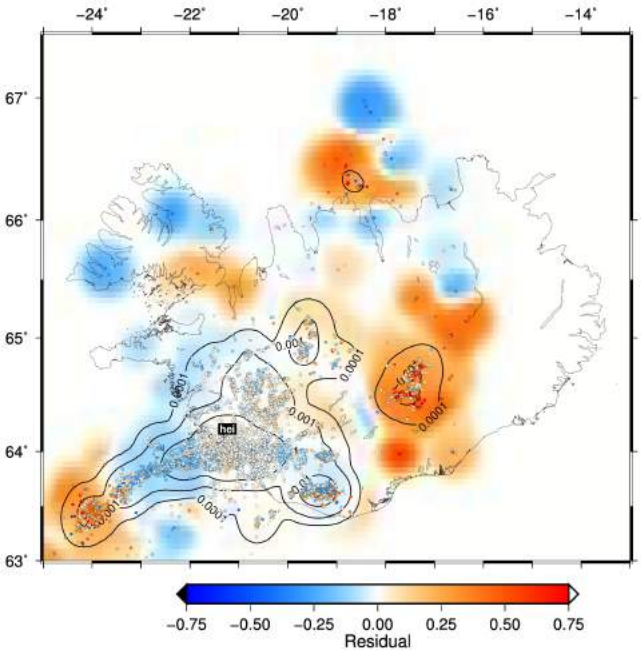

sol

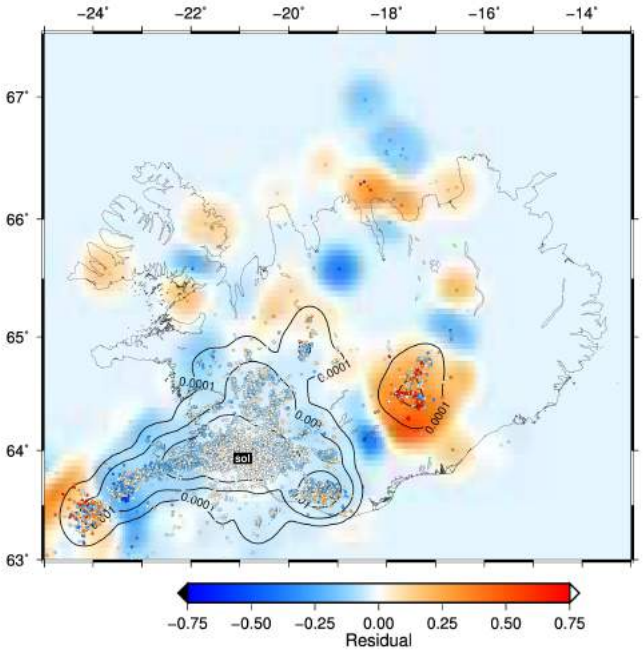

asm

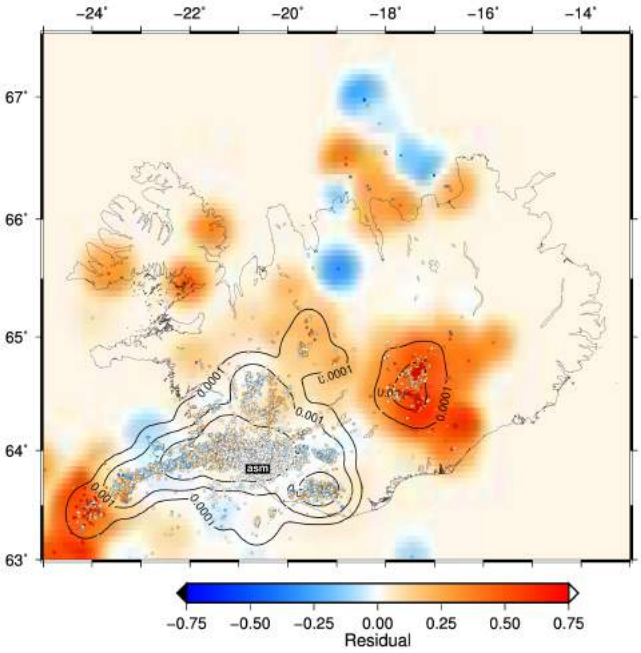

sau

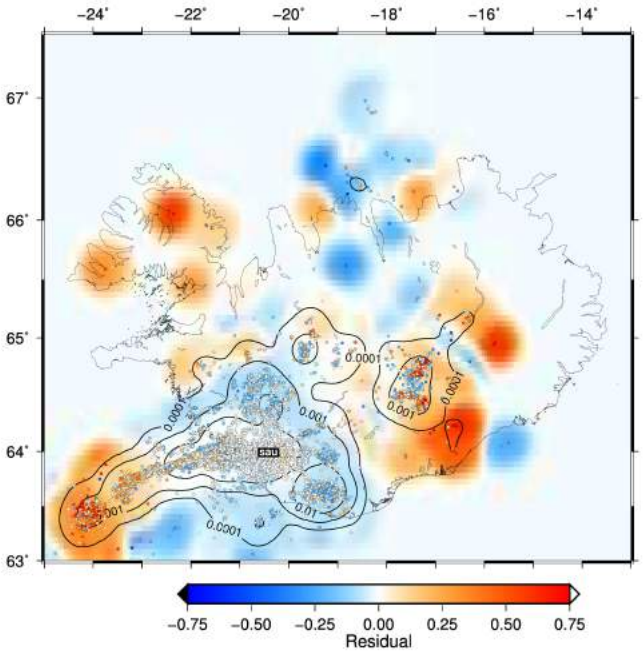

hau

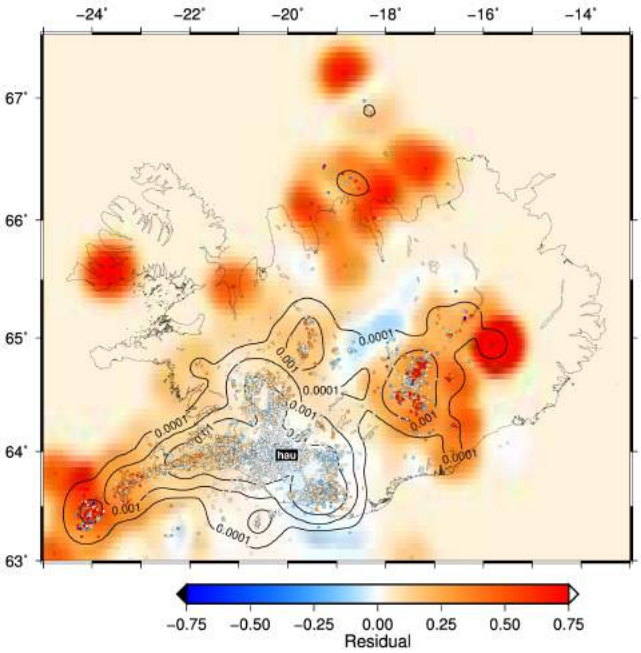

ves

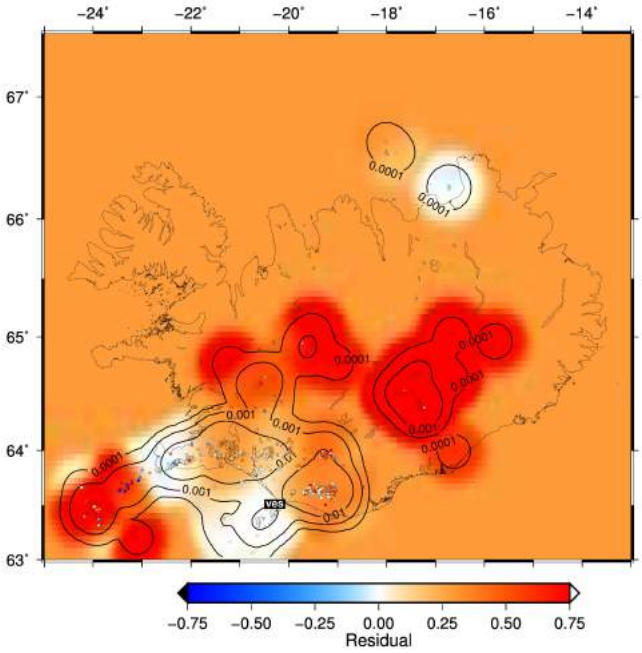

mid

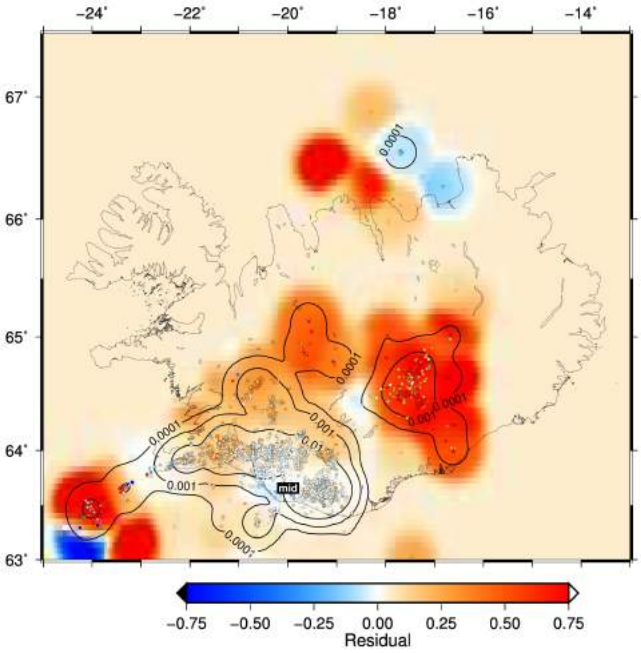

smj

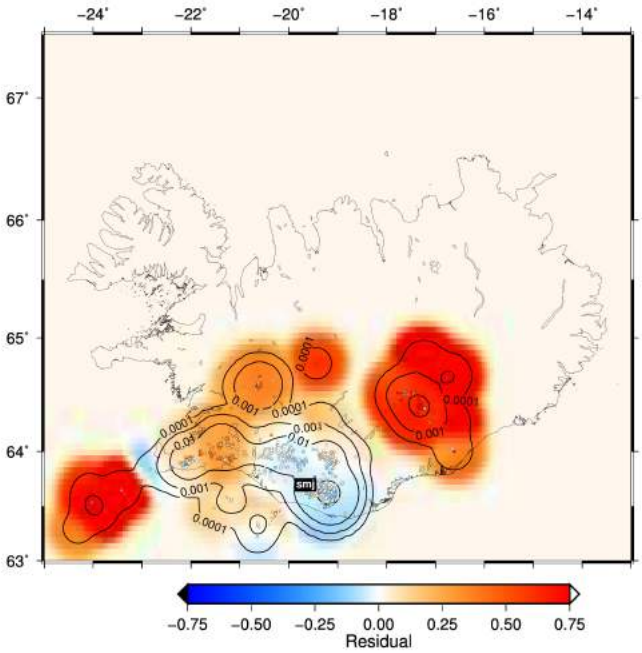

god

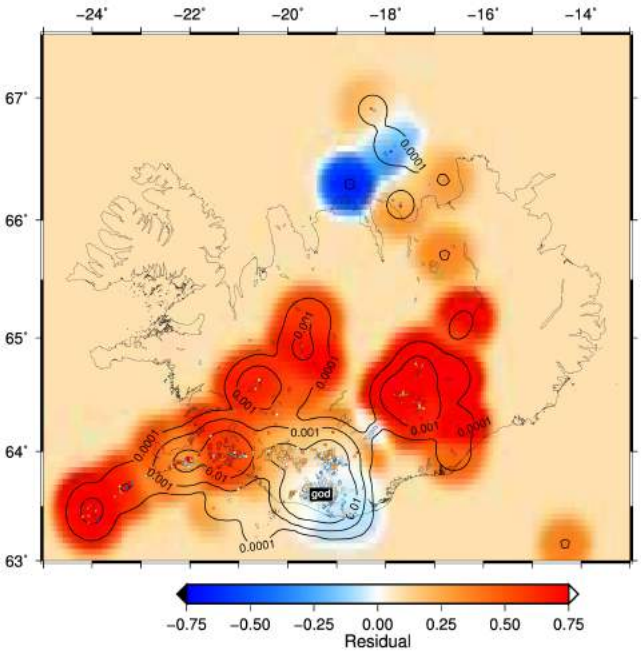

esk

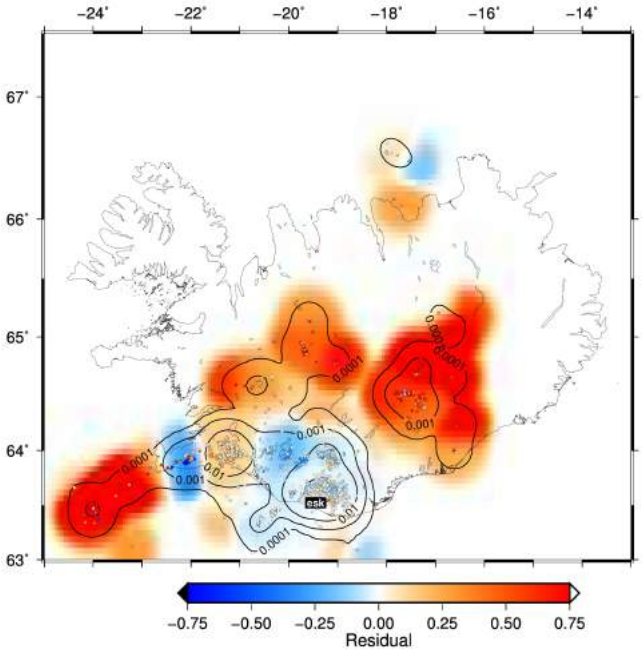

alf

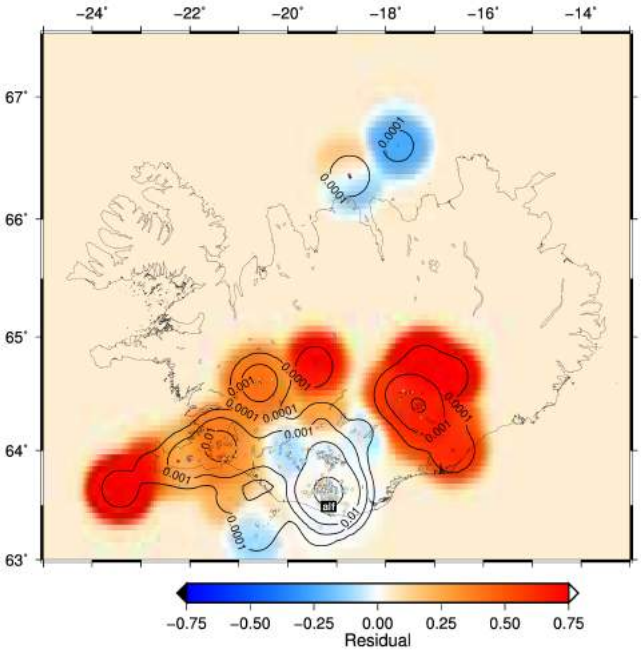

skh

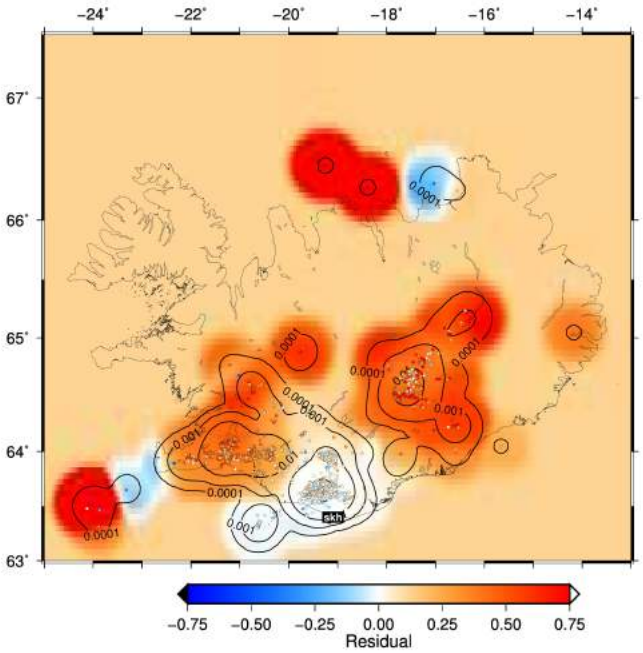

hvo

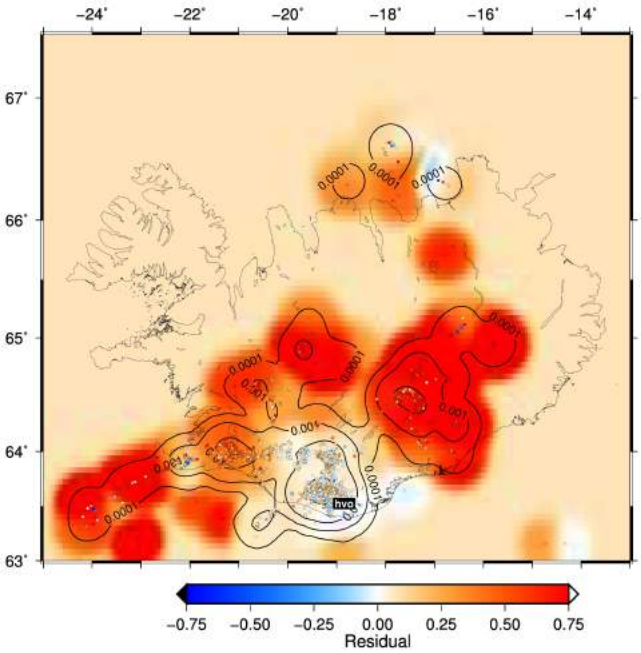

rju

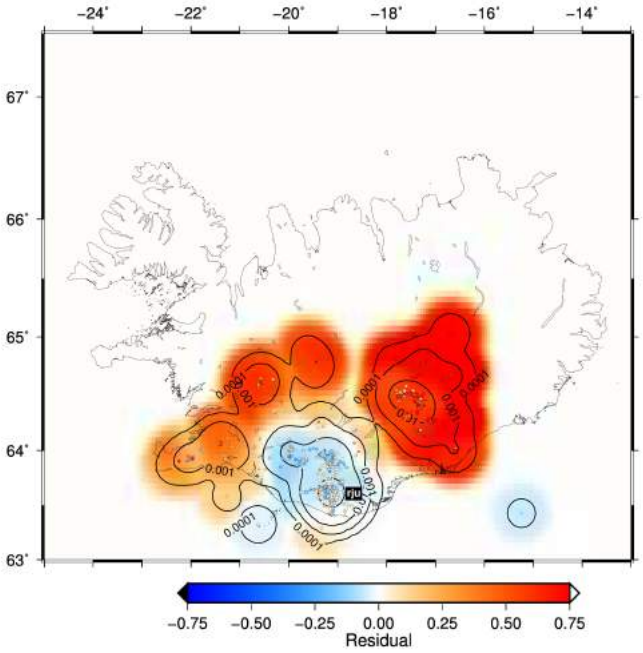
−24°
−22°
−20°
−18°
−16°
−14°
67°
66°
65°
64°
63°
rju
−0.75
−0.50
−0.25
0.00
0.25
0.50
0.75
Residual

snb

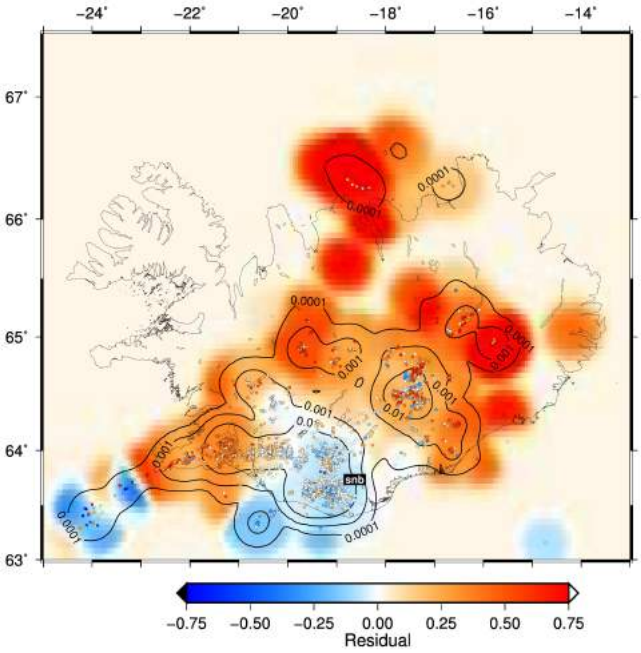
−24°
−22°
−20°
−18°
−16°
−14°
67°
66°
65°
64°
63°
snb
−0.75
−0.50
−0.25
0.00
0.25
0.50
0.75
Residual

sly

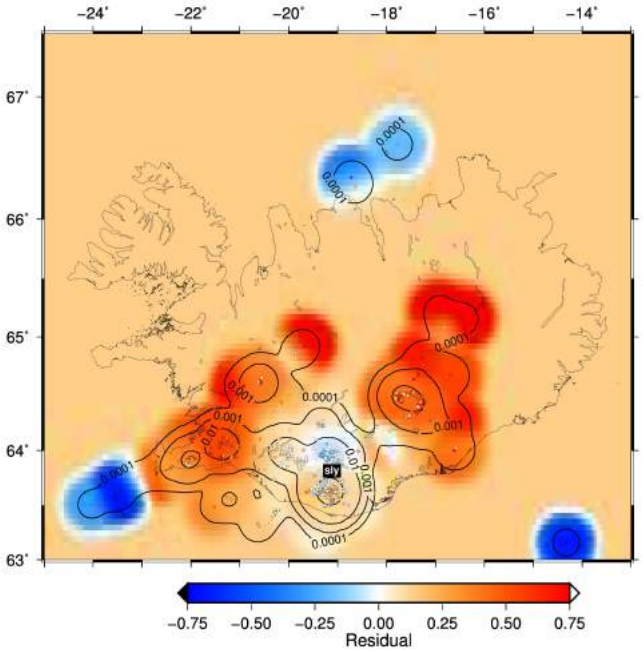
−24°
−22°
−20°
−18°
−16°
−14°
67°
66°
65°
64°
63°
sly
−0.75
−0.50
−0.25
0.00
0.25
0.50
0.75
Residual

fag

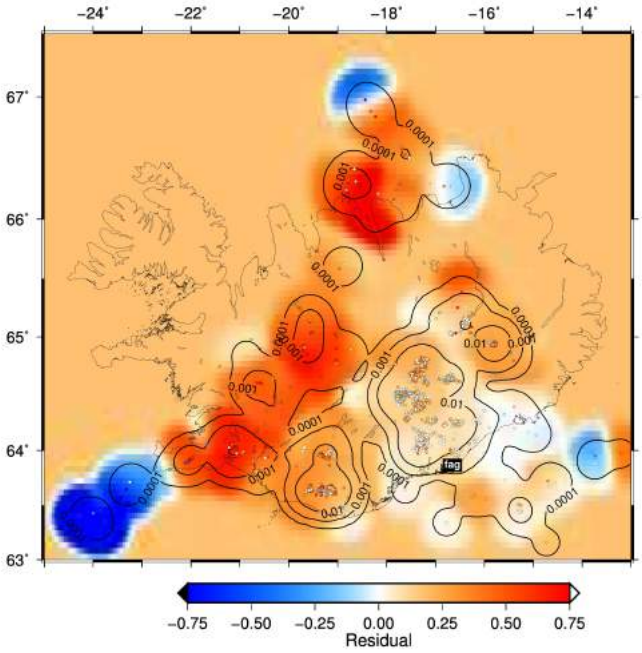
−24°
−22°
−20°
−18°
−16°
−14°
67°
66°
65°
64°
63°
fag
−0.75
−0.50
−0.25
0.00
0.25
0.50
0.75
Residual

kal

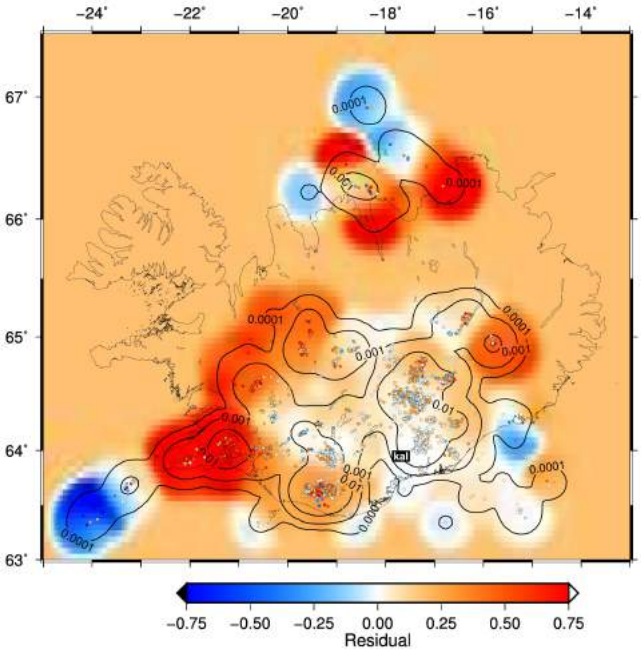
−24°
−22°
−20°
−18°
−16°
−14°
67°
66°
65°
64°
63°
kal
−0.75
−0.50
−0.25
0.00
0.25
0.50
0.75
Residual

grf

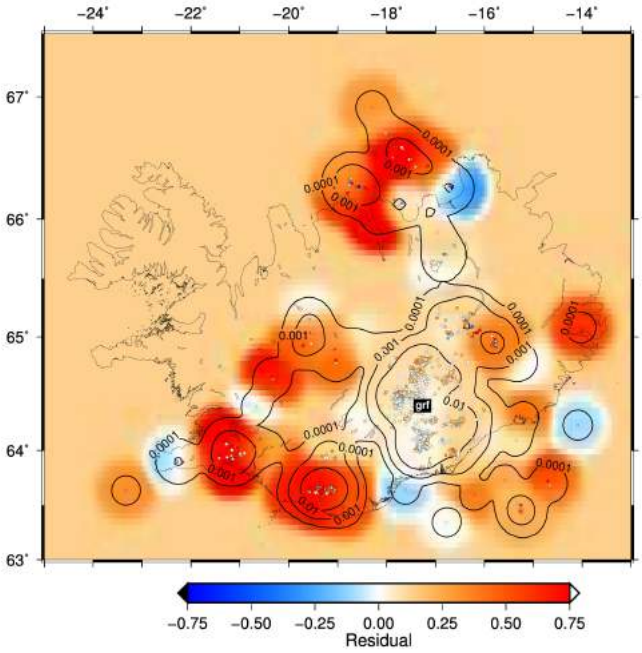
−24°
−22°
−20°
−18°
−16°
−14°
67°
66°
65°
64°
63°
grf
−0.75
−0.50
−0.25
0.00
0.25
0.50
0.75
Residual

vat

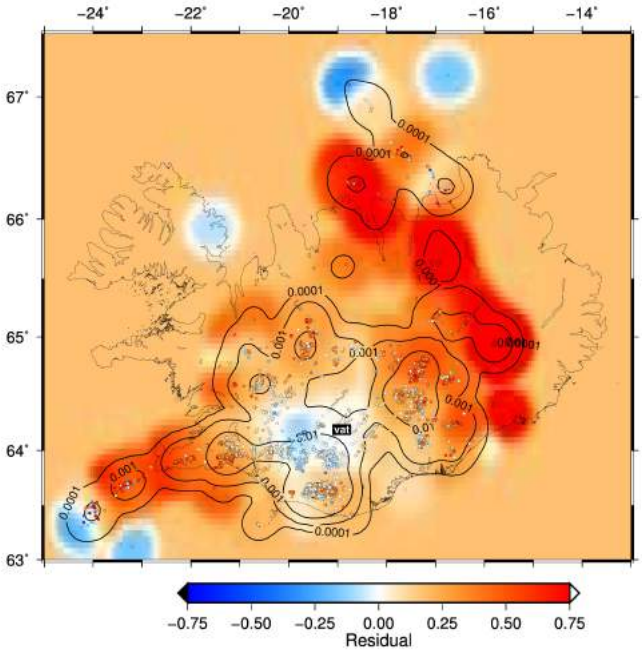

jok

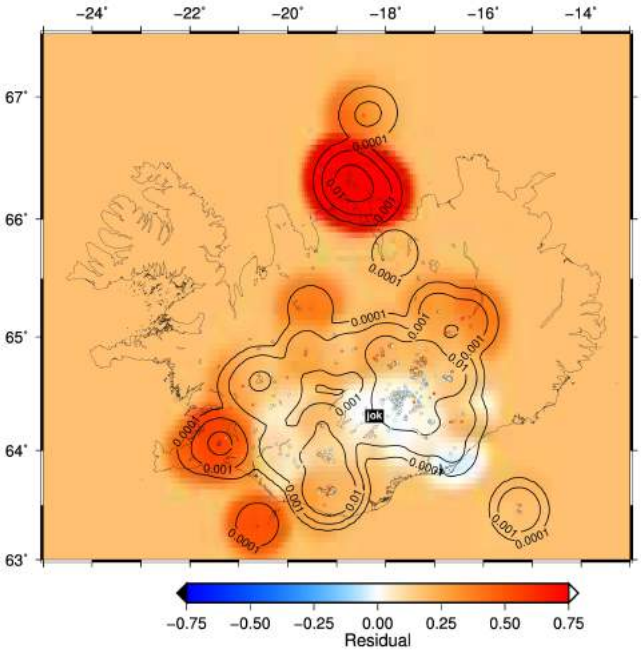

skr

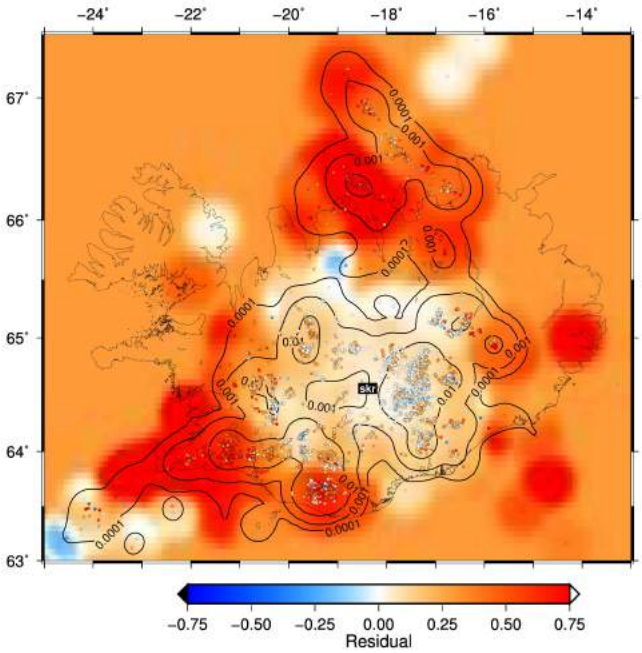

dyn

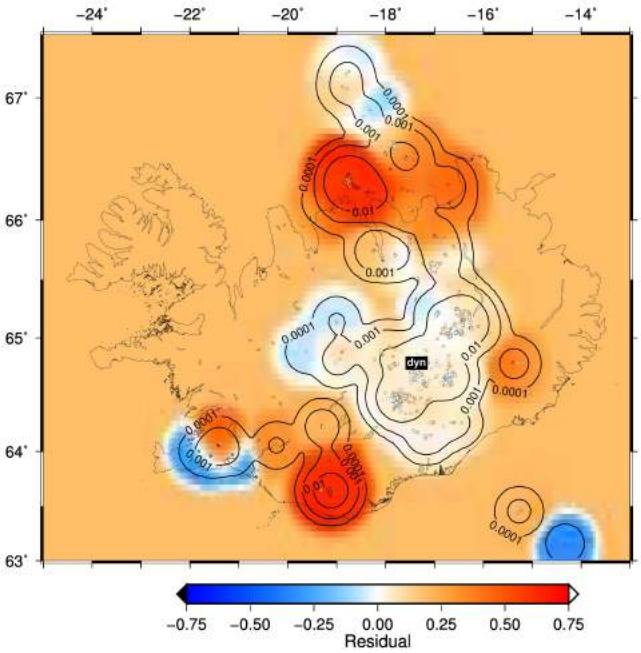

mko

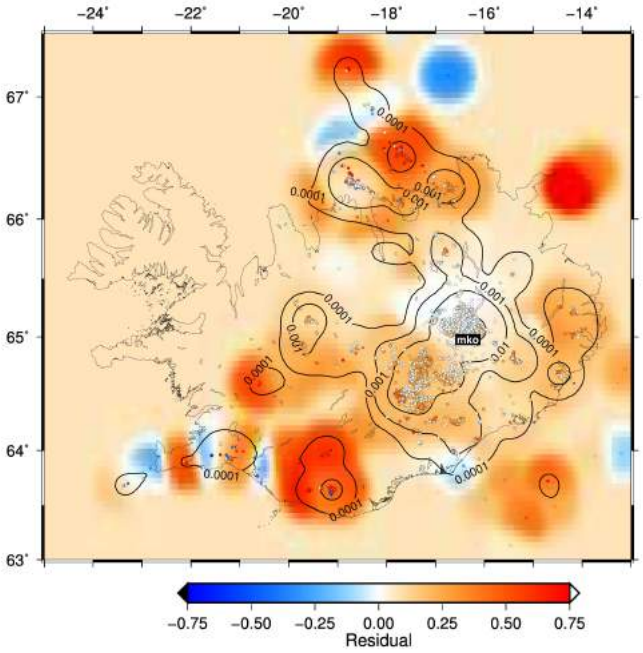

vsh

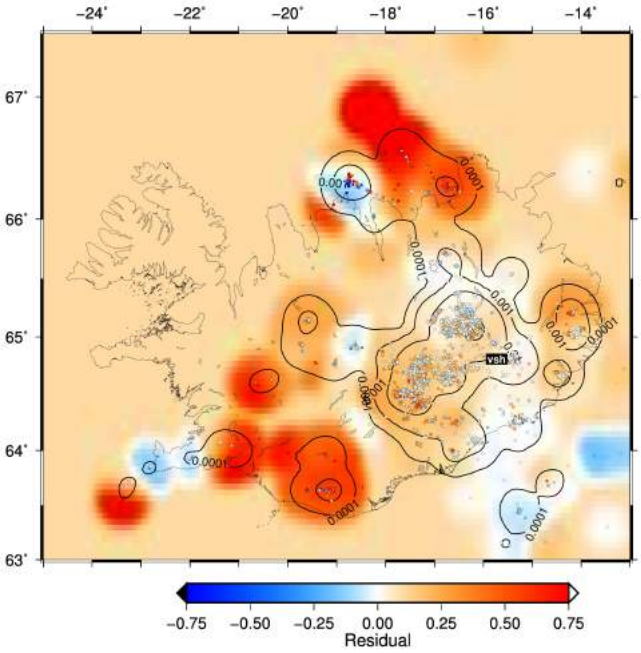

bru

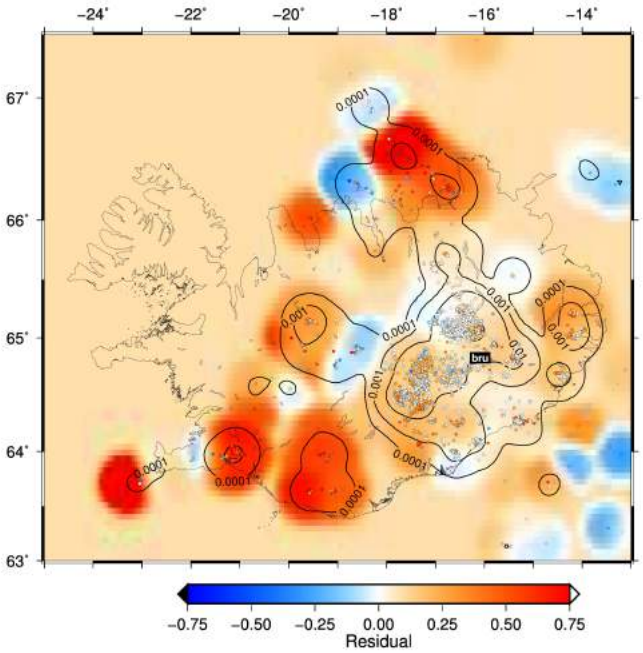

kre

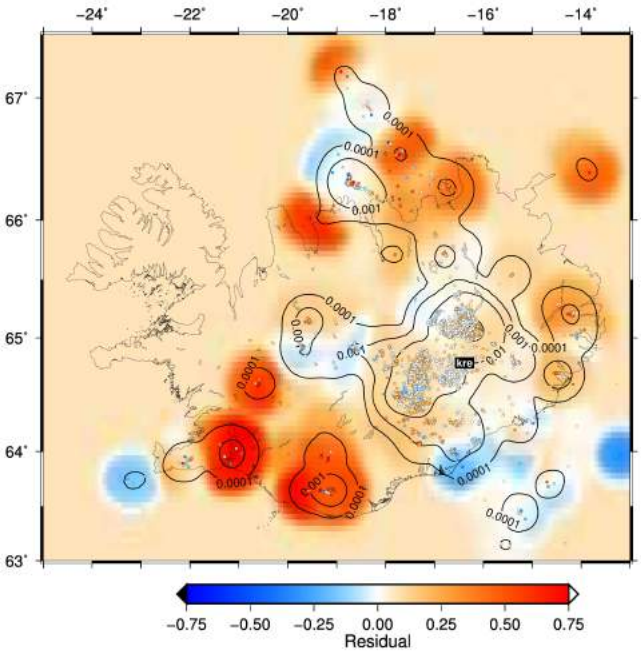

hva

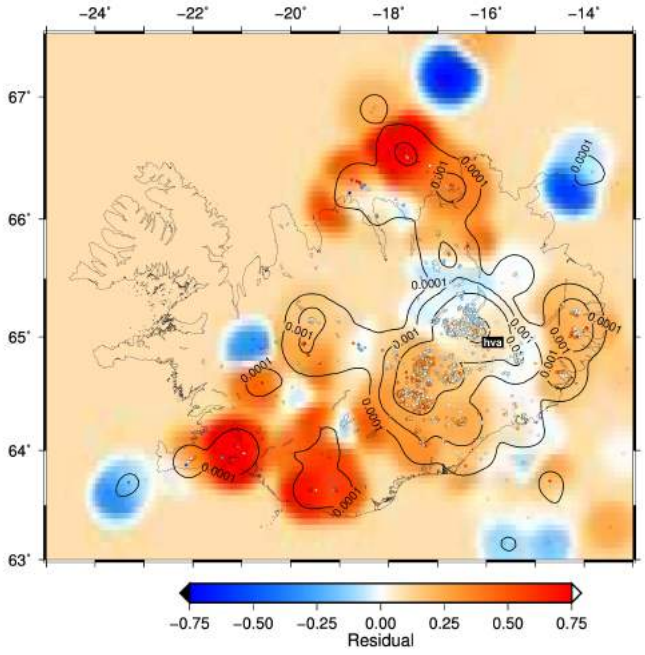
−24°
−22°
−20°
−18°
−16°
−14°
67°
66°
65°
64°
63°
hva
−0.75
−0.50
−0.25
0.00
0.25
0.50
0.75
Residual

ada

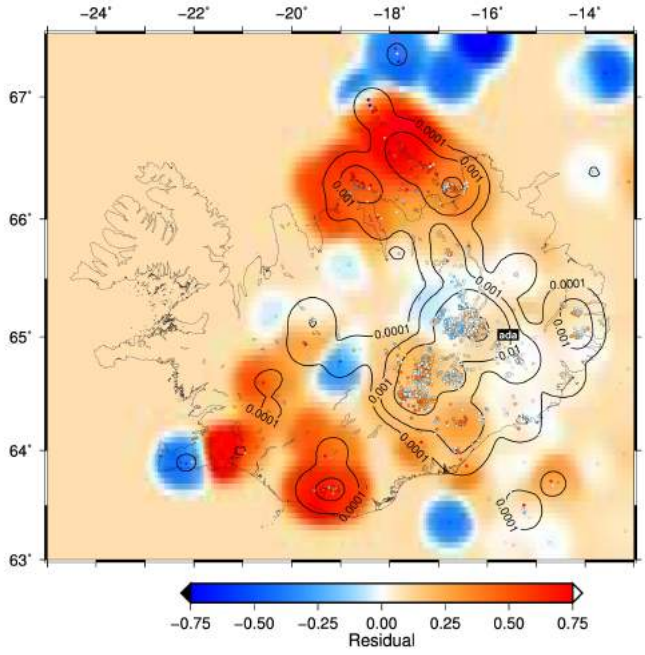
−24°
−22°
−20°
−18°
−16°
−14°
67°
66°
65°
64°
63°
ada
−0.75
−0.50
−0.25
0.00
0.25
0.50
0.75
Residual

glu

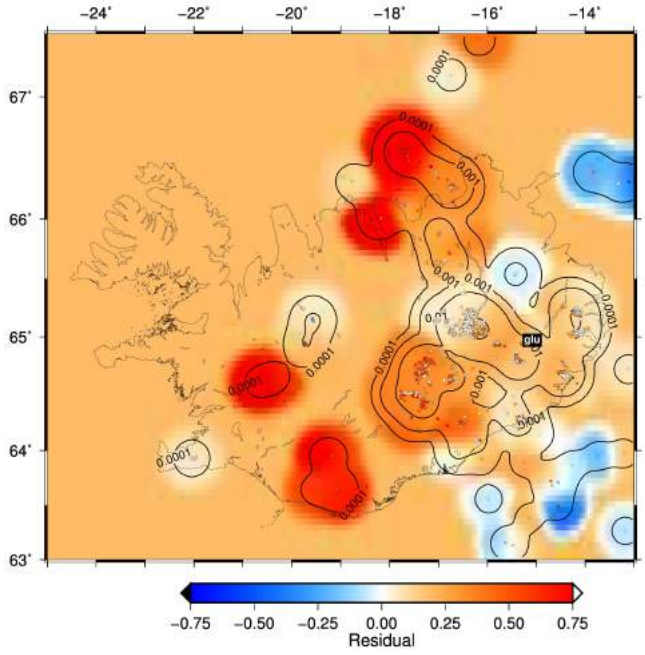
−24°
−22°
−20°
−18°
−16°
−14°
67°
66°
65°
64°
63°
glu
−0.75
−0.50
−0.25
0.00
0.25
0.50
0.75
Residual

sig

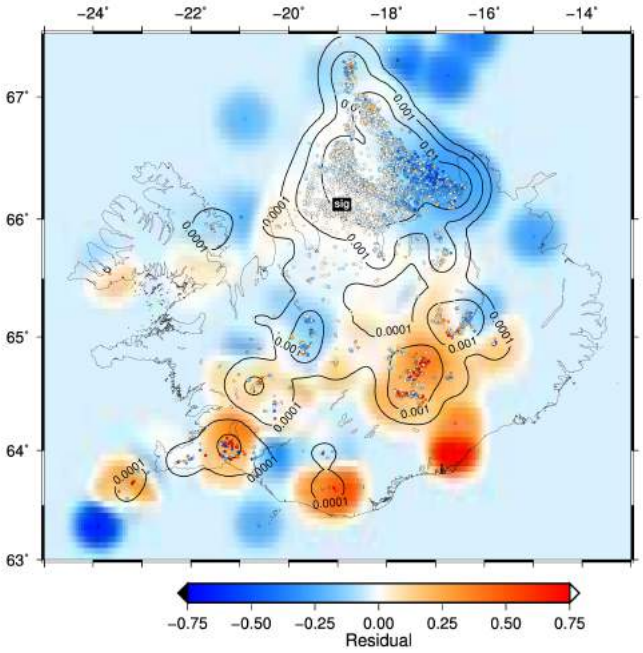

hla

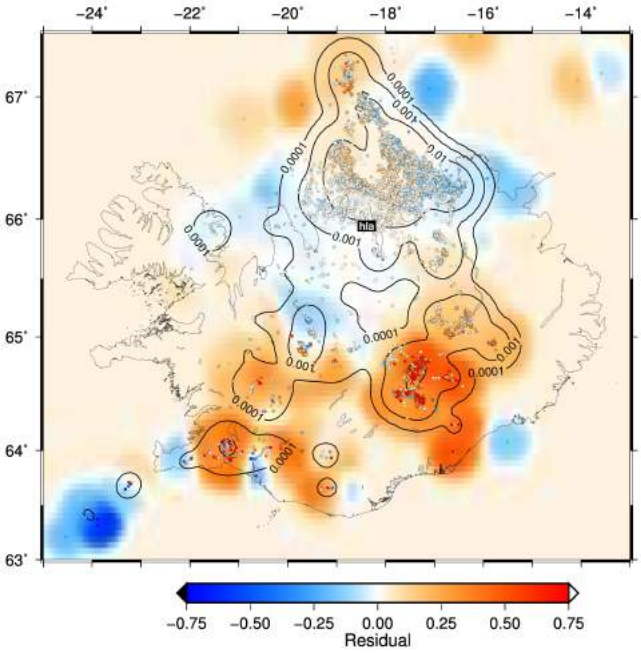

fla

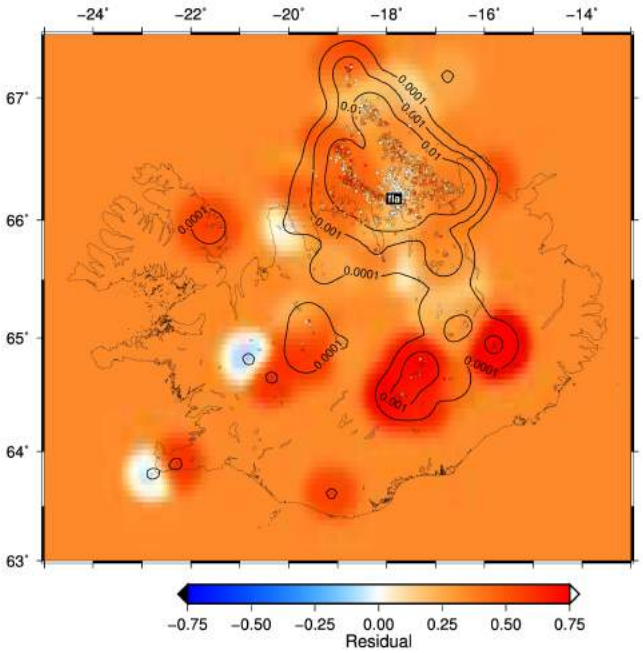

bre

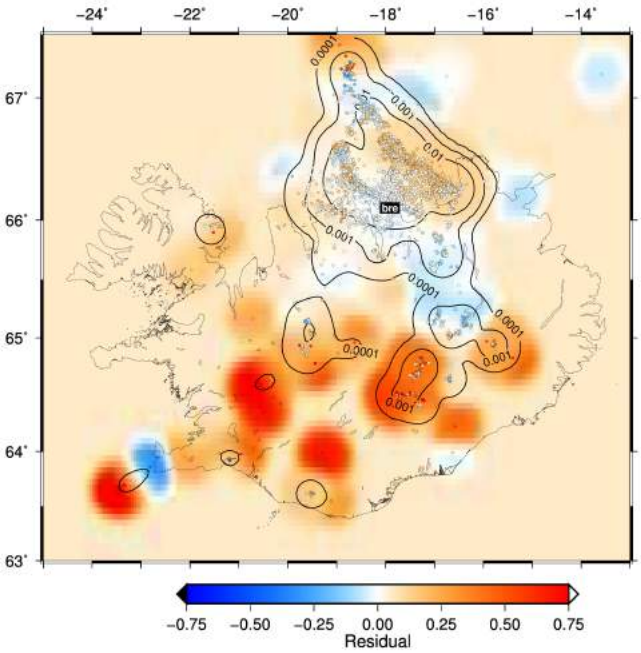

ren

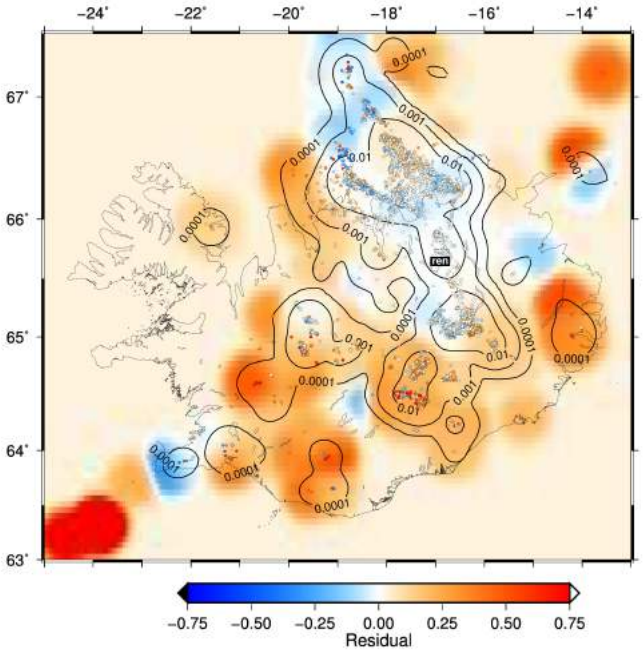

kvo

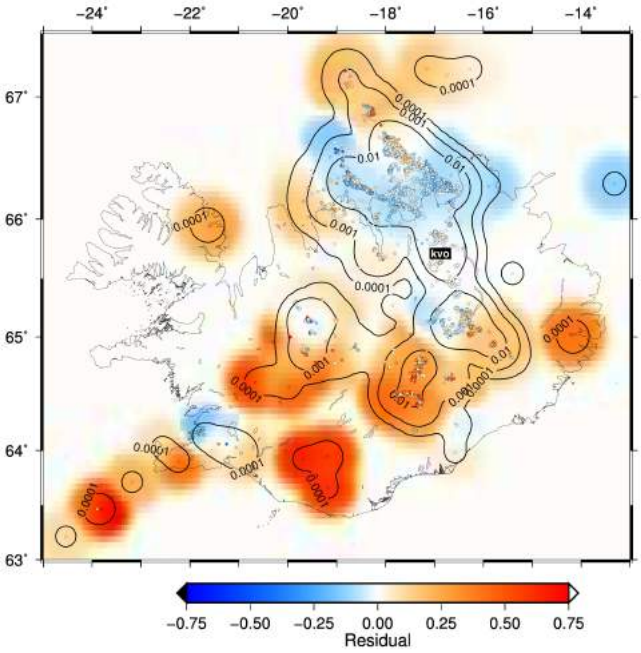

gha

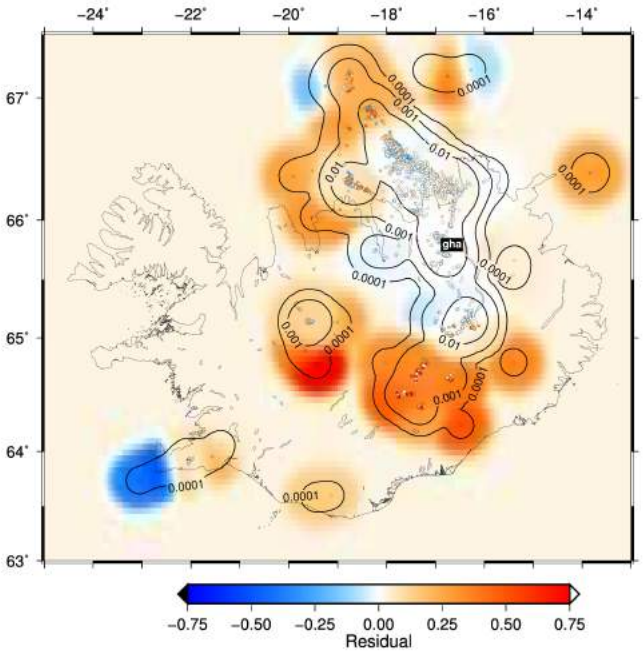

ghs

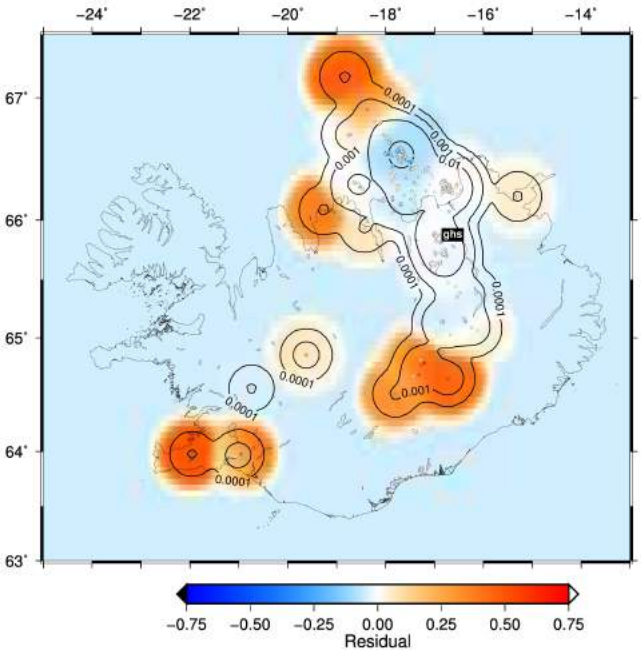

ski

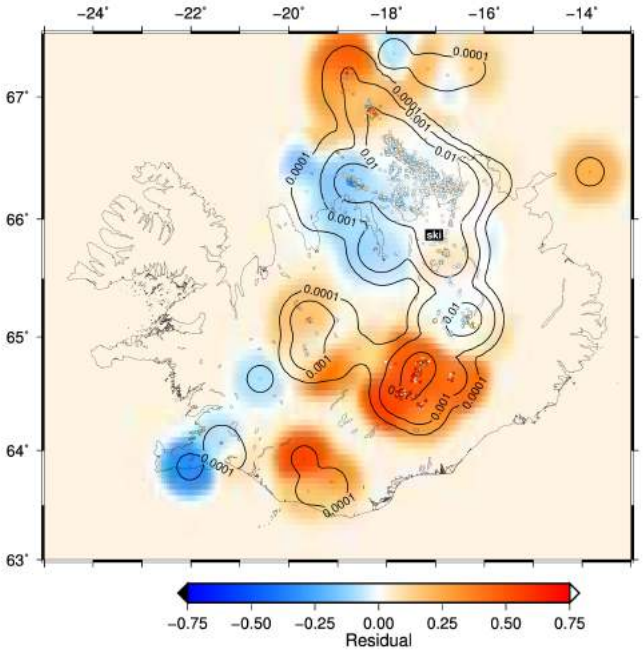

dim

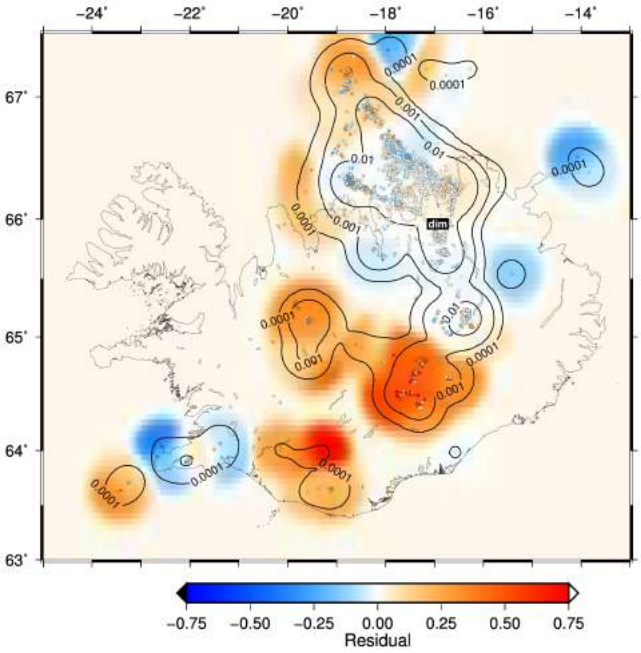

gra

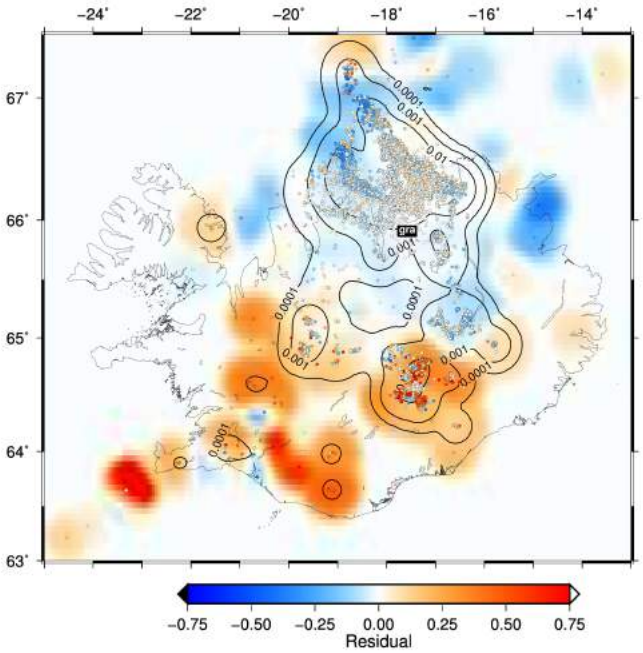

hed

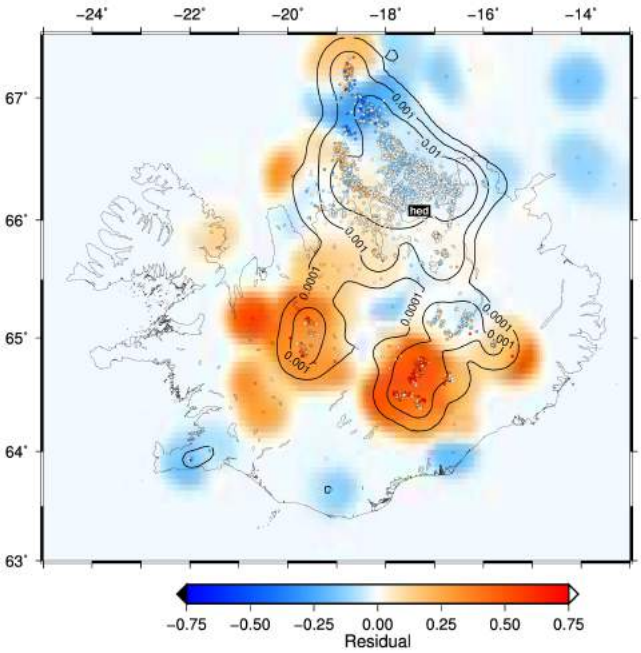

ask

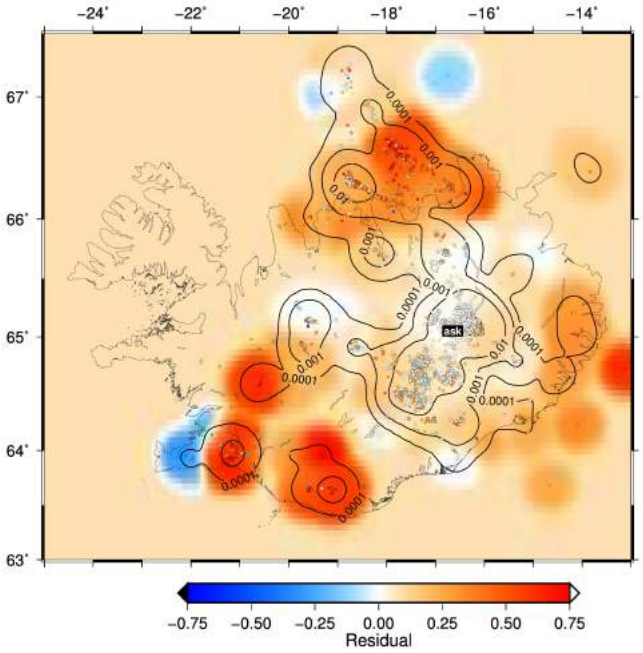

sva

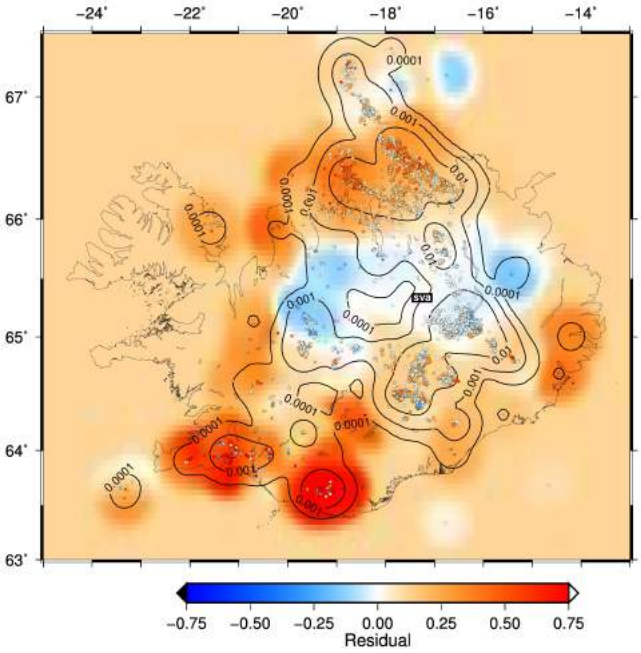

mel

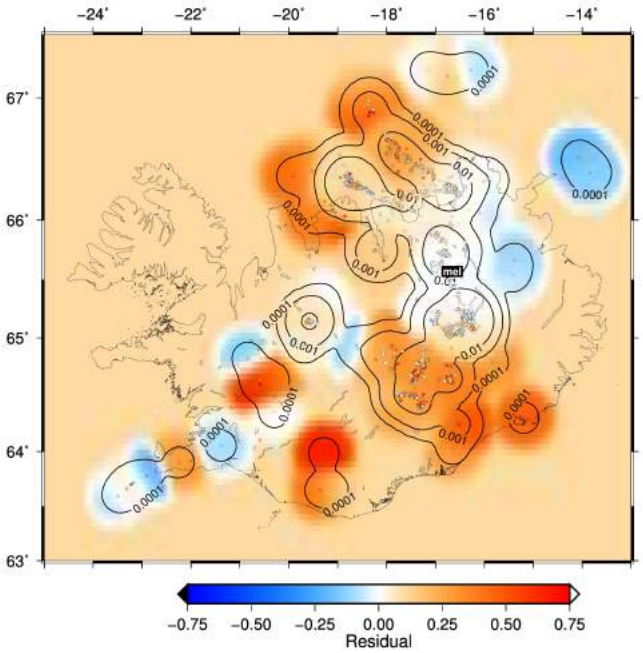

grs

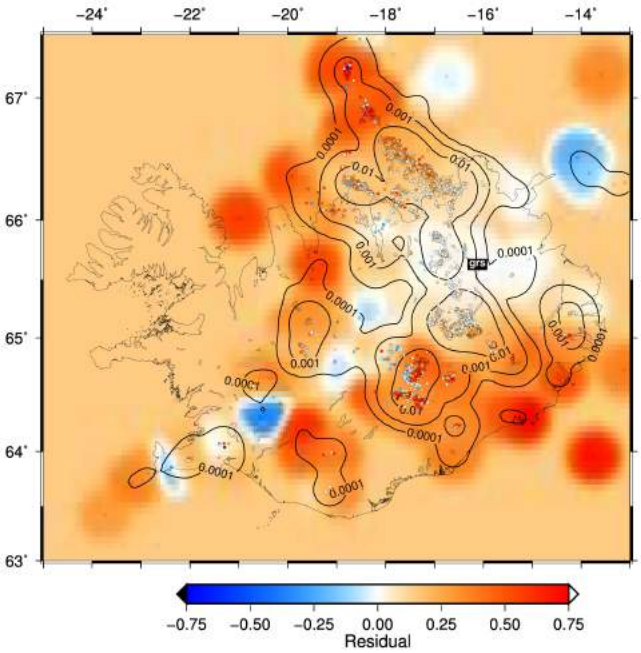

hrn

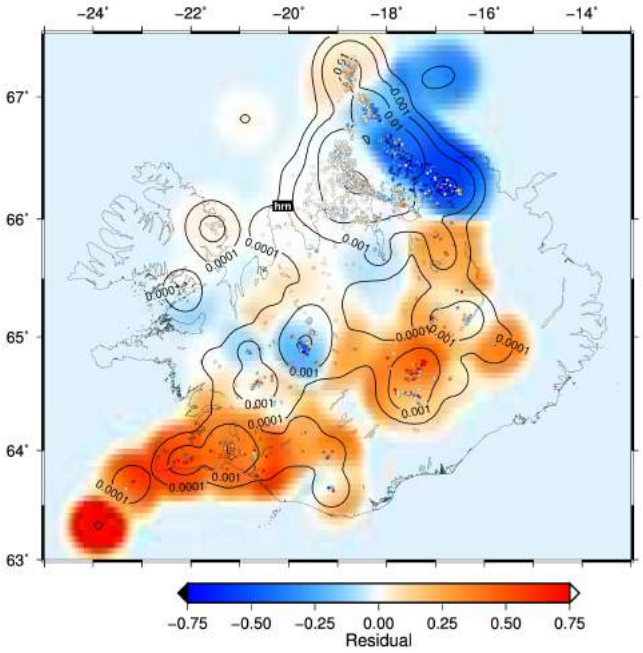

gri

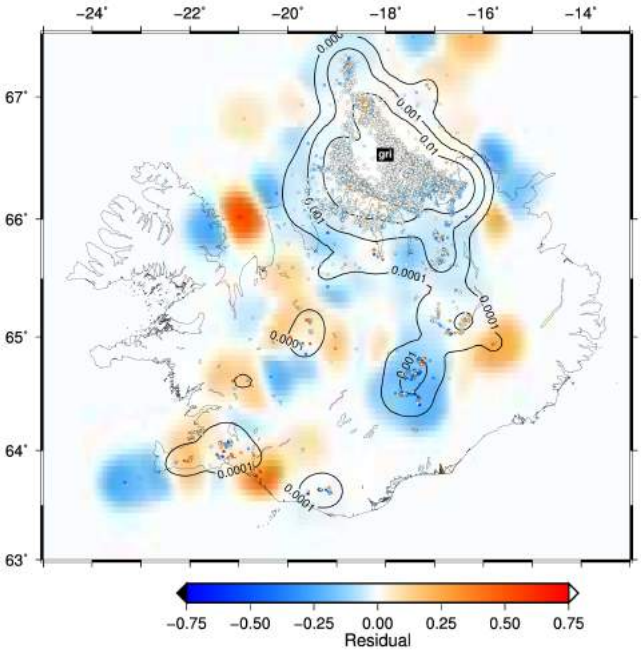

lei

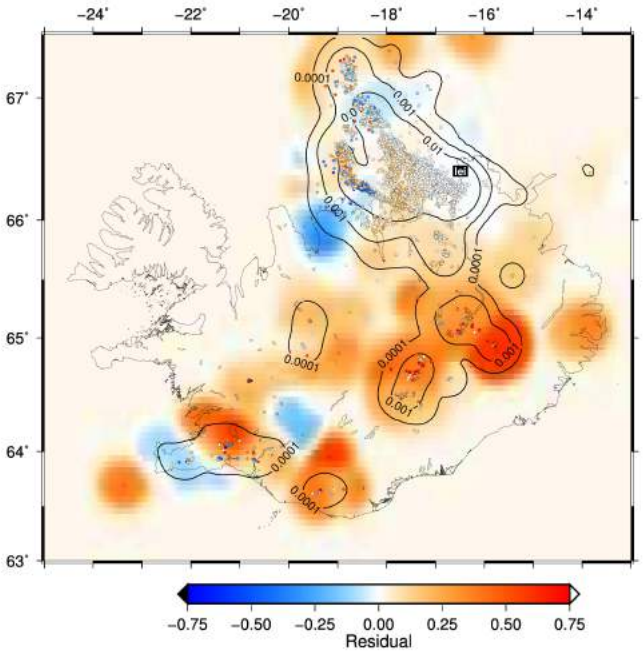

gil

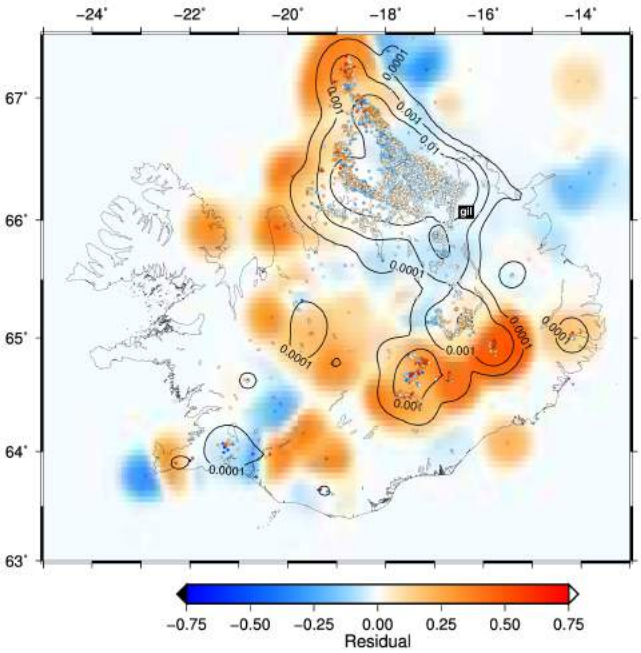

asb

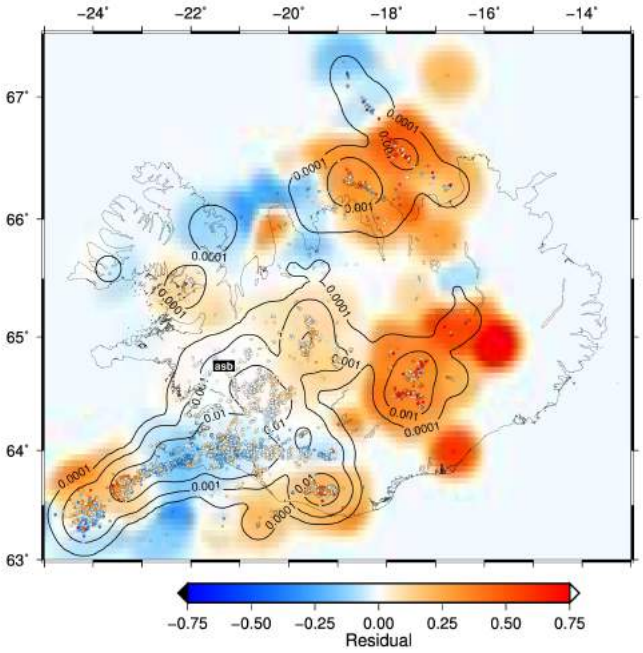

hve

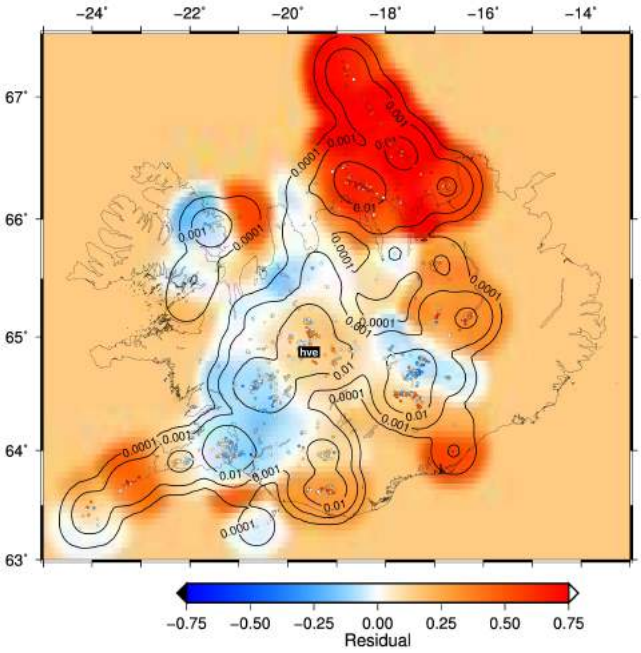

kud

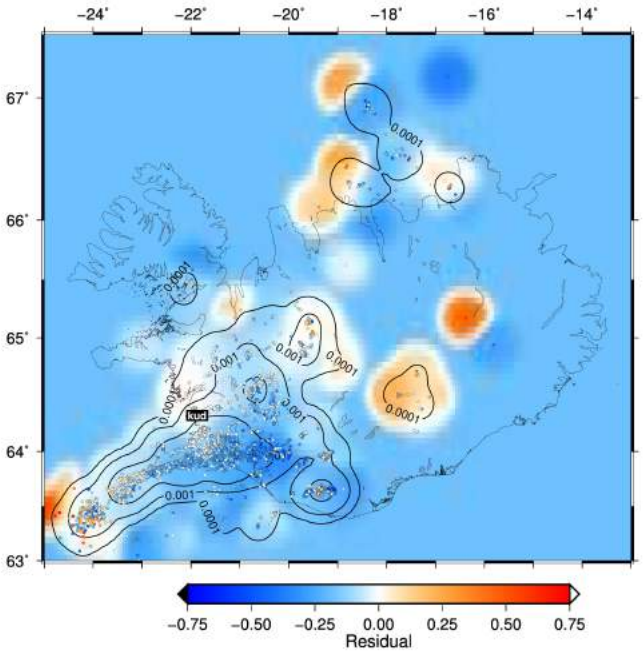

gyg

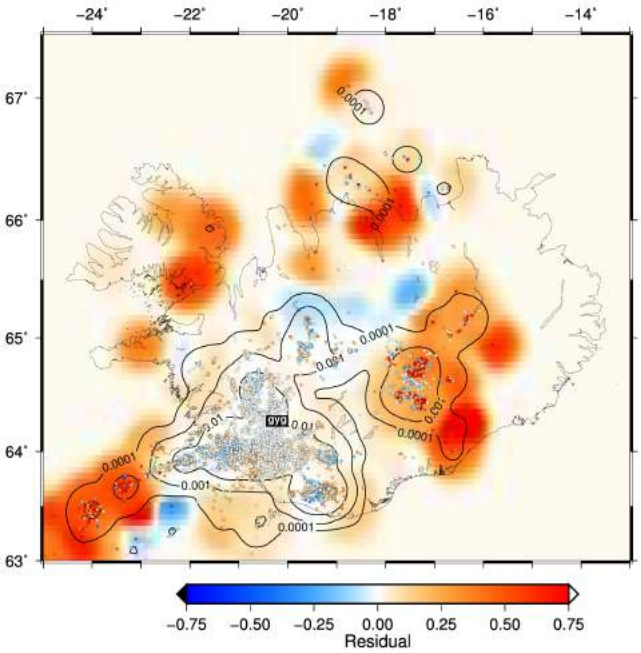

Appendix C

The deterministic component of empirical travel time: Station by station comparison of S-wave residuals.

The following maps show the travel-time residuals relative to predictions of the SIL model (circles) and the deterministic component (continuos colour) of empirical travel times for all 65 stations in the SIL network that we have analysed. The maps show data and results from S-wave residuals only. The two-dimensional interpolation that defines the deterministic component of the empirical travel time is calculated using a moving average over a Gaussian function that is 10 km in width. The contours indicate the combined weights of the data that contribute to the estimate at each point and are a useful guide about robustness. The running average is based on many nearby data where this combined weight is high.

The figures are organized with four maps per page. Those show both S-wave residuals and their interpolations for a number of nearby stations as indicated. This allows for a geographical comparison of results.

It is evident from this comparison that the travel-time residuals are quite coherent from one station to the next when they are closely spaced. Note that the residual mean has not been removed. This is indicated by the background colour and will reflect a combined effect of station elevation and possibly anomalous shallow structure immediately beneath each station. Such an effect is particularly clear for station fla (page C15), which has a significantly positive average. Nearby station bre has a different average dispite the fact that it is only a few km away. The residual patterns of the two stations are quite similar. Station ves (page C7) also has a significantly positive average, as do stations in the highlands (page C11). Station kud in western Iceland (page C20) is at the other end of the spectrum with a significantly negative (fast) average.

nyl

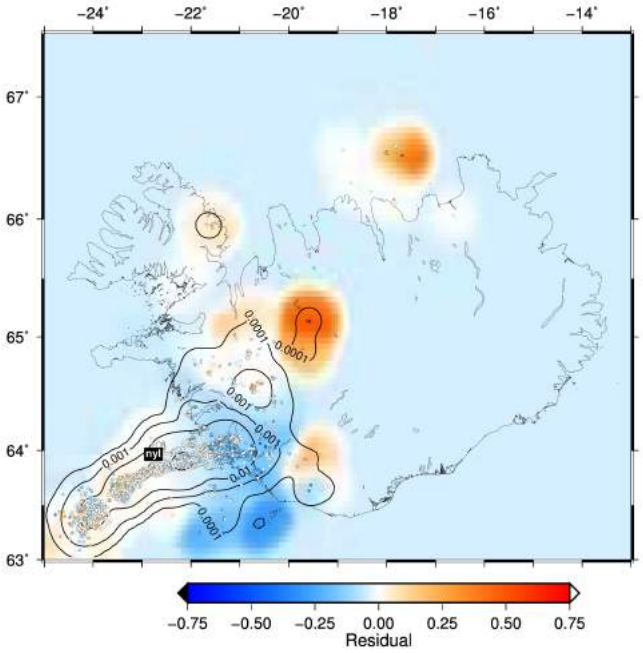

rne

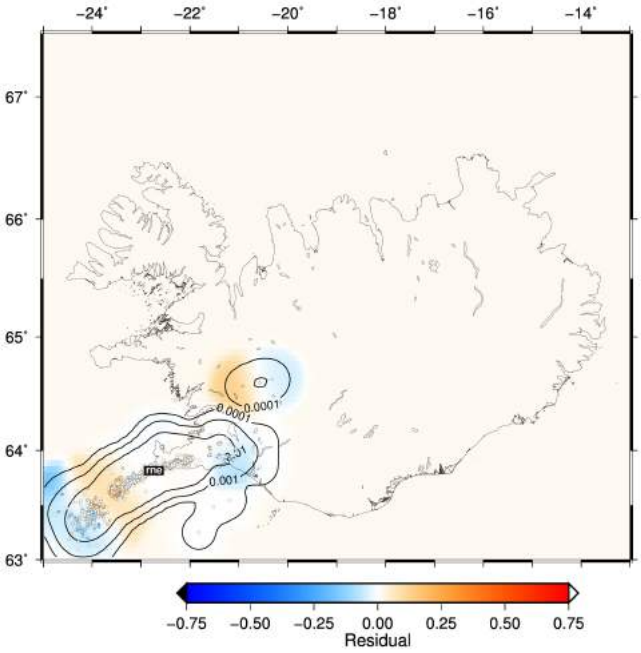

vog

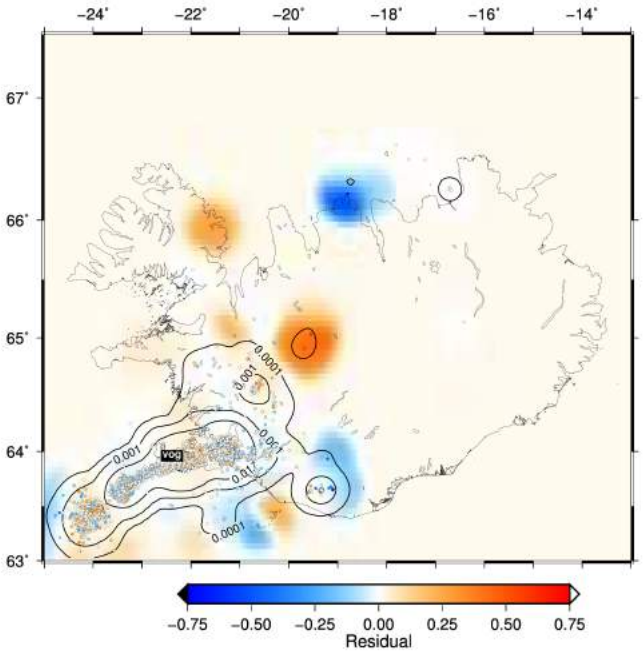

grv

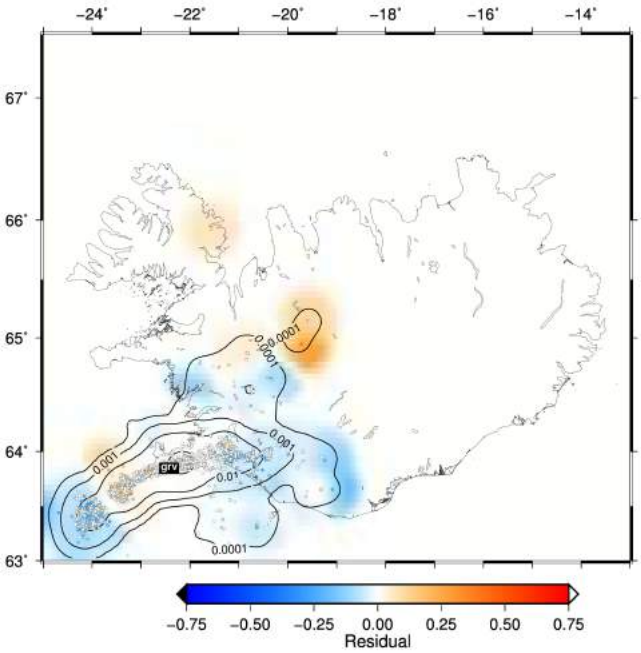

kri

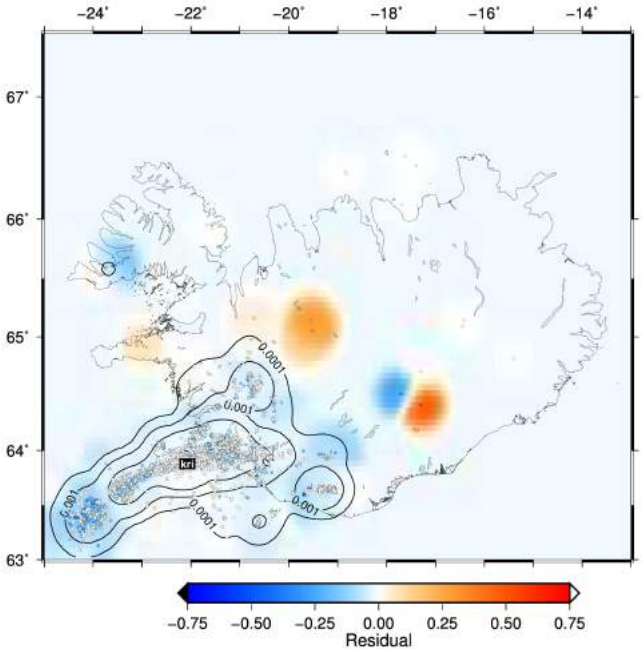

vos

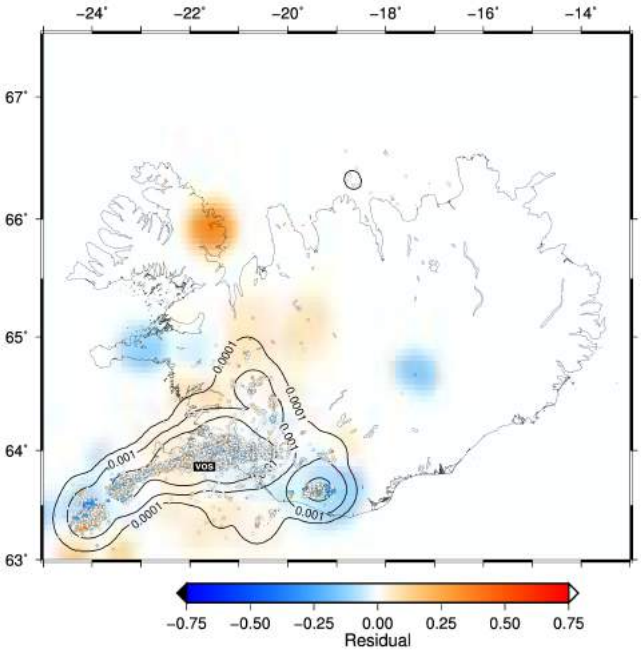

kas

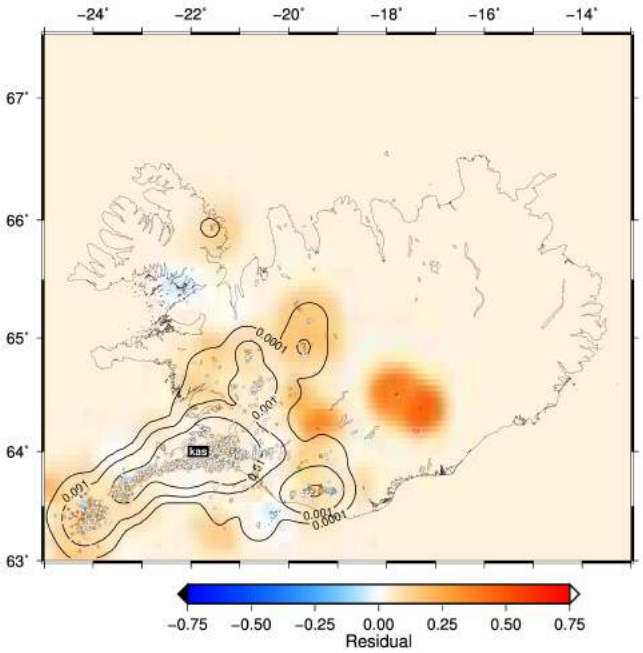

haf

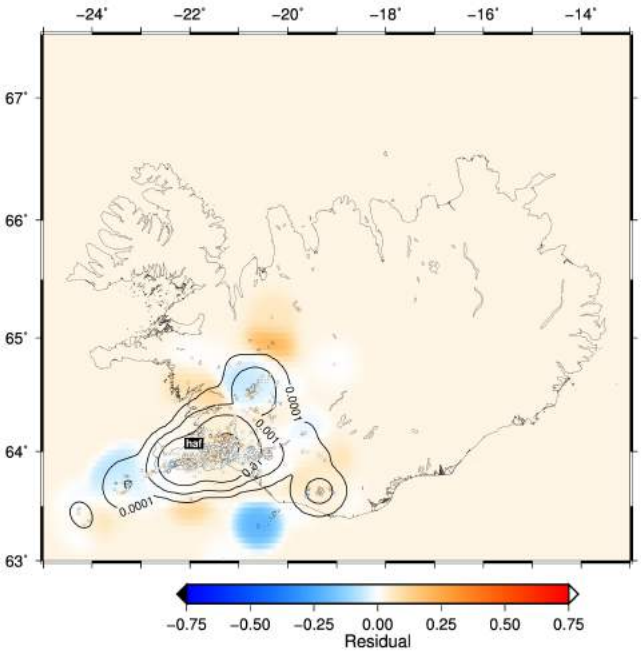

bja

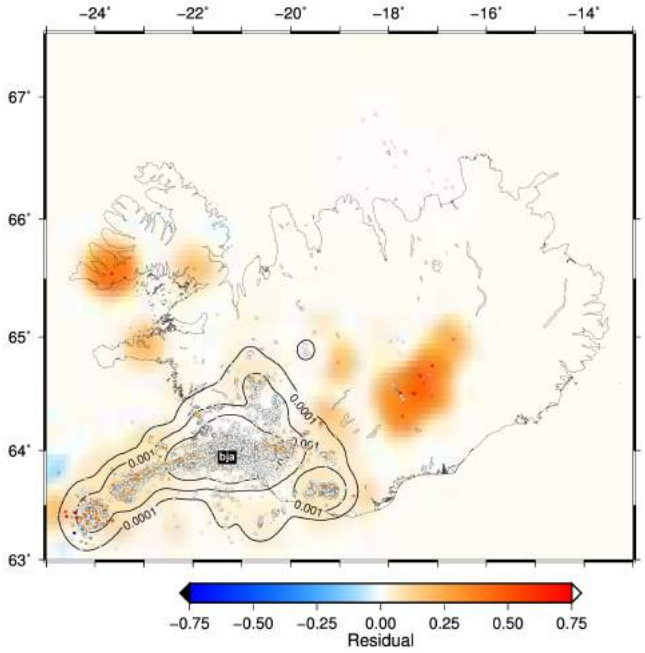

san

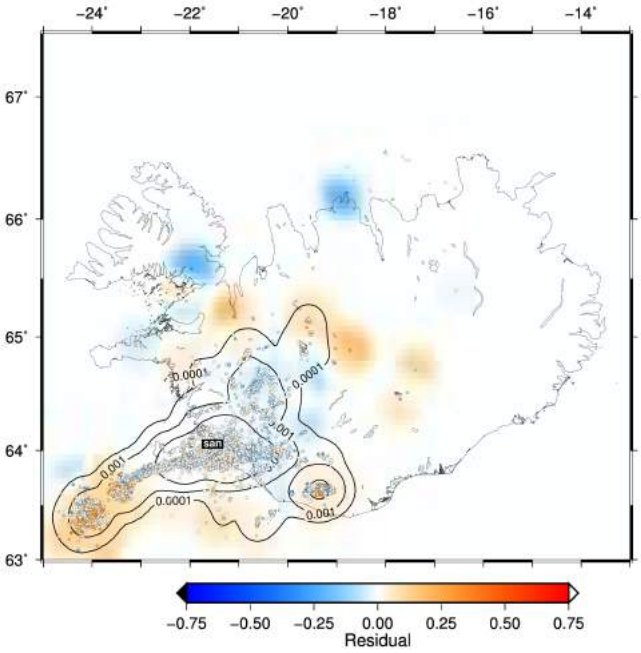

kro

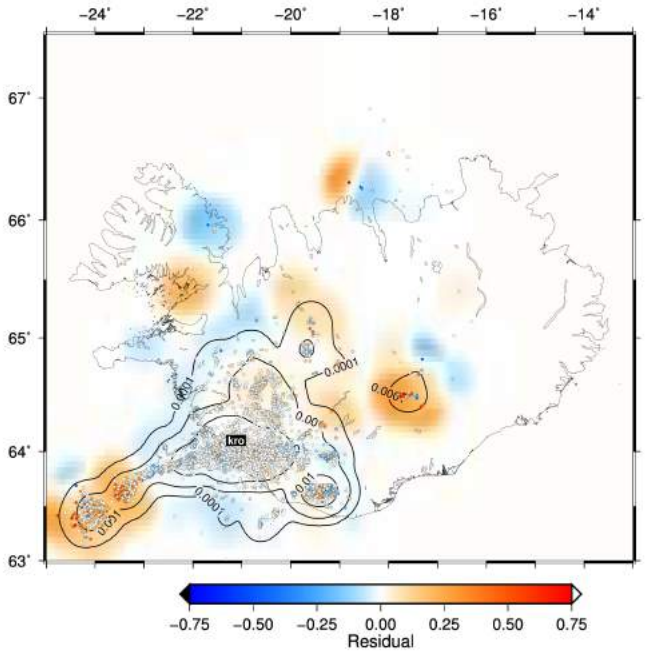

hei

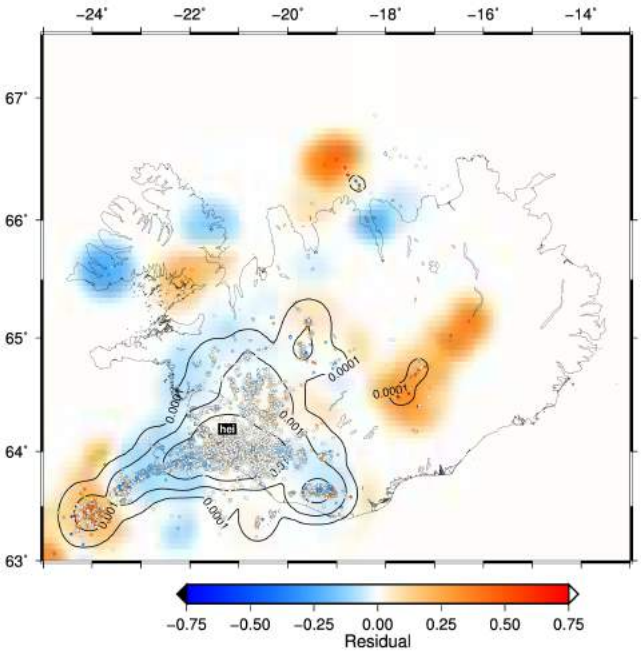

sol

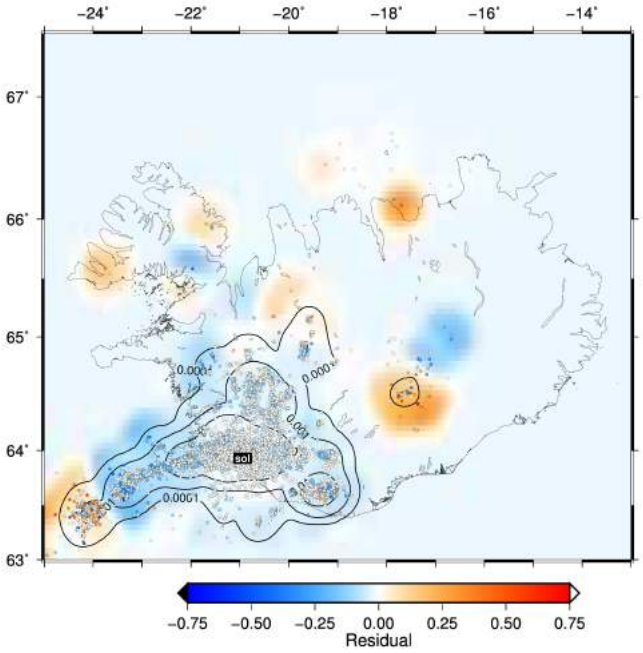

asm

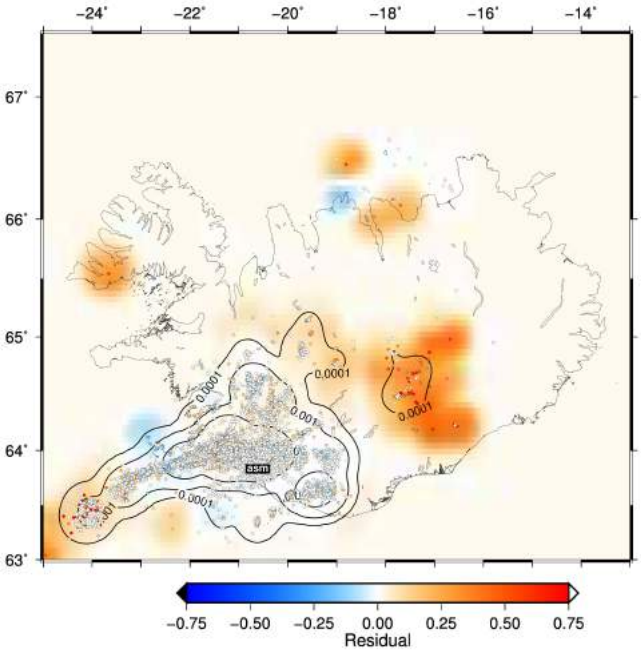

sau

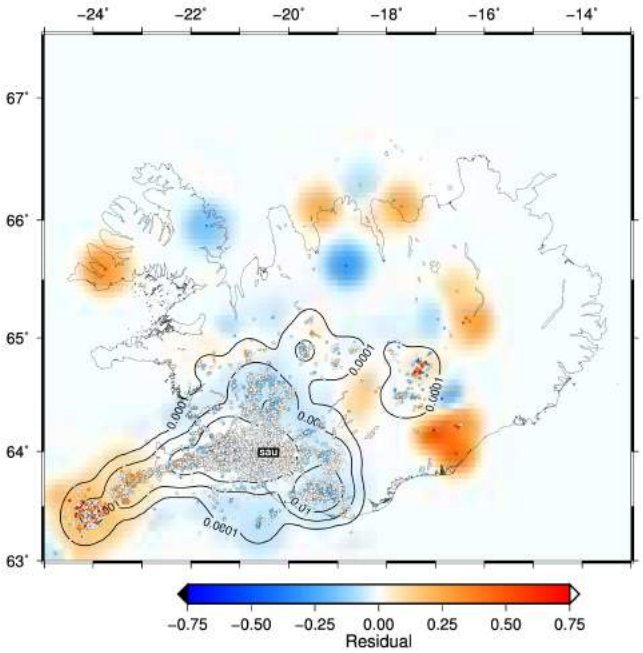

hau

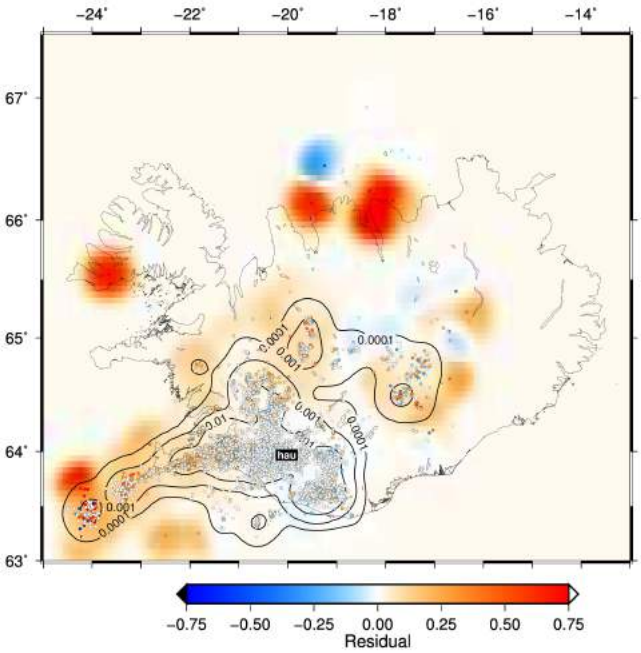

ves

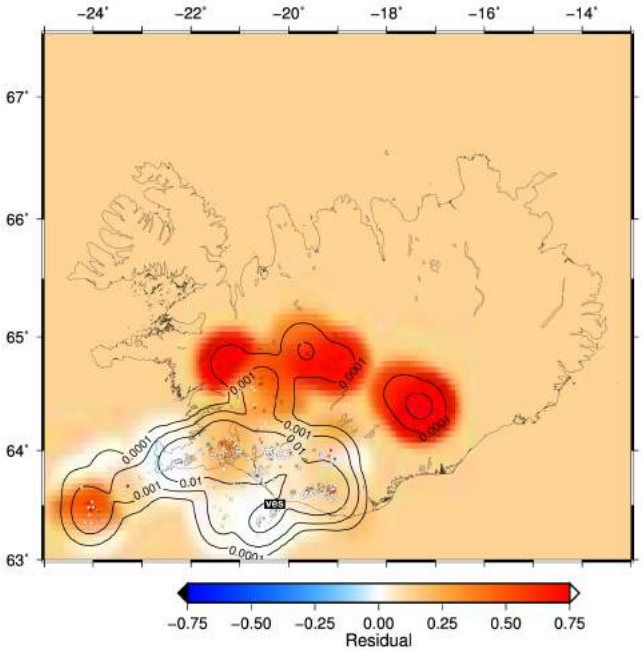

mid

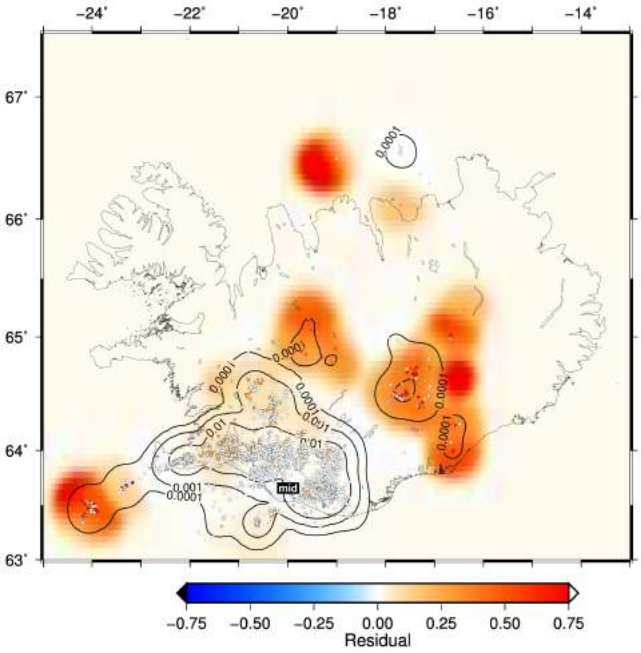

smj

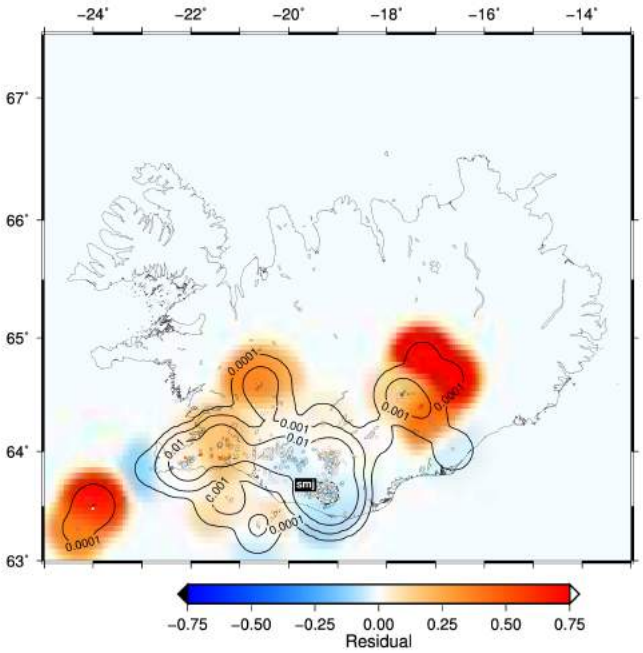

god

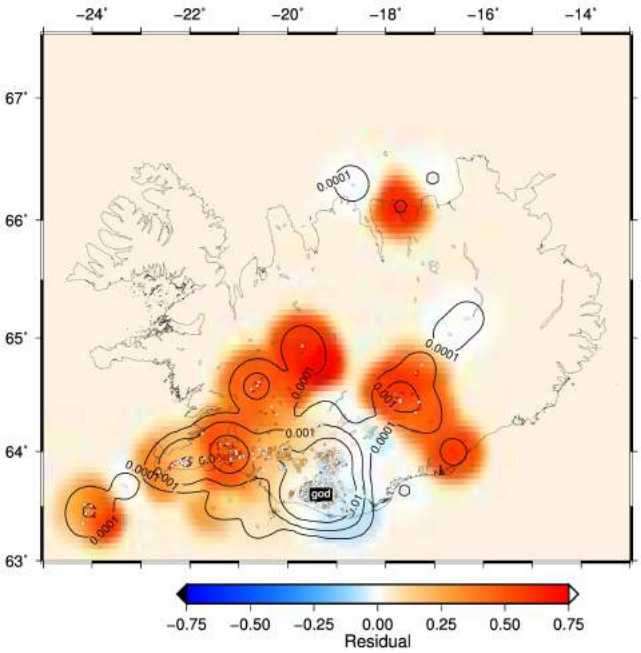

esk

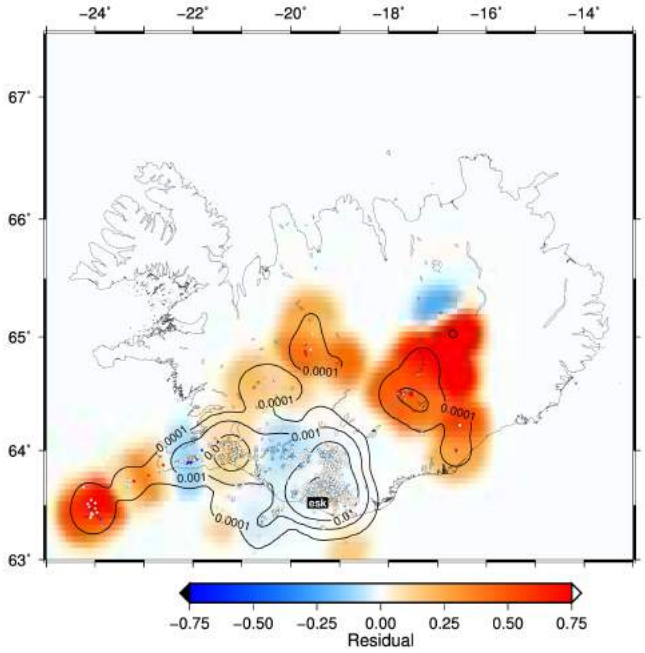

alf

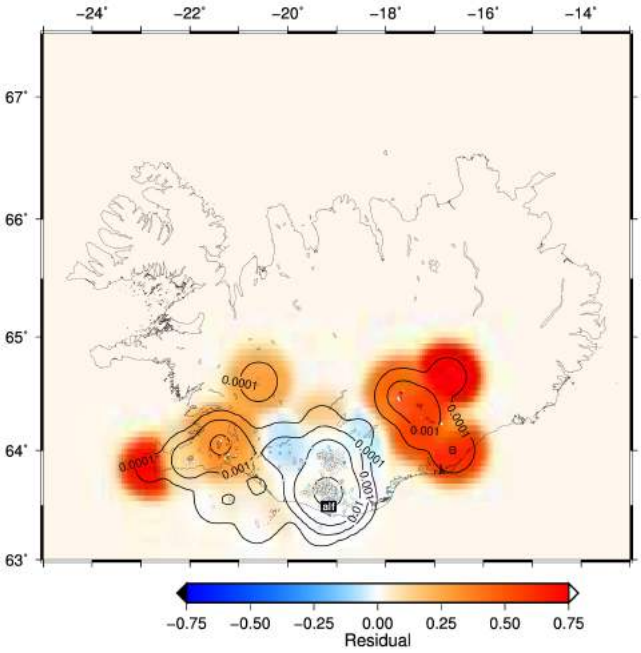

skh

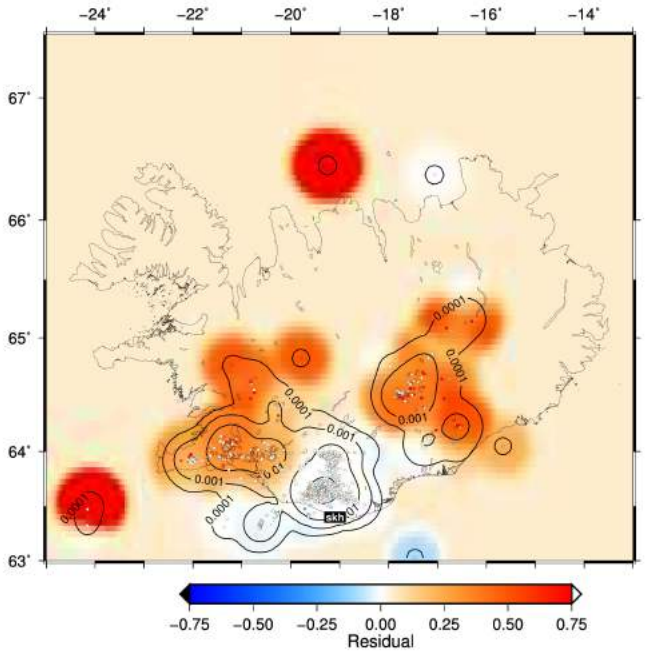

hvo

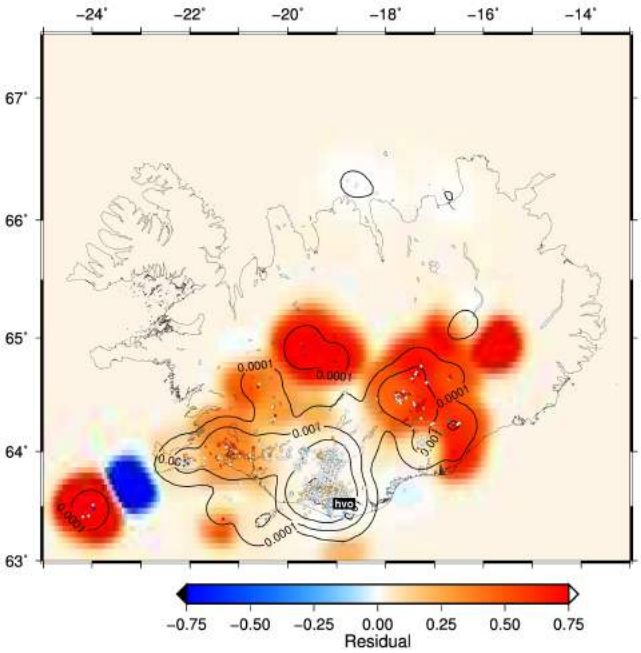

rju

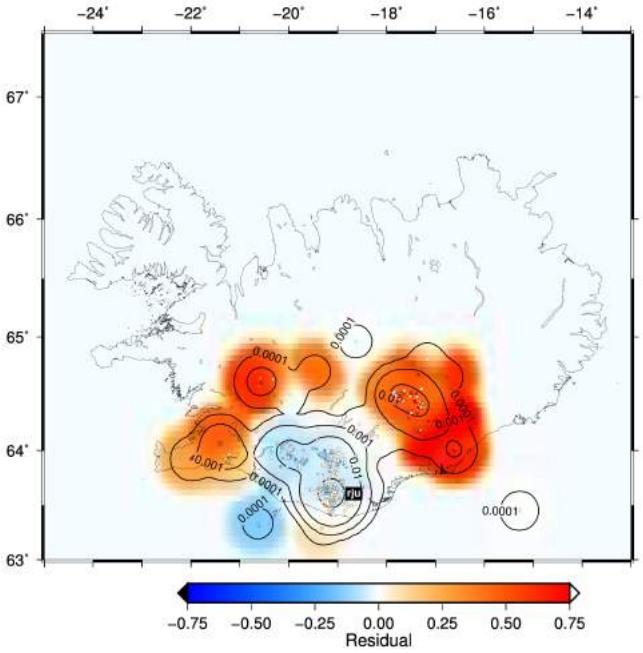
−24°
−22°
−20°
−18°
−16°
−14°
67°
66°
65°
64°
63°
rju
−0.75
−0.50
−0.25
0.00
0.25
0.50
0.75
Residual

snb

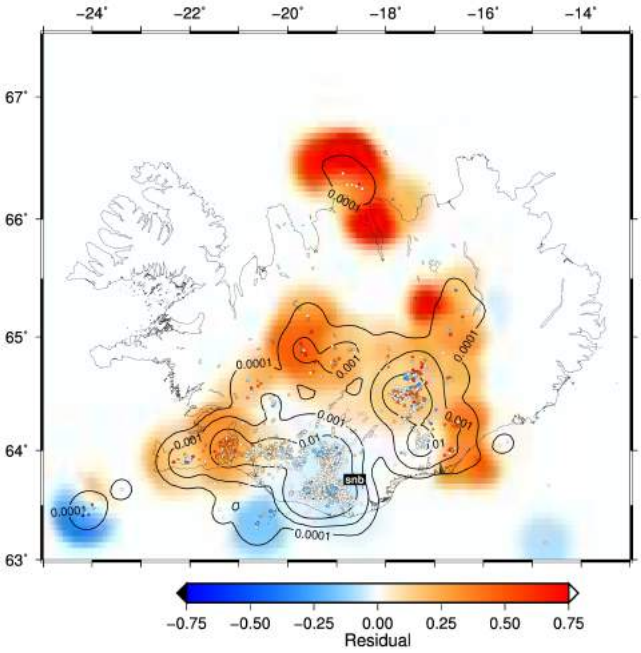
−24°
−22°
−20°
−18°
−16°
−14°
67°
66°
65°
64°
63°
snb
−0.75
−0.50
−0.25
0.00
0.25
0.50
0.75
Residual

sly

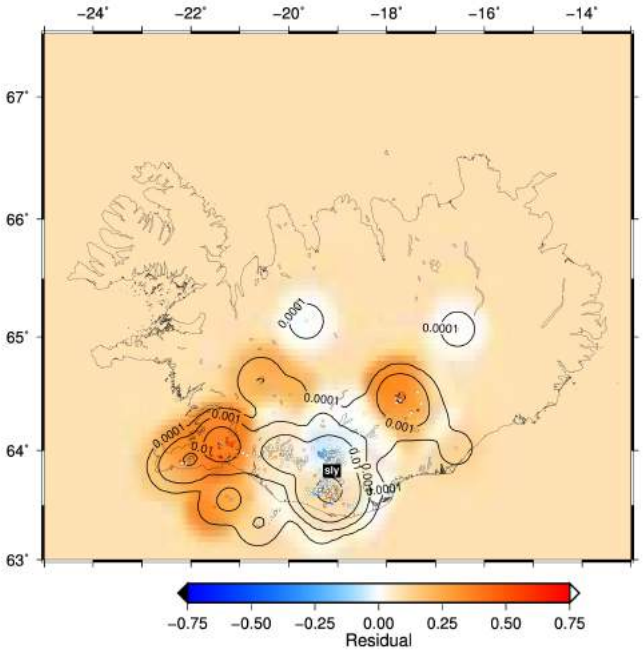
−24°
−22°
−20°
−18°
−16°
−14°
67°
66°
65°
64°
63°
sly
−0.75
−0.50
−0.25
0.00
0.25
0.50
0.75
Residual

fag

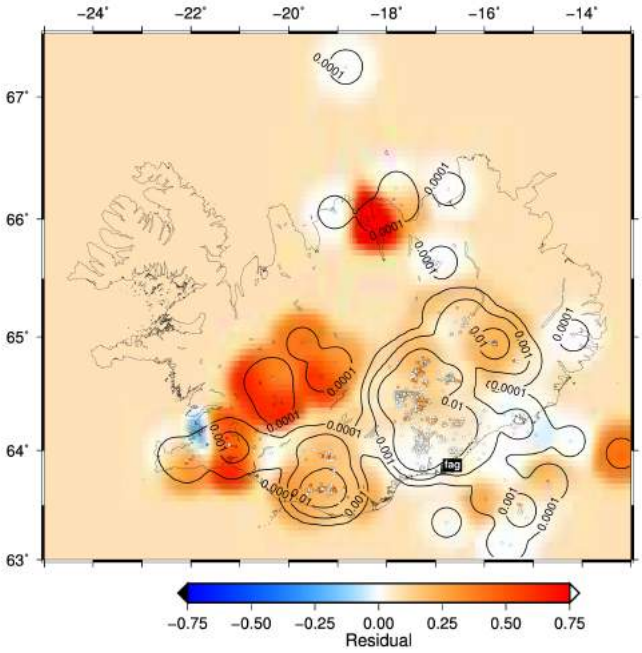
−24°
−22°
−20°
−18°
−16°
−14°
67°
66°
65°
64°
63°
fag
−0.75
−0.50
−0.25
0.00
0.25
0.50
0.75
Residual

kal

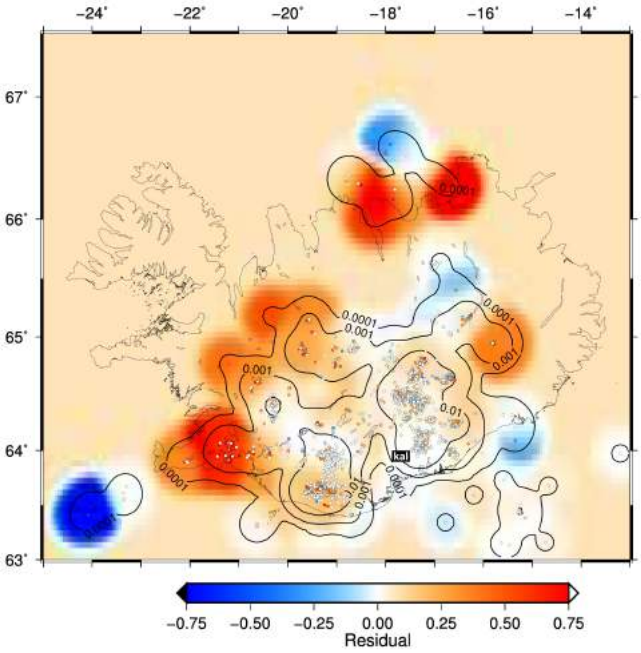
−24°
−22°
−20°
−18°
−16°
−14°
67°
66°
65°
64°
63°
kal
−0.75
−0.50
−0.25
0.00
0.25
0.50
0.75
Residual

grf

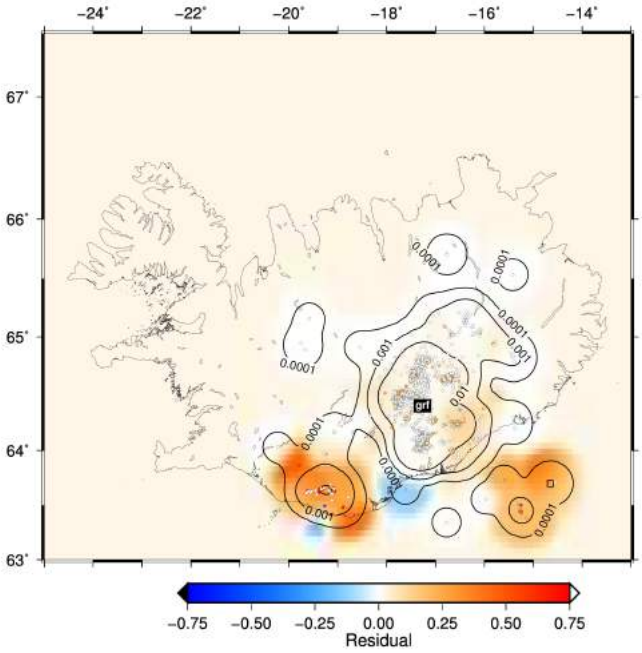
−24°
−22°
−20°
−18°
−16°
−14°
67°
66°
65°
64°
63°
grf
−0.75
−0.50
−0.25
0.00
0.25
0.50
0.75
Residual

vat

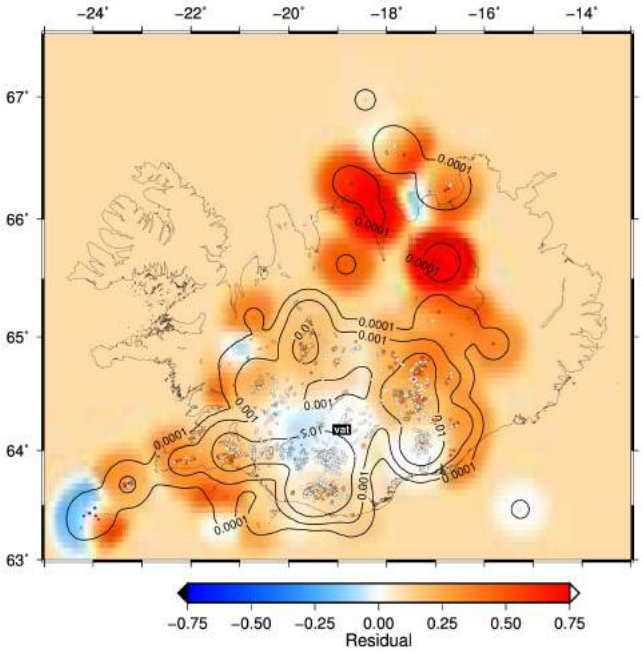

jok

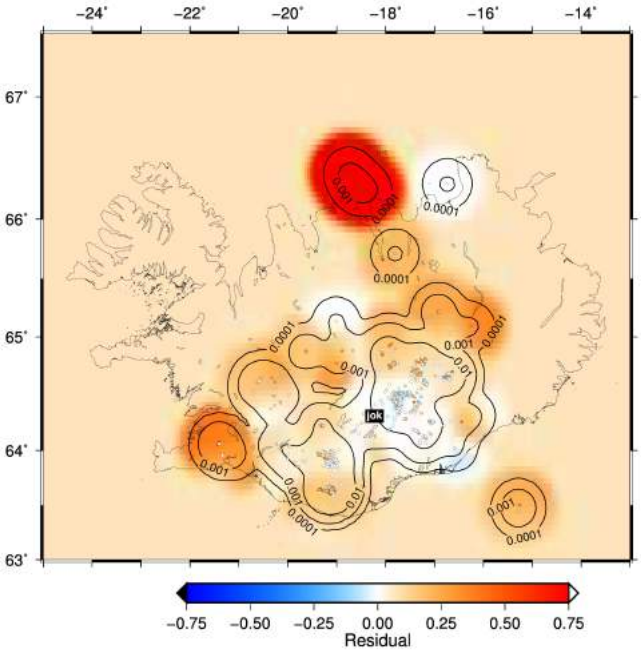

skr

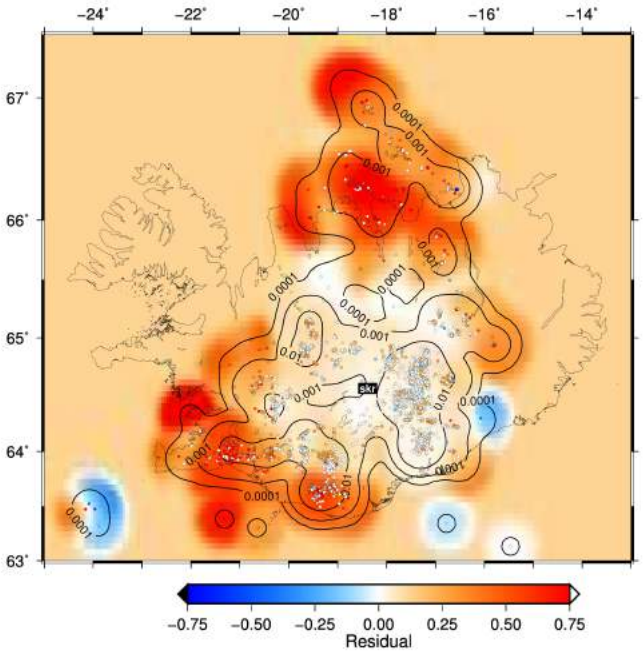

dyn

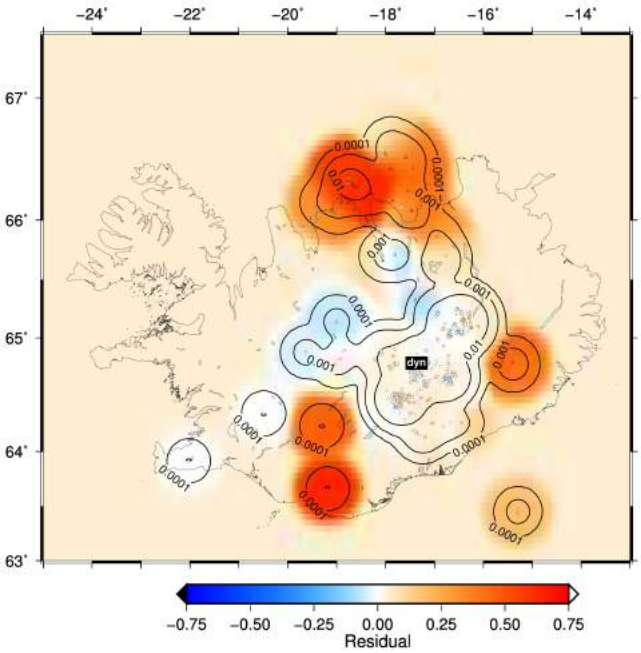

mko

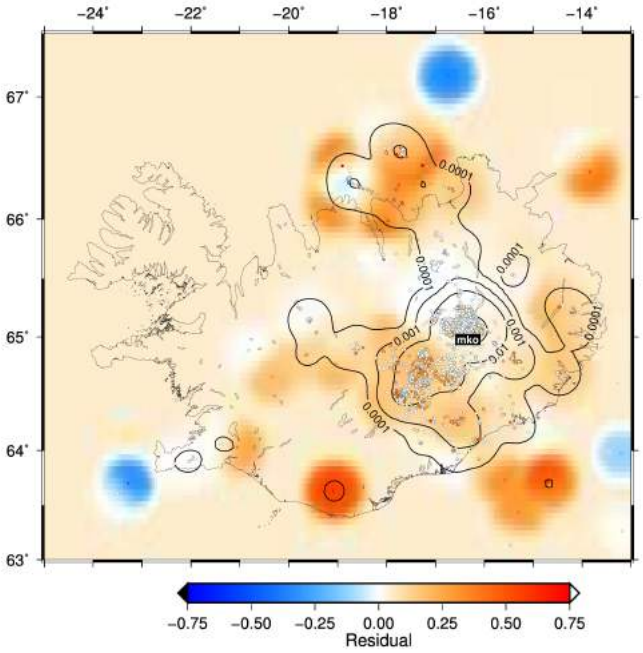

vsh

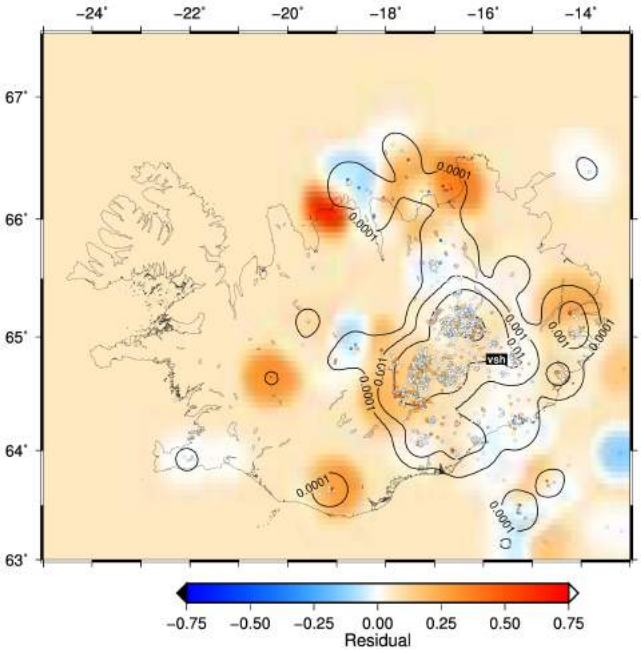

bru

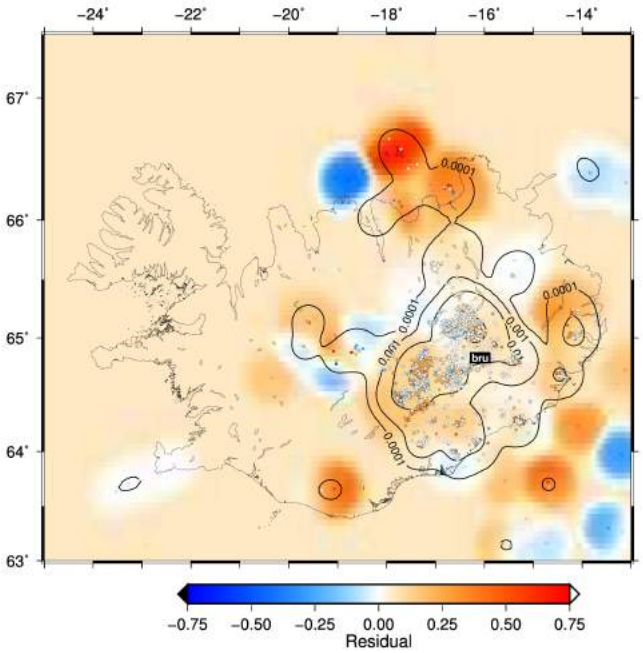

kre

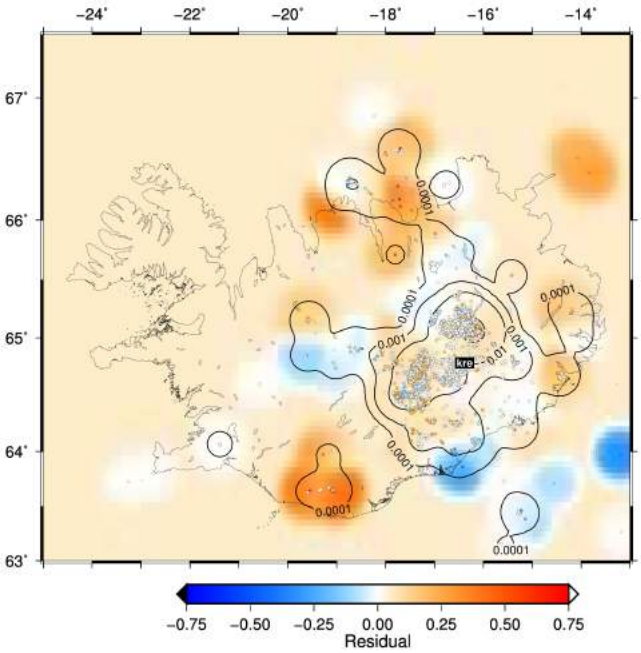

hva

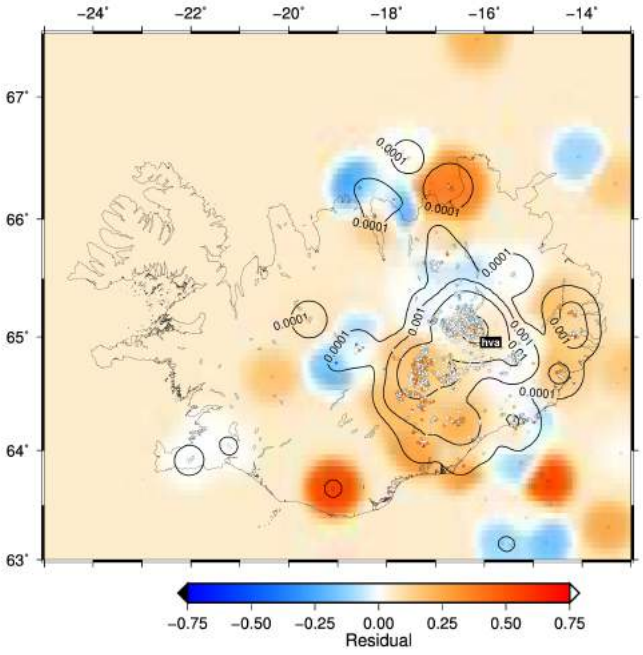
−24°
−22°
−20°
−18°
−16°
−14°
67°
66°
65°
64°
63°
hva
0.0001
0.001
0.01
−0.75
−0.50
−0.25
0.00
0.25
0.50
0.75
Residual

ada

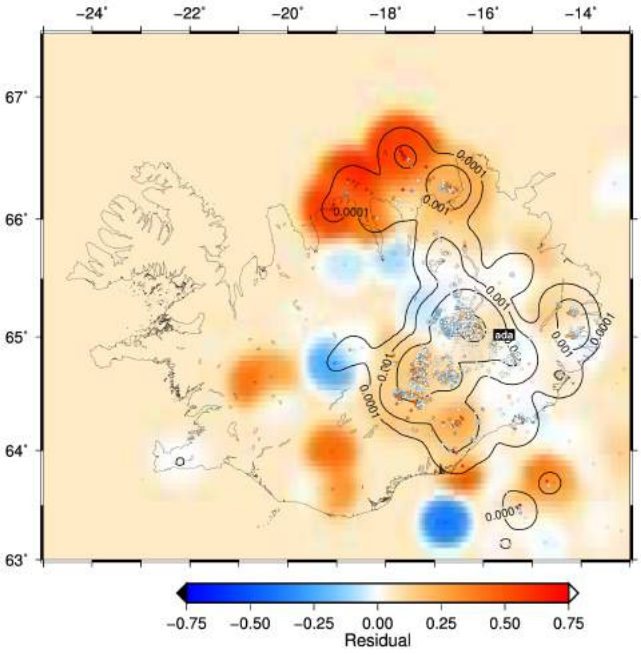
−24°
−22°
−20°
−18°
−16°
−14°
67°
66°
65°
64°
63°
ada
0.0001
0.001
0.01
−0.75
−0.50
−0.25
0.00
0.25
0.50
0.75
Residual

glu

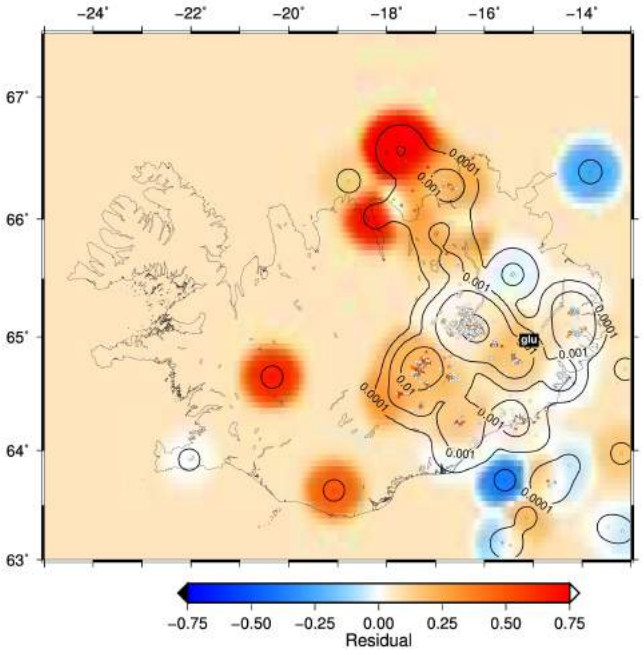
−24°
−22°
−20°
−18°
−16°
−14°
67°
66°
65°
64°
63°
glu
0.0001
0.001
0.01
−0.75
−0.50
−0.25
0.00
0.25
0.50
0.75
Residual

sig

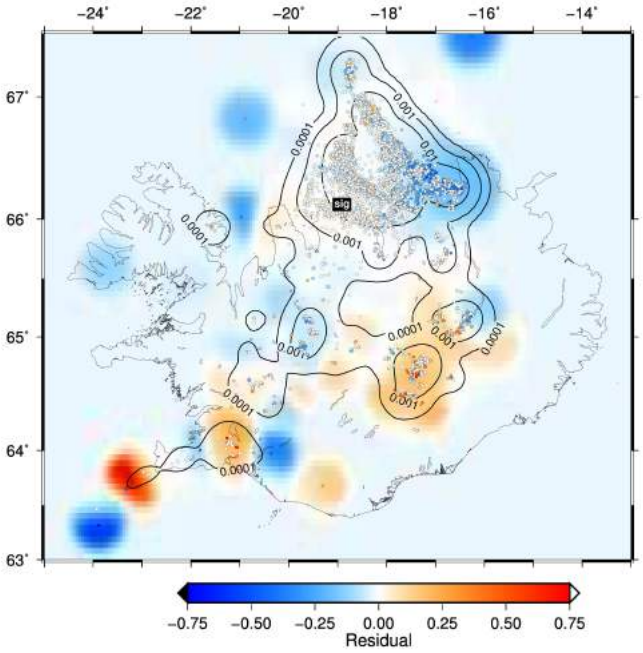

hla

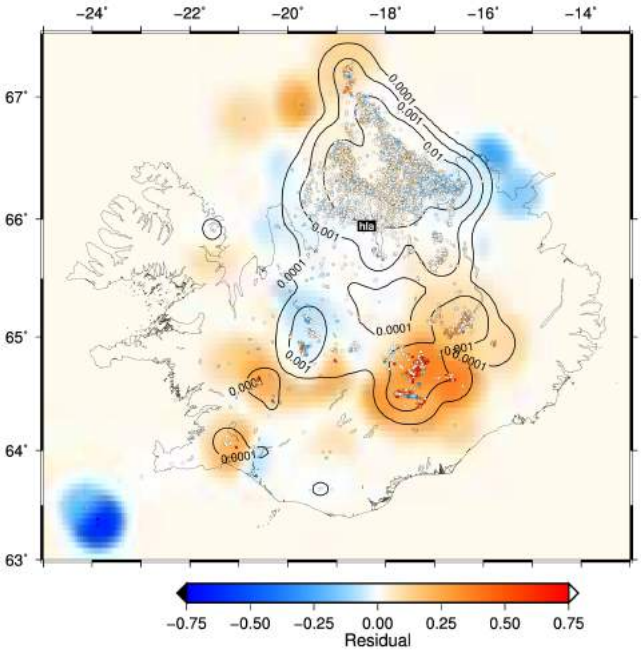

fla

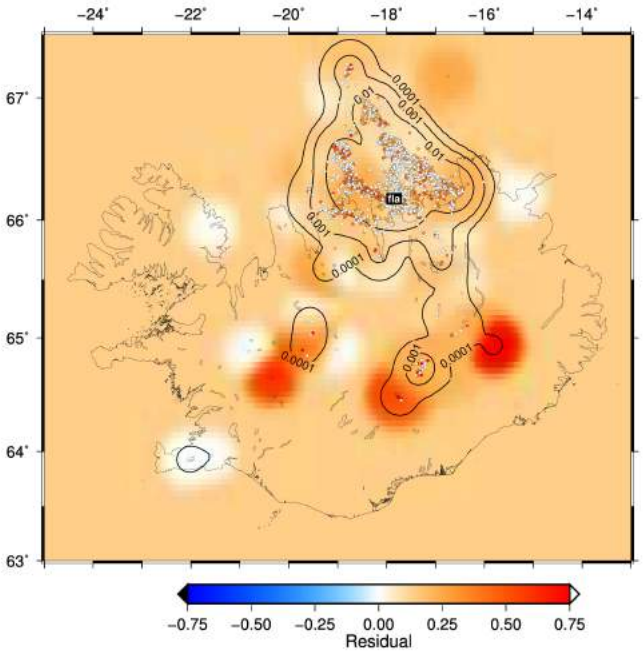

bre

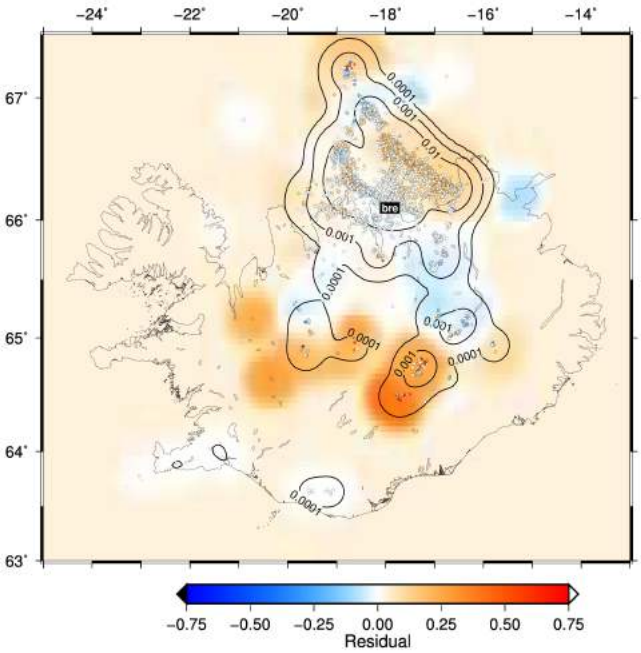

ren

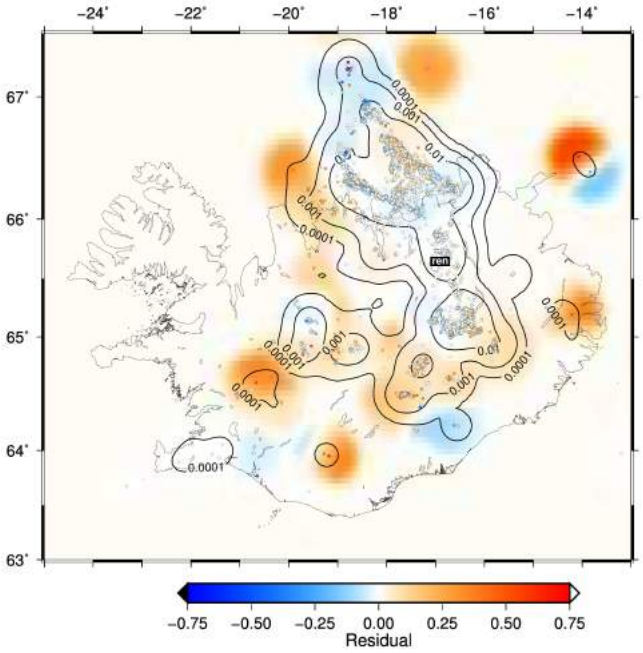

kvo

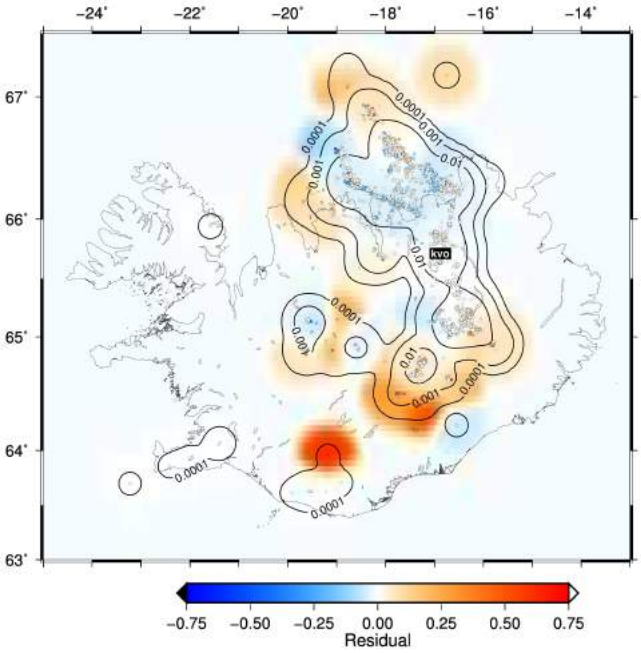

gha

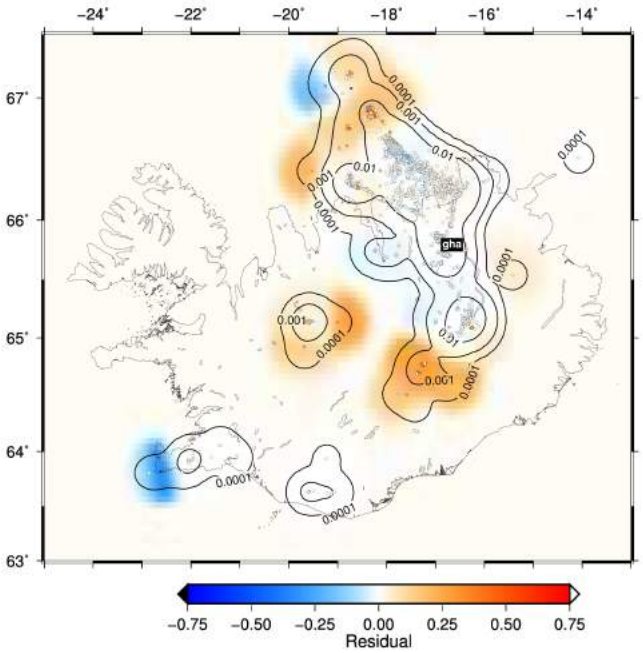

ghs

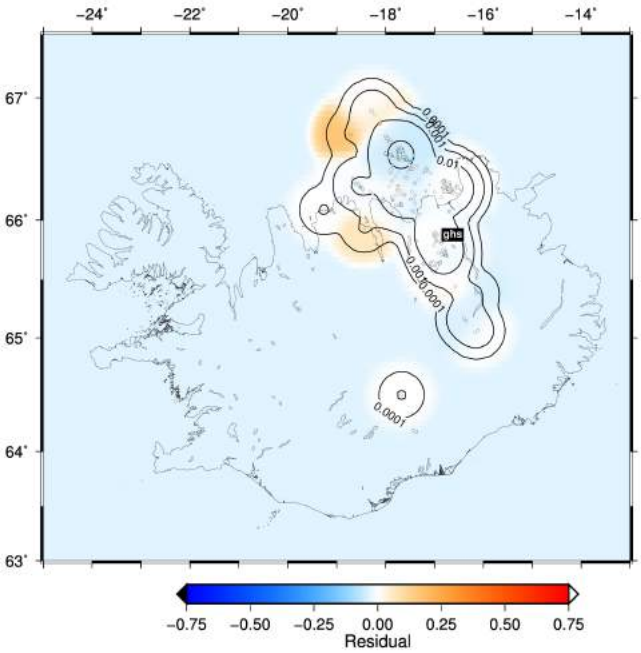

ski

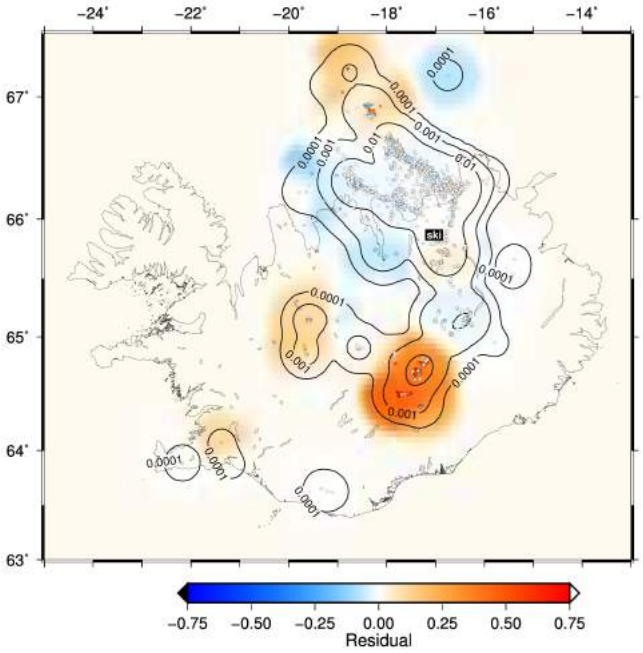

dim

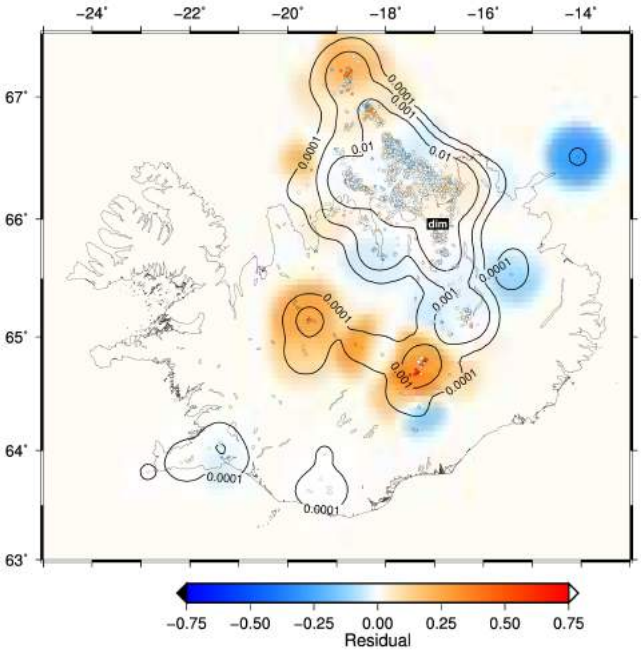

gra

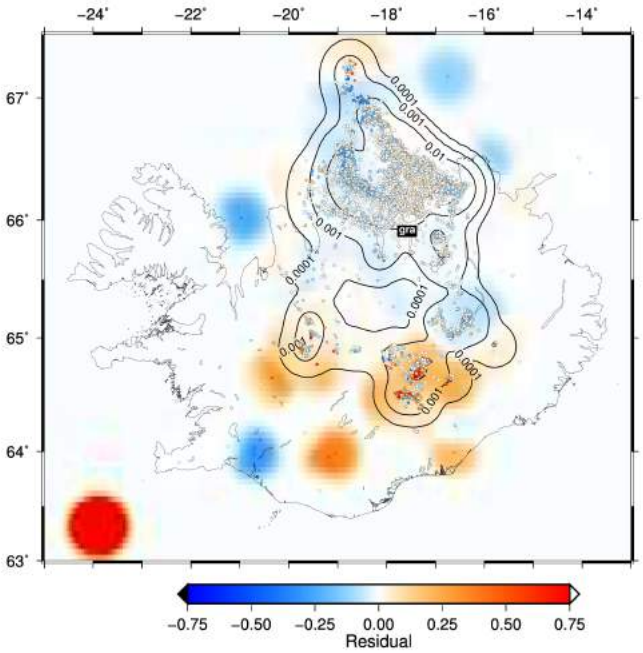

hed

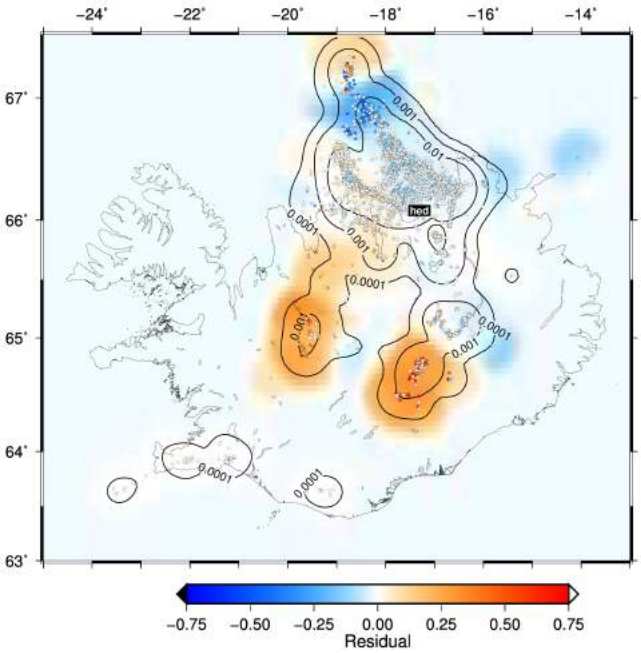

ask

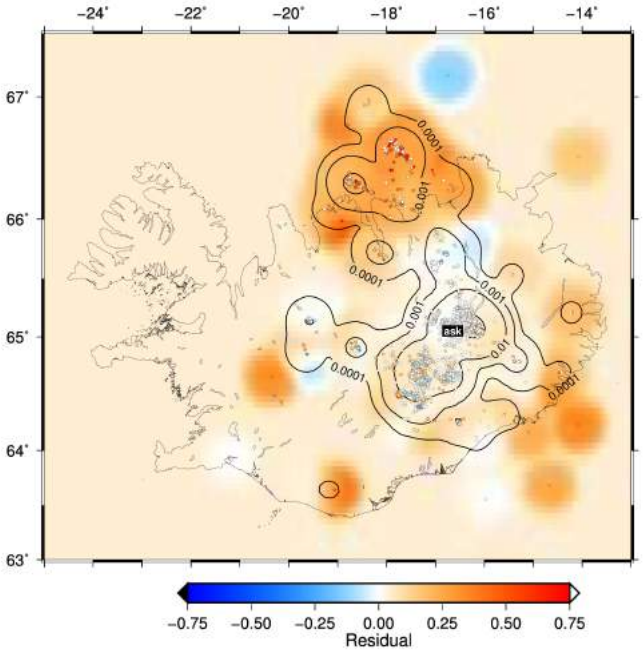

sva

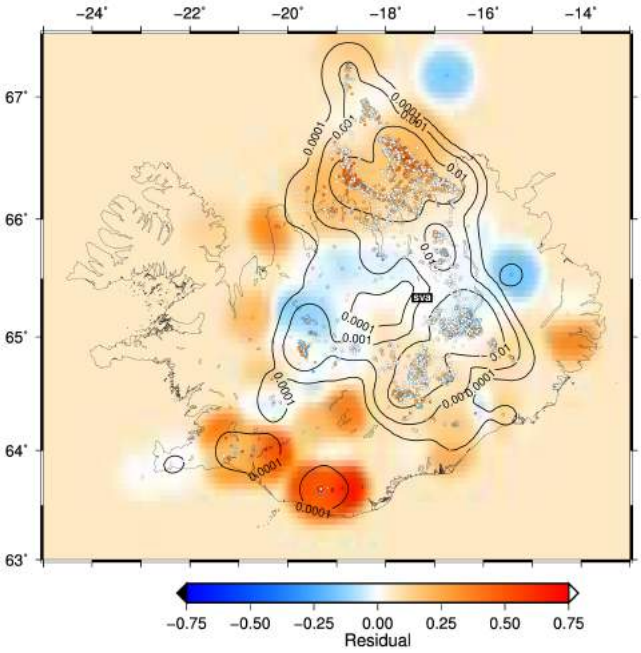

mel

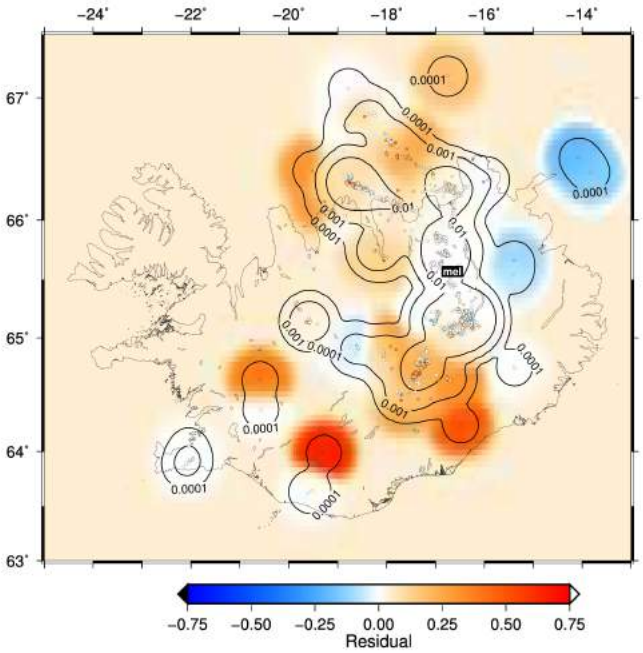

grs

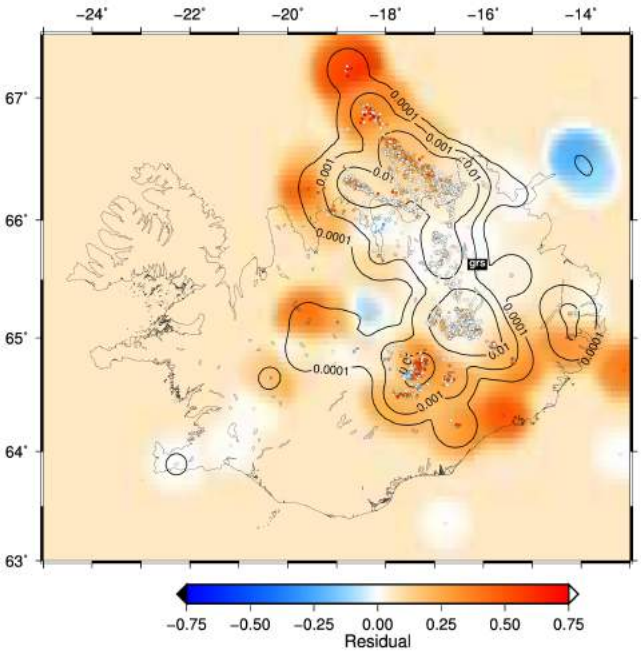

hrn

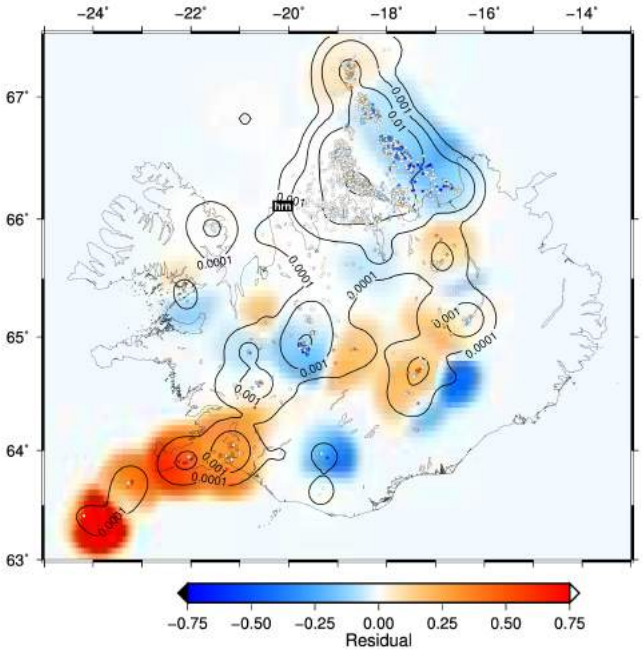

gri

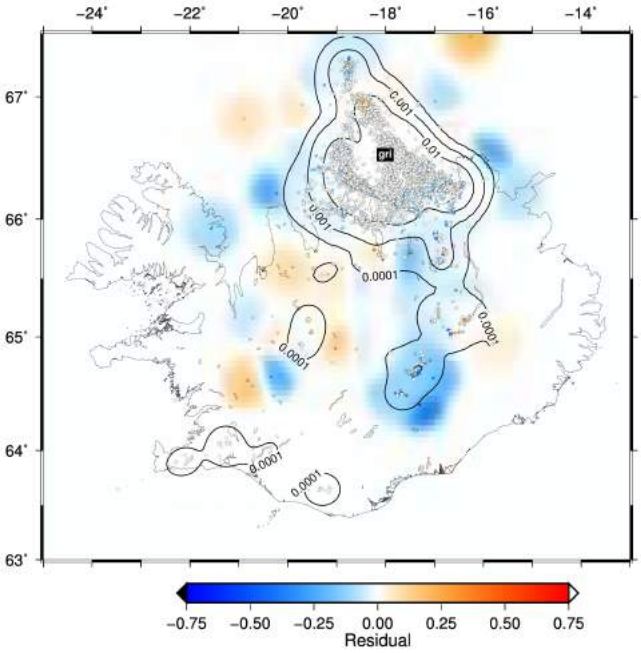

lei

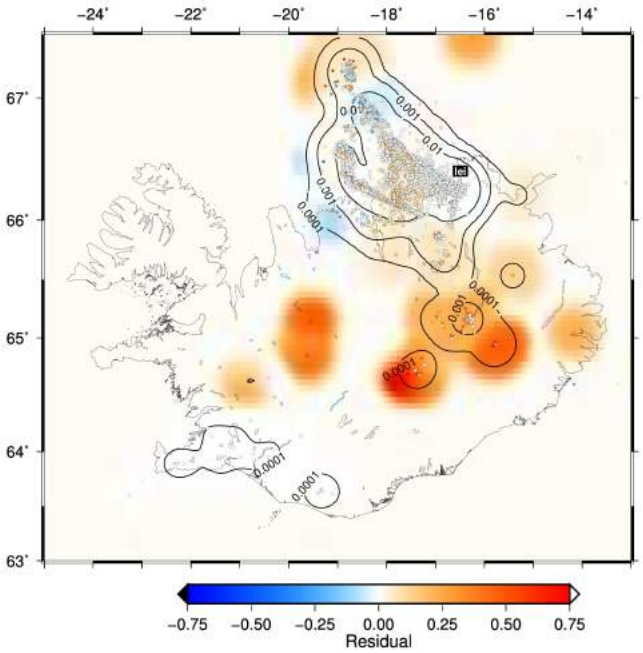

gil

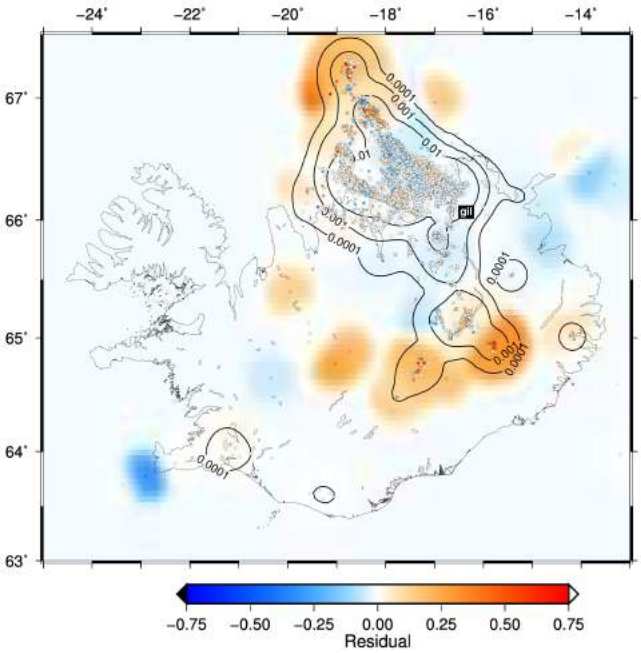

asb

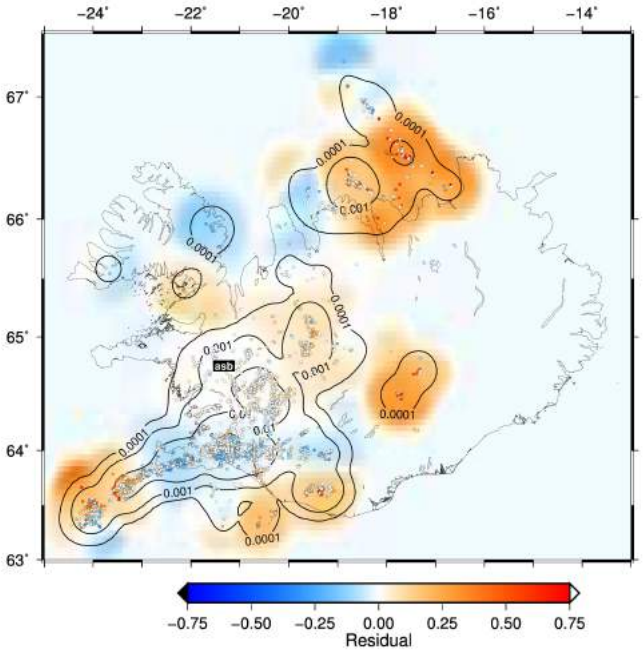

hve

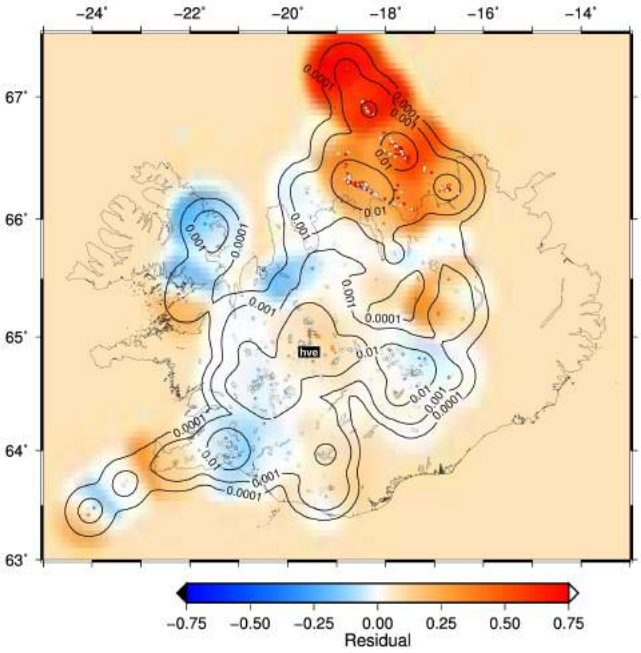

kud

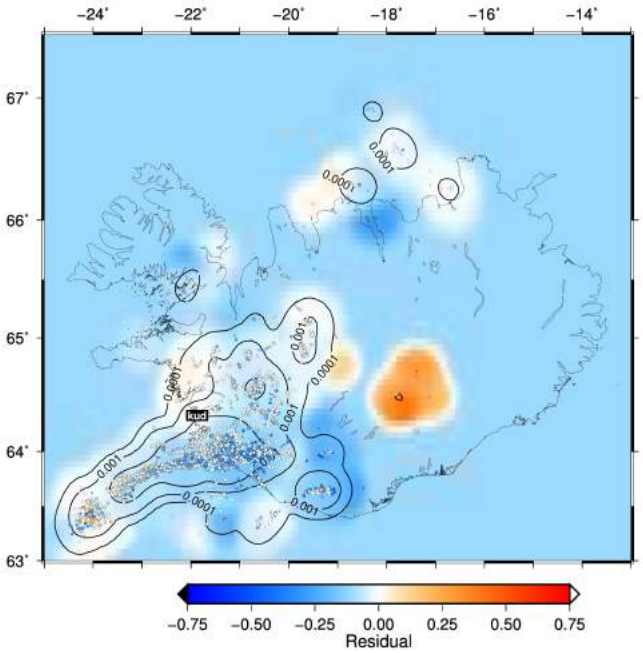

gyg

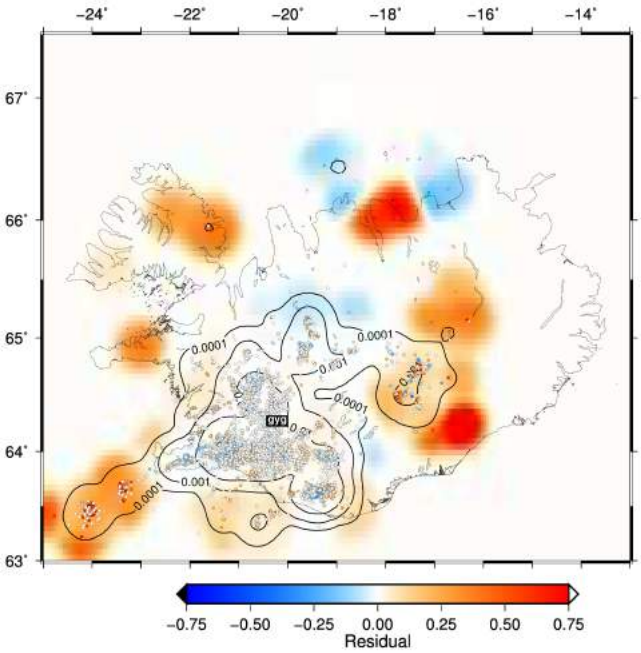

Appendix E

Auto-covariance of the stochastic component of ETTs

The following figures show auto-covariance functions of the estimated stochastic structural component of empirical travel times for both P-wave and S-wave residuals. Results from three adjacent stations are presented on each page with the station code indicated above each frame.

The structure of the auto-covariance is often complex, which is not surprising since this is a simple representation of the functions variation that assumes spatial stationarity. Nevertheless, the figures indicate the degree of variation (as variance) and have maximum amplitude around zero offset, often contained in a peak with a width of 3–15 km, roughly confined to the averaging scale used to estimate the deterministic component of the ETTs. In some cases there is a suggestion that some of the error may have been partially absorbed in the ETTs as a peak at zero offset, i.e. an incoherent peak. The structure of the P-wave and S-wave auto-covariance is often similar, suggesting a correlation of P- and S-wave residuals on small scales.

P-wave

S-wave

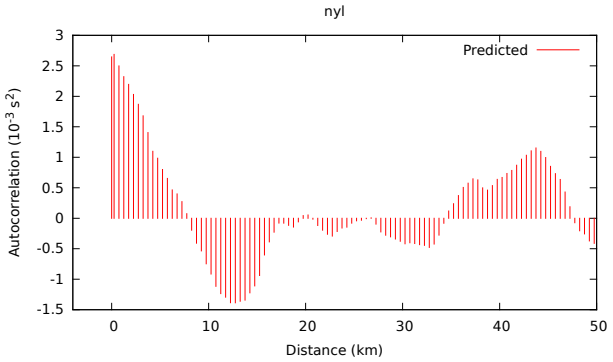

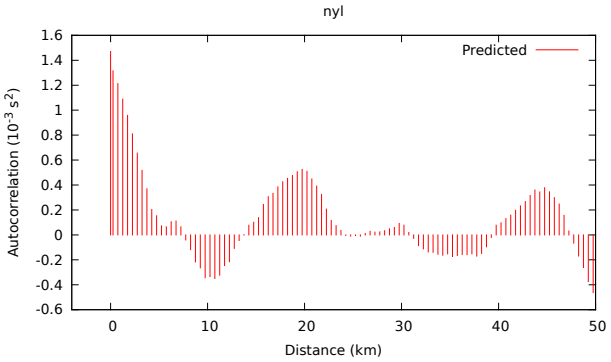

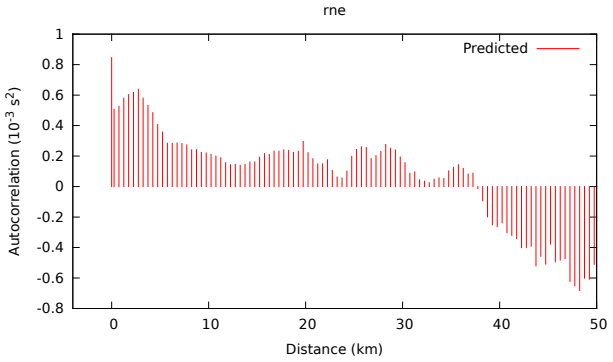

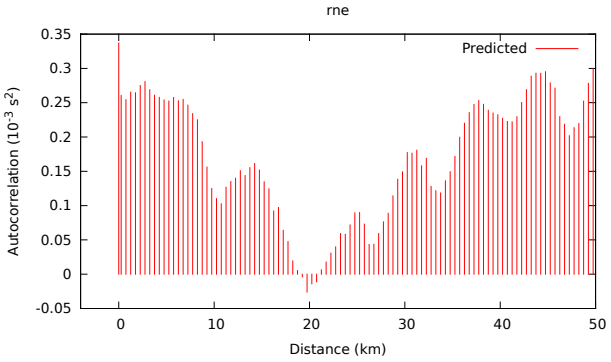

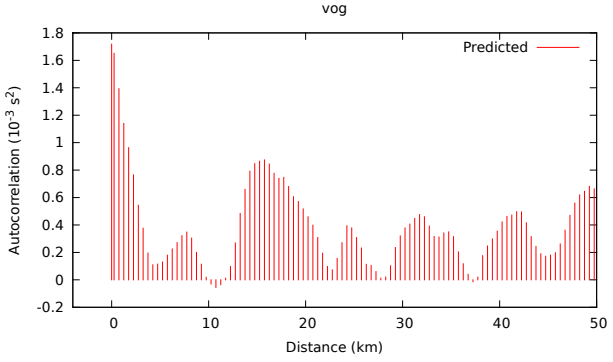

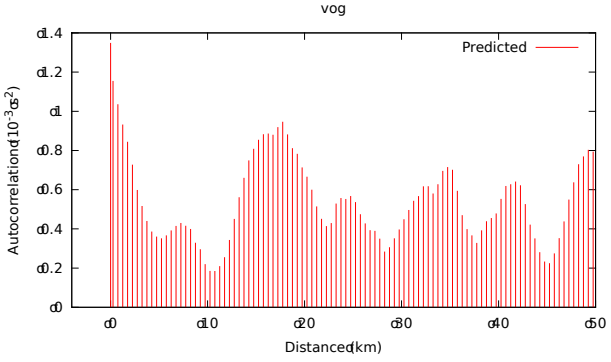

E2

P-wave

S-wave

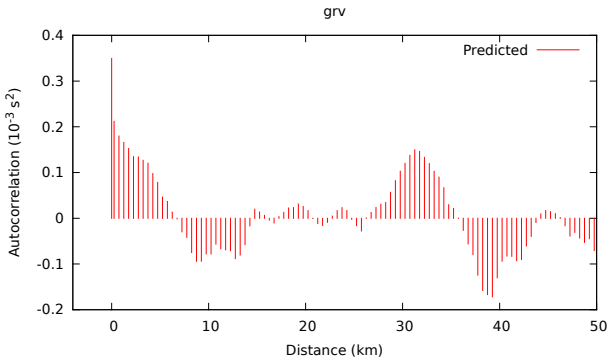
grv
Predicted
Autocorrelation (10^{-3} s^2)
Distance (km)

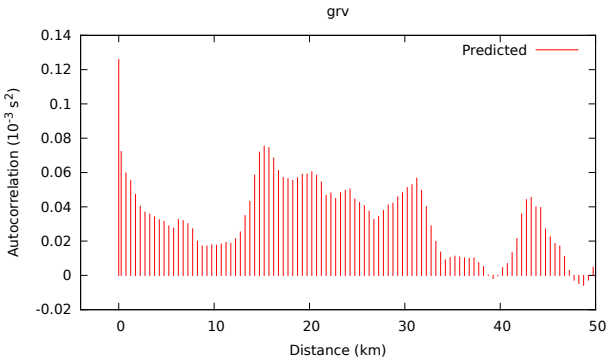
grv
Predicted
Autocorrelation (10^{-3} s^2)
Distance (km)

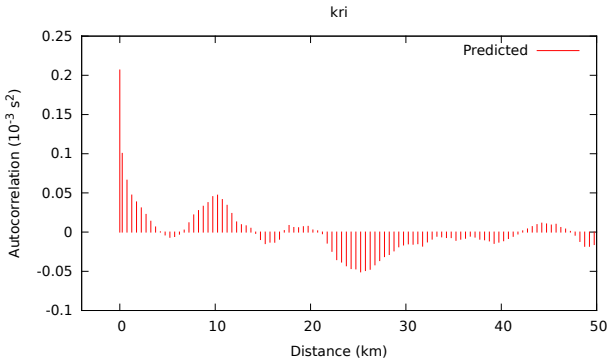
kri
Predicted
Autocorrelation (10^{-3} s^2)
Distance (km)

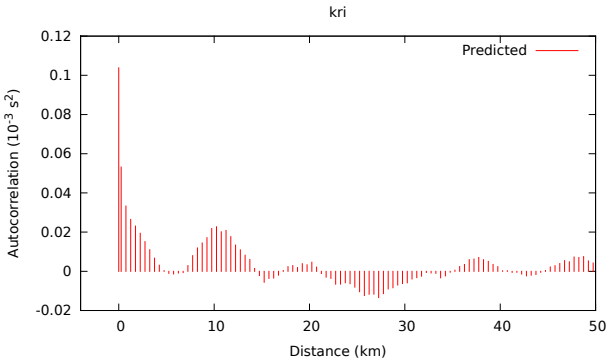
kri
Predicted
Autocorrelation (10^{-3} s^2)
Distance (km)

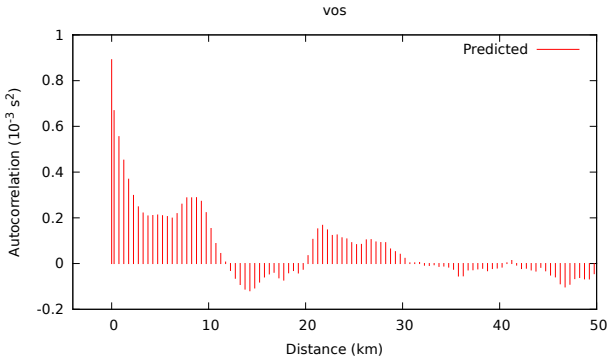
vos
Predicted
Autocorrelation (10^{-3} s^2)
Distance (km)

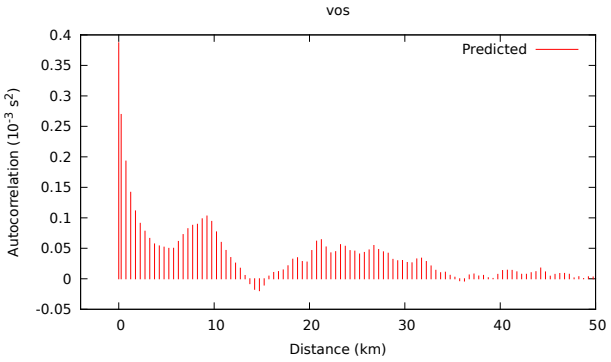
vos
Predicted
Autocorrelation (10^{-3} s^2)
Distance (km)

P-wave

S-wave

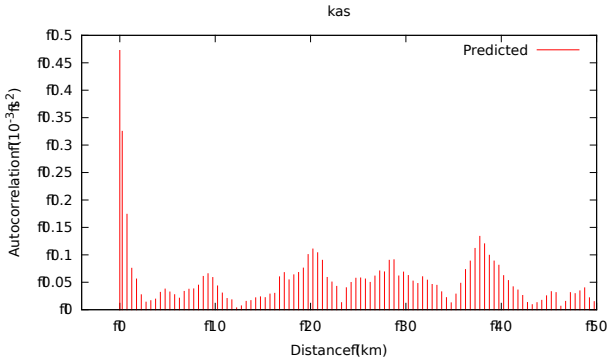
kas
Predicted
Autocorrelation (10^-3 s^2)
Distance (km)

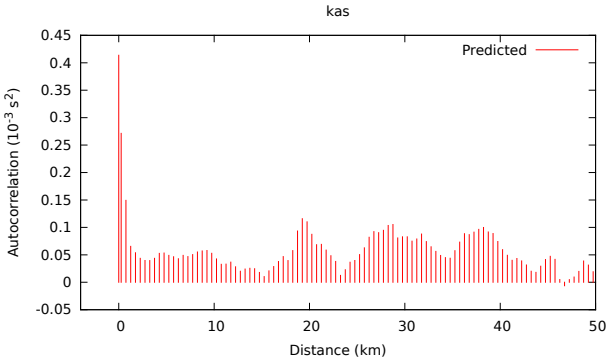
kas
Predicted
Autocorrelation (10^-3 s^2)
Distance (km)

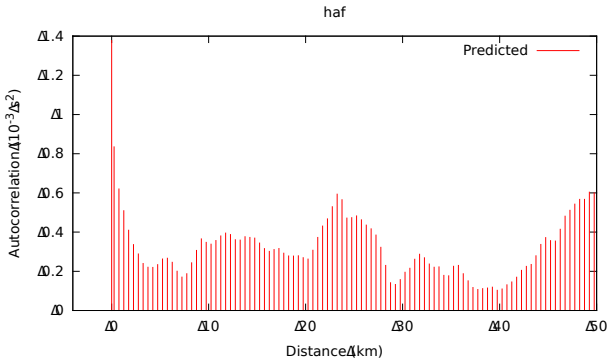
haf
Predicted
Autocorrelation (10^-3 s^2)
Distance (km)

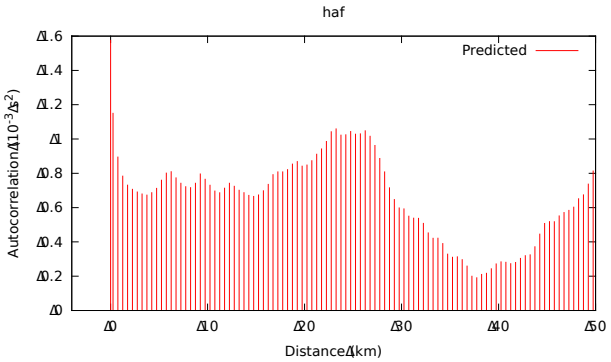
haf
Predicted
Autocorrelation (10^-3 s^2)
Distance (km)

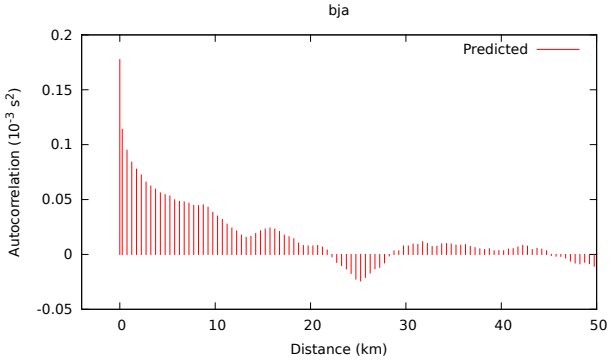
bja
Predicted
Autocorrelation (10^-3 s^2)
Distance (km)

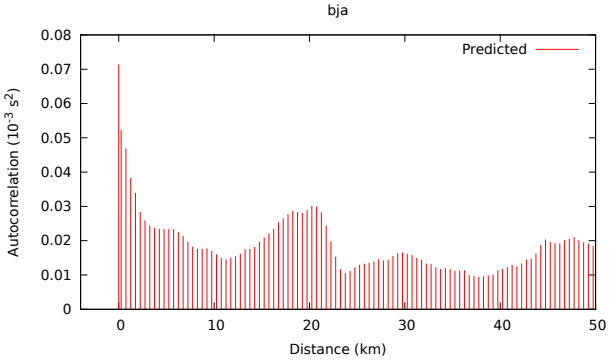
bja
Predicted
Autocorrelation (10^-3 s^2)
Distance (km)

P-wave

S-wave

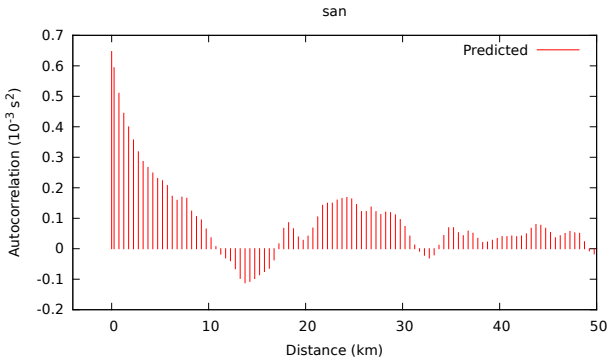
san
Predicted
Autocorrelation (10^{-3} s^2)
Distance (km)

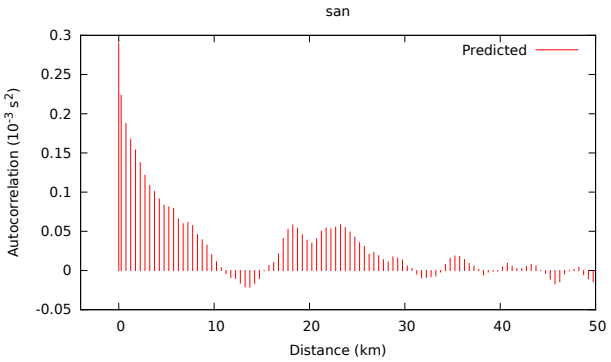
san
Predicted
Autocorrelation (10^{-3} s^2)
Distance (km)

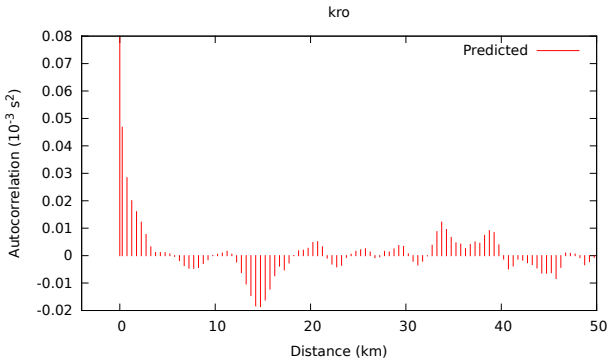
kro
Predicted
Autocorrelation (10^{-3} s^2)
Distance (km)

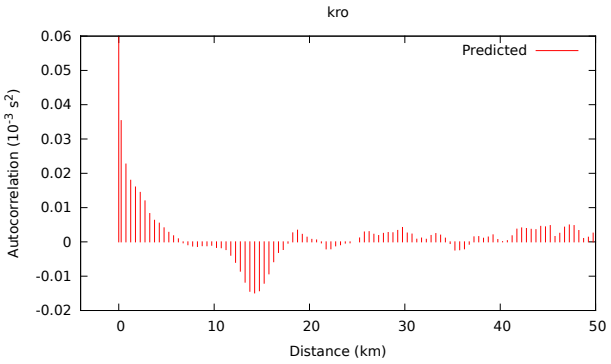
kro
Predicted
Autocorrelation (10^{-3} s^2)
Distance (km)

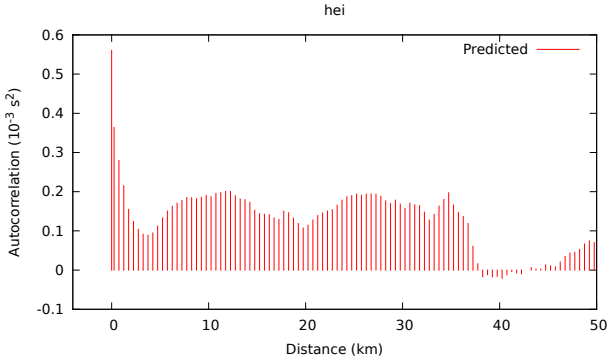
hei
Predicted
Autocorrelation (10^{-3} s^2)
Distance (km)

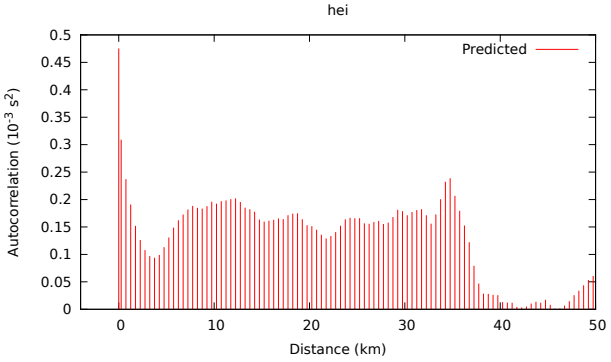
hei
Predicted
Autocorrelation (10^{-3} s^2)
Distance (km)

P-wave

S-wave

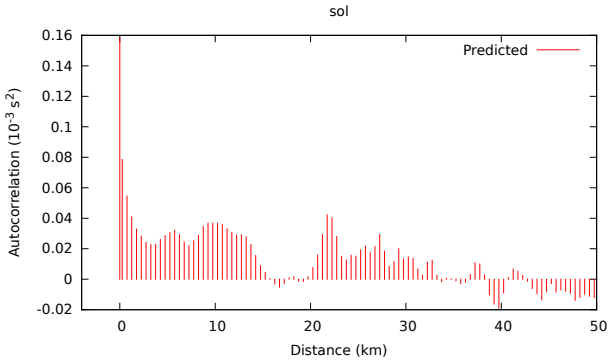
sol
Predicted
Autocorrelation (10^{-3} s^2)
Distance (km)

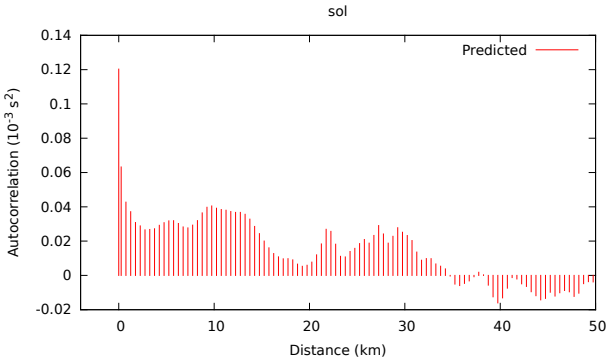
sol
Predicted
Autocorrelation (10^{-3} s^2)
Distance (km)

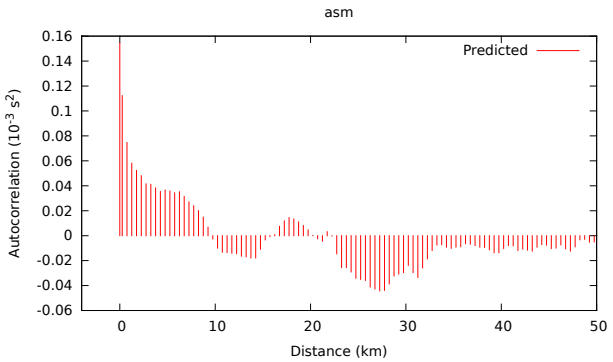
asm
Predicted
Autocorrelation (10^{-3} s^2)
Distance (km)

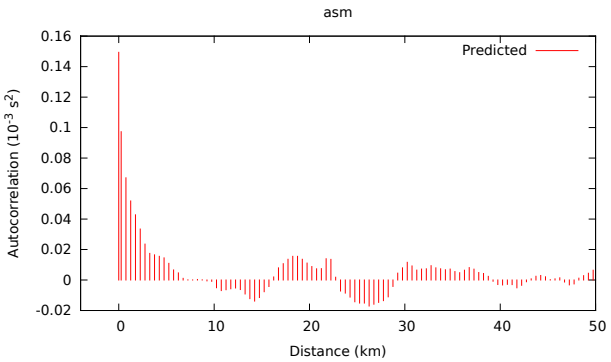
asm
Predicted
Autocorrelation (10^{-3} s^2)
Distance (km)

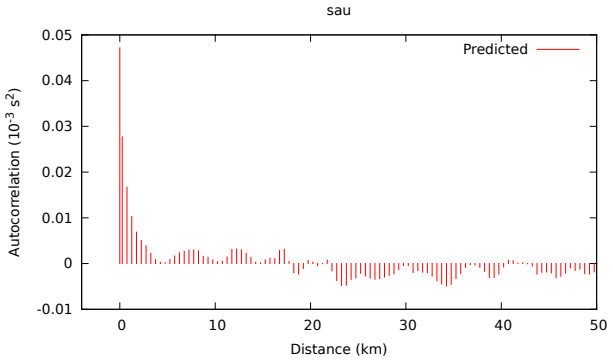
sau
Predicted
Autocorrelation (10^{-3} s^2)
Distance (km)

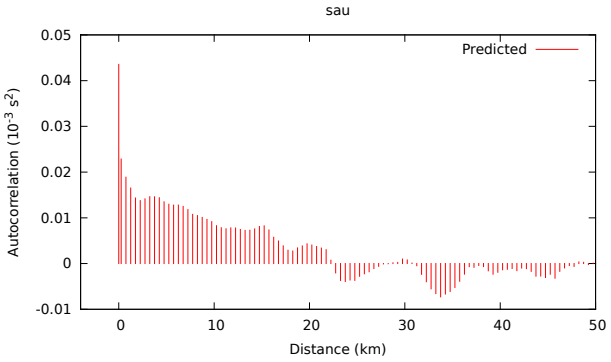
sau
Predicted
Autocorrelation (10^{-3} s^2)
Distance (km)

P-wave

S-wave

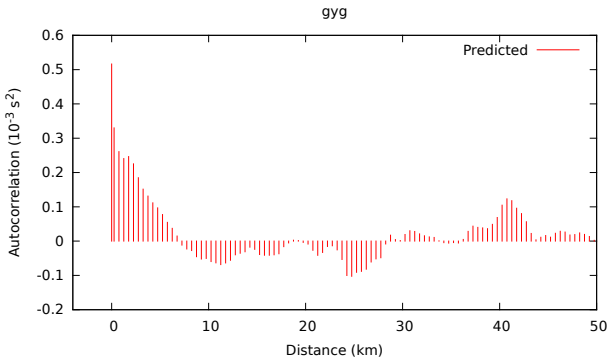
gyg
Predicted
Autocorrelation (10^{-3} s^2)
Distance (km)

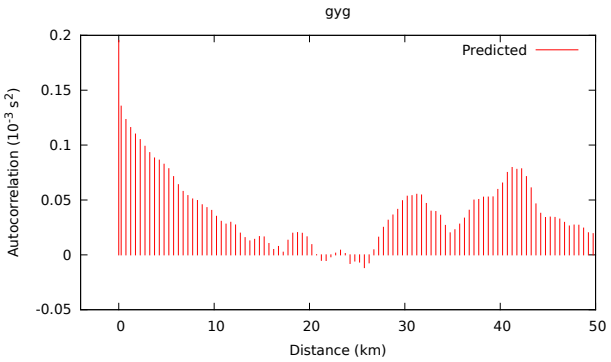
gyg
Predicted
Autocorrelation (10^{-3} s^2)
Distance (km)

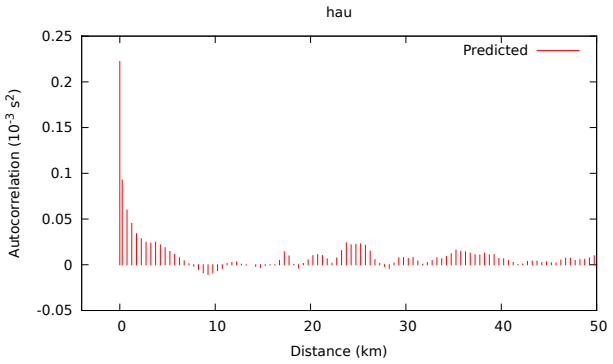
hau
Predicted
Autocorrelation (10^{-3} s^2)
Distance (km)

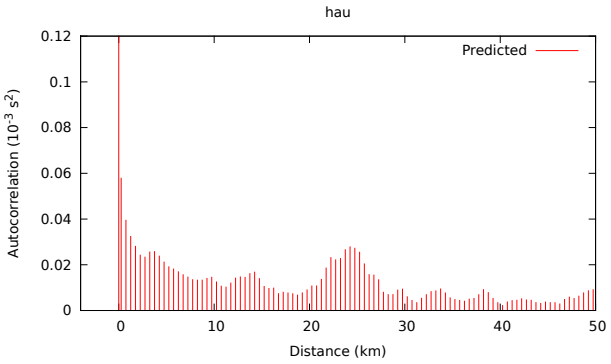
hau
Predicted
Autocorrelation (10^{-3} s^2)
Distance (km)

P-wave

S-wave

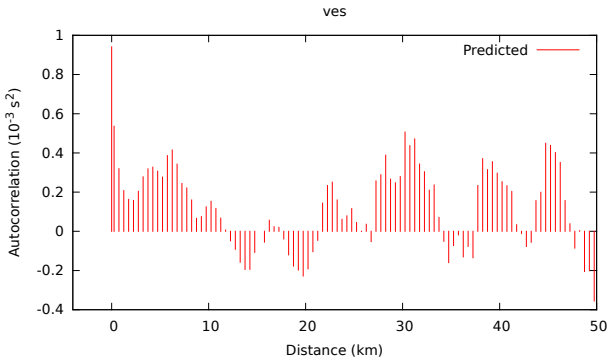
ves
Predicted
Autocorrelation (10-3 s2)
Distance (km)

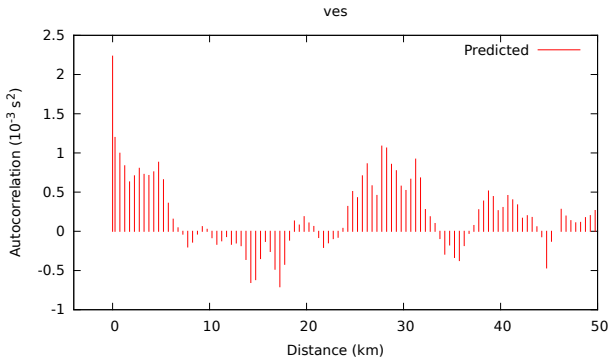
ves
Predicted
Autocorrelation (10-3 s2)
Distance (km)

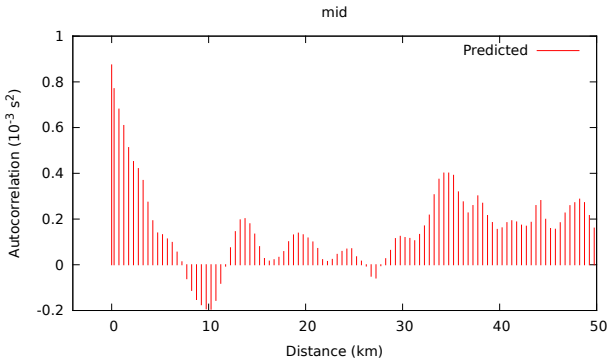
mid
Predicted
Autocorrelation (10-3 s2)
Distance (km)

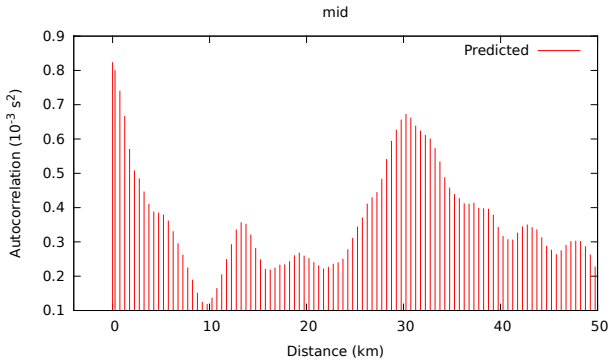
mid
Predicted
Autocorrelation (10-3 s2)
Distance (km)

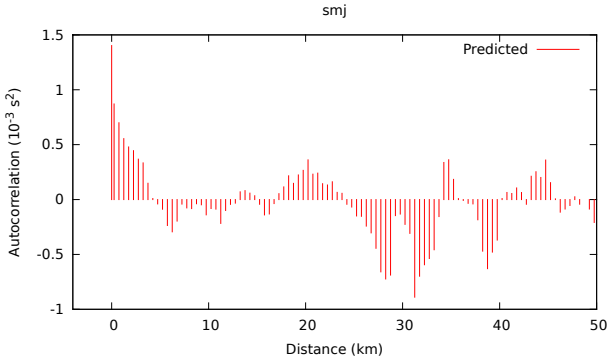
smj
Predicted
Autocorrelation (10-3 s2)
Distance (km)

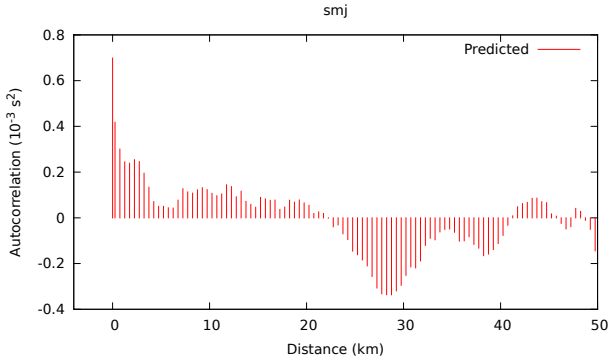
smj
Predicted
Autocorrelation (10-3 s2)
Distance (km)

P-wave

S-wave

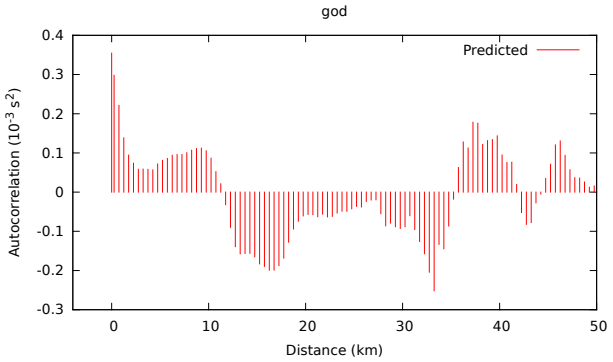
god
Predicted
Autocorrelation (10^{-3} s^2)
Distance (km)

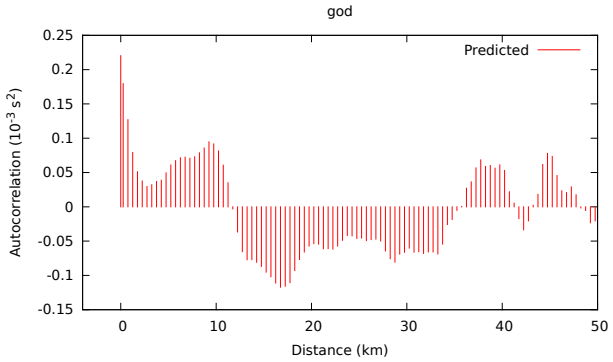
god
Predicted
Autocorrelation (10^{-3} s^2)
Distance (km)

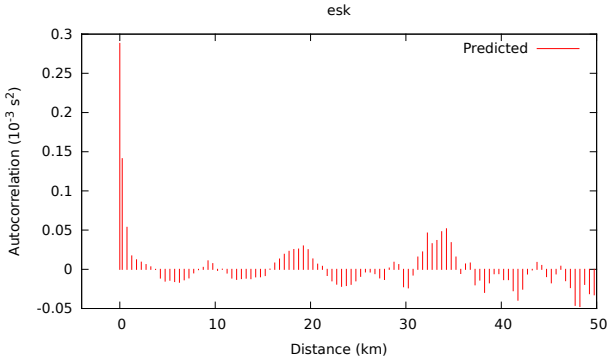
esk
Predicted
Autocorrelation (10^{-3} s^2)
Distance (km)

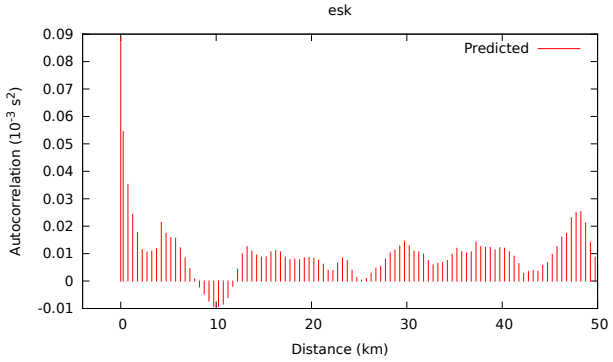
esk
Predicted
Autocorrelation (10^{-3} s^2)
Distance (km)

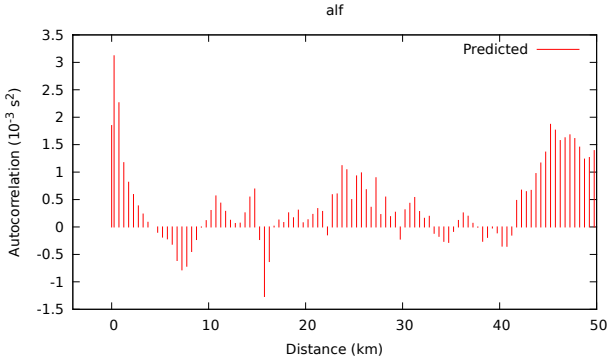
alf
Predicted
Autocorrelation (10^{-3} s^2)
Distance (km)

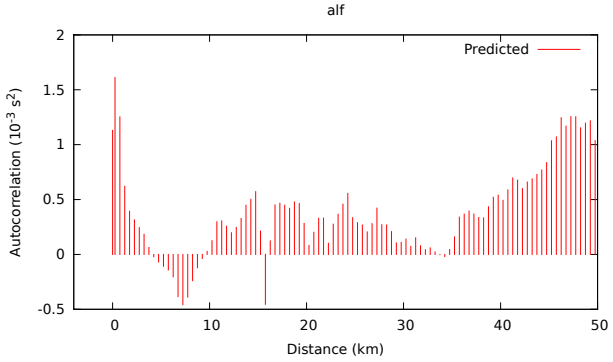
alf
Predicted
Autocorrelation (10^{-3} s^2)
Distance (km)

P-wave

S-wave

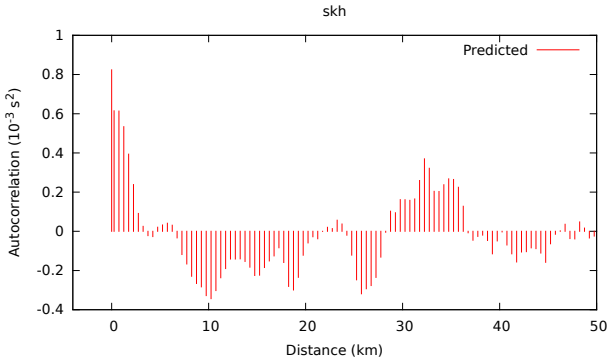
skh
Predicted
Autocorrelation (10^{-3} s^2)
Distance (km)

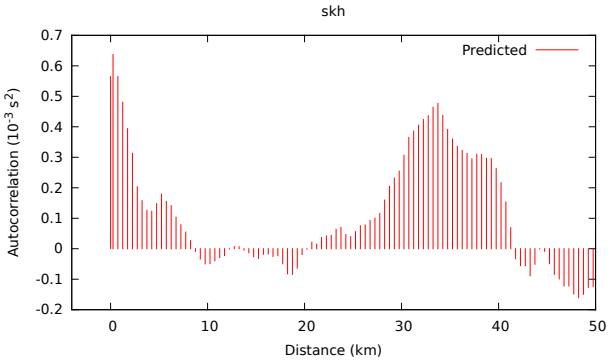
skh
Predicted
Autocorrelation (10^{-3} s^2)
Distance (km)

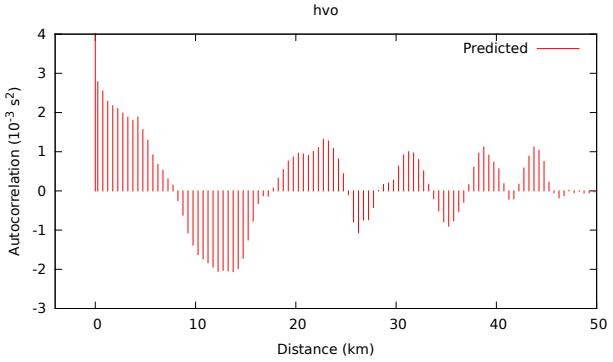
hvo
Predicted
Autocorrelation (10^{-3} s^2)
Distance (km)

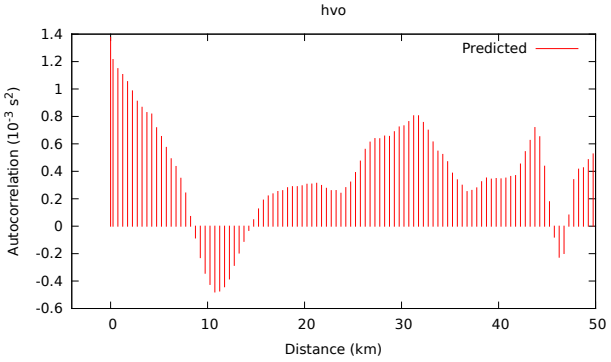
hvo
Predicted
Autocorrelation (10^{-3} s^2)
Distance (km)

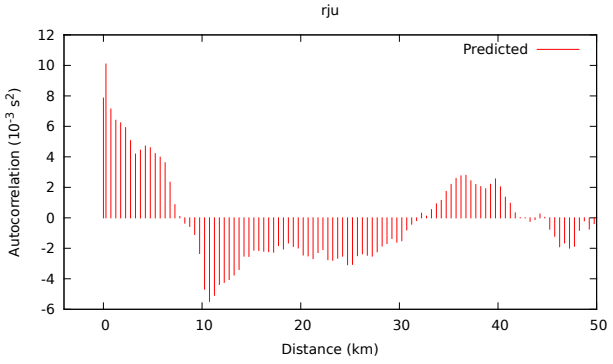
rju
Predicted
Autocorrelation (10^{-3} s^2)
Distance (km)

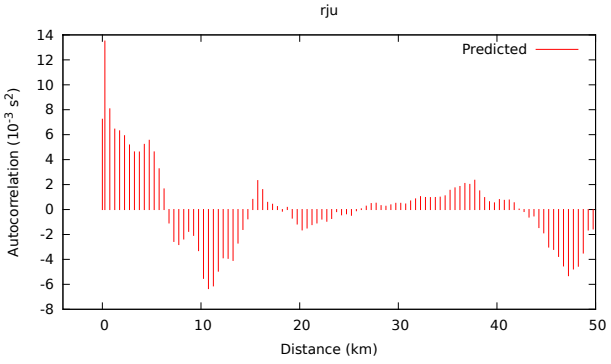
rju
Predicted
Autocorrelation (10^{-3} s^2)
Distance (km)

P-wave

S-wave

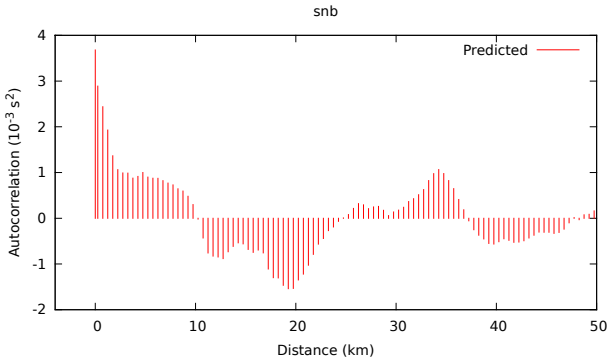
snb
Predicted
Autocorrelation (10^{-3} s^2)
Distance (km)

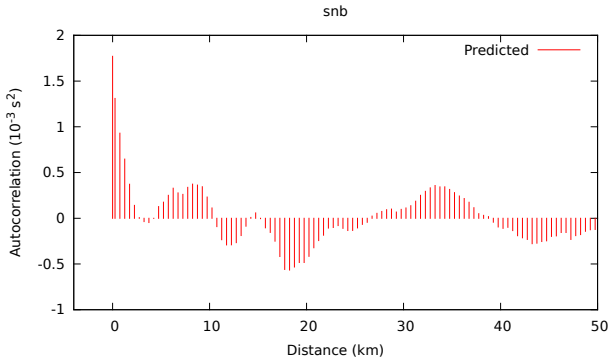
snb
Predicted
Autocorrelation (10^{-3} s^2)
Distance (km)

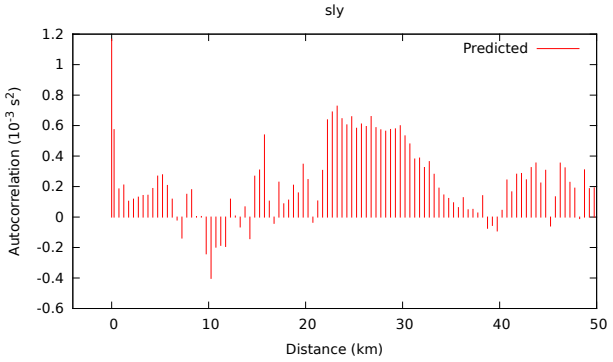
sly
Predicted
Autocorrelation (10^{-3} s^2)
Distance (km)

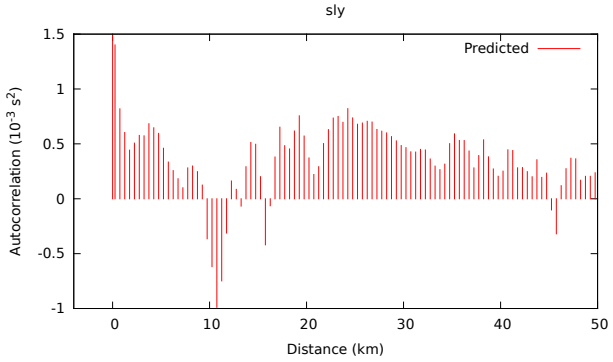
sly
Predicted
Autocorrelation (10^{-3} s^2)
Distance (km)

P-wave

S-wave

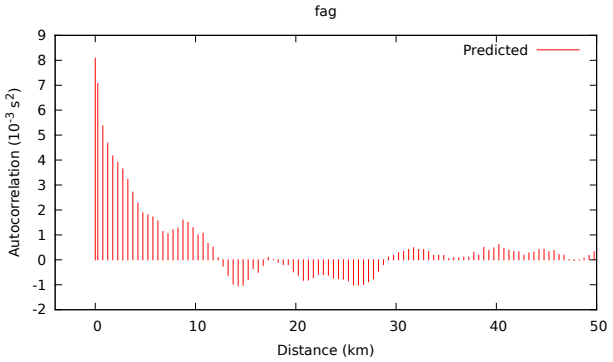
fag
Predicted
Autocorrelation (10-3 s2)
Distance (km)

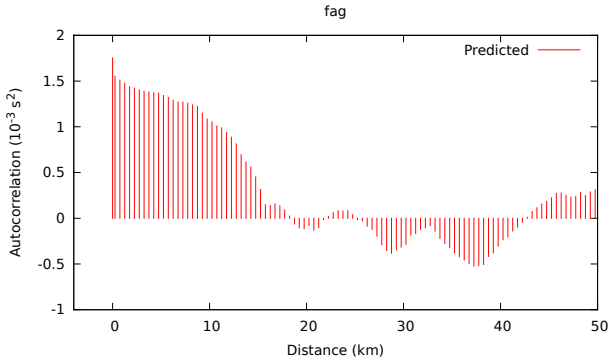
fag
Predicted
Autocorrelation (10-3 s2)
Distance (km)

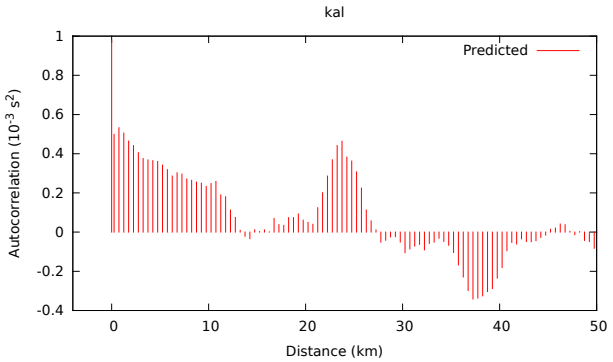
kal
Predicted
Autocorrelation (10-3 s2)
Distance (km)

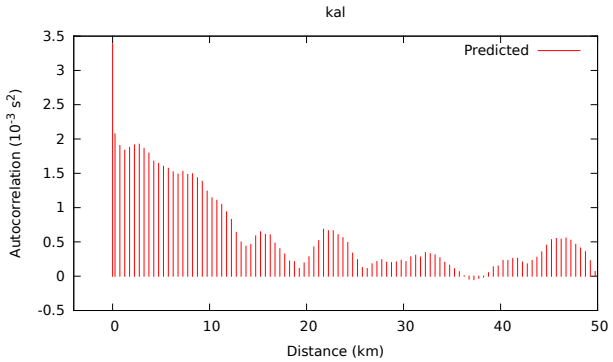
kal
Predicted
Autocorrelation (10-3 s2)
Distance (km)

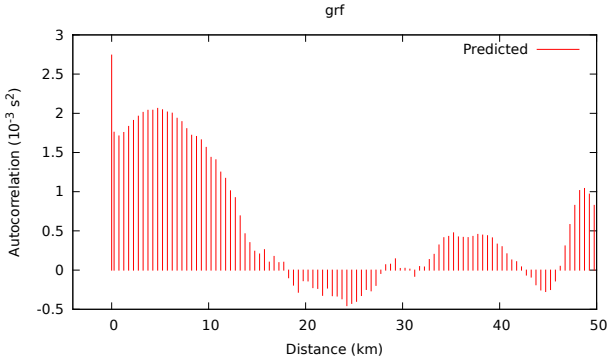
grf
Predicted
Autocorrelation (10-3 s2)
Distance (km)

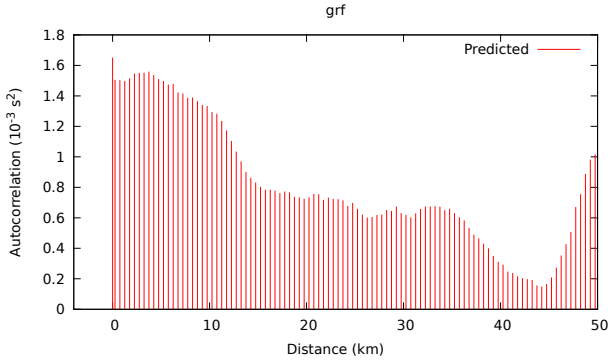
grf
Predicted
Autocorrelation (10-3 s2)
Distance (km)

P-wave

S-wave

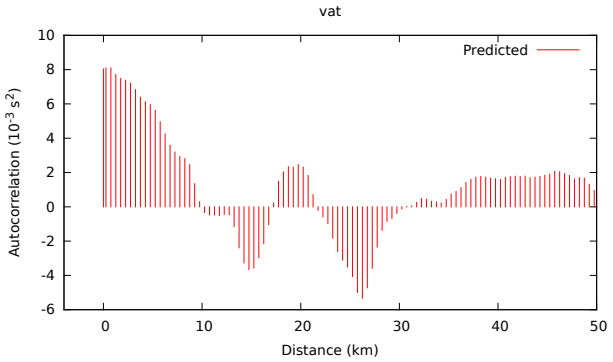
vat
Predicted
Autocorrelation (10^{-3} s^2)
Distance (km)

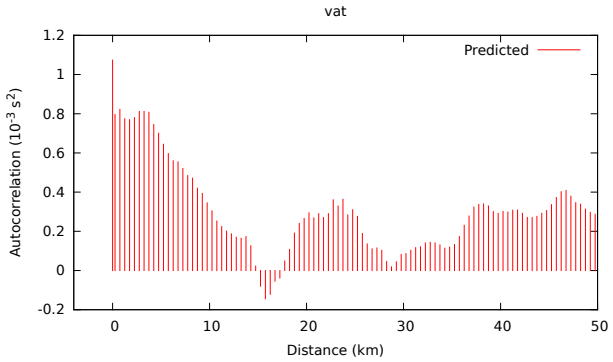
vat
Predicted
Autocorrelation (10^{-3} s^2)
Distance (km)

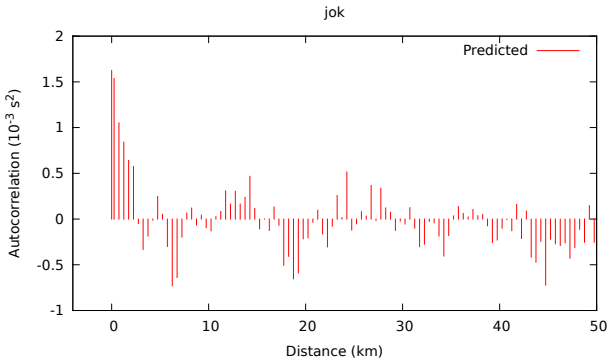
jok
Predicted
Autocorrelation (10^{-3} s^2)
Distance (km)

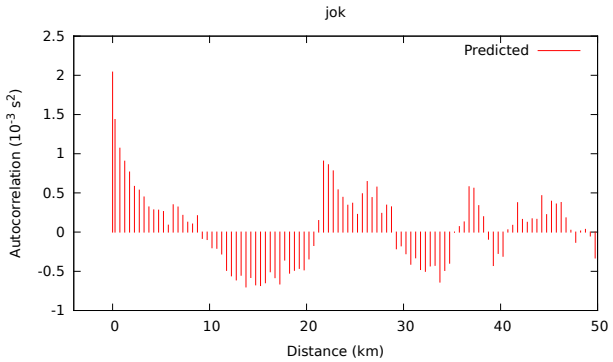
jok
Predicted
Autocorrelation (10^{-3} s^2)
Distance (km)

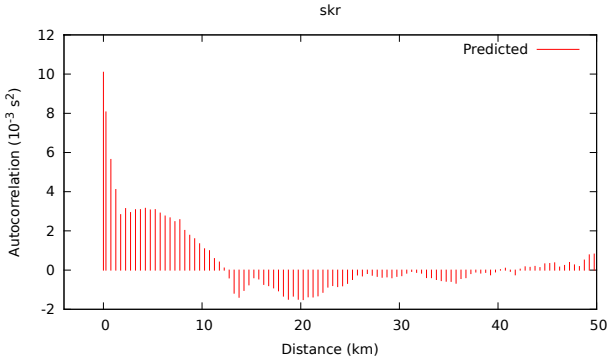
skr
Predicted
Autocorrelation (10^{-3} s^2)
Distance (km)

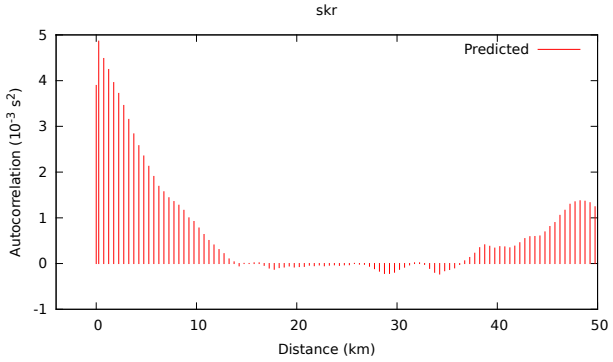
skr
Predicted
Autocorrelation (10^{-3} s^2)
Distance (km)

P-wave

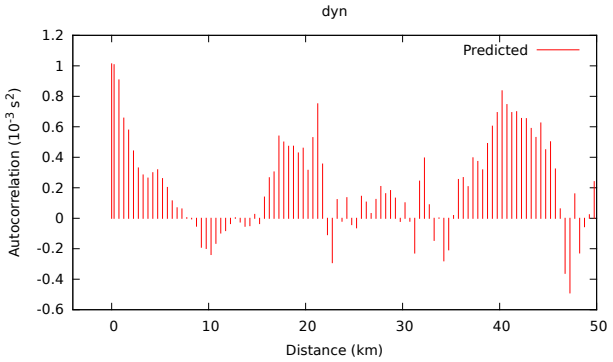
dyn
Predicted
Autocorrelation (10^{-3} s^2)
Distance (km)
1.2
1
0.8
0.6
0.4
0.2
0
-0.2
-0.4
-0.6
0
10
20
30
40
50

S-wave

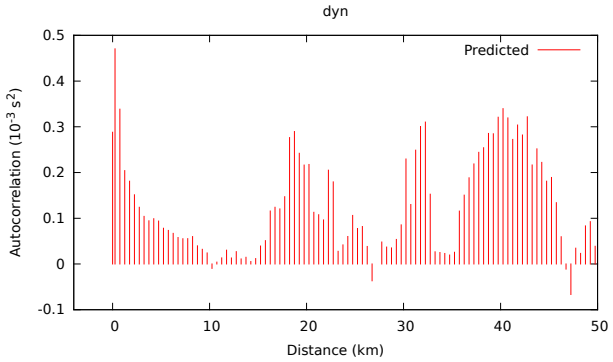
dyn
Predicted
Autocorrelation (10^{-3} s^2)
Distance (km)
0.5
0.4
0.3
0.2
0.1
0
-0.1
0
10
20
30
40
50

P-wave

S-wave

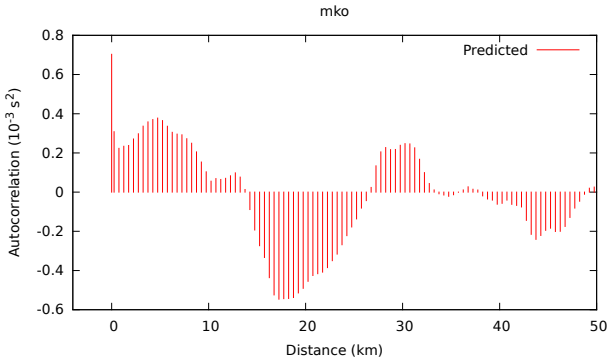
mko
Predicted
Autocorrelation (10-3 s2)
Distance (km)

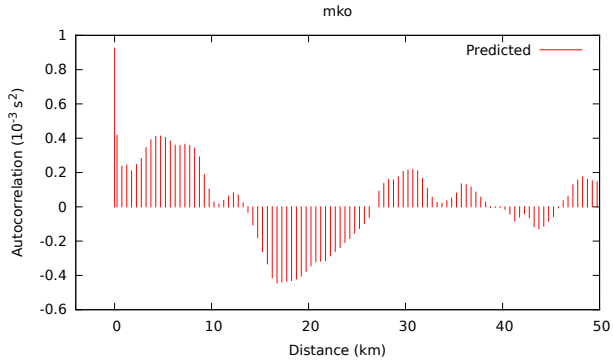
mko
Predicted
Autocorrelation (10-3 s2)
Distance (km)

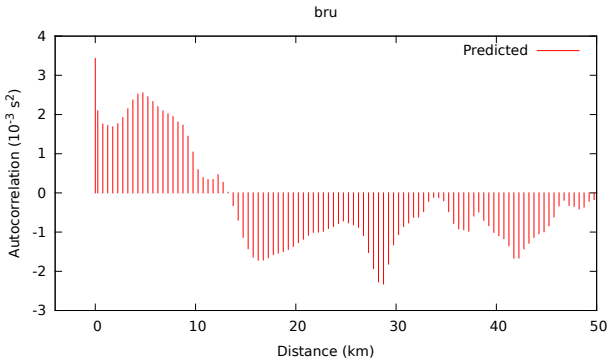
bru
Predicted
Autocorrelation (10-3 s2)
Distance (km)

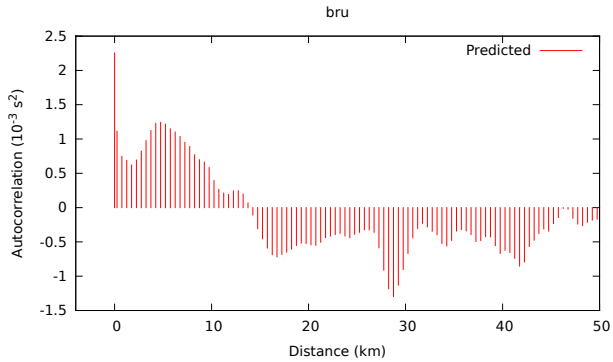
bru
Predicted
Autocorrelation (10-3 s2)
Distance (km)

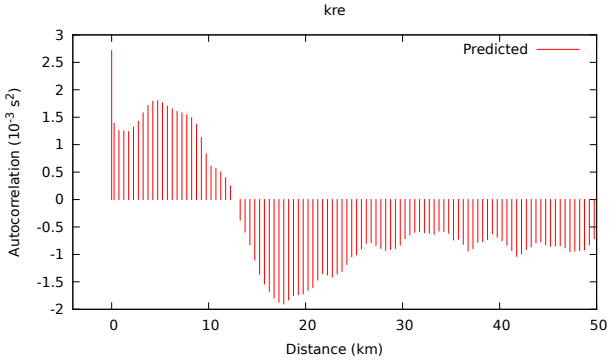
kre
Predicted
Autocorrelation (10-3 s2)
Distance (km)

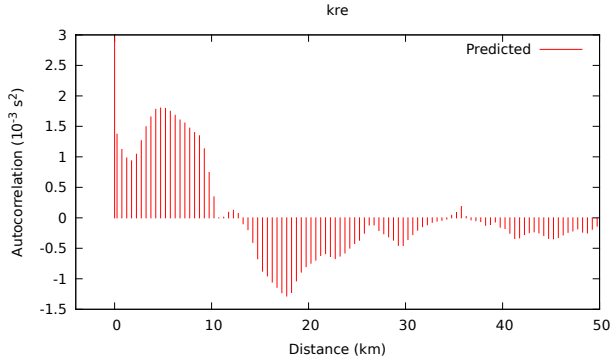
kre
Predicted
Autocorrelation (10-3 s2)
Distance (km)

P-wave

S-wave

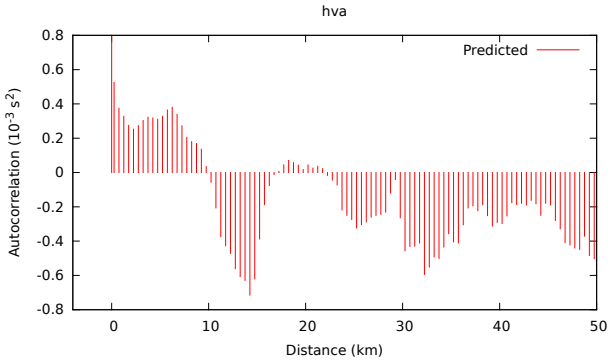
hva
Predicted
Autocorrelation (10-3 s2)
Distance (km)

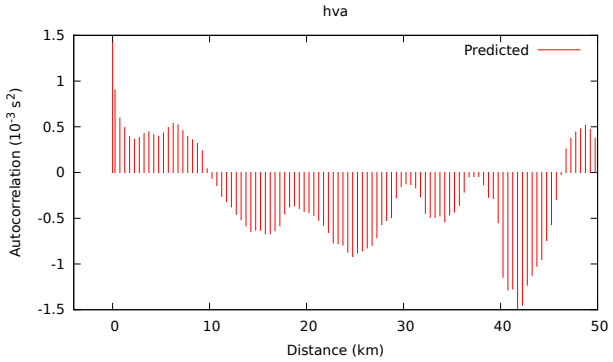
hva
Predicted
Autocorrelation (10-3 s2)
Distance (km)

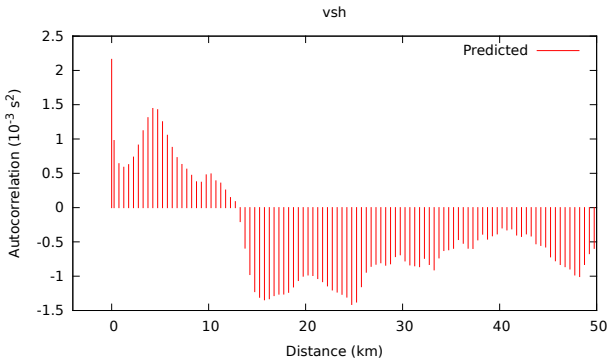
vsh
Predicted
Autocorrelation (10-3 s2)
Distance (km)

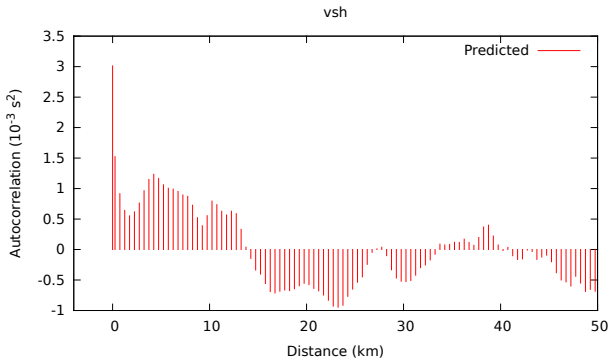
vsh
Predicted
Autocorrelation (10-3 s2)
Distance (km)

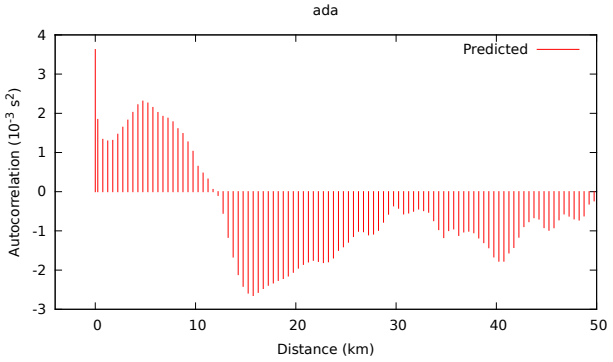
ada
Predicted
Autocorrelation (10-3 s2)
Distance (km)

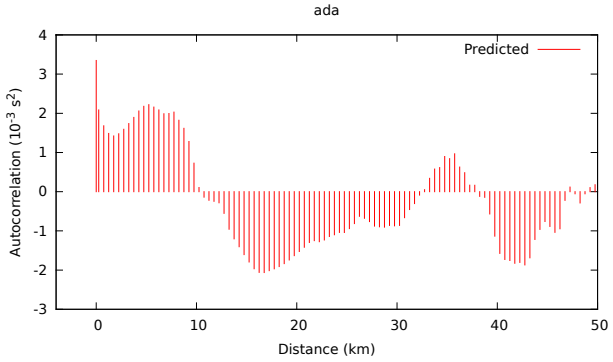
ada
Predicted
Autocorrelation (10-3 s2)
Distance (km)

P-wave

S-wave

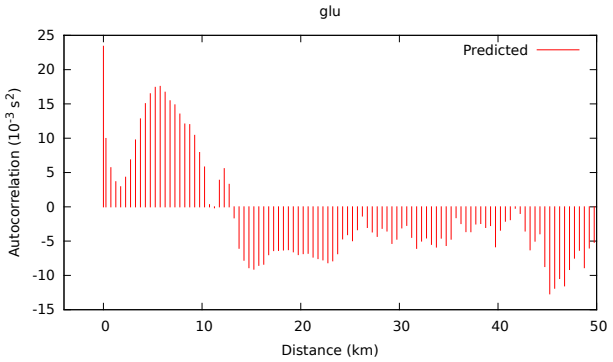
glu
Predicted
Autocorrelation (10^{-3} s^2)
Distance (km)

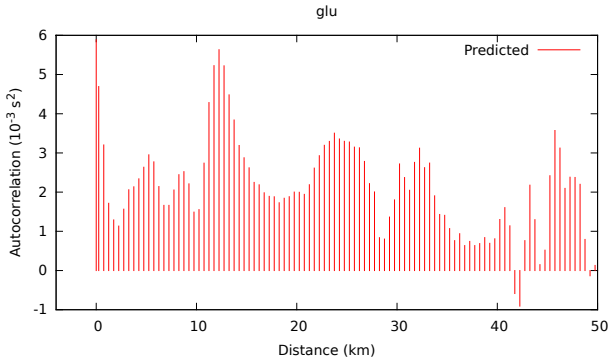
glu
Predicted
Autocorrelation (10^{-3} s^2)
Distance (km)

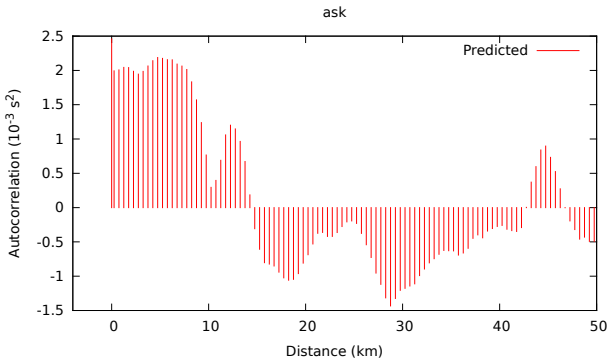
ask
Predicted
Autocorrelation (10^{-3} s^2)
Distance (km)

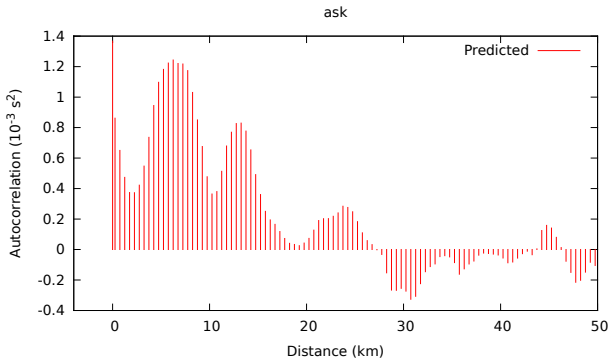
ask
Predicted
Autocorrelation (10^{-3} s^2)
Distance (km)

P-wave

S-wave

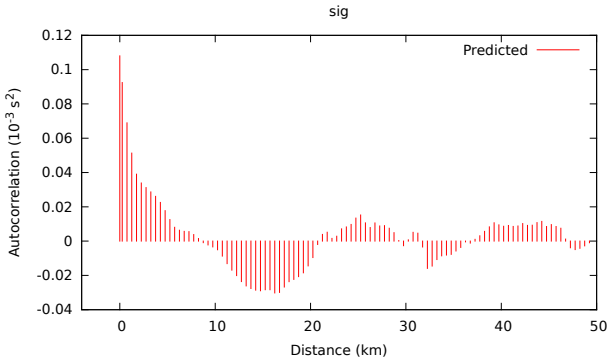
sig
Predicted
Autocorrelation (10^{-3} s^2)
Distance (km)

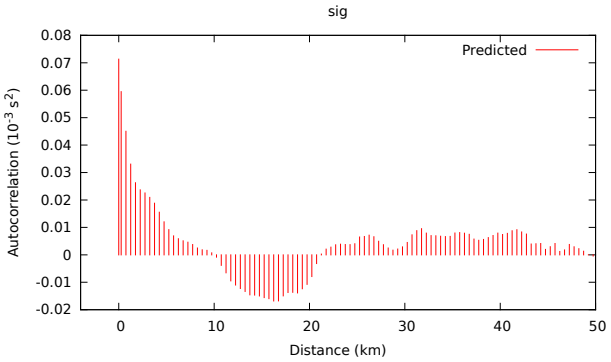
sig
Predicted
Autocorrelation (10^{-3} s^2)
Distance (km)

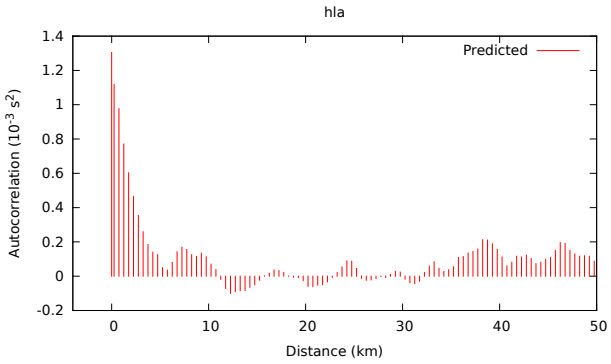
hla
Predicted
Autocorrelation (10^{-3} s^2)
Distance (km)

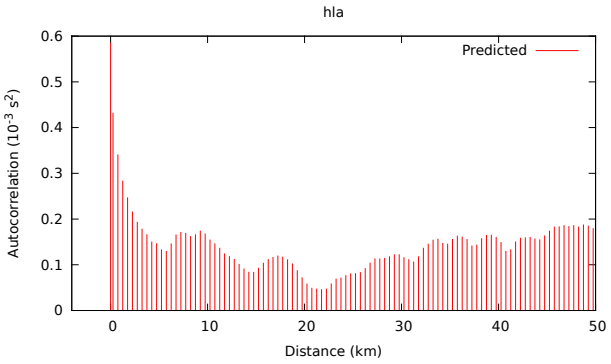
hla
Predicted
Autocorrelation (10^{-3} s^2)
Distance (km)

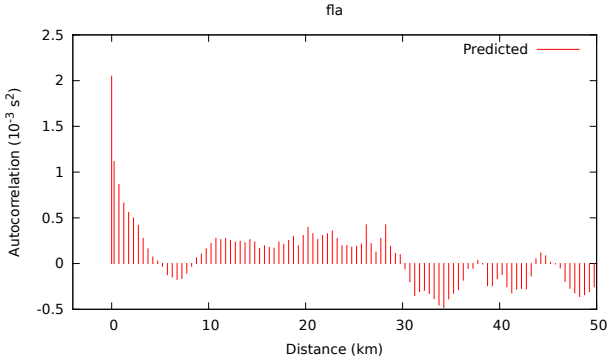
fla
Predicted
Autocorrelation (10^{-3} s^2)
Distance (km)

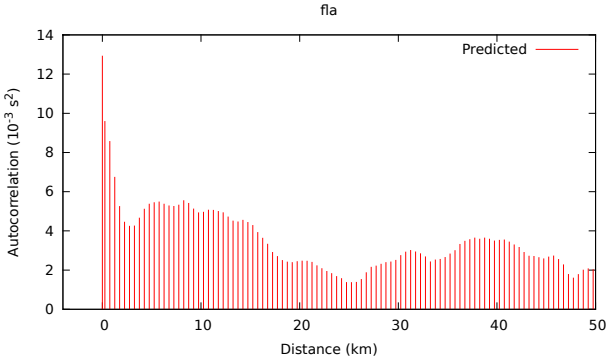
fla
Predicted
Autocorrelation (10^{-3} s^2)
Distance (km)

P-wave

S-wave

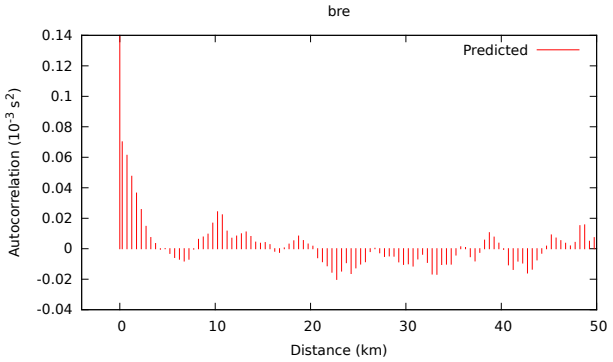
bre
Predicted
Autocorrelation (10^{-3} s^2)
Distance (km)

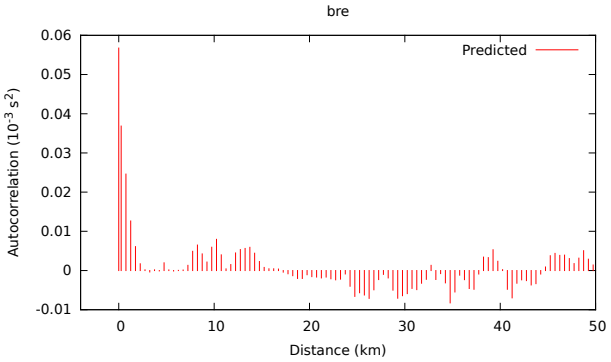
bre
Predicted
Autocorrelation (10^{-3} s^2)
Distance (km)

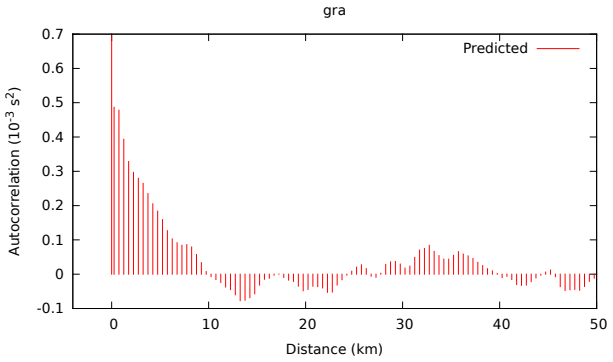
gra
Predicted
Autocorrelation (10^{-3} s^2)
Distance (km)

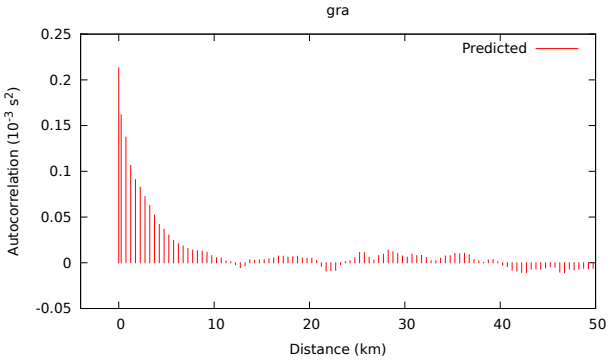
gra
Predicted
Autocorrelation (10^{-3} s^2)
Distance (km)

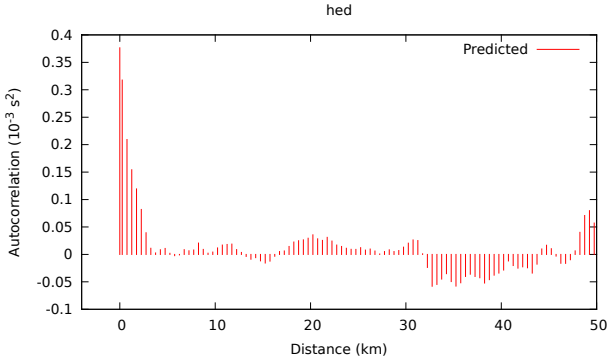
hed
Predicted
Autocorrelation (10^{-3} s^2)
Distance (km)

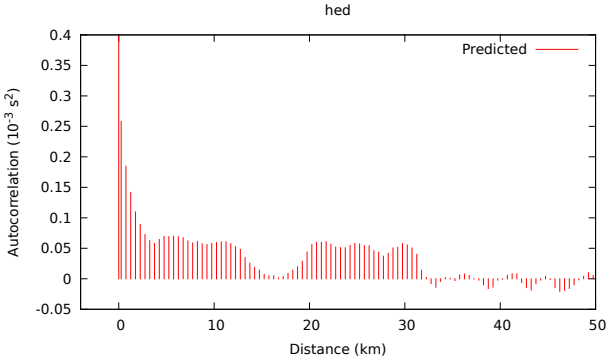
hed
Predicted
Autocorrelation (10^{-3} s^2)
Distance (km)

P-wave

S-wave

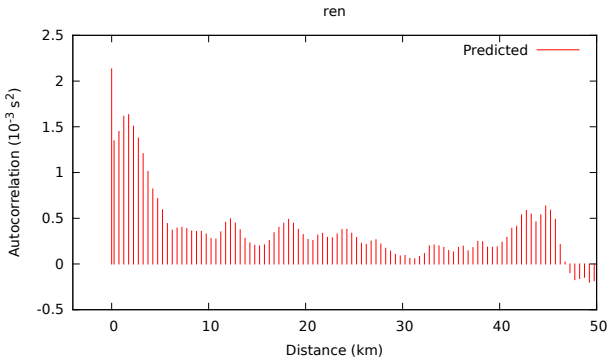
ren
Predicted
Autocorrelation (10^{-3} s^2)
Distance (km)

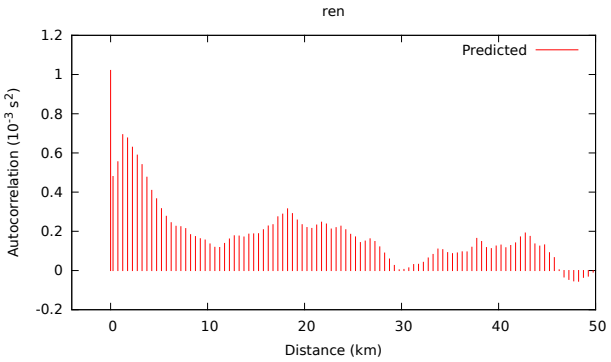
ren
Predicted
Autocorrelation (10^{-3} s^2)
Distance (km)

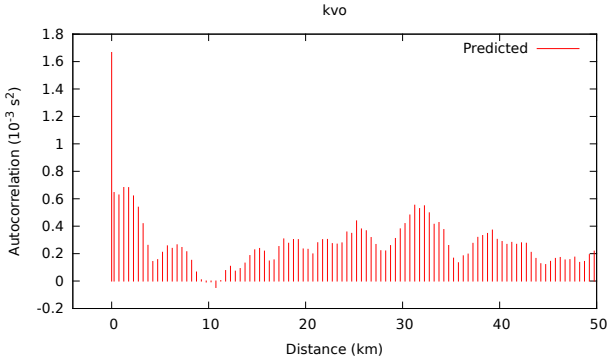
kvo
Predicted
Autocorrelation (10^{-3} s^2)
Distance (km)

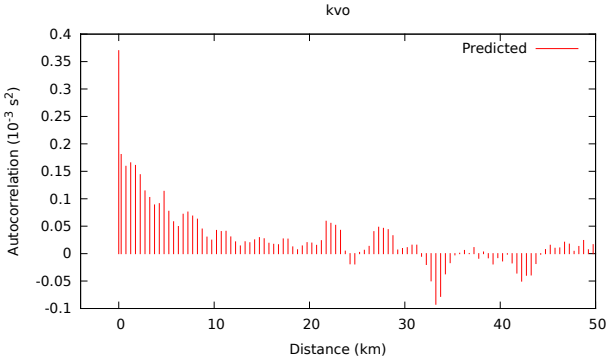
kvo
Predicted
Autocorrelation (10^{-3} s^2)
Distance (km)

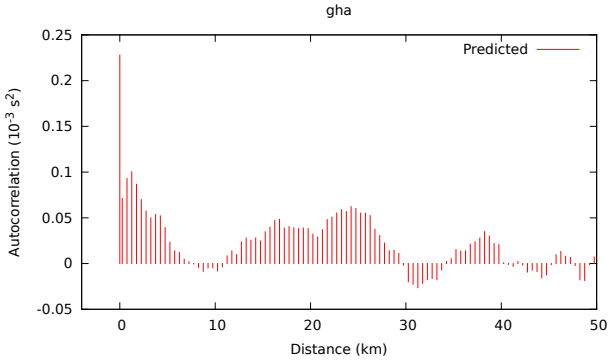
gha
Predicted
Autocorrelation (10^{-3} s^2)
Distance (km)

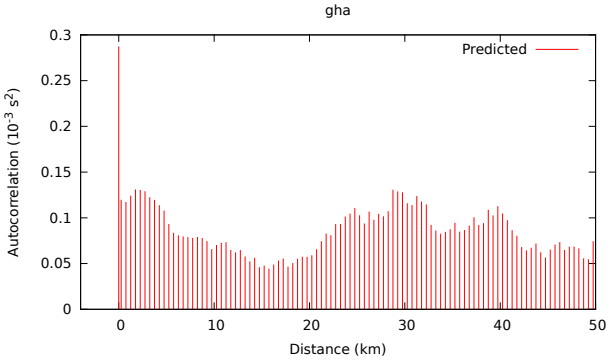
gha
Predicted
Autocorrelation (10^{-3} s^2)
Distance (km)

P-wave

S-wave

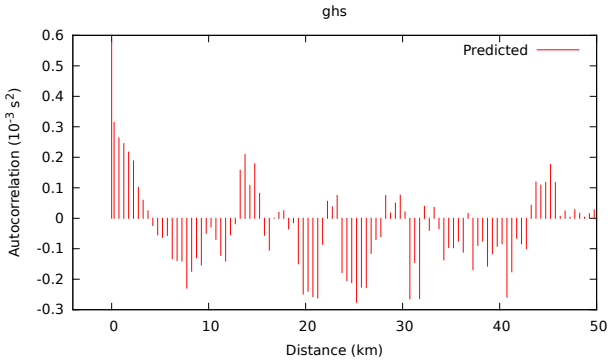
ghs
Predicted
Autocorrelation (10^{-3} s^2)
Distance (km)

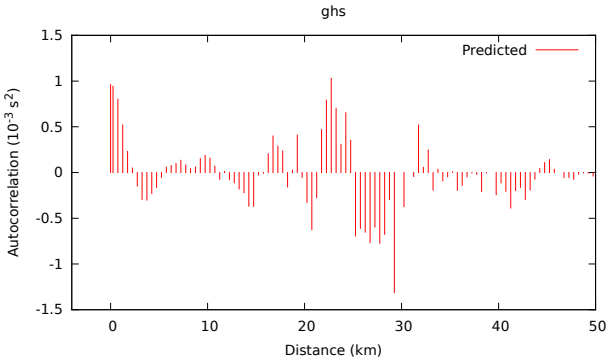
ghs
Predicted
Autocorrelation (10^{-3} s^2)
Distance (km)

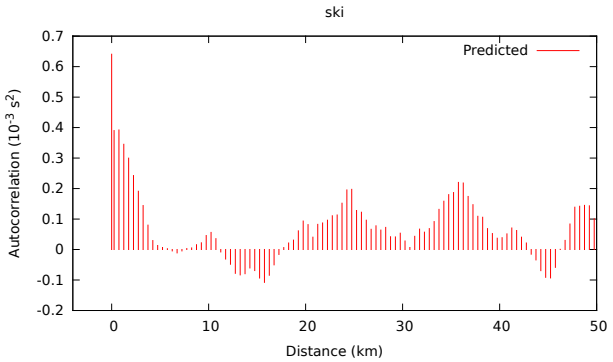
ski
Predicted
Autocorrelation (10^{-3} s^2)
Distance (km)

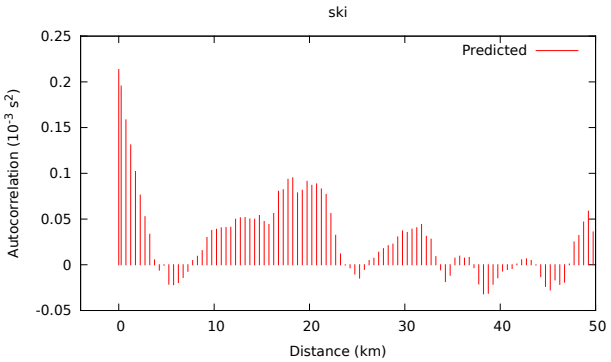
ski
Predicted
Autocorrelation (10^{-3} s^2)
Distance (km)

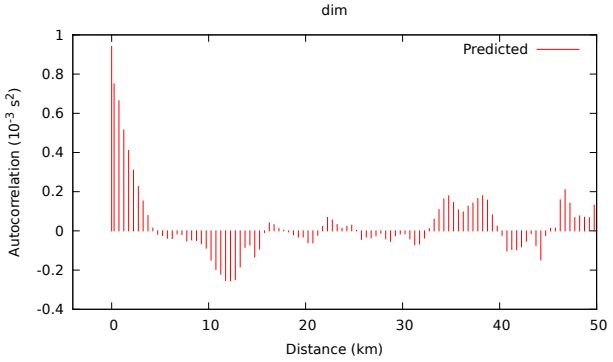
dim
Predicted
Autocorrelation (10^{-3} s^2)
Distance (km)

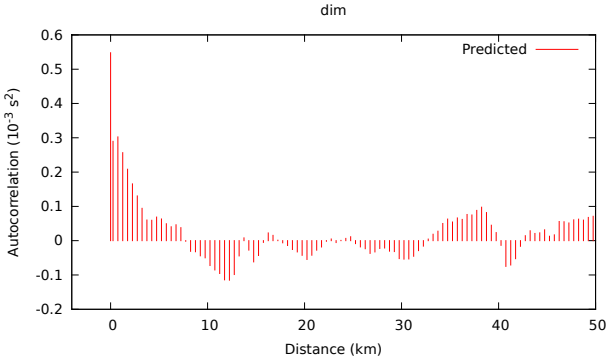
dim
Predicted
Autocorrelation (10^{-3} s^2)
Distance (km)

P-wave

S-wave

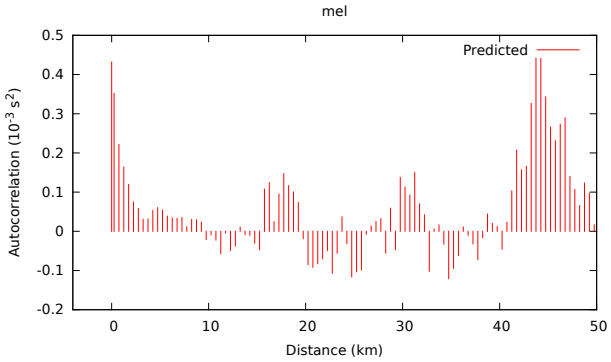
mel
Predicted
Autocorrelation (10-3 s2)
Distance (km)

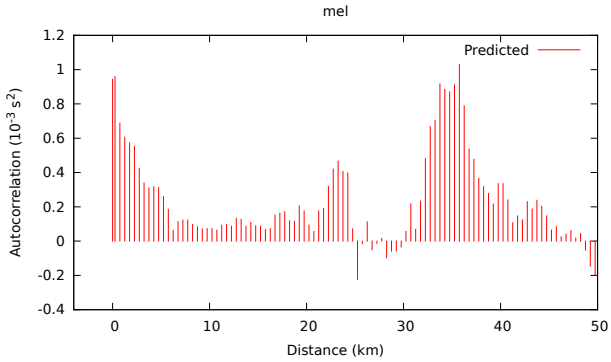
mel
Predicted
Autocorrelation (10-3 s2)
Distance (km)

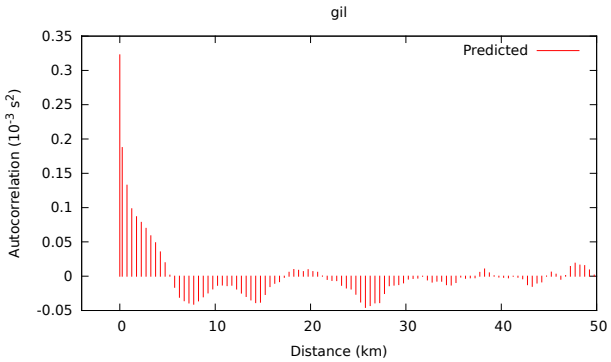
gil
Predicted
Autocorrelation (10-3 s2)
Distance (km)

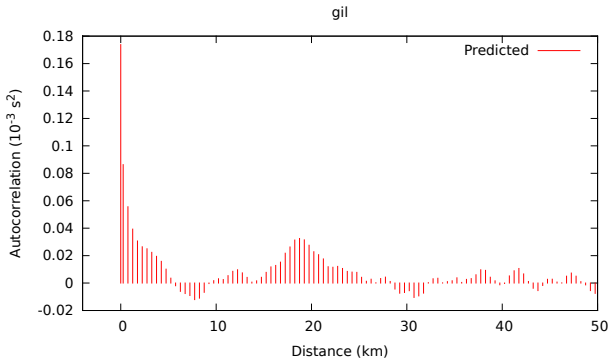
gil
Predicted
Autocorrelation (10-3 s2)
Distance (km)

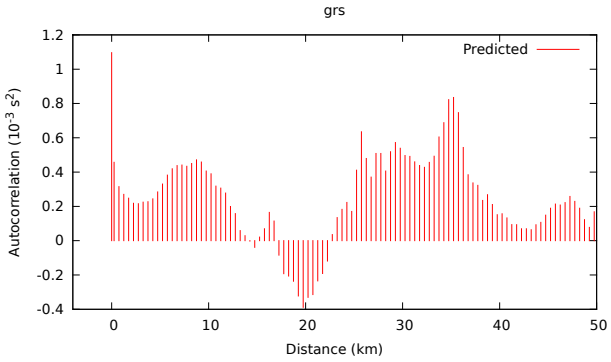
grs
Predicted
Autocorrelation (10-3 s2)
Distance (km)

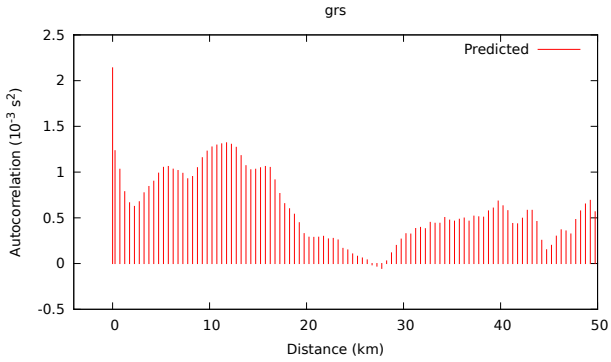
grs
Predicted
Autocorrelation (10-3 s2)
Distance (km)

P-wave

S-wave

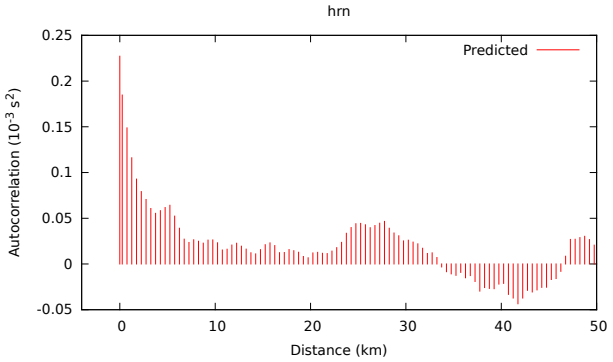
hrn
Predicted
Autocorrelation (10-3 s2)
Distance (km)

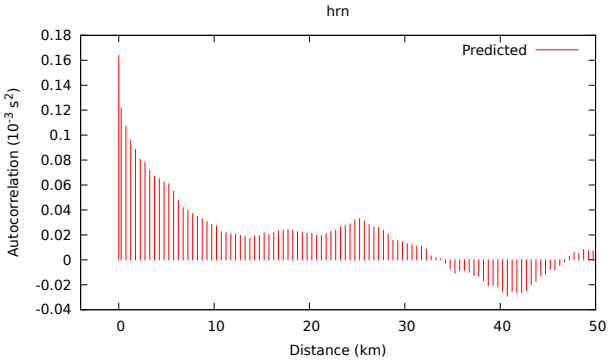
hrn
Predicted
Autocorrelation (10-3 s2)
Distance (km)

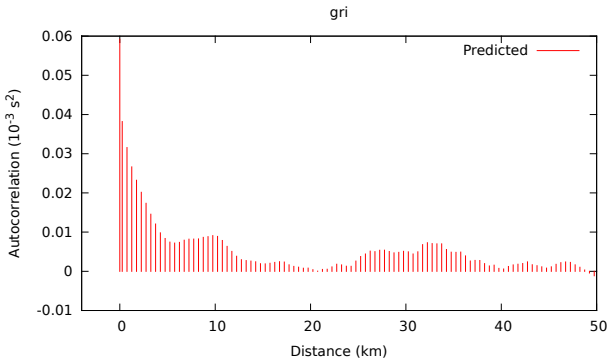
gri
Predicted
Autocorrelation (10-3 s2)
Distance (km)

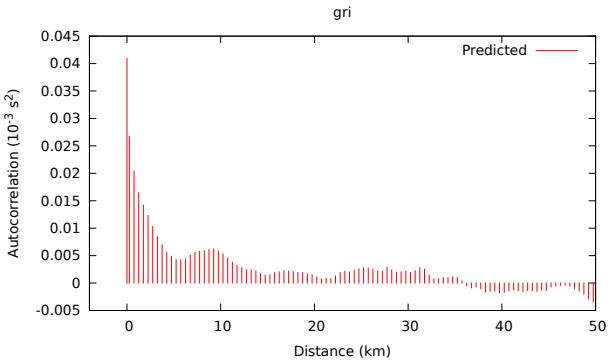
gri
Predicted
Autocorrelation (10-3 s2)
Distance (km)

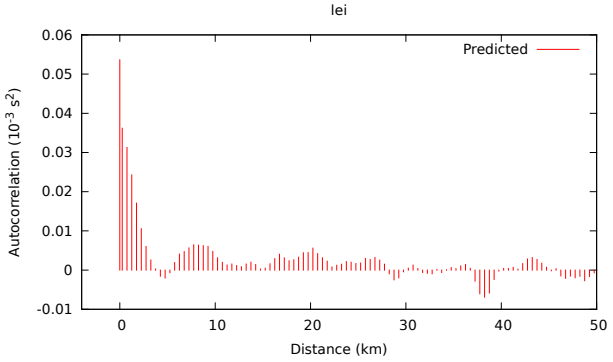
lei
Predicted
Autocorrelation (10-3 s2)
Distance (km)

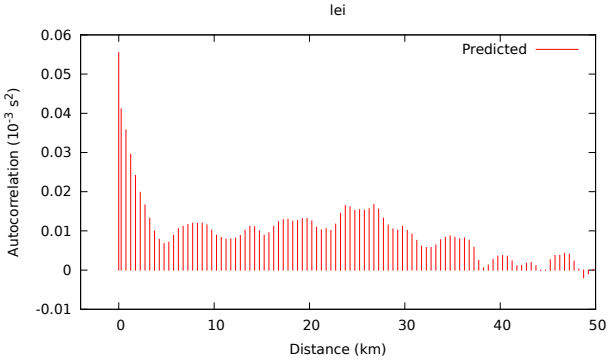
lei
Predicted
Autocorrelation (10-3 s2)
Distance (km)

P-wave

S-wave

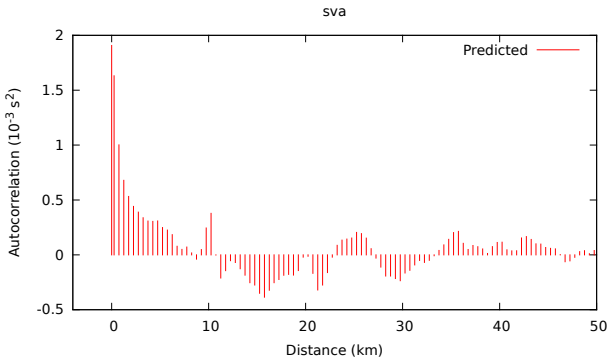
sva
Predicted
Autocorrelation (10^{-3} s^2)
Distance (km)

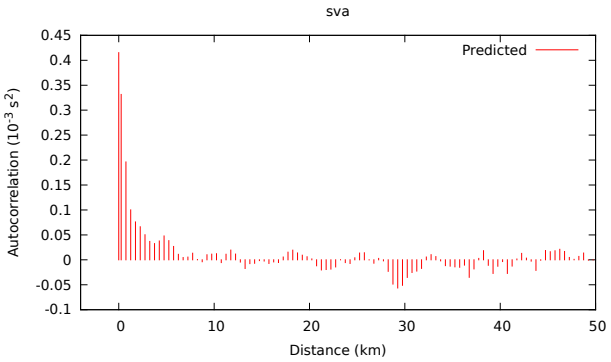
sva
Predicted
Autocorrelation (10^{-3} s^2)
Distance (km)

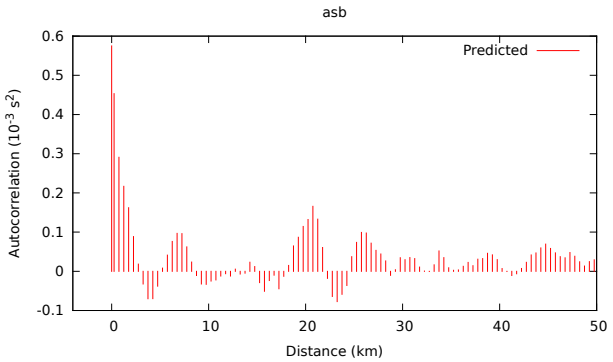
asb
Predicted
Autocorrelation (10^{-3} s^2)
Distance (km)

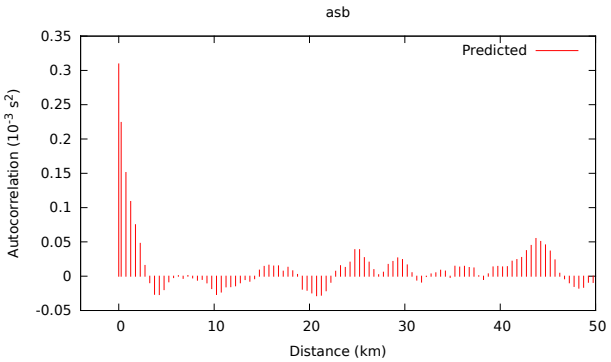
asb
Predicted
Autocorrelation (10^{-3} s^2)
Distance (km)

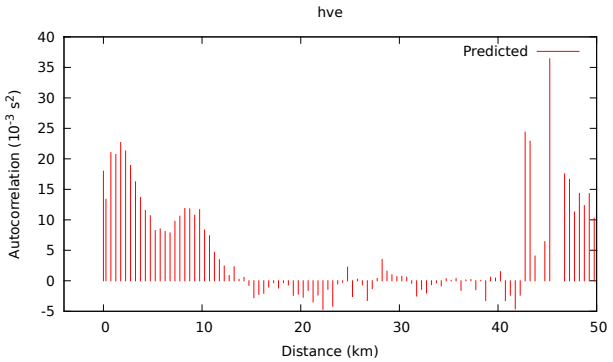
hve
Predicted
Autocorrelation (10^{-3} s^2)
Distance (km)

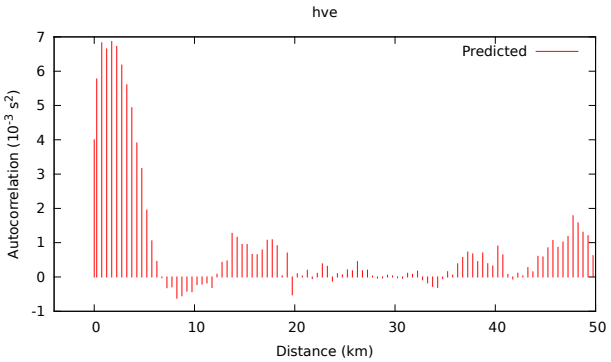
hve
Predicted
Autocorrelation (10^{-3} s^2)
Distance (km)

P-wave

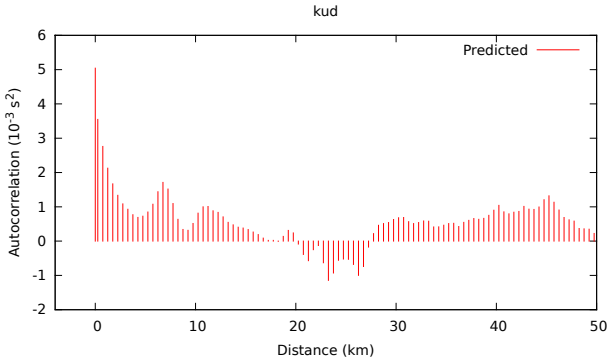
kud
Predicted
Autocorrelation (10-3 s2)
Distance (km)
6
5
4
3
2
1
0
-1
-2
0
10
20
30
40
50

S-wave

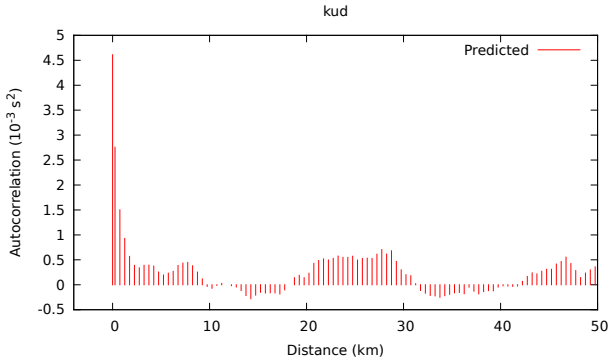
kud
Predicted
Autocorrelation (10-3 s2)
Distance (km)
5
4.5
4
3.5
3
2.5
2
1.5
1
0.5
0
-0.5
0
10
20
30
40
50

Appendix F

Auto-covariance of noise

The following figures show auto-covariance functions of the estimated noise for both P-wave and S-wave residuals. Results from three adjacent stations are presented on each page with the station code indicated above each frame.

The structure of the auto-covariance is with some exceptions very simple, i.e. a large value at zero offset followed by significantly smaller variation around zero covariance at finite offset. This indicates that the identification of the noise component as a spatially incoherent signal has been successful. In the relatively few cases where significant signal remains at finite offset, in particular where that is correlated for P- and S-wave residuals, suggests that some of the spatially coherent signal has leaked into the error estimate. In exceptional cases the noise covariance behaves erratically. This occurs exclusively at stations with quite few data (e.g. station fed). The behavior of station fag is strange and not understood.

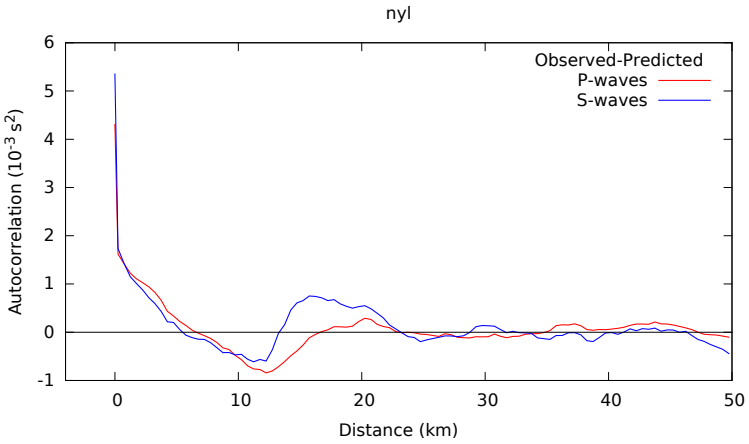
nyl
Observed-Predicted
P-waves
S-waves
Autocorrelation (10-3 s2)
Distance (km)
6
5
4
3
2
1
0
-1
0
10
20
30
40
50

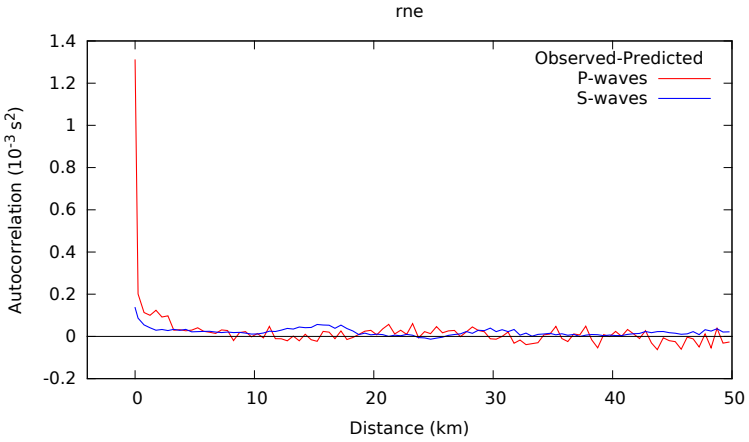
rne
Observed-Predicted
P-waves
S-waves
Autocorrelation (10-3 s2)
Distance (km)
1.4
1.2
1
0.8
0.6
0.4
0.2
0
-0.2
0
10
20
30
40
50

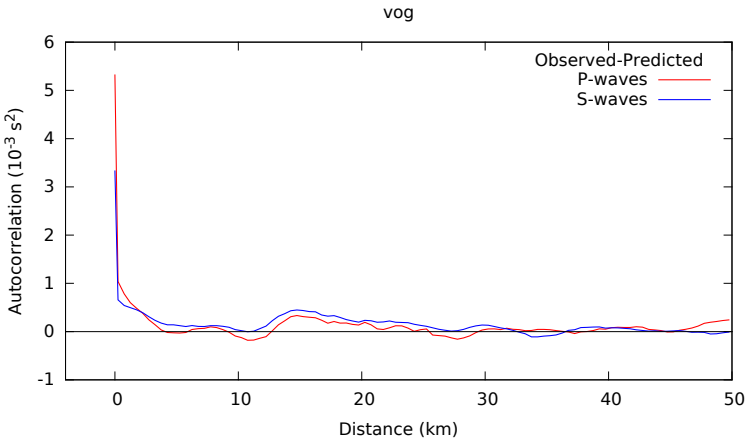
vog
Observed-Predicted
P-waves
S-waves
Autocorrelation (10-3 s2)
Distance (km)
6
5
4
3
2
1
0
-1
0
10
20
30
40
50

F2

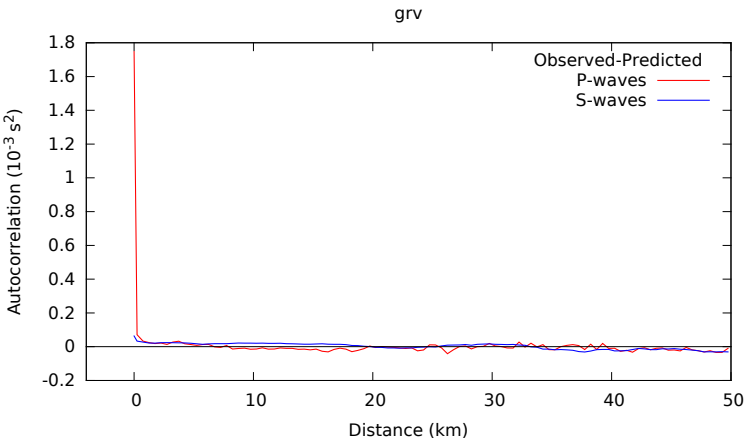
grv
Observed-Predicted
P-waves
S-waves
Autocorrelation (10-3 s2)
Distance (km)
1.8
1.6
1.4
1.2
1
0.8
0.6
0.4
0.2
0
-0.2
0
10
20
30
40
50

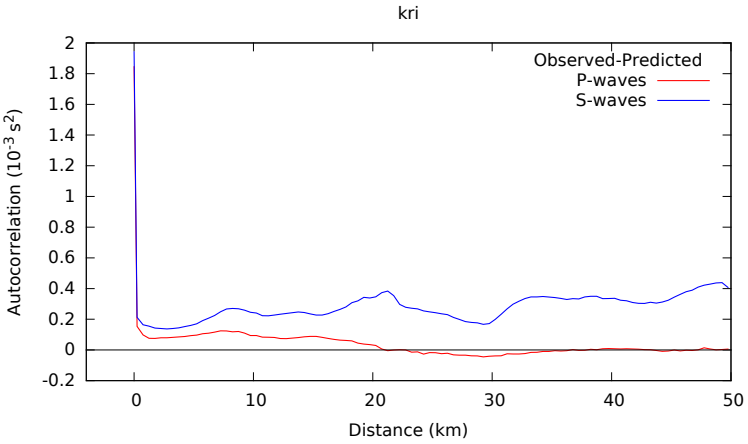
kri
Observed-Predicted
P-waves
S-waves
Autocorrelation (10-3 s2)
Distance (km)
2
1.8
1.6
1.4
1.2
1
0.8
0.6
0.4
0.2
0
-0.2
0
10
20
30
40
50

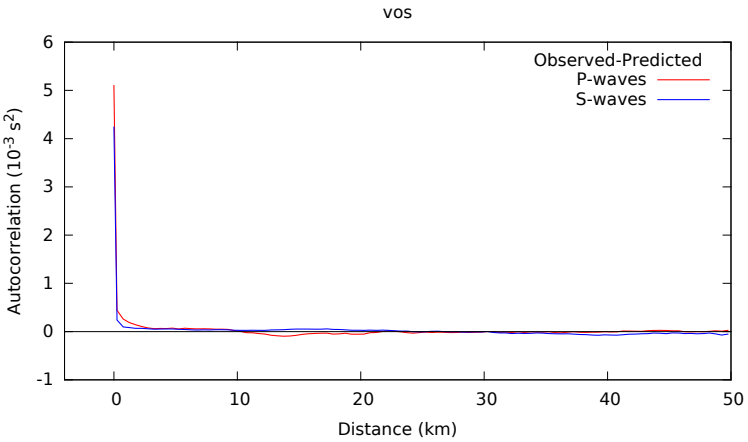
vos
Observed-Predicted
P-waves
S-waves
Autocorrelation (10-3 s2)
Distance (km)
6
5
4
3
2
1
0
-1
0
10
20
30
40
50

F3

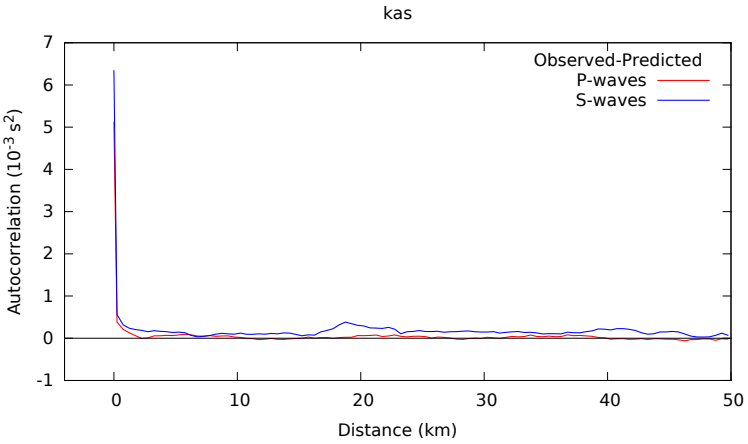
kas
Observed-Predicted
P-waves
S-waves
Autocorrelation (10-3 s2)
Distance (km)
7
6
5
4
3
2
1
0
-1
0
10
20
30
40
50

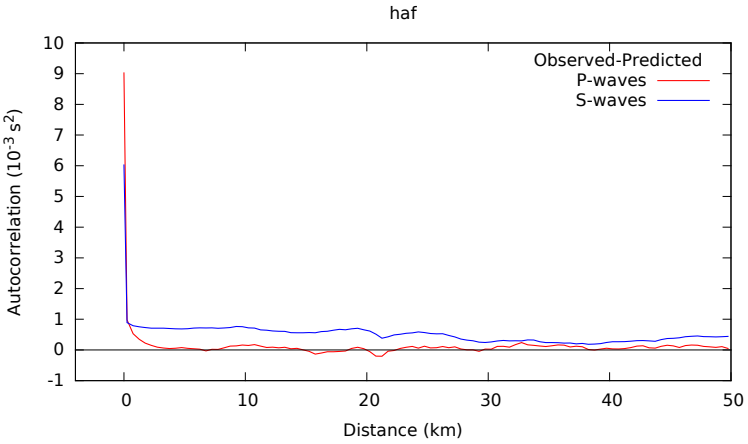
haf
Observed-Predicted
P-waves
S-waves
Autocorrelation (10-3 s2)
Distance (km)
10
9
8
7
6
5
4
3
2
1
0
-1
0
10
20
30
40
50

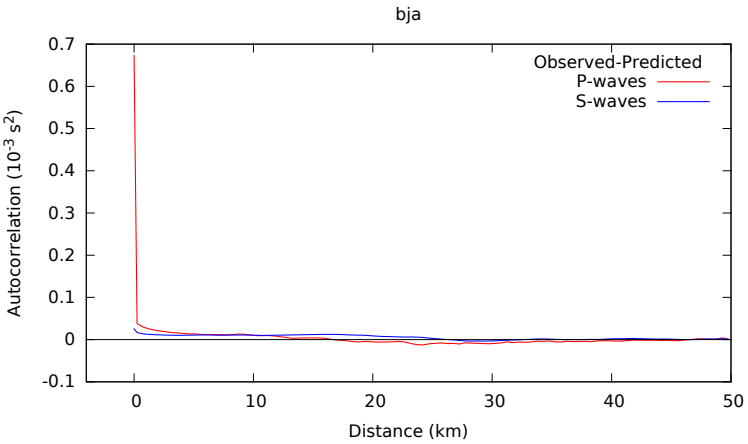
bja
Observed-Predicted
P-waves
S-waves
Autocorrelation (10-3 s2)
Distance (km)
0.7
0.6
0.5
0.4
0.3
0.2
0.1
0
-0.1
0
10
20
30
40
50

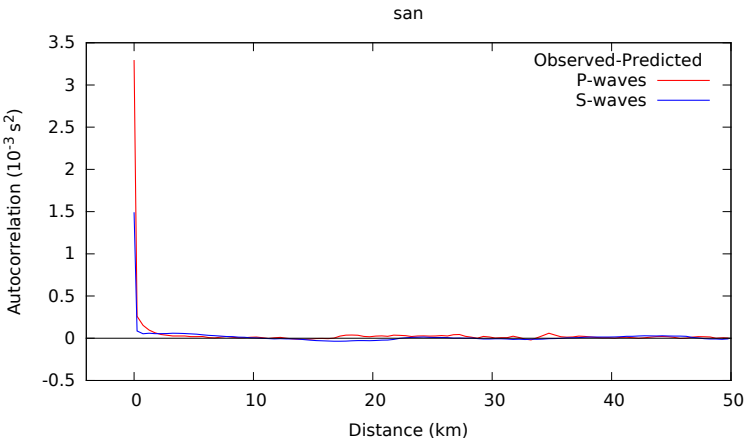
san
Observed-Predicted
P-waves
S-waves
Autocorrelation (10-3 s2)
Distance (km)
3.5
3
2.5
2
1.5
1
0.5
0
-0.5
0
10
20
30
40
50

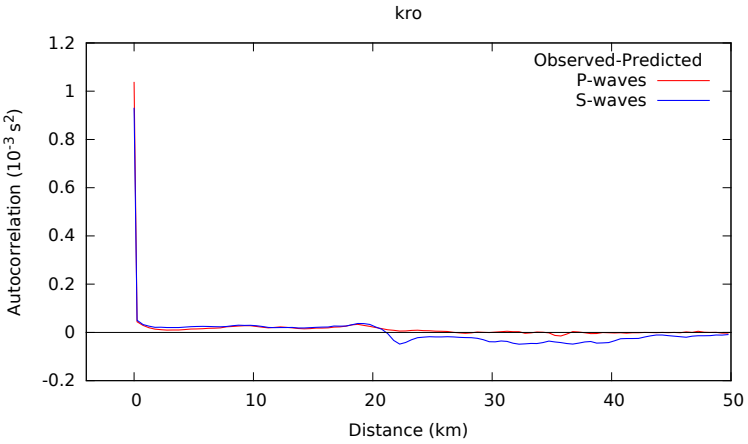
kro
Observed-Predicted
P-waves
S-waves
Autocorrelation (10-3 s2)
Distance (km)
1.2
1
0.8
0.6
0.4
0.2
0
-0.2
0
10
20
30
40
50

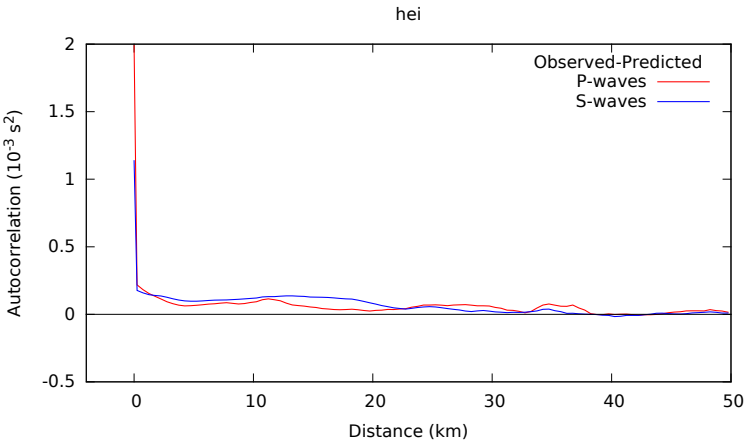
hei
Observed-Predicted
P-waves
S-waves
Autocorrelation (10-3 s2)
Distance (km)
2
1.5
1
0.5
0
-0.5
0
10
20
30
40
50

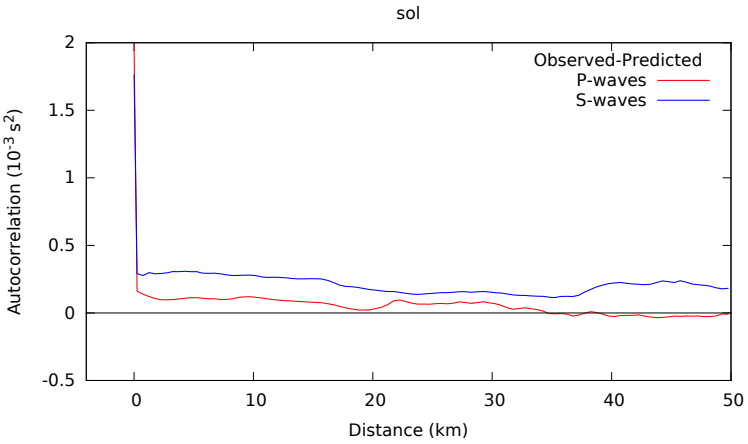
sol
Observed-Predicted
P-waves
S-waves
Autocorrelation (10-3 s2)
Distance (km)
2
1.5
1
0.5
0
-0.5
0
10
20
30
40
50

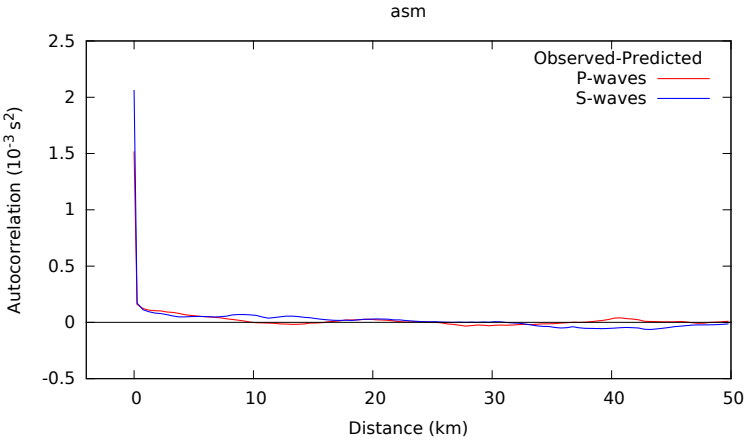
asm
Observed-Predicted
P-waves
S-waves
Autocorrelation (10-3 s2)
Distance (km)
2.5
2
1.5
1
0.5
0
-0.5
0
10
20
30
40
50

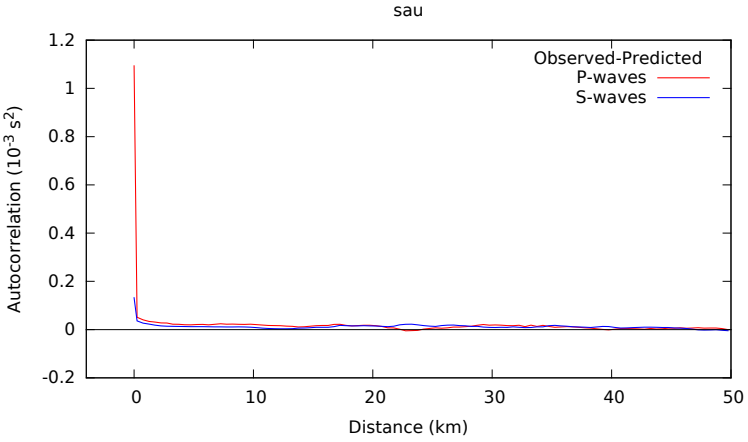
sau
Observed-Predicted
P-waves
S-waves
Autocorrelation (10-3 s2)
Distance (km)
1.2
1
0.8
0.6
0.4
0.2
0
-0.2
0
10
20
30
40
50

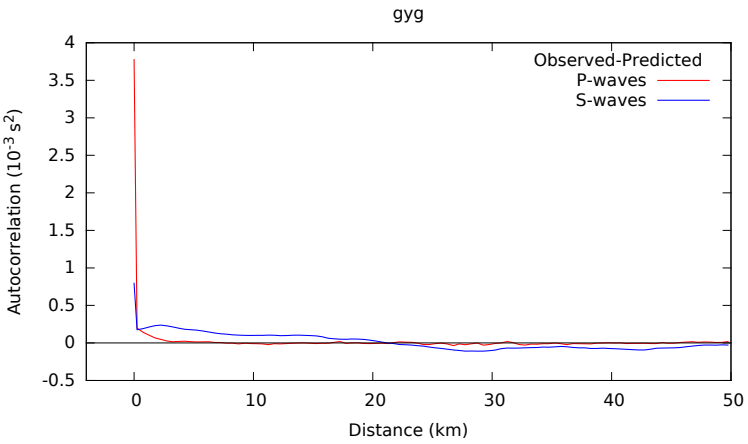
gyg
Observed-Predicted
P-waves
S-waves
Autocorrelation (10-3 s2)
Distance (km)
4
3.5
3
2.5
2
1.5
1
0.5
0
-0.5
0
10
20
30
40
50

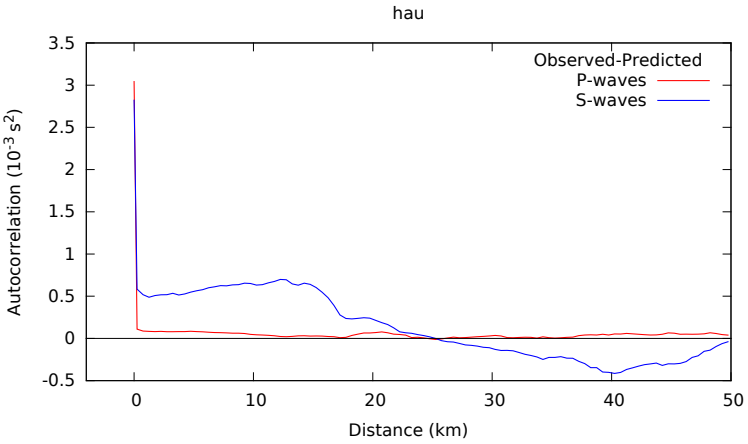
hau
Observed-Predicted
P-waves
S-waves
Autocorrelation (10-3 s2)
Distance (km)
3.5
3
2.5
2
1.5
1
0.5
0
-0.5
0
10
20
30
40
50

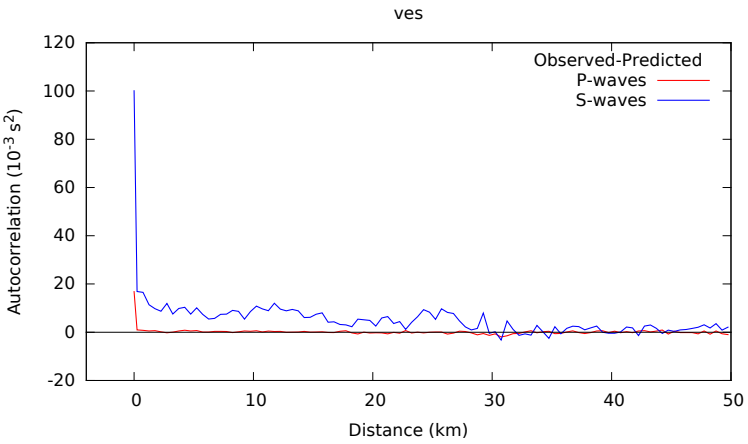
ves
Observed-Predicted
P-waves
S-waves
Autocorrelation (10-3 s2)
Distance (km)
120
100
80
60
40
20
0
-20
0
10
20
30
40
50

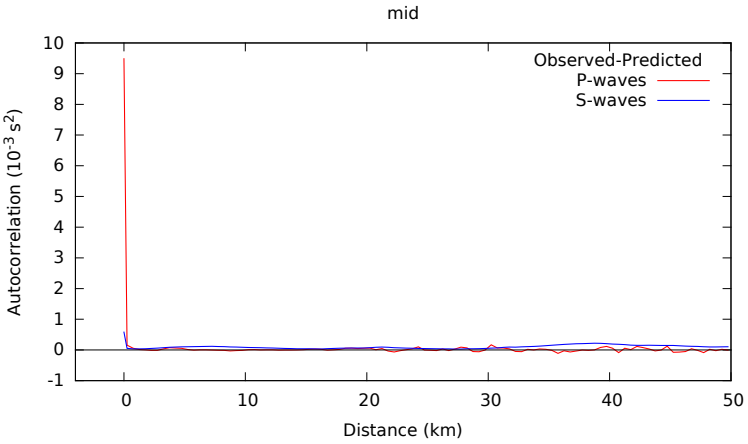
mid
Observed-Predicted
P-waves
S-waves
Autocorrelation (10-3 s2)
Distance (km)
10
9
8
7
6
5
4
3
2
1
0
-1
0
10
20
30
40
50

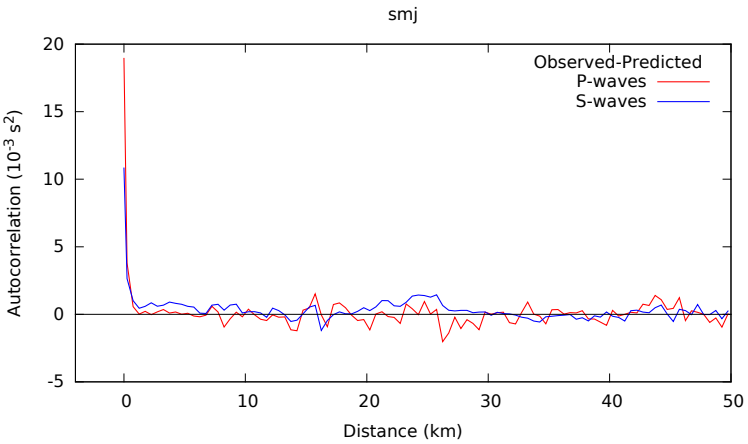
smj
Observed-Predicted
P-waves
S-waves
Autocorrelation (10-3 s2)
Distance (km)
20
15
10
5
0
-5
0
10
20
30
40
50

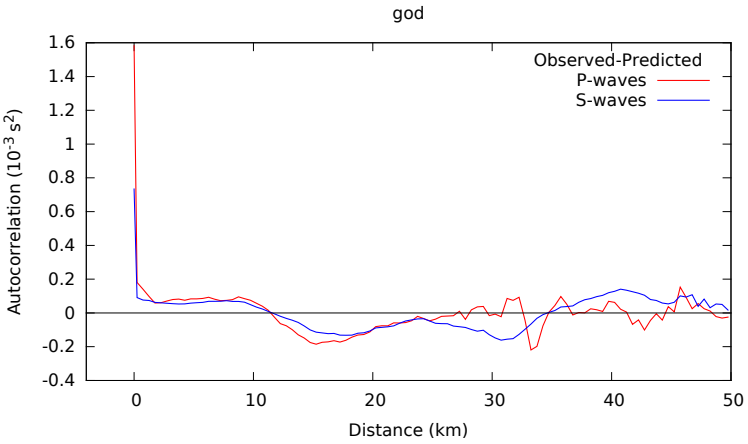
god
Observed-Predicted
P-waves
S-waves
Autocorrelation (10-3 s2)
Distance (km)
1.6
1.4
1.2
1
0.8
0.6
0.4
0.2
0
-0.2
-0.4
0
10
20
30
40
50

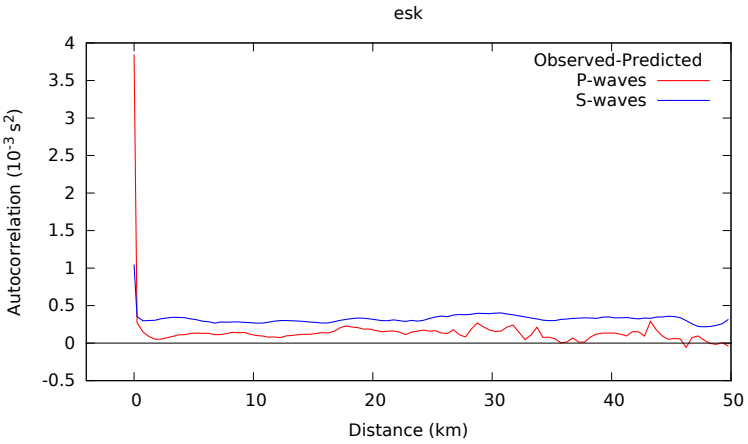
esk
Observed-Predicted
P-waves
S-waves
Autocorrelation (10-3 s2)
Distance (km)
4
3.5
3
2.5
2
1.5
1
0.5
0
-0.5
0
10
20
30
40
50

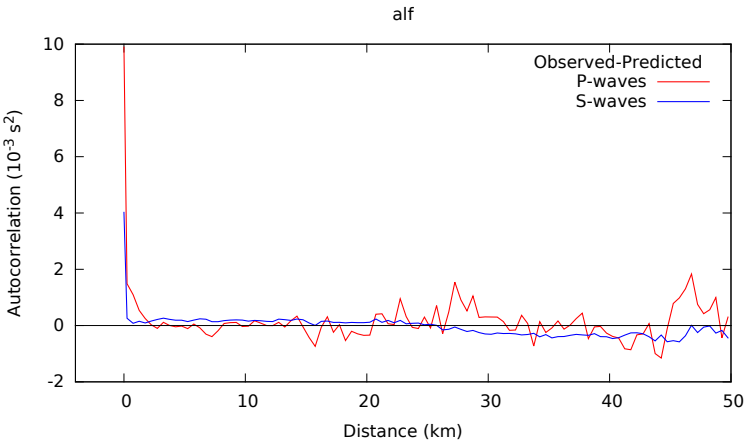
alf
Observed-Predicted
P-waves
S-waves
Autocorrelation (10-3 s2)
Distance (km)
10
8
6
4
2
0
-2
0
10
20
30
40
50

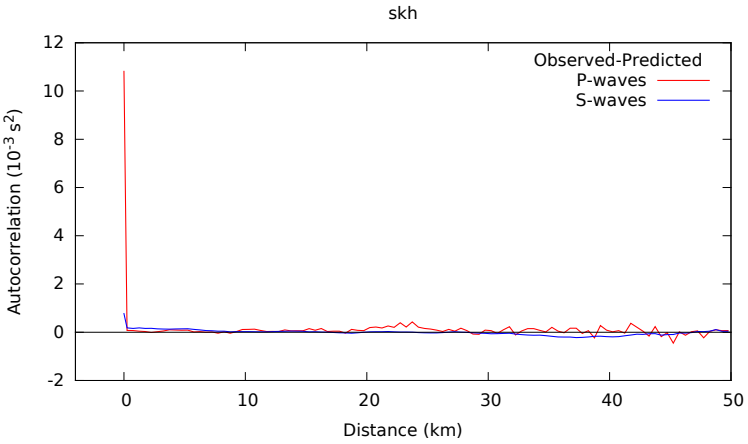
skh
Observed-Predicted
P-waves
S-waves
Autocorrelation (10-3 s2)
Distance (km)

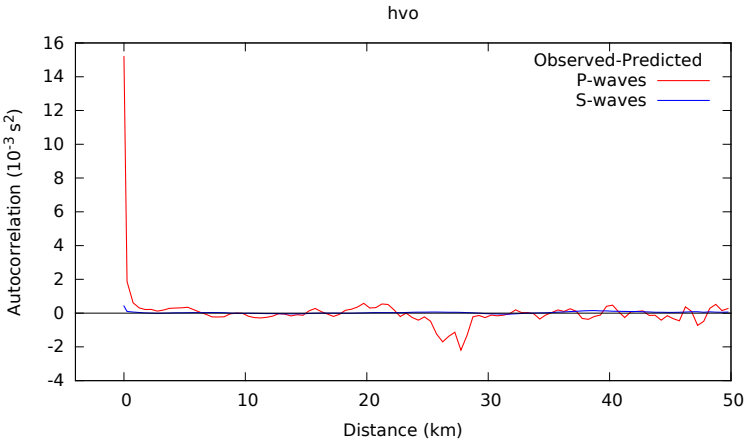
hvo
Observed-Predicted
P-waves
S-waves
Autocorrelation (10-3 s2)
Distance (km)

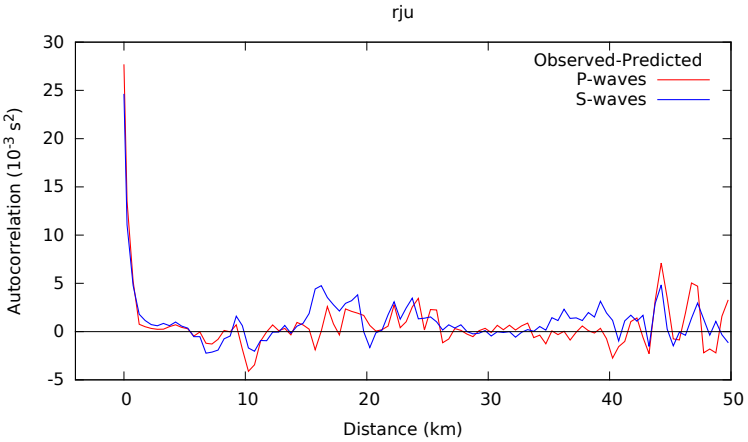
rju
Observed-Predicted
P-waves
S-waves
Autocorrelation (10-3 s2)
Distance (km)

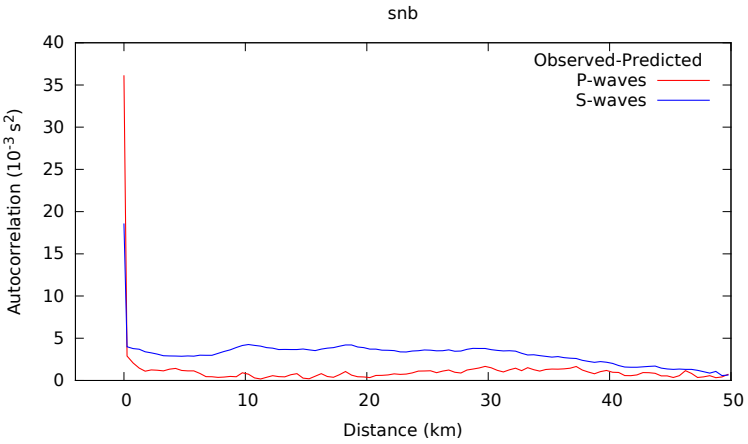
snb
Observed-Predicted
P-waves
S-waves
Autocorrelation (10-3 s2)
Distance (km)
0
5
10
15
20
25
30
35
40
0
10
20
30
40
50

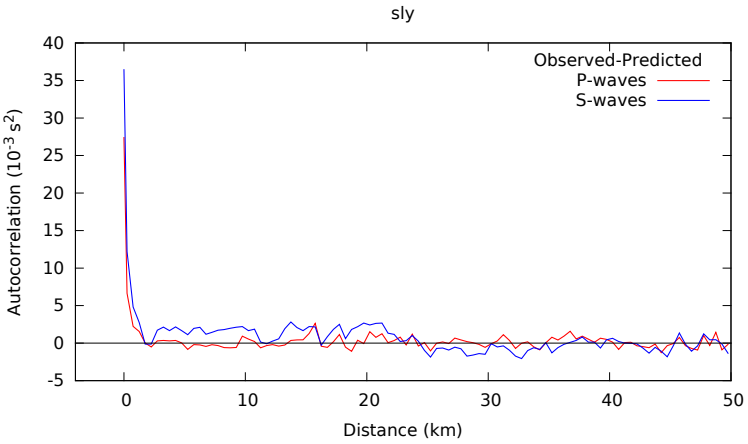
sly
Observed-Predicted
P-waves
S-waves
Autocorrelation (10-3 s2)
Distance (km)
-5
0
5
10
15
20
25
30
35
40
0
10
20
30
40
50

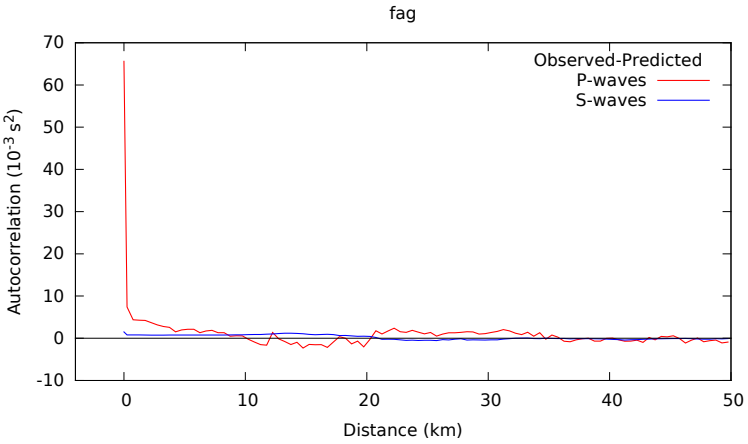
fag
Observed-Predicted
P-waves
S-waves
Autocorrelation (10-3 s2)
Distance (km)
70
60
50
40
30
20
10
0
-10
0
10
20
30
40
50

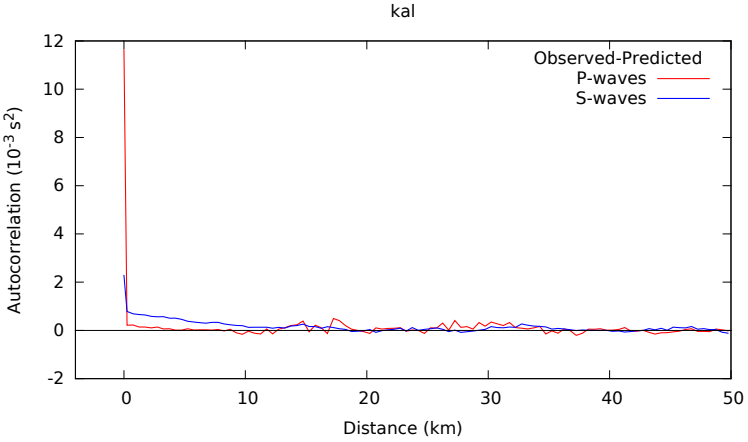
kal
Observed-Predicted
P-waves
S-waves
Autocorrelation (10-3 s2)
Distance (km)
12
10
8
6
4
2
0
-2
0
10
20
30
40
50

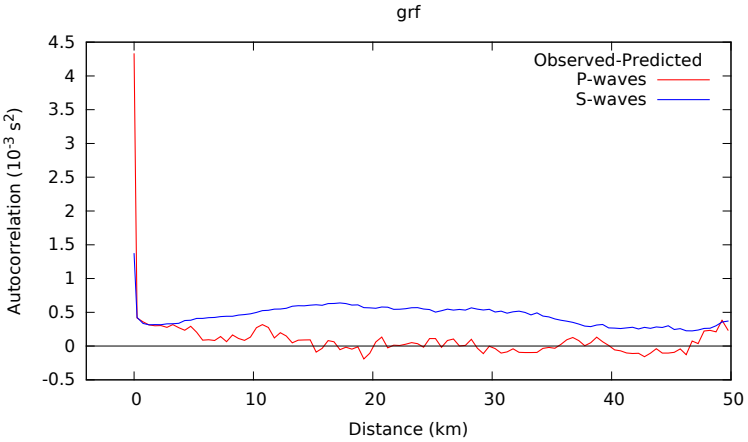
grf
Observed-Predicted
P-waves
S-waves
Autocorrelation (10-3 s2)
Distance (km)
4.5
4
3.5
3
2.5
2
1.5
1
0.5
0
-0.5
0
10
20
30
40
50

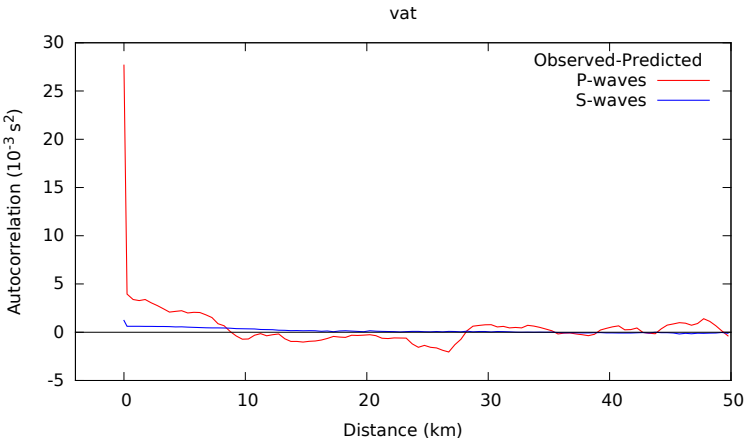
vat
Observed-Predicted
P-waves
S-waves
Autocorrelation (10-3 s2)
Distance (km)
30
25
20
15
10
5
0
-5
0
10
20
30
40
50

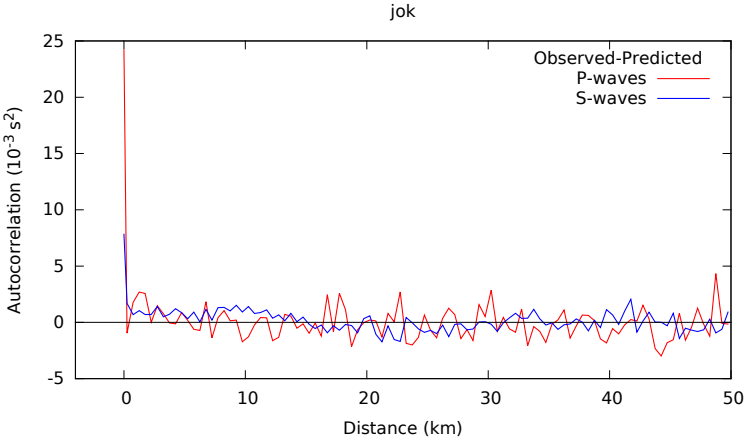
jok
Observed-Predicted
P-waves
S-waves
Autocorrelation (10-3 s2)
Distance (km)
25
20
15
10
5
0
-5
0
10
20
30
40
50

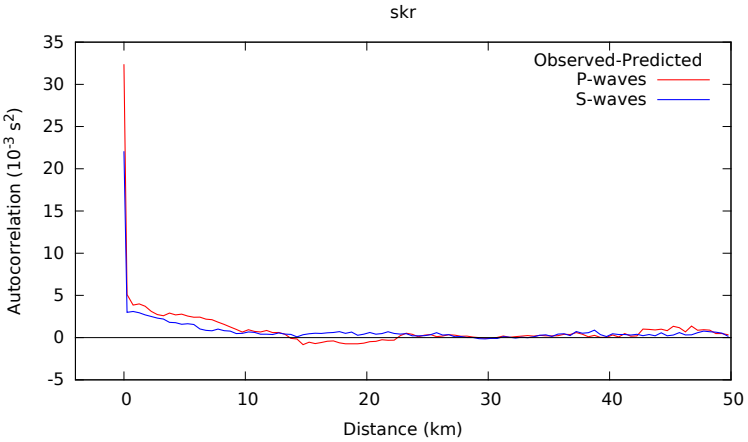
skr
Observed-Predicted
P-waves
S-waves
Autocorrelation (10-3 s2)
Distance (km)
35
30
25
20
15
10
5
0
-5
0
10
20
30
40
50

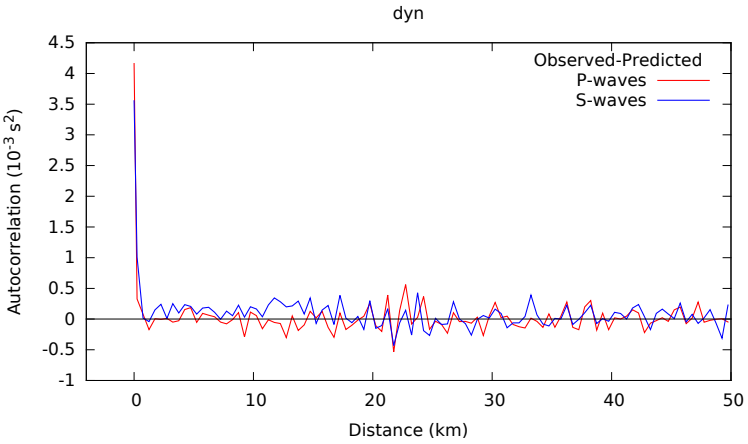
dyn
Observed-Predicted
P-waves
S-waves
Autocorrelation (10-3 s2)
Distance (km)
4.5
4
3.5
3
2.5
2
1.5
1
0.5
0
-0.5
-1
0
10
20
30
40
50

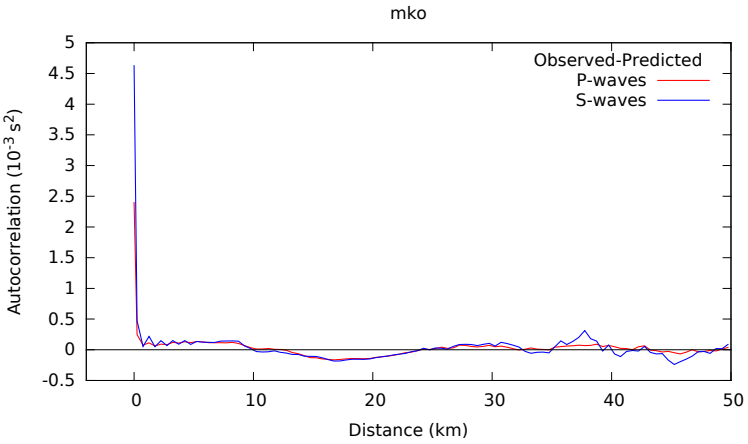
mko
Observed-Predicted
P-waves
S-waves
Autocorrelation (10-3 s2)
Distance (km)

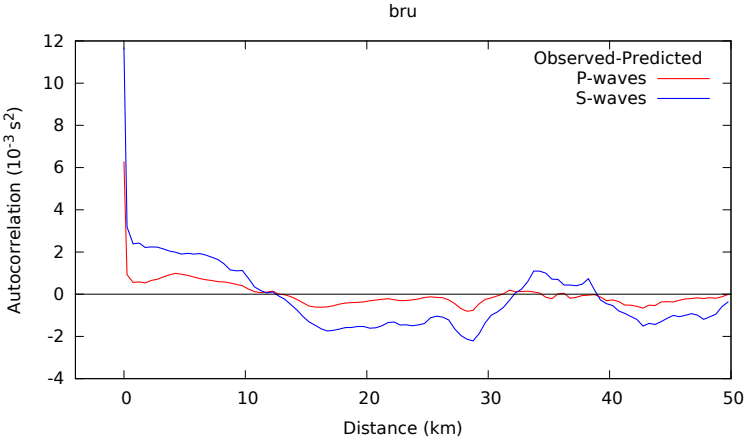
bru
Observed-Predicted
P-waves
S-waves
Autocorrelation (10-3 s2)
Distance (km)

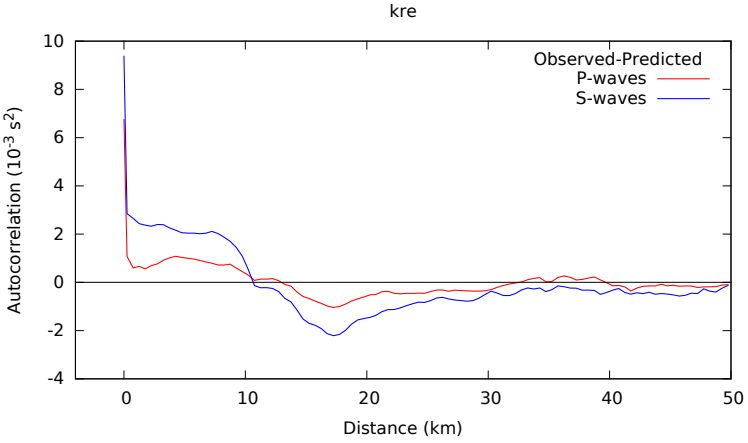
kre
Observed-Predicted
P-waves
S-waves
Autocorrelation (10-3 s2)
Distance (km)

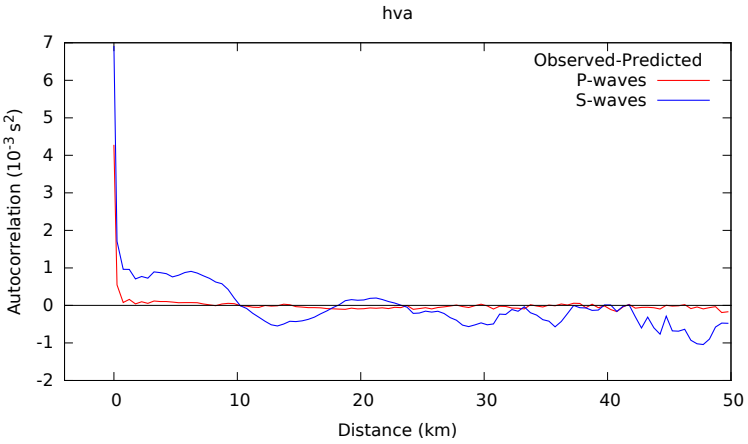
hva
Observed-Predicted
P-waves
S-waves
Autocorrelation (10-3 s2)
Distance (km)
7
6
5
4
3
2
1
0
-1
-2
0
10
20
30
40
50

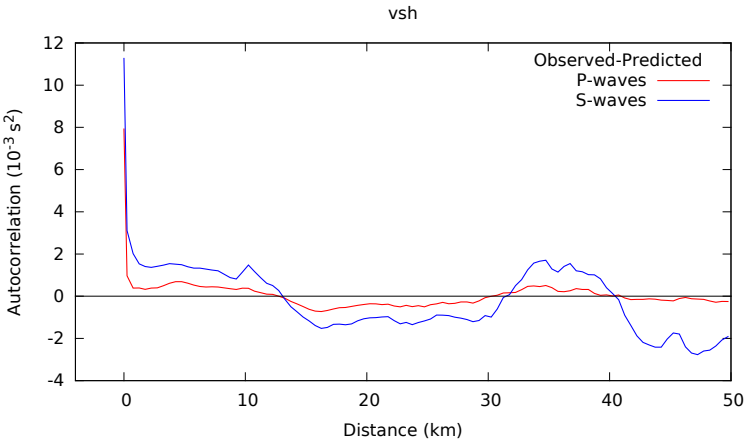
vsh
Observed-Predicted
P-waves
S-waves
Autocorrelation (10-3 s2)
Distance (km)
12
10
8
6
4
2
0
-2
-4
0
10
20
30
40
50

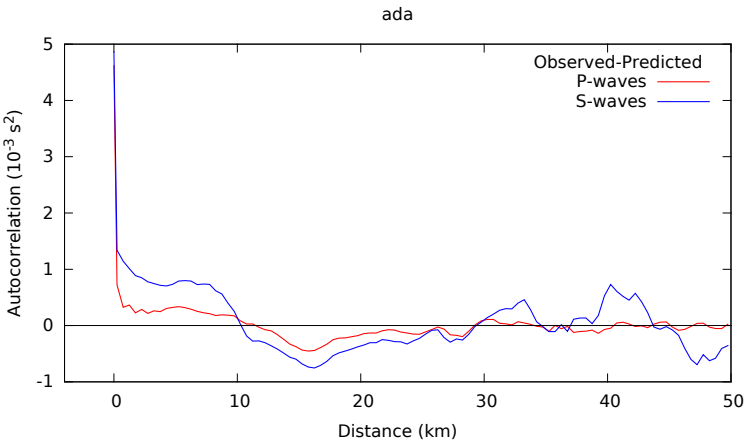
ada
Observed-Predicted
P-waves
S-waves
Autocorrelation (10-3 s2)
Distance (km)
5
4
3
2
1
0
-1
0
10
20
30
40
50

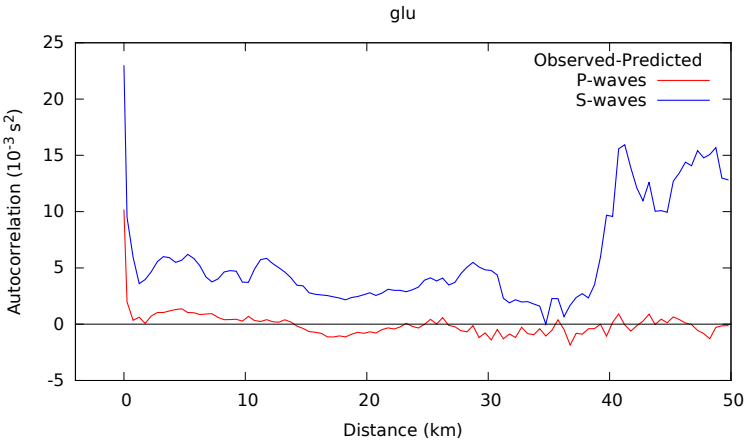
glu
Observed-Predicted
P-waves
S-waves
Autocorrelation (10-3 s2)
Distance (km)
25
20
15
10
5
0
-5
0
10
20
30
40
50

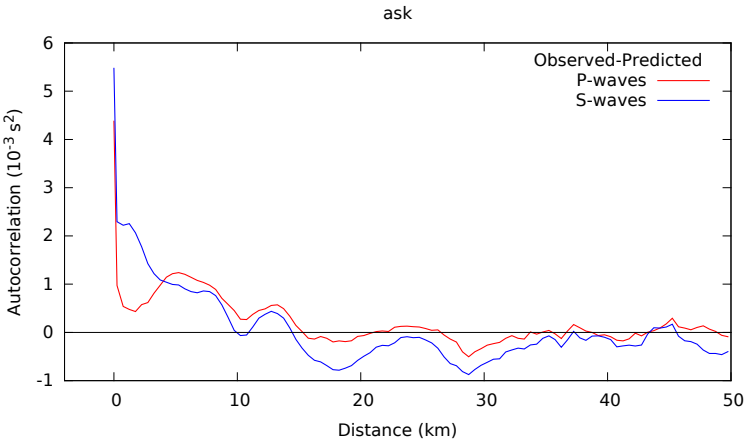
ask
Observed-Predicted
P-waves
S-waves
Autocorrelation (10-3 s2)
Distance (km)
6
5
4
3
2
1
0
-1
0
10
20
30
40
50

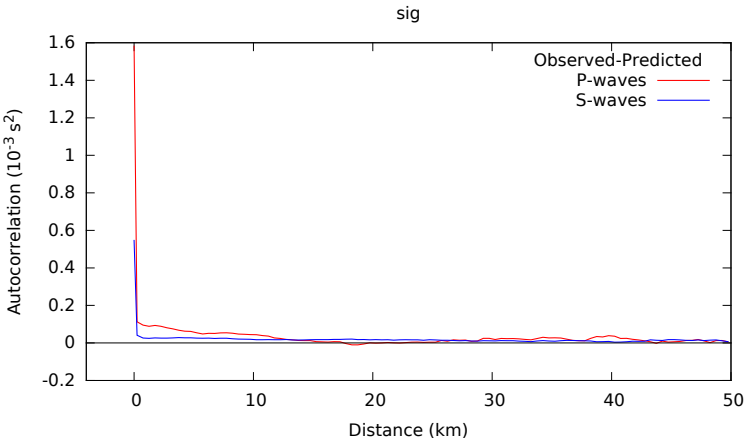
sig
Observed-Predicted
P-waves
S-waves
Autocorrelation (10-3 s2)
Distance (km)
1.6
1.4
1.2
1
0.8
0.6
0.4
0.2
0
-0.2
0
10
20
30
40
50

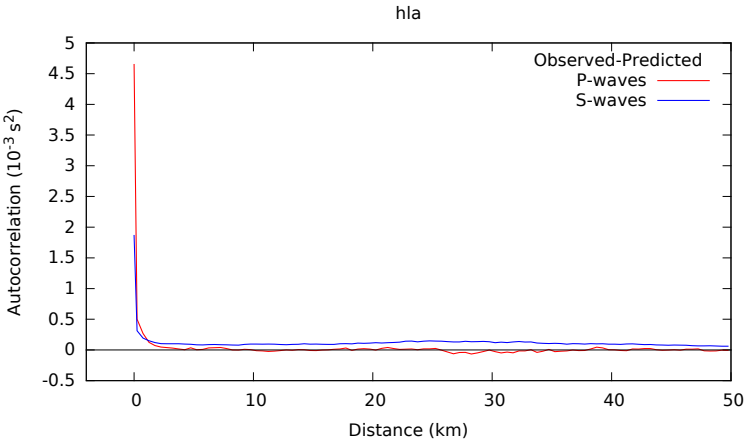
hla
Observed-Predicted
P-waves
S-waves
Autocorrelation (10-3 s2)
Distance (km)
5
4.5
4
3.5
3
2.5
2
1.5
1
0.5
0
-0.5
0
10
20
30
40
50

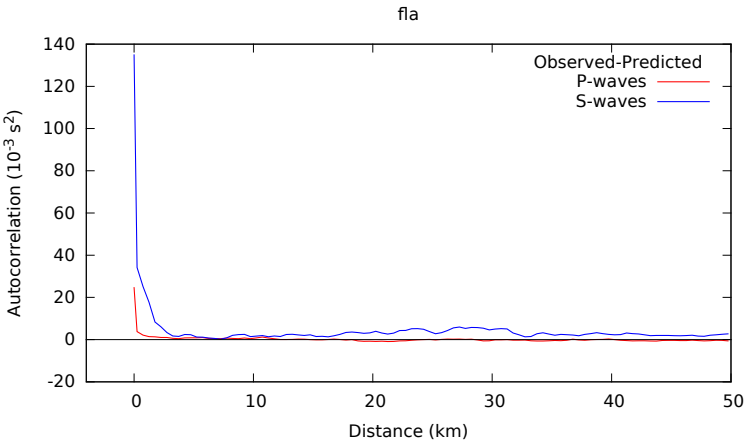
fla
Observed-Predicted
P-waves
S-waves
Autocorrelation (10-3 s2)
Distance (km)
140
120
100
80
60
40
20
0
-20
0
10
20
30
40
50

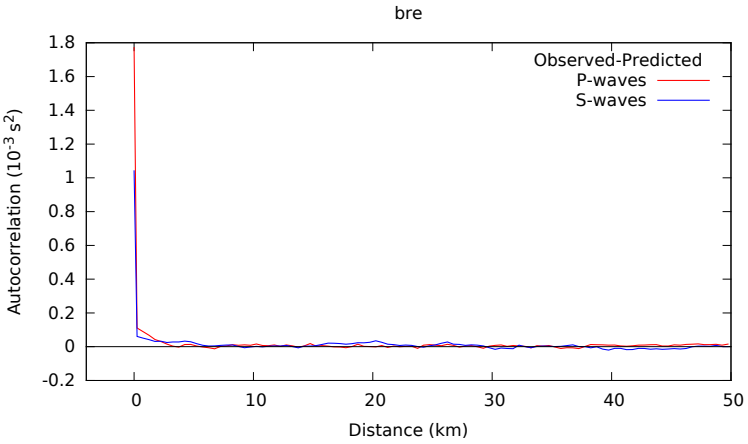
bre
Observed-Predicted
P-waves
S-waves
Autocorrelation (10-3 s2)
Distance (km)
1.8
1.6
1.4
1.2
1
0.8
0.6
0.4
0.2
0
-0.2
0
10
20
30
40
50

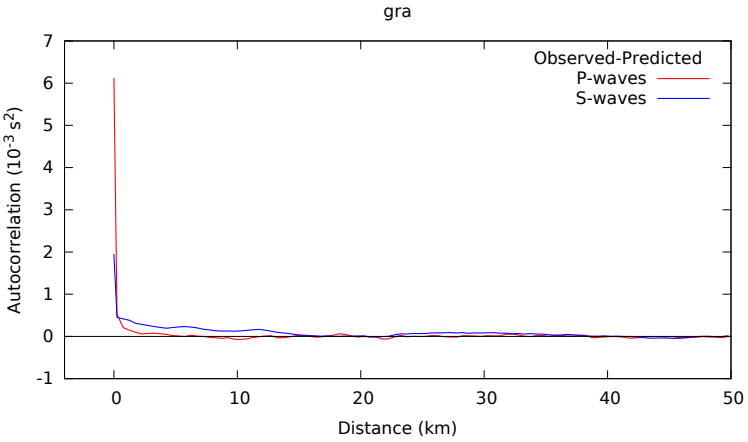
gra
Observed-Predicted
P-waves
S-waves
Autocorrelation (10-3 s2)
Distance (km)
7
6
5
4
3
2
1
0
-1
0
10
20
30
40
50

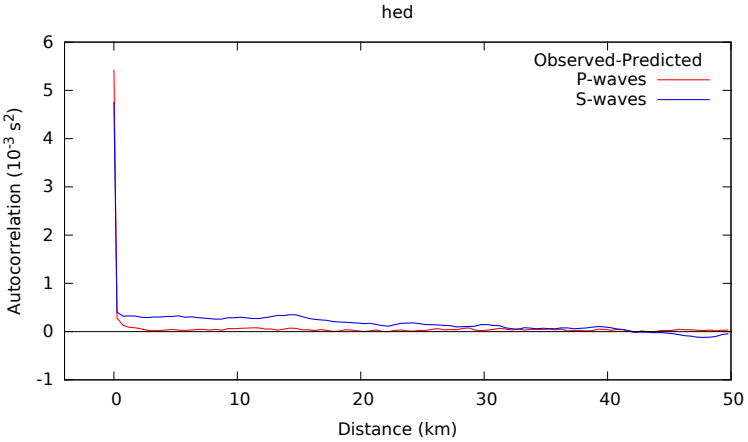
hed
Observed-Predicted
P-waves
S-waves
Autocorrelation (10-3 s2)
Distance (km)
6
5
4
3
2
1
0
-1
0
10
20
30
40
50

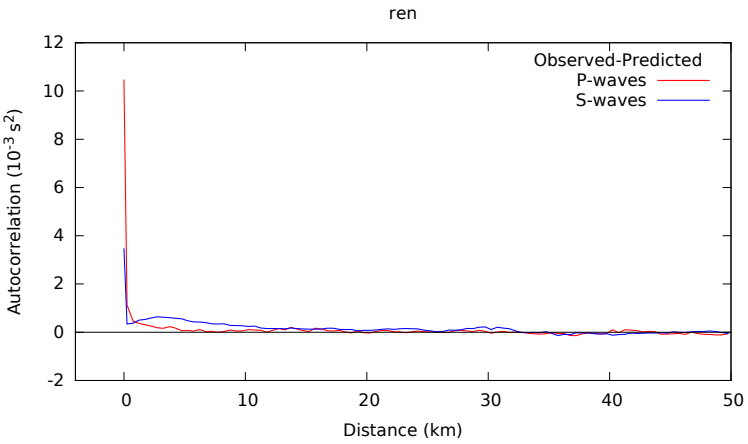
ren
Observed-Predicted
P-waves
S-waves
Autocorrelation (10-3 s2)
Distance (km)
12
10
8
6
4
2
0
-2
0
10
20
30
40
50

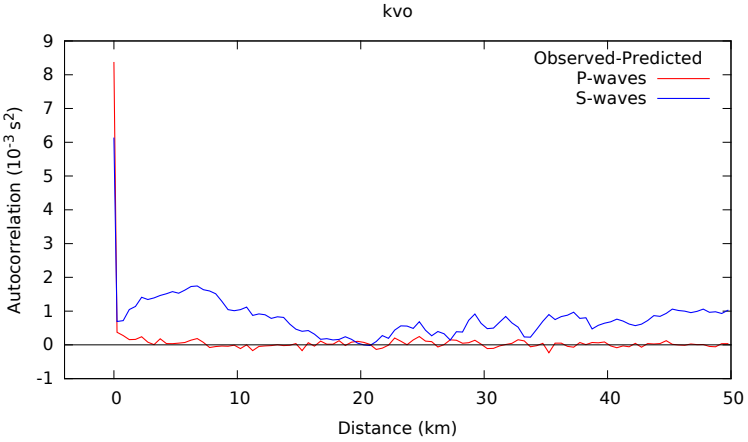
kvo
Observed-Predicted
P-waves
S-waves
Autocorrelation (10-3 s2)
Distance (km)
9
8
7
6
5
4
3
2
1
0
-1
0
10
20
30
40
50

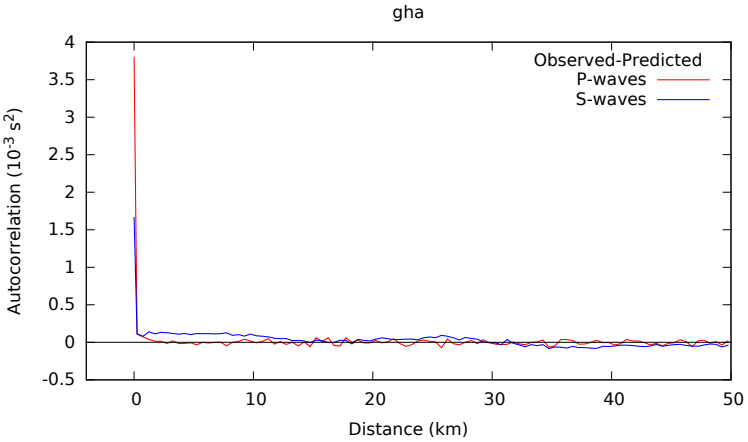
gha
Observed-Predicted
P-waves
S-waves
Autocorrelation (10-3 s2)
Distance (km)
4
3.5
3
2.5
2
1.5
1
0.5
0
-0.5
0
10
20
30
40
50

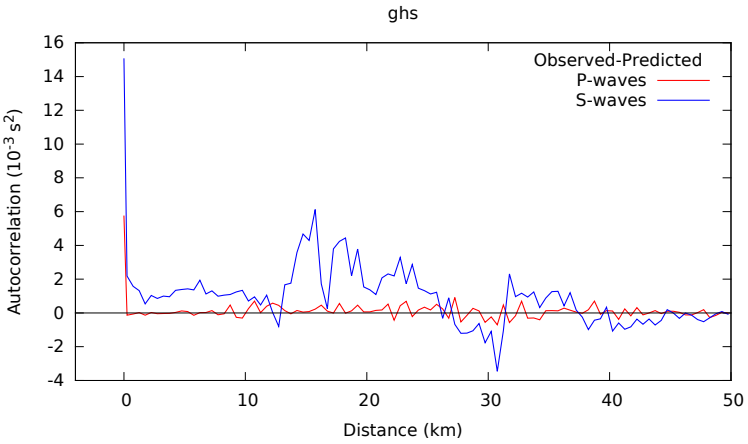
ghs
Observed-Predicted
P-waves
S-waves
Autocorrelation (10-3 s2)
Distance (km)
16
14
12
10
8
6
4
2
0
-2
-4
0
10
20
30
40
50

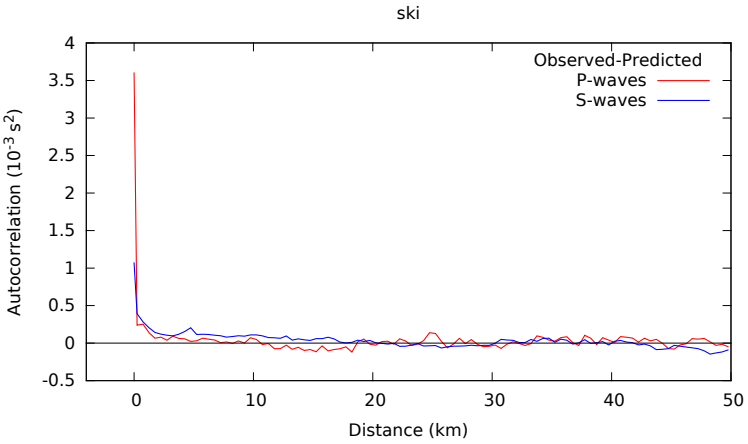
ski
Observed-Predicted
P-waves
S-waves
Autocorrelation (10-3 s2)
Distance (km)
4
3.5
3
2.5
2
1.5
1
0.5
0
-0.5
0
10
20
30
40
50

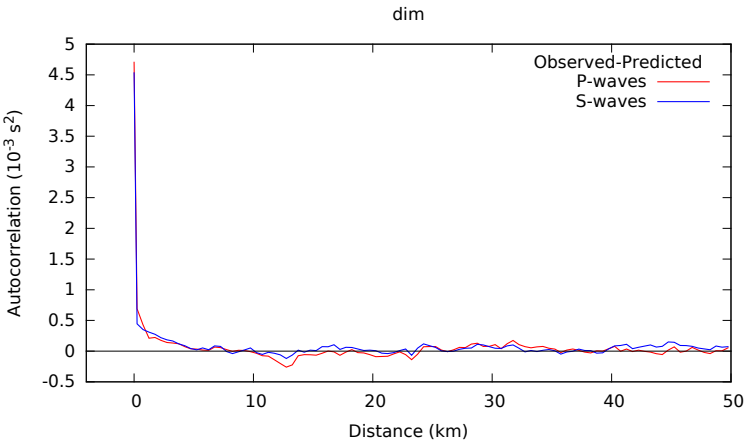
dim
Observed-Predicted
P-waves
S-waves
Autocorrelation (10-3 s2)
Distance (km)
5
4.5
4
3.5
3
2.5
2
1.5
1
0.5
0
-0.5
0
10
20
30
40
50

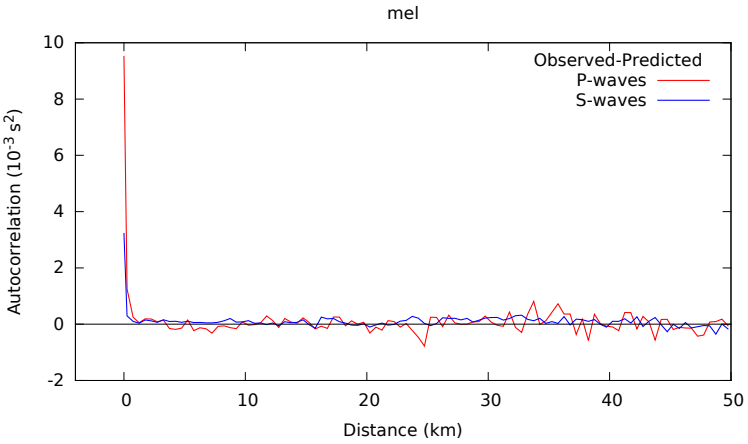
mel
Observed-Predicted
P-waves
S-waves
Autocorrelation (10-3 s2)
Distance (km)
10
8
6
4
2
0
-2
0
10
20
30
40
50

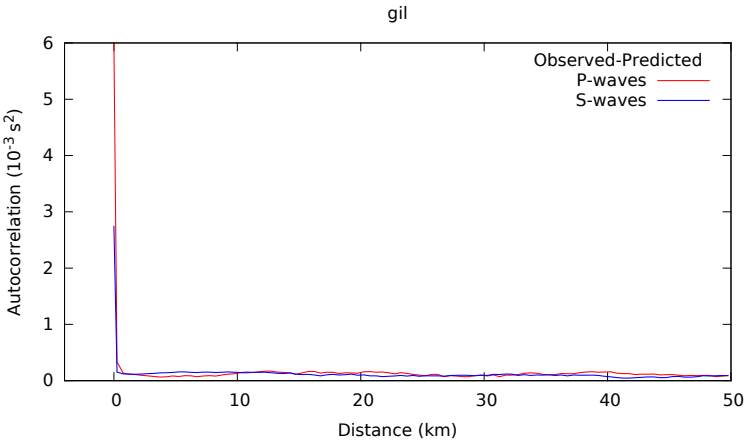
gil
Observed-Predicted
P-waves
S-waves
Autocorrelation (10-3 s2)
Distance (km)
6
5
4
3
2
1
0
0
10
20
30
40
50

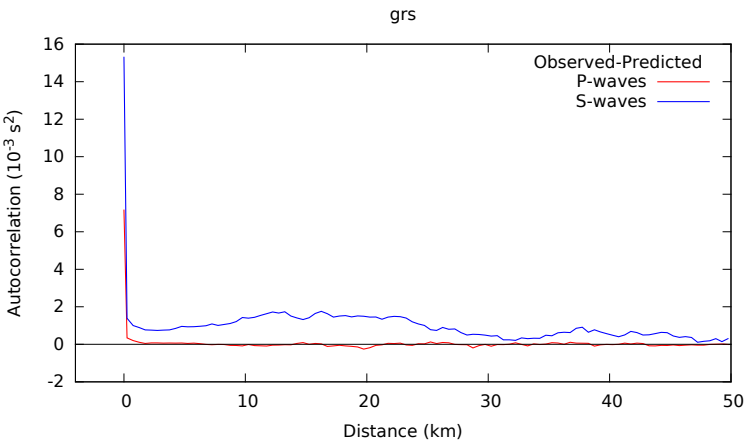
grs
Observed-Predicted
P-waves
S-waves
Autocorrelation (10-3 s2)
Distance (km)
16
14
12
10
8
6
4
2
0
-2
0
10
20
30
40
50

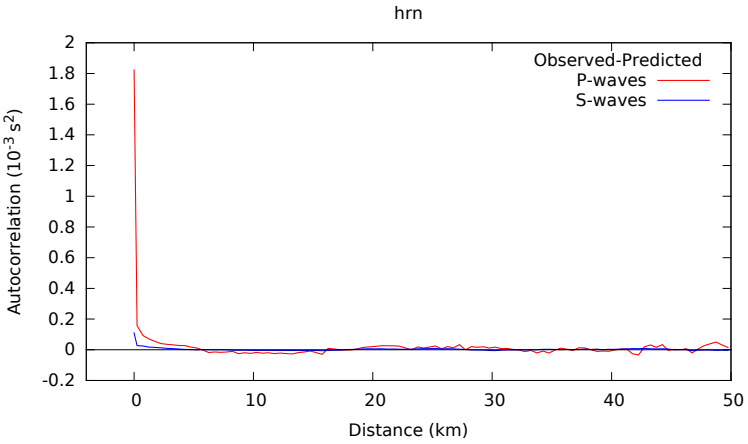
hrn
Observed-Predicted
P-waves
S-waves
Autocorrelation (10-3 s2)
Distance (km)
2
1.8
1.6
1.4
1.2
1
0.8
0.6
0.4
0.2
0
-0.2
0
10
20
30
40
50

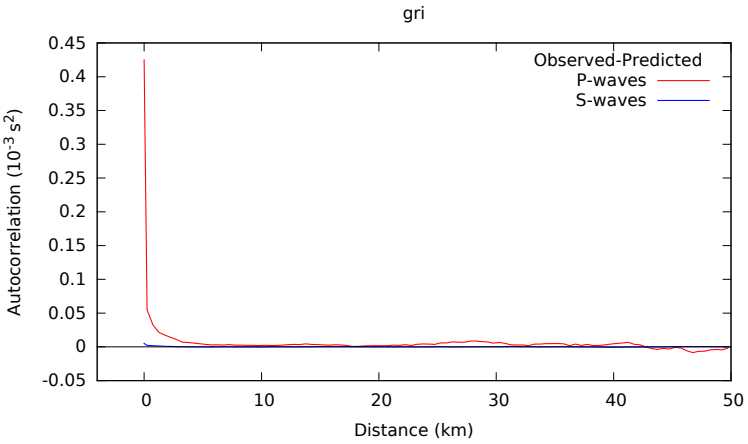
gri
Observed-Predicted
P-waves
S-waves
Autocorrelation (10-3 s2)
Distance (km)
0.45
0.4
0.35
0.3
0.25
0.2
0.15
0.1
0.05
0
-0.05
0
10
20
30
40
50

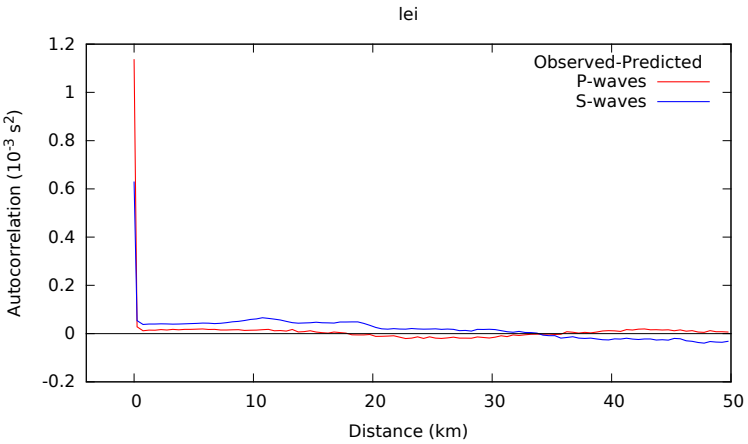
lei
Observed-Predicted
P-waves
S-waves
Autocorrelation (10-3 s2)
Distance (km)
1.2
1
0.8
0.6
0.4
0.2
0
-0.2
0
10
20
30
40
50

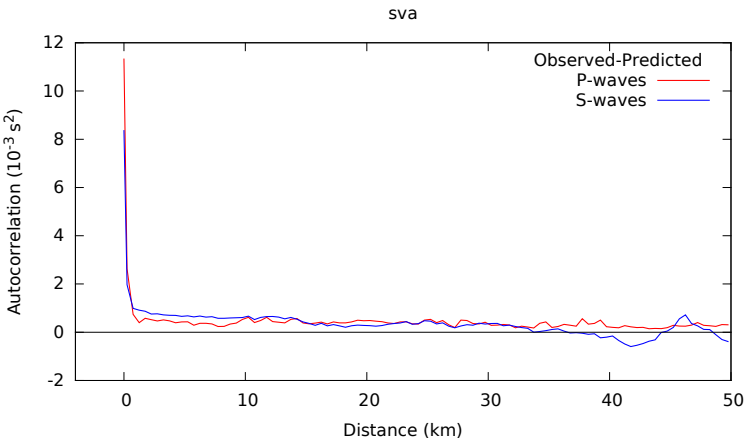
sva
Observed-Predicted
P-waves
S-waves
Autocorrelation (10-3 s2)
Distance (km)
12
10
8
6
4
2
0
-2
0
10
20
30
40
50

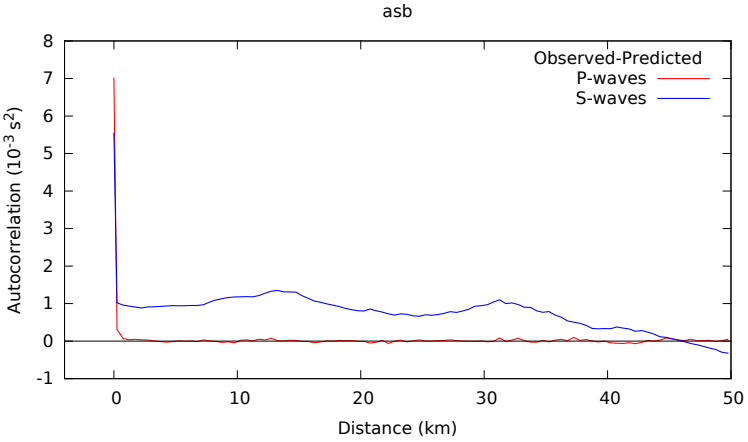
asb
Observed-Predicted
P-waves
S-waves
Autocorrelation (10-3 s2)
Distance (km)
8
7
6
5
4
3
2
1
0
-1
0
10
20
30
40
50

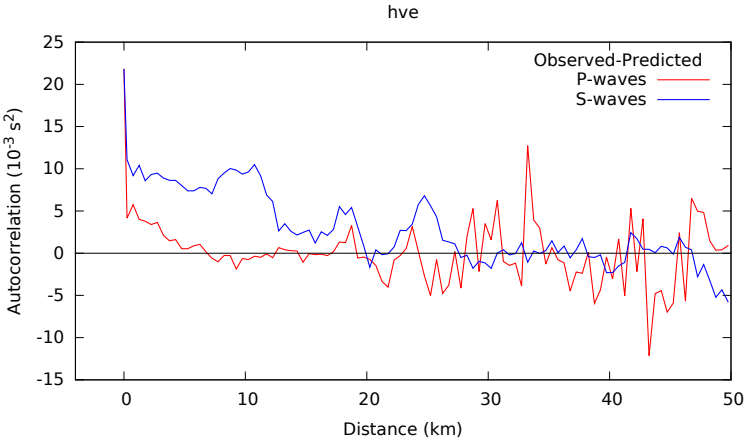
hve
Observed-Predicted
P-waves
S-waves
Autocorrelation (10-3 s2)
Distance (km)
25
20
15
10
5
0
-5
-10
-15
0
10
20
30
40
50

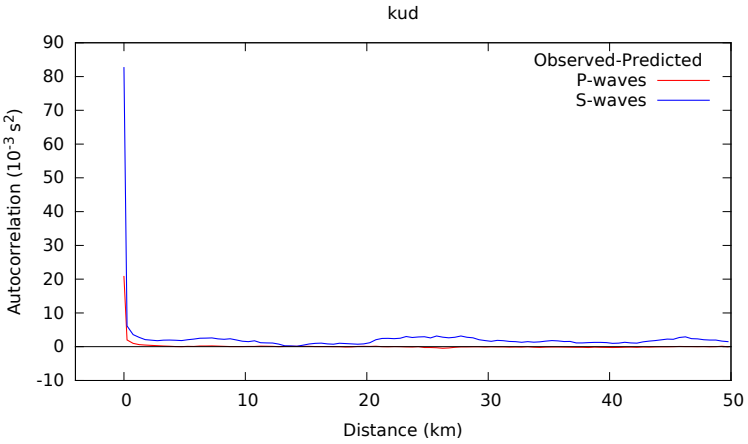
kud
Observed-Predicted
P-waves
S-waves
Autocorrelation (10-3 s2)
Distance (km)
90
80
70
60
50
40
30
20
10
0
-10
0
10
20
30
40
50

Appendix G

Relocations of the 1990-2012 SIL Catalog

The following are maps showing ipproximately 300.000 initial locations in the SIL Catalog and the same events after relocation using ETTs as a description of the forward problem predicting travel times. We present maps for most of the 16 subregions used by the IMO web page presenting event locations.Three of those regions are not shown. The first is the Western Fjords region, where no events are relocated. The second is the North Atlantic region. Again no events were relocated in this region. The third is the large version of the Tjörnes Fracture Zone, omitted here because it is redundant and less detailed as the small version of the same region. The regions are presented in the following order, with names used on the IMO web page in brackets and page number also listed for each map:

1)	Eastern Fjords	(East fjords)	G3
2)	Hengill	(Hengill)	G4
3)	Hofsjökull	(Hofsjökull)	G5
4)	Langjökull	(Langjökull)	G6
5)	Myrdalsjökull	(Myrdalsjökull)	G7
6)	Northern Volcanic Zone	(Myvatn)	G8
7)		(North Atlantic)	Omitted
8)	Reykjanes Peninsula	(Reykjanes peninsula)	G9
9)	Reykjanes Ridge	(Reykjanes ridge)	G10
10)	Southern Iceland	(Southern Iceland)	G11
11)	Western Iceland	(Snaefellsnes)	G12
12)	Tjörnes Fracture Zone	(Tjörnes fracture zone-small)	G13
13)		(Tjörnes fracture zone-large)	Omitted
14)	Vatnajökull	(Vatnajökull)	G14
15)		(West fjords)	Omitted
16)	Vestmanna Islands	(Vestmannaeyjar)	G15

The depth of each event is indicated with colours as defined in legends. The events are plotted in time order.

The effect of relocations on the epicentral distribution are not dramatic, but noticeable. We point out that, in particular on the outskirts of the SIL network the epicenters are clearly clustered. This is perhaps most noticeable in the Tjörnes Fracture Zone where the Husavik-Flatey lineament is clearly focussed. Also, the curious transverse bands of seismicity in between the Grimsey lineament and the Husavik-Flatey lineament are focussed. Seismicity on the Reykjanes is somewhat focussed, although almost certainly still artificially diffuse in the relocated distribution. Some of the artificial events (associated with construction) in the east of Iceland are slightly

more clustered in the relocated distribution. Another significant effect of the relocations is that the depth distribution of events is clearly more coherent in space, which is most evident in the regions of dense seismicity, e.g., in the Tjörnes Fracture Zone.

Eastern Fjords

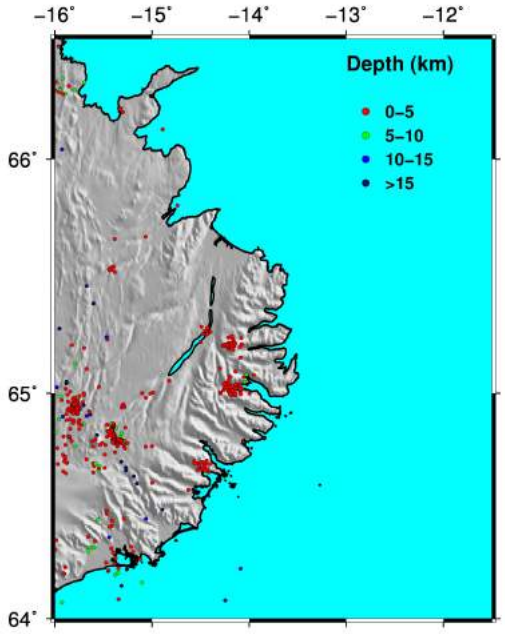

SIL

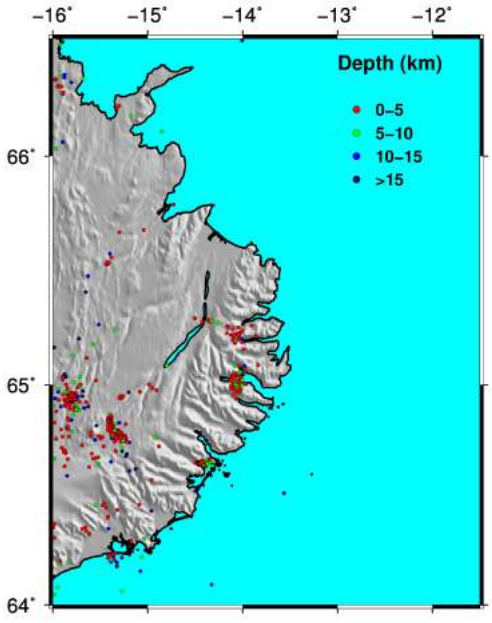

RELOCATION

Hengill

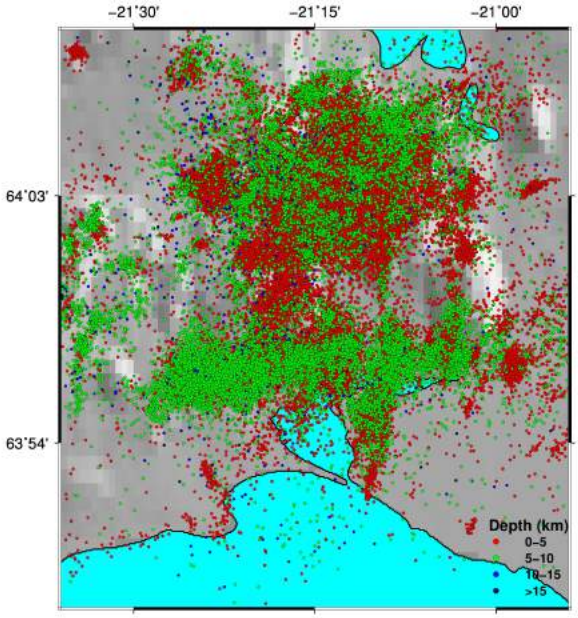

SIL

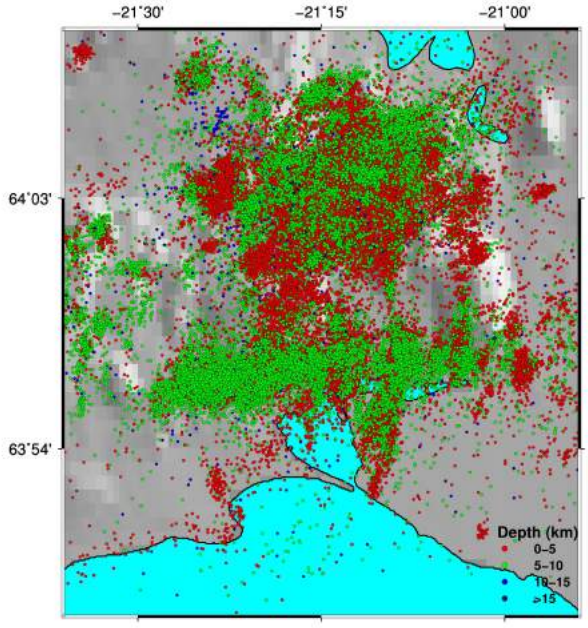

RELOCATION

Hofsjökull

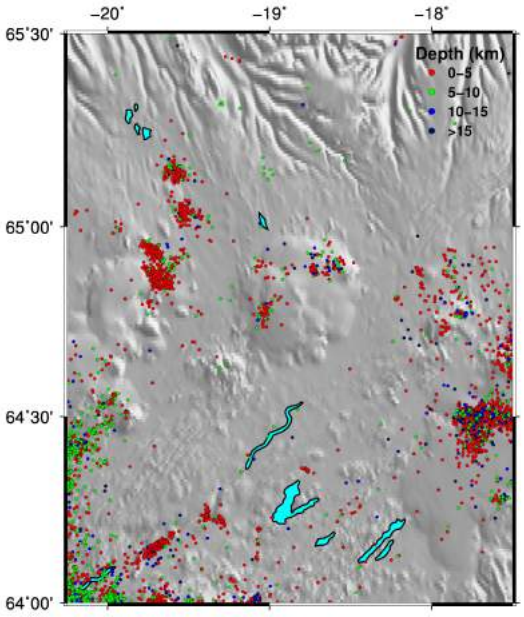

SIL

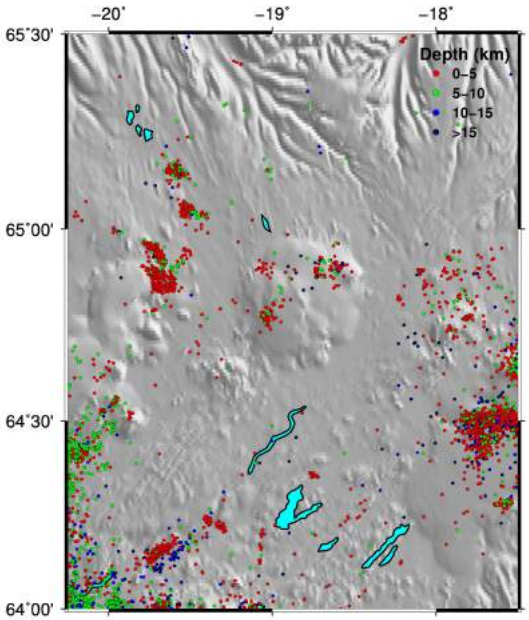

RELOCATION

Langjökull

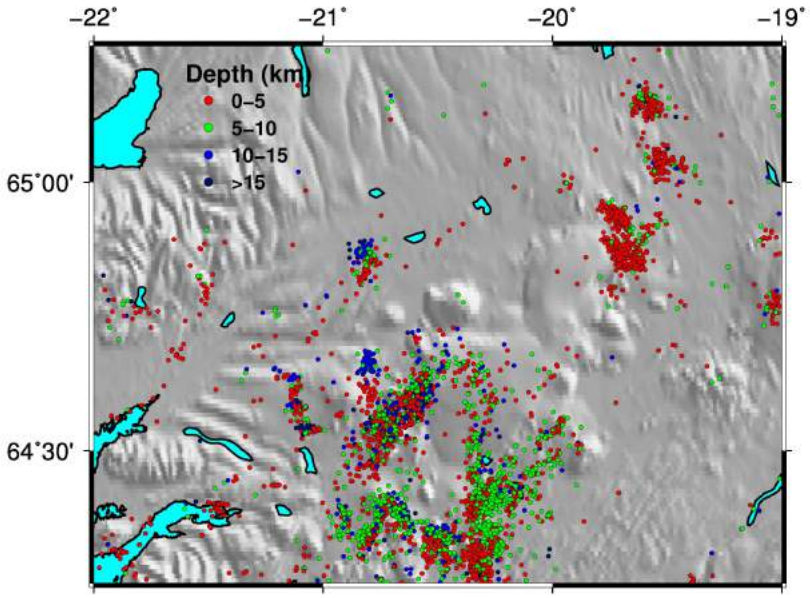

SIL

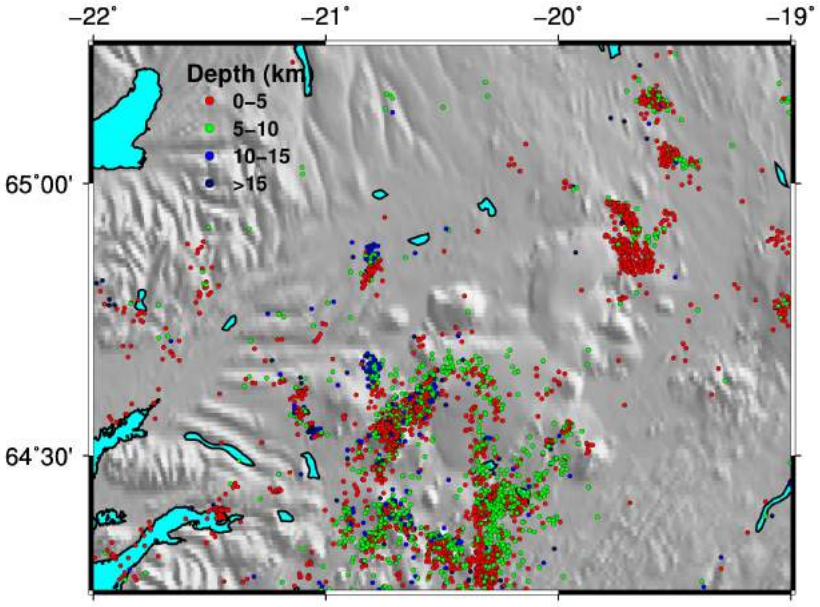

RELOCATION

Myrdalsjökull

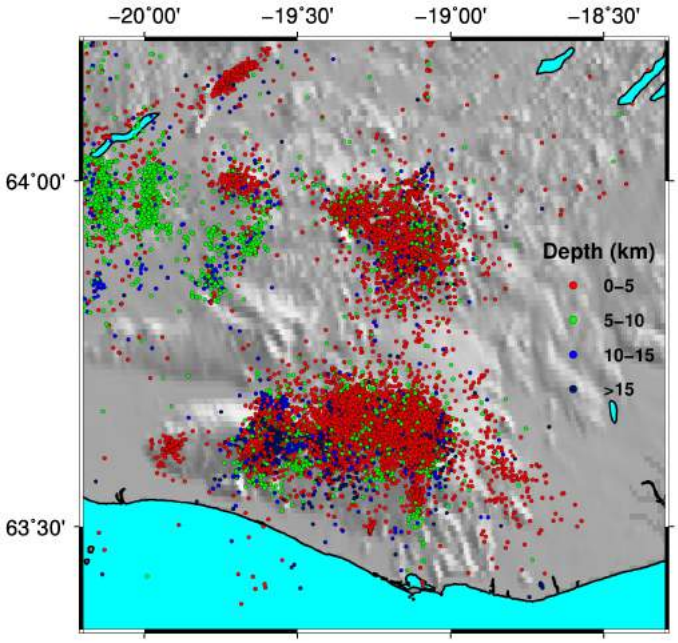

SIL

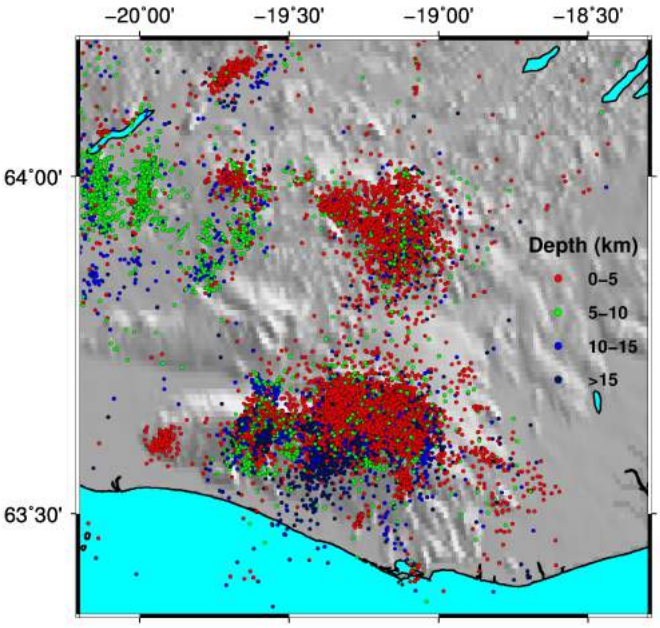

RELOCATION

Northern Volcanic Zone

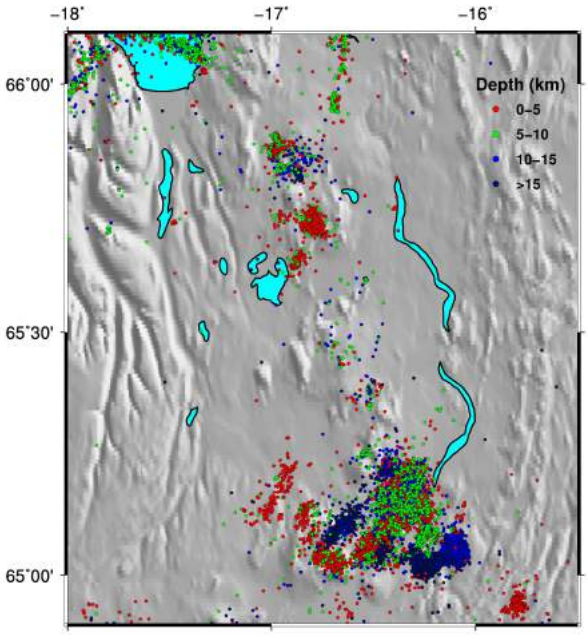

SIL

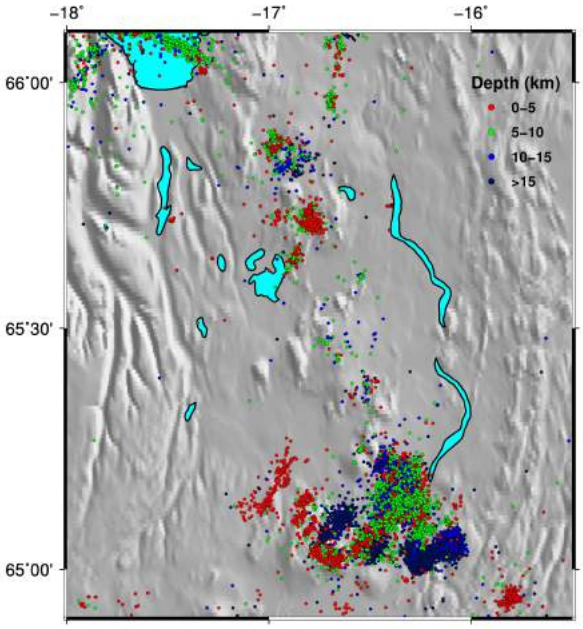

RELOCATION

Reykjanes Peninsula

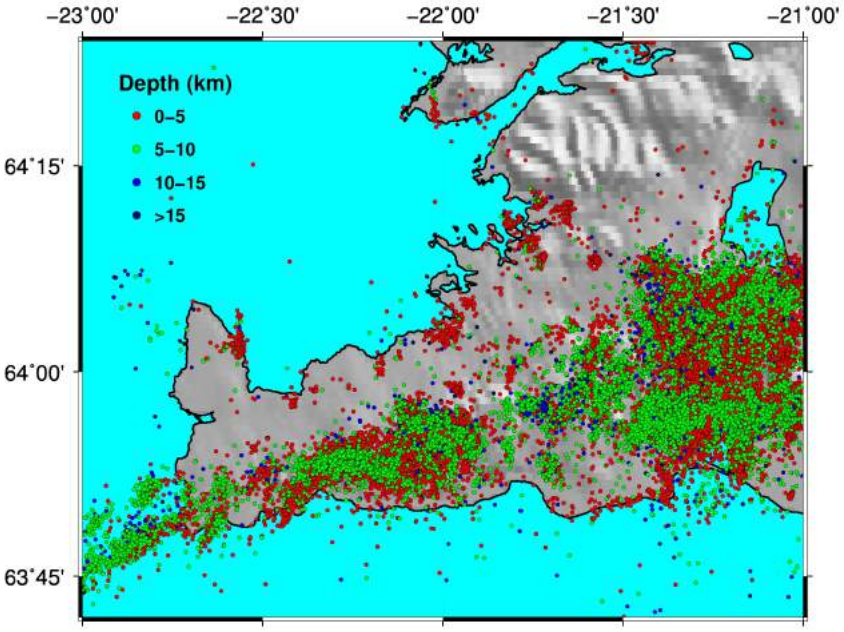

SIL

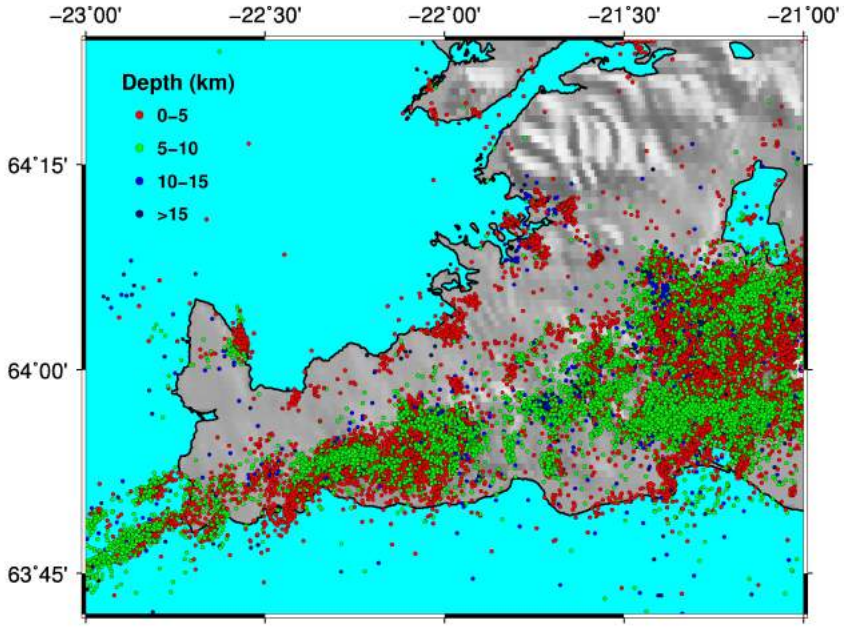

RELOCATION

Reykjanes Ridge

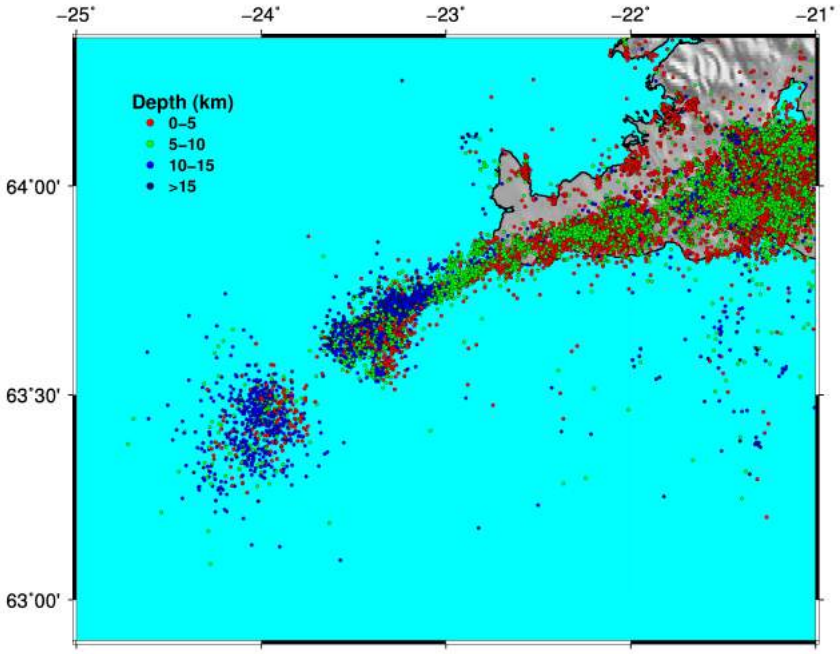

SIL

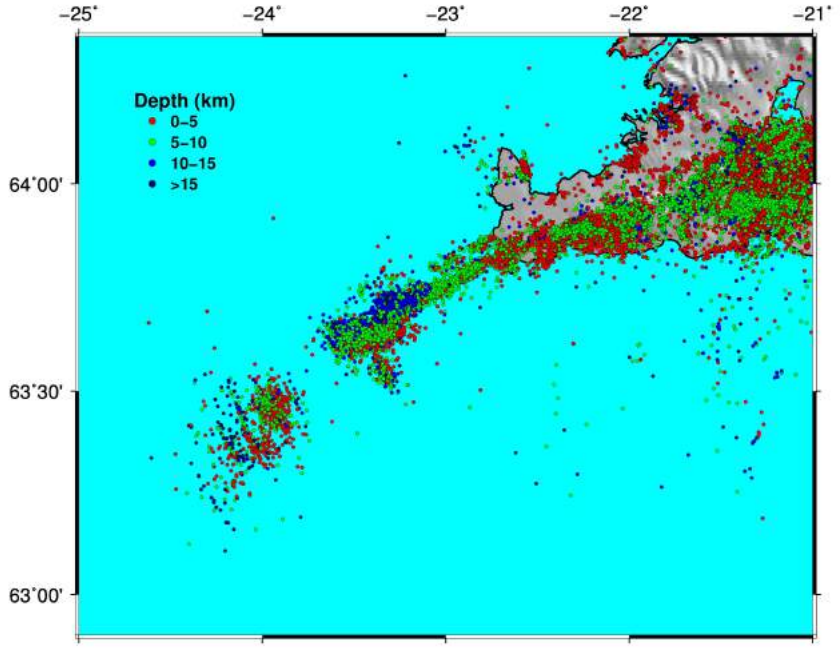

RELOCATION

Southern Iceland

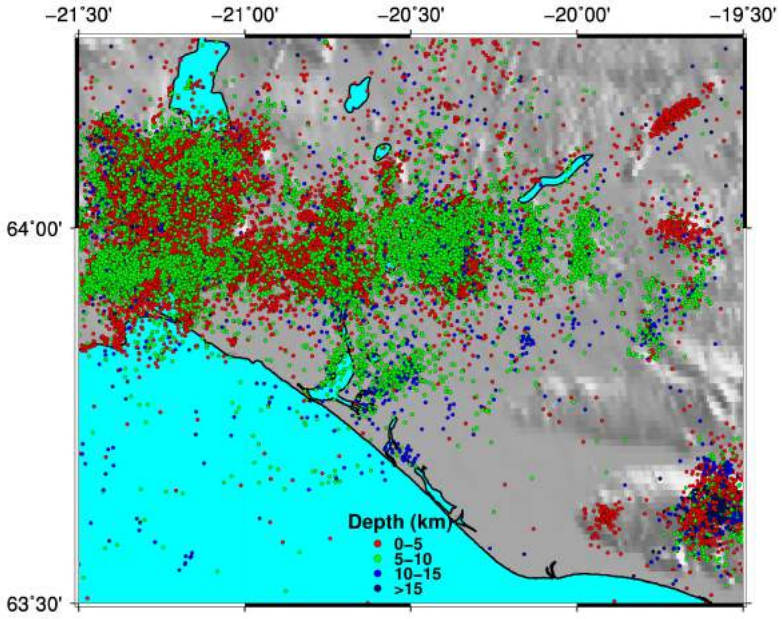

SIL

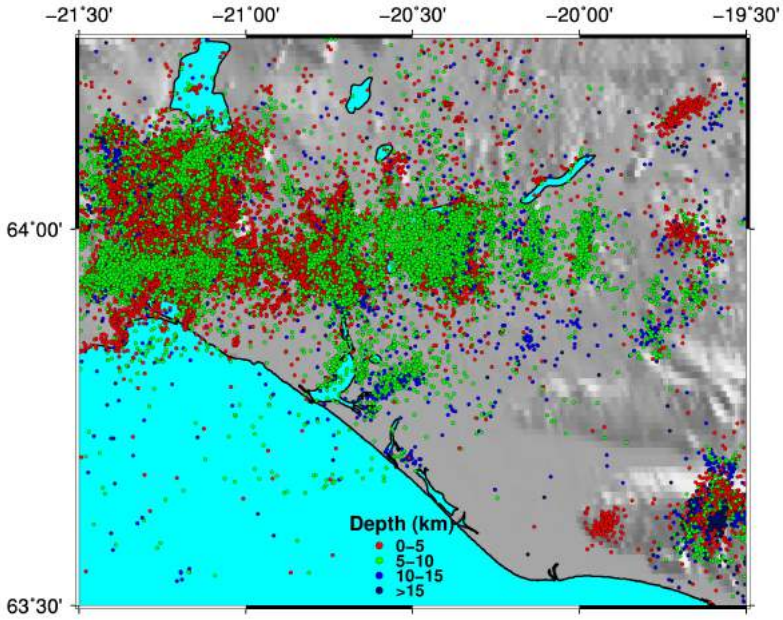

RELOCATION

Western Iceland

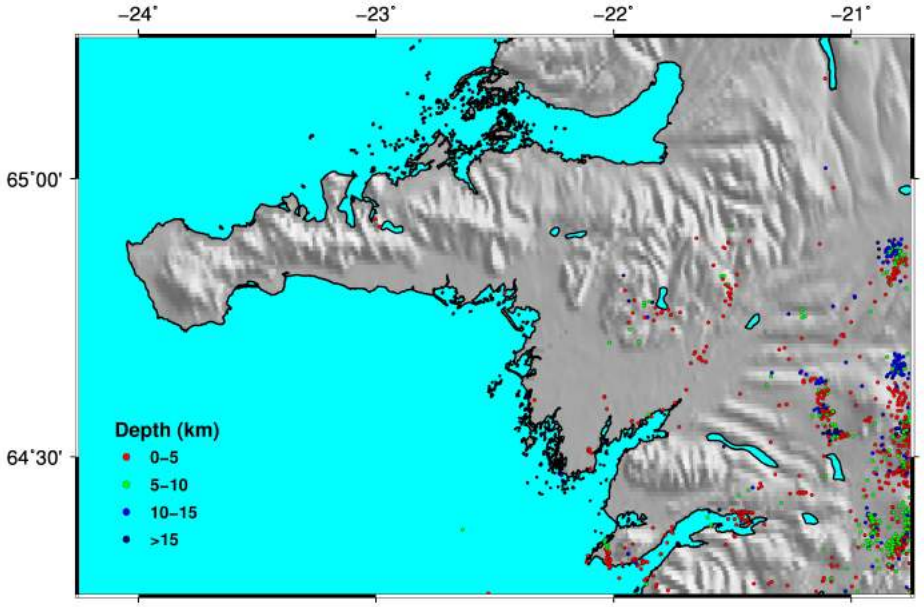

SIL

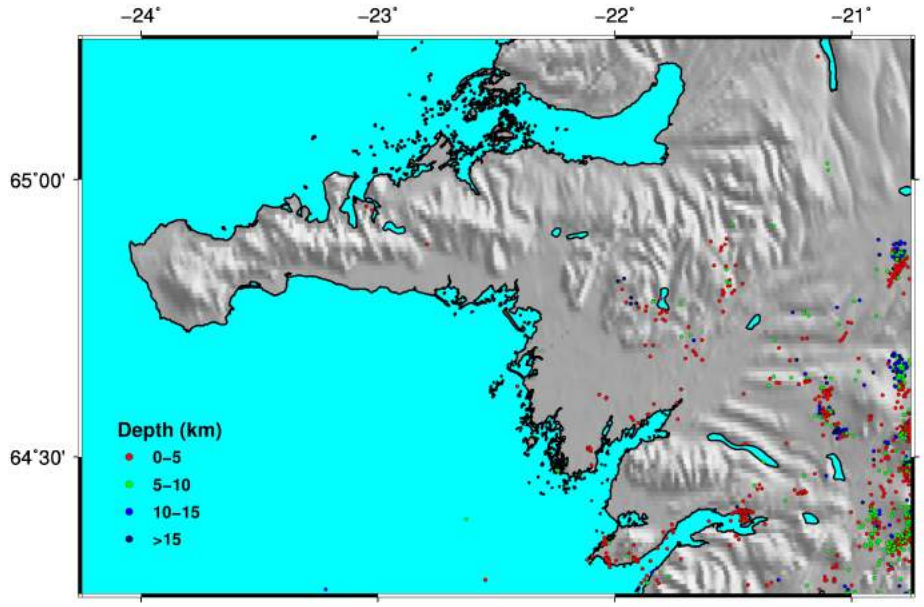

RELOCATION

Tjörnes Fracture Zone

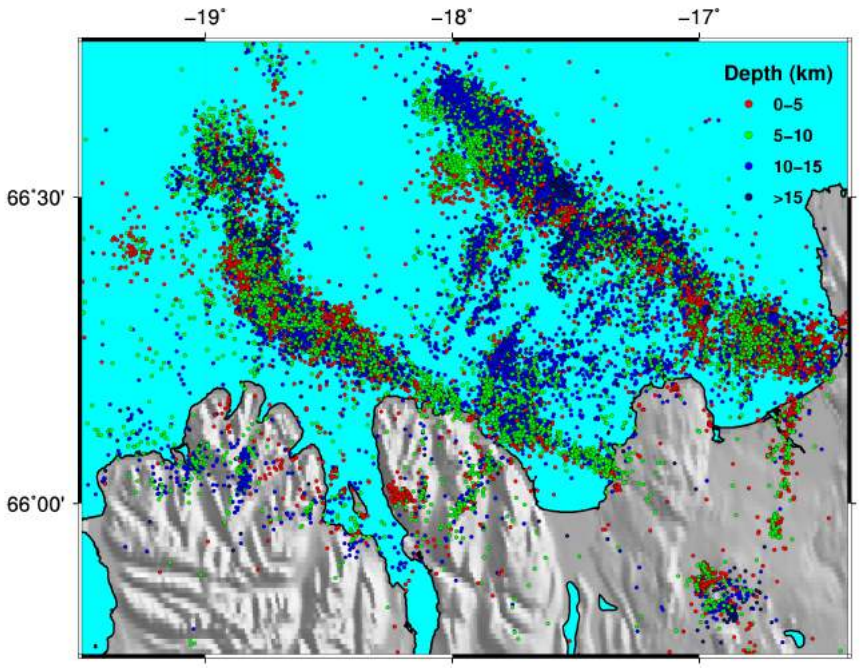

SIL

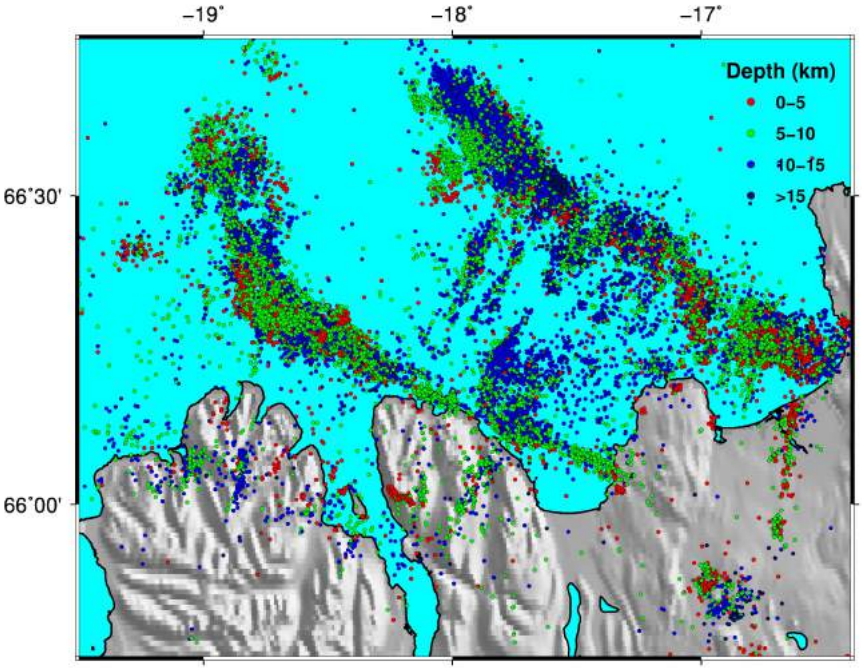

RELOCATION

Vatnajökull

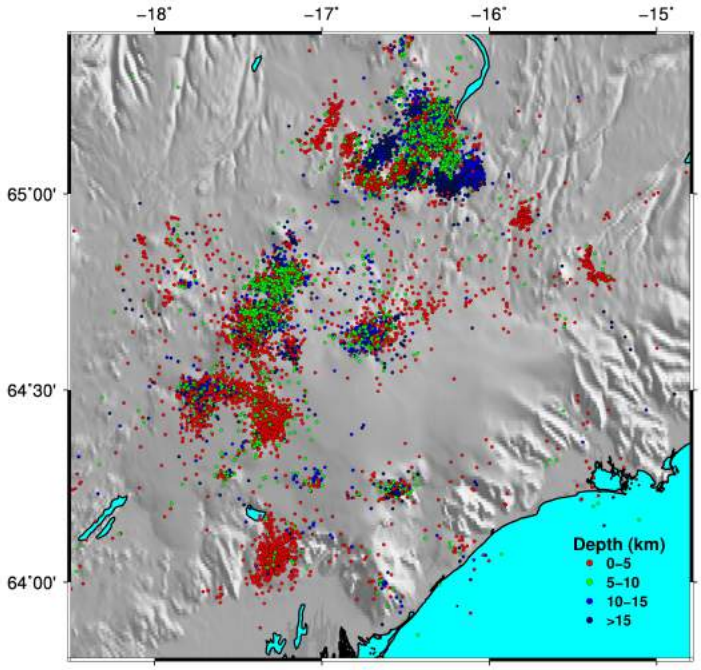

SIL

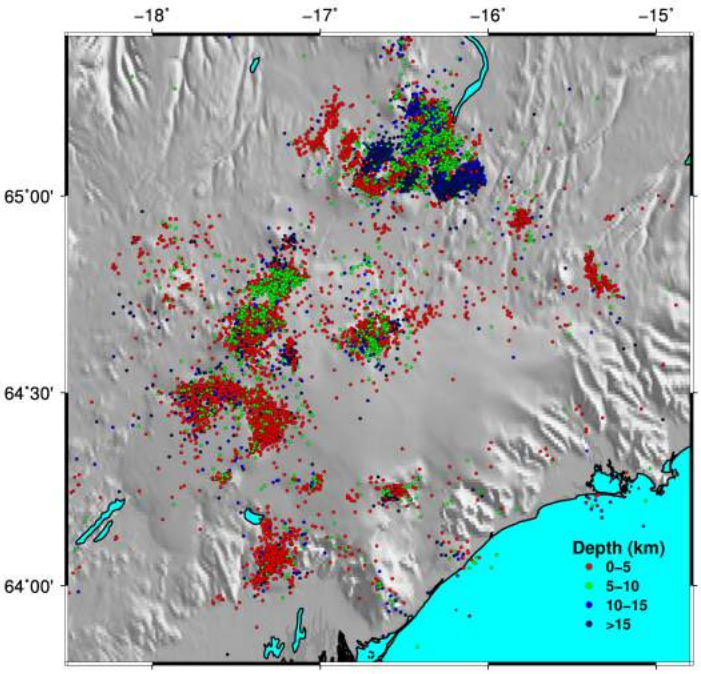

RELOCATION

Vestmanna Islands

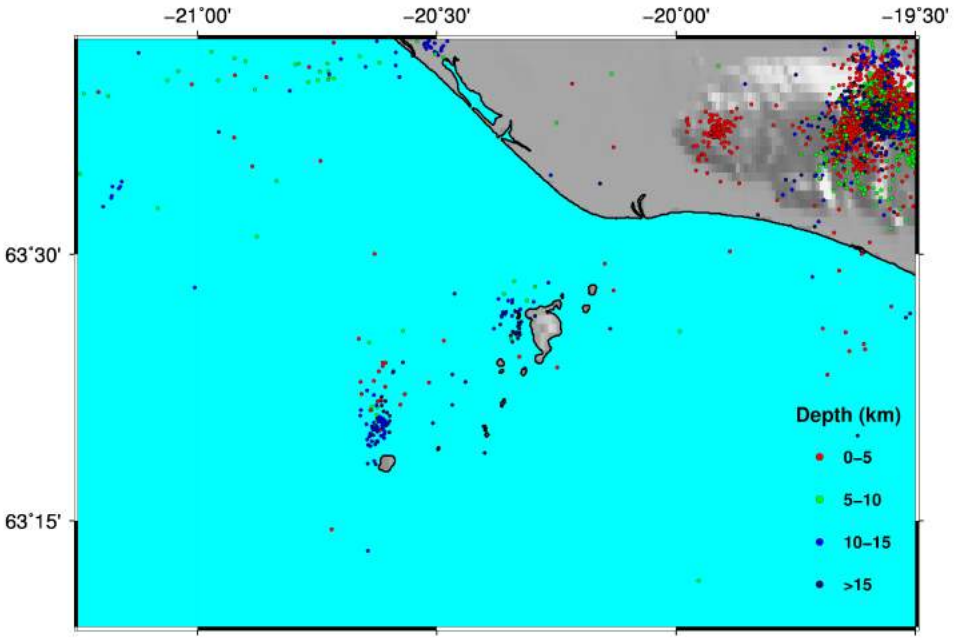

SIL

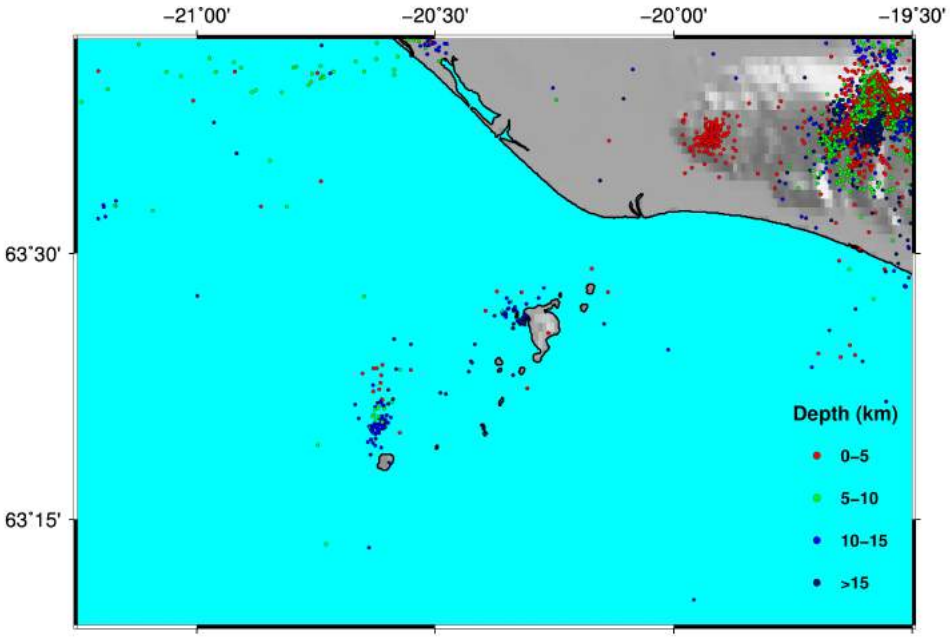

RELOCATION